JACOBS
UNIVERSITY

# Raman Spectroscopic Probing of Key Biological Events – Tumorigenesis, Hsp70 Chaperon Mechanisms, and Therapy Response

by

Patrice Donfack

A thesis submitted in partial fulfillment
of the requirements for the degree of

Doctor of Philosophy
in Physics

**Approved, Thesis Committee:**

Prof. Dr. Arnulf Materny
Jacobs University, Bremen, Germany

Prof. Dr. Jürgen Fritz
Jacobs University, Bremen, Germany

Prof. Dr. Michael Schmitt
Jena University, Jena, Germany

Date of Defense: May, $13^{th}$ 2011

School of Engineering and Science

# Raman Spectroscopic Probing of Key Biological Events – Tumorigenesis, Hsp70 Chaperon Mechanisms, and Therapy Response


PhD Thesis

by

Patrice Donfack

School of Engineering and Science
Jacobs University, Bremen, Germany
May, $13^{th}$ 2011

To

*My mother, brother Bertrand Nguefack, and sisters;*
*in remembrance of my late father and my late sister Elise.*
*And*
*My family, friends and everyone who has supported or helped*
*me throughout my eduction, studies, and research ···*

School of Engineering and Science
Jacobs University, Bremen, Germany

# PhD Thesis

## Raman Spectroscopic Probing of Key Biological Events – Tumorigenesis, Hsp70 Chaperon Mechanisms, and Therapy Response

## Abstract

Light scattering is the simplest and most common scenario where incident light with a certain energy or color corresponding to a given frequency, is bounced off any object or particle in all directions. While most of this scattered light appears unchanged (having the same color), Raman scattering represents a very small portion of the scattered light that has different colors corresponding to many components with frequencies different from that of the incident light. The Raman shifts, or the frequency differences observed in Raman scattering, represent the corresponding amounts of energy that are exchanged between a material system and the light incident on it, and which can fit into possible transitions within the material system. Therefore, the collection of all Raman shifts (Raman spectrum) for a given material are characteristic of the material properties, providing a way to identify and/or discriminate different molecular systems. The Raman process, as just defined, is linear, and is termed resonant Raman if the incident light frequency matches that of an electronic transition in the molecule, or surface enhanced Raman if the irradiated molecule is in close contact with a rough metal surface. Nonlinear Raman scattering involves multi-photon interactions.

In this thesis, Raman spectroscopy is applied as a noninvasive and nondestructive tool for the investigation of biological systems including biomolecules, cells, and tissue, both *in vivo* and *in vitro*. In particular, this thesis addresses key biological events such as cancer transformation and development, biological rhythm and hormonal deregulation, Hsp70 phenotypic variation and chaperon properties, and therapy response. In addition, a simple fabrication of special metallic nanoparticles and the interaction of a simple biomolecule at metal substrates are also covered. Combining different Raman techniques, the focus is not only to demonstrate the diagnostic capability of Raman spectroscopy for cancer and/or other pathological conditions. It is also directed toward noninvasive targeting of disease

biomarkers for a possible understanding of the molecular basis of disease onset and development. First, using a model cell line for skin carcinoma, it is demonstrated that Raman scattering not only can help to discriminate healthy skin keratinocytes from their cancerous counterparts, but also can provide molecular insights into genetic instabilities in the human keratinocytes cells HaCaT. Furthermore, the potential for Raman monitoring of lymphoma incidence and histological subtypes in subjects at risk is evaluated using spleen tissue of a lymphoma mouse model. Another animal model (Djungarian hamsters) is used to test Raman spectroscopy as an approach for the study of the biological rhythm associated with rhythmic hormonal regulation of the reproductive system in photoperiodically sensitive breeding mammals. This work highlights the possibility for noninvasive and nondestructive phenotypic sorting of cells sublines. In this respect, Raman microscopy has been used to gain specific insights into intracellular mechanisms leading to Hsp70 chaperon properties and associated phenotypic variation in colon carcinoma sublines. Additionally, in situ Raman monitoring of drug response has been achieved in this work. Finally, it is shown that biocompatible metal nanoparticles with specific geometry, and promising for molecular targeting, can be easily and reliably fabricated. Surface enhanced Raman studies on the simplest amino acid glycine reveal that, proteinaceous compounds can behave and interact in a complex concentration-dependent manner at metal interfaces. In this respect special designs for the fabrication of nanometal substrates can be beneficial for surface enhanced Raman investigations of biological systems.

Author: **Patrice Donfack**
Supervisor: Prof. Dr. Arnulf Materny

# Acknowledgments

The completion of this thesis marks an end to a lengthy experience in PhD, not without endurance and unpredictable circumstances, but with perseverance and hope in the end.
I am above all indebted to special support, care and unique commitment from my mother **Lucienne Toukem**, my brother **Bertrand Nguefack**, and my sister **Angèle Flore Mbieda**.
I would like to thank everyone who in one way or the other helped me or made me realize that I was able not only to finish my thesis, but also to complete it successfully. Hence, this work could not have been possible without the support from many people.

I am all the more indebted to my PhD advisor, **Prof. Dr. Arnulf Materny**, both for his supervision of my research, and for his trust and moral support from beginning on. His endless kindness and incredibly friendly humor and his moral support at a time I needed it the most all justify my perseverance and successful achievement.
I am also indebted to **Prof. Jiming Hu** for his co-supervision of the joint research projects included in this thesis, which were part of DAAD/CSC ppp (SCS = Chinese Scholarship Council; PPP = "Programme des Propjektbezogenen Personenaustauschs").
I am especially thankful to **Prof. Dr. Gabriele Multhoff**, **Prof. Dr. Claudia Brix**, **Prof. Dr. Alexander Lerchl**, and **Dr. Animesh Ojha** for their scientific support and collaborative help resulting in the main contributions of this thesis.

Both for their help, and especially for their friendship, I thank Vinu Namboodiri, Rasha Hassanein, Abraham Scaria, Mahesh Namboodiri, Binit Lukose, Mehdi M. Kazemi, Ajay Singh, Jakow Konradi, Malte Sackmann, Günter Flachenecker, Mohamed Elkhouly, and Bernd von der Kammer. For the same reason, I thank my collaborators Elena Sagitova, Animesh Ojha, Aiguo Shen, Wei Xie, Xiaodong Zhou, Jing Shen, Wei Wang and Toa Hu.
Ajay reminds me of my first days in Prof. Materny's group and my integration into the university social community. I owe my first truly skilled laser alignment tricks to Abraham. Malte often sacrificed his own working time just to help me and others. Vinu strengthens my love to physics via our enriched discussions ending usually with a toast and fun. With Vinu, Mahesh and Binit around me, we had a way to escape from stress by playing, and Vinu and I would help each other even in fun games. Seeing Günter and Mohamed was enough to be happy even in difficult times, since, besides their advice as senior scientists, they contributed to an incredibly friendly and fun atmosphere in Prof. Materny's group.
In view of the achievements throughout my PhD research overall, I am highly appreciative of my colleague and research partner **Dr. Rasha Hassanein** (**Rasha M. El-Abassy**) for her

great team spirit in teamwork resulting in several published works, which, though not described in the present thesis, have been mentioned in the "List of Publications"; thank you Rasha. For the same reason, I equally thank my research partner **Dr. Elena A. Sagitova**.

In connection with Prof. Hu research group, I am urged to acknowledge the great contribution from **Dr. Aiguo Shen** and **Dr. Wei Xie** as the main leaders of our joint projects, with whom I worked both at Jacobs University (Bremen, Germany) and at Wuhan University (Wuhan, China) on the projects described in chapter 7 (**Dr. Aiguo Shen**) and chapter 8 (**Dr. Xie Wei**). We did not only work together, but we also regularly took our brainstorming to the dining table while enjoying Chinese delicacies. Thank you Prof. Hu, Aiguo, Xie Wei, and Xiaodong for making my research visits in Wuhan an unforgettable experience.

In connection with Prof. Materny, Prof. Brix and Prof. Lerchl working groups, I am grateful to **Bernd von der Kammer**, **Maren Rehders** and **Karen Grote**, both for their collaboration and their highly valued lab assistance in the respective laboratories.

**I especially thank all my dear friends, including Kristin Fedeler, Abdurazak Mudesir and all others I have not explicitly named here, for their friendship, moral support and their continued positive thinking, especially when I appeared to have given up**.

On the social aspect, I am grateful to the college masters of Krupp college, Isabelle and Klaus Schmann, for their hospitality. Under their advice, I applied successfully to become a resident associate. I have held this position for nearly four years (since 2007) and have found in Krupp college a home away from home.

I am grateful to the DAAD (German Academic Exchange Service) for a 3.5 year doctoral grant and a 6-month grant for German language training. Both grants enabled me to embrace the German culture and carry out my PhD research.
I am also thankful to Jacobs University for another 8-month extension grant.

For my joint projects and my co-workers, financial supports by the National Natural Science Foundation of China (Nos. 30772058, 20705025), the NSFC-KOSEF Scientific Cooperation Program (No. 20711140390, China), the Foundation of Chemo/Biosensing and Chemometrics (Hunan University, China), the PPP (DAAD and Chinese Scholarship Council, CSC), the DFG (German Research Foundation, MA 1564/16-1 and MA 1564/18-1), and the A.v. Humboldt Foundation are highly acknowledged.

**Patrice Donfack**
Bremen, April 19, 2011

# Contents

# List of Figures

# List of Tables

# Glossary

**CARS** Coherent anti-Stokes Raman scattering

**CCD** Charge-coupled device

**CDNB** 1-Chloro-2,4-dinitrobenzene

**CRS** Confocal Raman spectroscopy

**CSRS** Coherent Stokes Raman scattering

**CT** Computer tomography

**BCC** Basal cell carcinoma

**DMEM** Dulbecco's Modified Eagle's Medium

**ECM** Extracellular matrix

**EDTA** Ethylene-diamine-tetraacetic acid; a chelating (two-pronged) molecule used to sequester most divalent (or trivalent) metal ions, such as calcium ($Ca^{2+}$) and magnesium ($Mg^{2+}$), copper ($Cu^{2+}$), or iron ($Fe^{2+}$ / $Fe^{3+}$)

**EDX** Energy-dispersive X-ray

**EM** Electromagnetic; referring to light

**EMF** Electromagnetic field

**EXD** Energy dispersive X-ray diffraction

**FACS** Fluorescence activated cell sorting; also spelled FACScan when referring to the experiment itself

**FCS** Fetal calf serum

**FITC** Fluorescein isothiocyanate, used for cell sorting in FACScan analysis

**GFP** Green fluorescence protein

**GSH** Glutathione

**GSM** Global System for Mobile Communication

**GST** Glutathione S-Transferase

**HRS** Hyper Raman scattering

**HRTEM** High resolution transmission electron microscopy

**HSCs** Hepatic stellate cells (HSCs)

**I3C** Indole-3-carbinol

**ICCD** Intensified charge-coupled device

**ICP-OES** Inductively Coupled Plasma Optical Emission Spectrometry

**IR** Infrared, when referring to a region of the Em spectrum, and to spectroscopy

**LB** Lymphoblastic lymphoma: large and mixture of large and small lymphocytes

**LL** Lymphoblastic lymphoma or small lymphoblastic lymphoma: small lymphocytes

**mAb** Monoclonal antibody

**MRI** Magnetic resonance imaging

**MRS** Micro-Raman spectroscopy

**NMR** Nuclear magnetic resonance

**NOPA** Noncollinear optical parametric amplifier

**OARS** Optical activity Raman spectroscopy

**OPA** Optical parametric amplifier

**PBS** Phosphate buffer saline

**PCA** Principal component analysis

**PFA** Paraformaldehyde

**RS** Raman scattering or spectroscopy, when referring to the spontaneous and therefore linear Raman scattering

**ROT** Raman optical trapping spectroscopy

**SCC** Squamous cell carcinoma

**SERS** Surface enhanced Raman scattering

**SRS** Stimulated Raman scattering

**SRGS** Stimulated Raman gain scattering

**SRLS** Stimulated Raman loss scattering

**TEM** Transmission electron microscopy

**UMTS** Universal Mobile Telecommunication System

**UV** Ultra violet

**VIS** Visible light

**WBC** White blood cell

# 1. Introduction

## 1.1 The Raman Effect and Birth of Raman Spectroscopy

The Raman effect, which forms the basis of Raman spectroscopy, is an interesting physical phenomenon, first predicted as early as in 1923 by Smekal and observed experimentally for the first time by CV Raman in 1928.[1] The Raman effect is basically the inelastic scattering of monochromatic light by matter. Following the interaction of matter with an incident monochromatic radiation of frequency $\omega_0$, Raman *et al.* did observe that the scattering pattern encompasses among others the strongest centered component at the same frequency $\omega_0$. This corresponds to the already familiar form of scattering known as elastic or Rayleigh scattering. Interestingly, they also observed pairs of weak components at $\omega_0 \pm \omega_M$, for which the frequency differences with respect to the incident radiation corresponded to known transitions observed in the infrared spectra of molecules. Consequently, Raman *et al.* reported these new components as "new form of scattering" that were later referred to as Raman scattering after their discovery by CV Raman.[1] These new components are termed Stokes $(\omega_0 - \omega_M)$ and anti-Stokes $(\omega_0 + \omega_M)$ bands or lines and are then understood to collectively constitute the Raman spectrum. The frequency shifts observed $\Delta\omega \equiv \omega_M$, also termed Raman shifts, represent the corresponding amounts of energy that are exchanged between a material system and the light incident on it, and which can fit into possible transitions within the material system. Therefore, the observed shifts in frequency are associated with equivalent changes in the internal energy of the system. As a matter of fact, the collection of all Raman shifts (or a Raman spectrum) for a given material are characteristic of the material properties, providing a way for molecular identification and/or discrimination between different molecular systems. In general, the different amounts of energy (quanta) exchanged between the material and the incident light are characteristic of the energy differences for rotational (in gas phase) and vibrational transitions in molecules, electronic transitions (in atoms), vibronic transitions as well as phononic transitions in crystals. In a Raman spectrum, the anti-Stokes Raman bands are much weaker since they involve less

probable processes. These processes require that the material system must be in an excited state before the interaction with light: Only in this case will the material be able to release energy quanta to the incident radiation or, equivalently, to scatter light at frequencies higher than that of the incident radiation. Therefore, in practice, because most molecules are found in their ground state (e.g.: vibrational, rotational, etc.), only the Stokes Raman bands are easily observed and exploited at room temperature. In molecules, the vibrational frequencies $\omega_M$ depend on the molecular structure and symmetry. The corresponding Raman line shapes are defined by the molecular surroundings. Therefore, the Raman spectroscopy is known as a powerful tool for probing molecular vibrations. The measured spectra serve as molecular fingerprints able to differentiate between different molecular systems.

## 1.2 Progress Toward Various Applications

An analogy to infrared absorption accompanied the discovery of the Raman effect. Both Raman scattering and infrared absorption help to measure molecular vibrational modes. However, they obey different selection rules determined by symmetry concepts. Not all vibrational modes of any molecule can be excited by either technique alone. On the one hand, infrared activity of any vibrational mode is solely determined by a net change of the molecular dipole moment by the corresponding molecular motion during the interaction. On the other hand, Raman active vibrations are those which yield a net change of the molecular polarizability at the equilibrium configuration. Relative intensities of different Raman modes are then correlated with the degree of modulation of the molecular polarizability ellipsoid by each mode of vibration. Consequently, certain modes observed in infrared spectroscopy may not be observed in Raman spectroscopy and vice-versa, and the two methods appear to be rather complementary. However, some variants of Raman scattering that followed the discovery of the Raman effect can help to excite other vibrations or combination modes that are neither observed by spontaneous Raman nor infrared absorption.
Considerable progress in the implementation of Raman spectroscopy [2,3] has been achieved, and many related techniques have emerged, fostered by the need to improve the efficiency of the Raman effect. In fact, Raman scattering is an inherently weak process, accounting for only one out of $10^8$ incident photons. Unlike absorption or photoluminescence spectroscopy, all light scattering phenomena are characterized by nonresonant light-matter interactions where the incident excitation frequency $\omega_0$ is not required to match any direct transition in the material system. In the case of Raman scattering, if the excitation at $\omega_0$ approaches the electronic ground state absorption frequency, a resonant enhancement of the Raman effect by a factor of approx. $10^4$ up to $10^8$ is observed.[4–9] This phenomenon is

called Resonance Raman scattering or spectroscopy (RRS). In addition, enhanced Raman sensitivity can also happen through other routes including both nonlinear and linear Raman processes. A good example is surface enhanced Raman scattering (SERS), first observed by Fleischmann *et al.*[10–16] from molecules adsorbed on a rough metal surface. With the use of coined metal substrates, nanodots structures or colloidal nanoparticles (NPs), made from noble metals, SERS yields highly intense Raman scattering. Giant enhancement up to $10^{12}$ orders of magnitude or higher has been reported.[14,17–25]

As compared to the faster and less expensive infrared spectroscopy most commonly used initially, first experimentation of the Raman effect was extremely difficult. It required very long integration time (many hours) due to inadequate light sources and the relatively low intensity achievable. Raman spectroscopy was ultimately revolutionized with the development in the early sixties of commercial CW visible lasers, and later on, of new sustainable monochromatic laser sources of reliable stability, with narrow and highly directional beams and high intensity. The development of microelectronics with the introduction of stepper motor drivers, photons counting, optical multichannel analyzers, digital acquisition and computer processing, and efficient collection modes, has helped to improve the technique further, making Raman spectroscopy a very versatile technique[2,3] as opposed to infrared spectroscopy. In fact, modern laser Raman spectroscopy now includes nonlinear related scattering phenomena such N-photons scattering processes with $N \geq 2$, and novel linear Raman techniques. Nonlinear Raman techniques include but are not limited to coherent anti-Stokes Raman spectroscopy (CARS), coherent Stokes Raman spectroscopy (CSRS), stimulated Raman gain spectroscopy (SRGS), stimulated Raman loss spectroscopy (SRLS), hyper and second hyper Raman spectroscopy, Stokes and anti-Stokes hyper- and second hyper Raman spectroscopy and so on. Linear Raman techniques include, besides the spontaneous normal Raman scattering, novel variants such as optical activity Raman spectroscopy (OARS), Raman optical tweezers (ROT), and spatially offset Raman spectroscopy. Among nonlinear Raman techniques, CARS is a very popular candidate for biological investigations. In fact, for strong incident fields, CARS becomes more sensitive than the spontaneous Raman scattering, and provides faster solutions for achieving both temporally and spatially resolved imaging capabilities. Stimulated Raman scattering (SRS) provides further advantages by yielding true Raman line shapes, in contrast to CARS which suffers from a non-resonant background that leads to the distortion of Raman bands. Due to the aforementioned advances in instrumentation, CARS, SRS and Raman spectra can be recorded within very short times (microseconds to only a few minutes) from small amounts of samples. The samples can be of any state (solid liquid, or gas).

# Scope and Objectives

## 1.3 The Scope of this Thesis

This work covers the application of Raman scattering for the investigation of interesting biological systems and the associated biochemical events. The main focus is in the implementation of the normal spontaneous Raman scattering (or simply, Raman spectroscopy). However, considerations for combining various Raman techniques are also of interest when this can enhance the capability for biological investigation. The biological systems of interest include, but are not limited to mammalian cells or model cell lines, animal models, healthy and diseased tissue, and biomolecules. It is of paramount relevance to better understand key mechanisms that would shed light onto intrinsic and specific biochemical variations associated with important biological events. The main topics covered in this thesis includes cancer transformation (skin cancer, blood cancer, colon carcinoma, etc), biological rhythm and seasonal hormonal regulation of reproductive functions, chaperon effect (phenotypic variation, and tumor progression), tissue injury (liver fibrosis) and drug response, and metal nanoparticle fabrication and biomolecular interactions. The understanding of the biological events listed above should have an underlying benefit for therapy. Noninvasive and nondestructive techniques are becoming increasingly popular in biology, and represent a general interest in this thesis. In an attempt to address the above mentioned challenges, this thesis brings contributions from a long term project, which combines research interdisciplinarity and professional expertise. Raman spectroscopy techniques are now well established in physics, chemistry and in some biomedical fields. However, the results discussed in this thesis are restricted to the use of the spontaneous Raman technique, which is the main focus of this work. This linear Raman technique can be made rather simple even to non experts, and delivers molecular-level insights based directly on the vibrational biophysical and biochemical contrast.

Biomolecular imaging is not the main focus of this work. When the interest is about imaging potential biomolecular targets within cells or tissue, other linear Raman techniques such as SERS, and non linear Raman techniques such as CARS and SRS, are more sensitive and suitable. These variants of the Raman technique can offer sensitivity comparable to or even better than fluorescence in some cases.[21,26–30] At the same time they can provide better (as compare to fluorescence) biochemical resolution based on the Raman vibrational contrast. The implementation of CARS or SRS microscopy is only briefly mentioned in this work. SERS may be also applied to interrogate the molecular environment of biomarkers than just to image them. This can help to discover unknown biomarkers by enhancing their weak

Raman signal. Therefore, also within the scope of this work, the design of metal substrates, and the elucidation of the behavior of key biomolecular functional groups at SERS metal substrates are of interest. This can be helpful for the retrieval of meaningful biological information from SERS of biological systems.

## 1.4 The Specific Goals of this Thesis

The most specific goals of this thesis include the following points.

- The thesis is aimed at gaining specific molecular insights for the diagnosis and the monitoring of biological events including cancer, hormonal deregulation, tissue injury, immune response and drug response.

- It is attempted to show the feasibility of extracting the relevant information contained in the rather complex Raman spectra of biological cells/tissue, while delineating unspecific spectral variations. In order to hit this mark, rigorous and reliable spectral processing and correction is combined with robust multivariate analysis tools.

- Fluorescence techniques, though more sensitive, are limited to the information about the labeled markers only. Therefore, an important goal of this thesis is to demonstrate, with concrete examples, the potential for an overall, noninvasive and non destructive, biochemical characterization within the cell using Raman spectroscopy. The idea here is to lay a Raman spectroscopic basis for the sorting of cell sublines of colon carcinoma.

- Hormonal activity in many physiological changes or in many diseases and enzymatic or proteolytic cleavage of the extracellular matrix in cancer are required for disease development and/or expansion. In this respect, the understanding of the transport mechanisms of the immunostimulating biomolecular chaperon Hsp70 is one of the most specific goals of this thesis. It is also attempted to demonstrate the potential of a Raman spectroscopic approach for the study of the biological rhythm which involves hormonal deregulation as a function of environmental conditions.

- Finally, an example for a simple fabrication of peanut-like nanoparticles is described, and as far as metal substrates are concerned, this work is also aimed at showing the relevance for the understanding of how key biological functional groups behave at the rough surface of noble metals. This is elucidated by SERS, UV-VIS, and TEM studies of the amino acid glycine.

## 1.5 Summary of Contributions

Considering the specific goals of this thesis, the most relevant contributions in the biomedical application of Raman scattering techniques include the following points:

- Understanding of the underlying mechanisms of biomolecular transformation in skin carcinoma: Toward a microRaman characterization of a skin carcinoma model.
  See **Chapter 4**

- Monitoring of tumor infiltration in the AKR/J lymphoma mouse model. This mouse model is used to evaluate potential health hazards of electromagnetic fields exposure in subjects.
  See **Chapter 5.1**

- Monitoring hormonal deregulation of the reproductive system in photoperiodically sensitive breeding mammals – Toward the implementation of Raman spectroscopy as an approach for the study of the biological rhythm associated with seasonal fluctuations in the photoperiod length.
  See **Chapter 5.2**

- Raman implementation in flow cytometry: Toward label-free cell sorting of colon carcinoma sublines (CX- and CX+) – Insights into detailed transport mechanisms of the chaperon protein Hsp70 associated with the phenotypic variation in the CX-/CX+ sublines. This particular aspect is important for probing early signs for the onsets of biomolecular changes associated with physiological transformation and/or disease progression as in the case of cancer.
  See **Chapter 6**

- Noninvasive Raman monitoring of drug response after liver tissue injury leading fibrosis: Toward Raman monitoring of prognosis.
  See **Chapter 7**

- Fabrication of new types of SERS substrates: Peanuts-like core-shell nanoparticles, with the potential for SERS investigations of biological systems.
  See **Chapter 8**

- SERS of a biological molecule: A critical concentration-dependent behavior of key biological functional groups (carboxylic and amino) at SERS noble metal interfaces – The case of the amino acid glycine has been studied.
  See **Chapter 9**

# Thesis Outline

This thesis is organized in ten chapters.

- **Chapter 1** gives a brief introduction to Raman scattering, a concise record of Raman scattering techniques, and a detailed layout of the scope and gaols of this thesis.
- **Chapter 2** presents theoretical concepts of the Raman scattering techniques mentioned in this thesis: First, this chapter describes the frequency dependence with the corresponding energy level diagrams of the most common Raman scattering processes, including both linear Raman processes, and non linear Raman processes (CARS, SRS, hyper and second hyper Raman). Then an introduction of the theoretical principle of Rayleigh and spontaneous Raman scattering is presented, focusing on the spontaneous Raman scattering which is the main focus in this thesis.
- **Chapter 3** recalls traditional and current methods for biological investigations, and summarizes the experimental implementation of several Raman scattering techniques. In addition, procedures for correct spectral processing and the combination of Raman spectroscopy with chemometrical analysis are described. Moreover, a brief overview of possible biomedical applications of Raman scatting is presented, with highlights on the specific examples or case studies essentially carried out in the framework of this thesis. These case studies represent the specific projects results or contributions of the thesis and are described separately in the next chapters (**Chapter 4** to **Chapter 9**)
- **Chapter 4**, **Chapter 5**(two contributions organized as **5.1** and **5.2**), **Chapter 6**, **Chapter 7**, **Chapter 8** and **Chapter 9**: See section "Summary of Contributions" above. The works described in these chapters are separate projects contributions or case studies extending from the studies of key biological events, including cancer diagnosis and monitoring of cancer development, the study of biological rhythms and hormonal deregulation, the study of detailed tumorigenicity steps and phenotypic variations, and the monitoring drug response, to the fabrication of special SERS substrates and the study of biomolecule-metal interactions.
- **Chapter 10** presents the general conclusion summarizing the different results obtained in the framework of this thesis, highlights the limitations of these thesis works, and gives potential prospects.

# 2. Theoretical Background

## Summary

A comprehensive classical and quantum mechanical treatment of Raman scattering processes has already been developed in the last century.[31–34] The mechanism underlying photon-mater interaction is interpreted by a quantum description of energy exchange with the scattering medium. Depending on the scattering order and the scatter properties, a non exhaustive division can be made into linear and incoherent, nonlinear coherent and super inelastic scattering mechanisms.

## 2.1 Diagrammatic Description of Raman Scattering Techniques

### 2.1.1 Rayleigh and Linear Vibrational Raman Scattering Models

Energy transfer models of light scattering are based on the photon description of the electromagnetic radiation. Linear scattering processes arise from the interaction of the material system with a single monochromatic excitation involving only one photon per scattering cycle. In molecules, vibrational energy levels with associated rotational states are quantized and lie just above electronic levels. During a scattering process, an excitation photon $\hbar\omega_0$ causes the molecule to transit from an initial state of energy $E_i$ to a final state of energy $E_f$ with emission of a photon $\hbar\omega_s$. As depicted in figure 2.1, the molecule's energy variation $\Delta E = E_f - E_i$ can happen in three different forms: $\Delta E = 0$ and $\omega_s = \omega_0$ describes an elastic process known as Rayleigh scattering; $\Delta E \neq 0$, and $\omega_s = \omega_0 \pm \Delta\omega$ where $\Delta\omega = \omega_M$ is the molecular vibrational frequency, describes pure vibrational Raman scattering. In this case, both the initial and the final vibrational states of the molecule belong to the electronic ground $S_g$. In general $\Delta\omega$ can be any characteristic transition frequency of the molecule. It can involve an electronic or vibronic term when the final vibrational state of the molecule belongs to the manifold of the $r^{th}$ excited electronic state $S_{e(r)}$ : This is known as electronic

(pure electronic transition) or vibronic (electronic-vibrational coupling) Raman scattering as depicted in figure 2.1 (c). Scattering lines at $\omega_s = \omega_0 - \omega_M$ are termed Stokes in analogy with the Stokes shift known for fluorescence, while lines at $\omega_s = \omega_0 + \omega_M$ are called anti-Stokes lines. However, unlike fluorescence, as a common behavior in all light scattering processes, the excitation frequency in the Raman effect is not required to be resonant with any molecular transition. In the Raman process, the exciting radiation at $\omega_0$ is then not absorbed in strict spectroscopic terms. Instead, it triggers the molecule and opens up spectroscopic transitions of frequencies $\omega_s$. Therefore, compared to infrared absorption and fluorescence, spontaneous Raman scattering is an inherently weak process. Only $10^{-8}$ fraction of incident photons can be inelastically scattered. However, as $\omega_0$ tends to the ground state electronic absorption, the so-called resonant Raman scattering occurs, with an enhancement of up to $10^8$ orders of magnitude. In general, different resonances can be distinguished, including pure vibrational Raman resonances (discrete and continuum) simply known as resonant Raman, as depicted in figure 2.1 (b'), as well as electronic (vibronic) Raman resonance. Finally, SERS can also be depicted diagrammatically by the energy

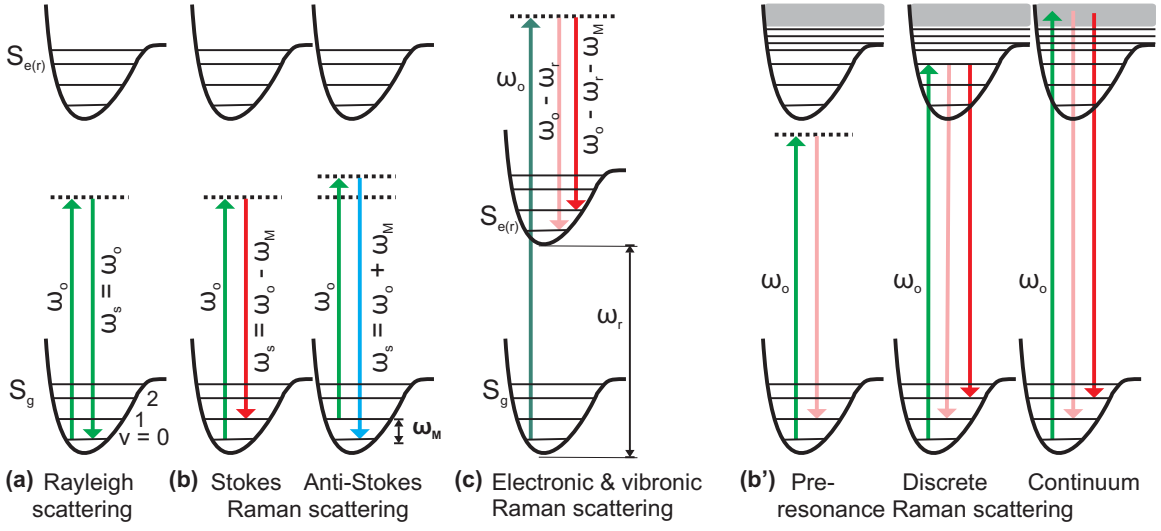


**Figure 2.1: Energy level diagram of (a) Raman and Rayleigh, and (b) resonant Raman scattering**

levels diagram in figure 2.1 (b). The gigantic enhancement observed in SERS is attributed to the interaction of the molecule with intense electromagnetic fields produced and confined at the rough metal surface due to the excitation of a surface plasmon.

Normal Raman scattering is a first order process, for which the intensity of the scattered radiation is directly proportional to the irradiance of the incident radiation. Therefore, Raman scattering is linear. For an individual scattering event SERS is also a linear process with respect to the total irradiance felt by the molecule. Because primarily scattered photons in this way can also be enhanced at the SERS metal substrate, the overall observed

SERS intensity shows a nonlinear power dependence of the original incident field intensity. Raman scattering is inherently incoherent; the scattered intensity from a system of N non-interacting molecules is proportional to the total number of molecules. This is also true for SERS but only for some concentration regimes. The actual SERS dependence on concentration is not unequivocal and is determined by the actual nature of molecule-metal interactions and the field strength.

### 2.1.2 Nonlinear Raman Scattering Processes

In high filed strength, intense non linear scattering occurs. Non linear Raman scattering involves processes in which, two, three or more photons of either the same or different energies participate together in a single scattering event to produce the signal or scattered photon. Such a scattered radiation can be made up of combinations of the actively interacting photons frequencies as shown in figure 2.2. Therefore, scattering of this nature is nonlinear. It includes higher order elastic and inelastic scattering processes, and stimulated and multicolor scattering phenomena such as CARS, CSRS, SRGS, SRLS, etc.

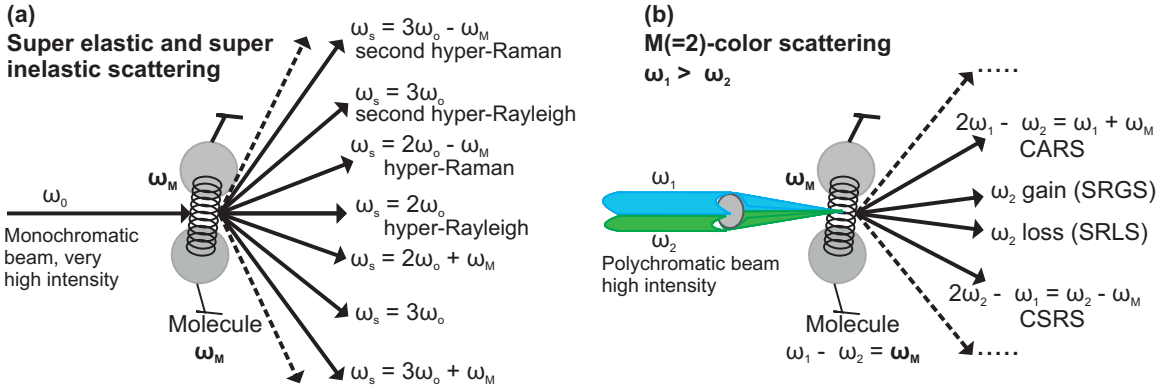


**Figure 2.2: Illustration of, (a) super elastic and super inelastic, and (b) M(=2)-color scattering**.

#### 2.1.2.1 Coherent Anti-Stokes and Coherent Stokes Raman Scattering (CARS and CSRS)

Multicolor scattering involves simultaneous excitation with different monochromatic radiations. If for instance the excitation beam is composed of overlapping coherent monochromatic radiations of frequencies $\omega_1$ and $\omega_2$, with $\omega_1 > \omega_2$, the frequency of the scattered radiation, $\omega_s$, is the result of various combinations of $\omega_1$ and $\omega_2$. The relation $\omega_s = 2\omega_1 - \omega_2$ is usually considered. By varying for example $\omega_2$ while keeping $\omega_1$ constant, a Raman resonance (different from electronic resonance) is observed when $\omega_1 - \omega_2 = \omega_M$, the vibrational frequency of the molecule. Therefore, the scattered radiation has frequency

$\omega_s \equiv \omega_{aS} = 2\omega_1 - \omega_2 = \omega_1 + \omega_M$, which represents an anti-Stokes Raman process with respect to $\omega_1$ and the phenomenon is called coherent anti-Stokes Raman scattering (CARS). Conversely, considering the combination $\omega_s = 2\omega_2 - \omega_1$ and by varying $\omega_1$, a similar strong scattering is observed only when once again the condition $\omega_1 - \omega_2 = \omega_M$ is satisfied. In this case, the scattered photon $\omega_s \equiv \omega_S = 2\omega_2 - \omega_1 = \omega_2 - (\omega_1 - \omega_2) = \omega_2 - \omega_M$, describes a Stokes Raman process relative to $\omega_2$ and is called coherent Stokes Raman scattering (CSRS). Depending on the order in which the lasers interact with the molecule, the exciting frequencies have been given different names. Figure 2.3 shows a schematic representation of CARS and CSRS. Both CARS and CSRS result from the interaction with 3 laser beams, since one of the exciting radiations, either the pump $\omega_1$ or the Stokes $\omega_2$ acts twice while the other acts once. They are therefore third order non linear Raman scattering processes in which the three interacting lasers can all be different. These two techniques can also be in electronic resonance and are, in such a case, referred to as resonant CARS and resonant CSRS. Both CARS and CSRS are passive processes since no

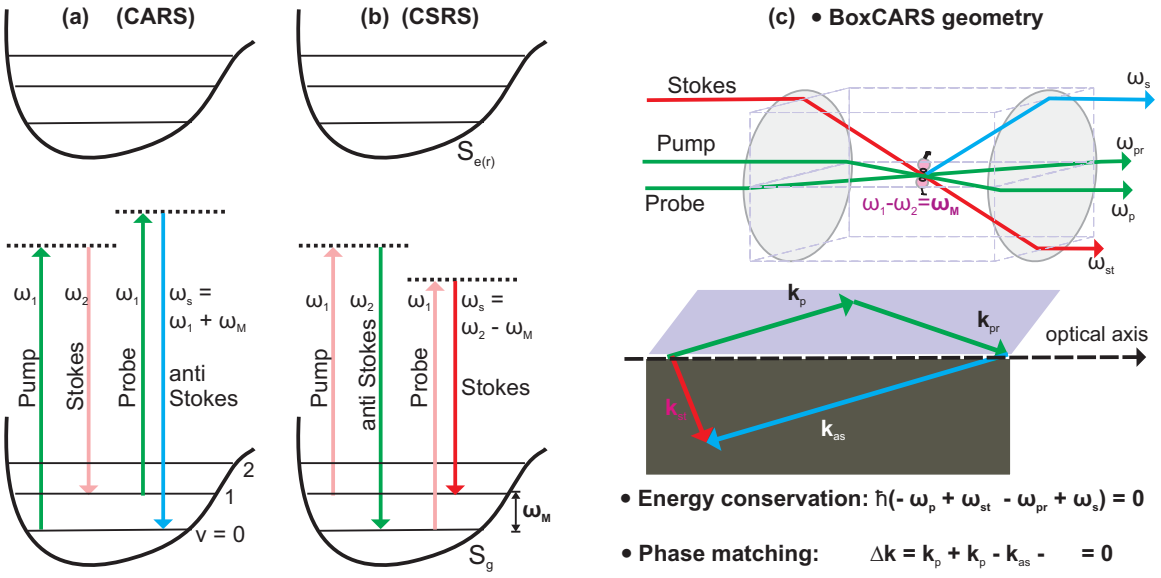


**Figure 2.3: Energy level diagram of (a) CARS and (b) CSRS.**

net exchange of energy occurs overall. Scattering signals are just linear combinations of the two coherently incident radiations, and are accordingly coherent. The observation of CARS or SCRS requires the three interacting lasers to coincide in time and space. There are two important conditions which have to be fulfilled: The energy conservation law that determines the CARS frequency, and the momentum conservation or phase matching condition that defines the direction of the CARS signal. The signal is generated only at the laser focus, and spectrally separated from the exciting lasers. Unlike for CSRS, the CARS signal is spectrally separated from any fluorescence that may be caused in the sample by

the exciting beams, since it is on the anti-Stokes side of the exciting lasers. These two aspect make CARS very suitable for fluorescence-free high resolution biological imaging and microscopy. In addition, the signal is highly directional and can be spatially separated using several beam arrangements, such as the folded box-CARS geometry as depicted in Figure 2.3 (c).

#### 2.1.2.2 Stimulated Raman Gain and Loss Scattering (SRGS and SRLS)

In the presence of the two exciting frequencies $\omega_1$ and $\omega_2$, and if the Raman resonance condition $\omega_1 - \omega_2 = \omega_M$ is fulfilled, scattering can occur at $\omega_s \equiv \omega_{SR-G} = \omega_2 = \omega_1 - \omega_M$: This is a Stokes Raman process leading to an increase or gain in intensity of the incident radiation of frequency $\omega_2$. Alternatively, scattering can also take place at $\omega_s \equiv \omega_{SR-L} = \omega_1 = \omega_2 + \omega_M$: This is an anti-Stokes Raman process relative to $\omega_2$, leading to intensity increase in the incident radiation of frequency $\omega_1$; this is equivalent to a corresponding decrease or loss in the component $\omega_2$. These two gain and loss processes are schematically similar to the spontaneous Raman diagram in figure 2.1 (a). However, they are taking place in the presence of the exciting Stokes radiation of frequency $\omega_{SR-G} = \omega_2 = \omega_1 - \omega_M$ (stimulated gain in $\omega_2$) and anti-Stokes radiation of frequency $\omega_{SR-L} = \omega_1 = \omega_2 + \omega_M$ (stimulated loss in $\omega_2$) in the incident beam, respectively. Therefore, they are called stimulated Raman gain scattering (SRGS) and stimulated Raman loss scattering (SRLS) respectively. SRGS and SRLS are non linear coherent scattering processes. Experimentally, the stimulated Raman gain or loss scattering can occur even without the explicit presence of the Raman Stokes or anti-Stokes components in the incident beam when the intensity becomes very large: Primarily scattered Stokes or anti-Stokes waves are intense enough and can be coupled together with the incident wave by the actual vibrating molecule and promote accordingly scattering of additional photons.

#### 2.1.2.3 High Order Spontaneous Processes: Hyper and Second Hyper Raman Scattering

Higher order scattering involves $n \geq 2$ photons from a single monochromatic radiation taking actively part in an unique scattering cycle. This becomes possible only when the incident light wave of frequency $\omega_0$ has a large enough irradiance. Hence, successive and instantaneous annihilation of $n$ incident photons $\hbar\omega_0$ can happen before a scattered photon $\hbar\omega_s$ is produced. Similar to spontaneous Raman and Rayleigh scattering, such scatters appear hyper-elastically at $\omega_s = n\omega_0$, and hyper-inelastically at $\omega_s = n\omega_0 \pm \omega_M$ where $\omega_M$ is a vibrational transition of the molecular system (for pure vibrational scattering). Figure 2.4

shows the energy level diagram for these higher order scattering processes, for $n = 2$ and $n = 3$. The inelastic part is termed hyper Raman scattering (HRS) for $n = 2$, second hyper Raman scattering (SHRS) for $n = 3$, and so on. Because HRS follows different selection rules, it has been shown to be able to excite certain vibrational modes, which are not possible in both spontaneous Raman scattering and infrared absorption.

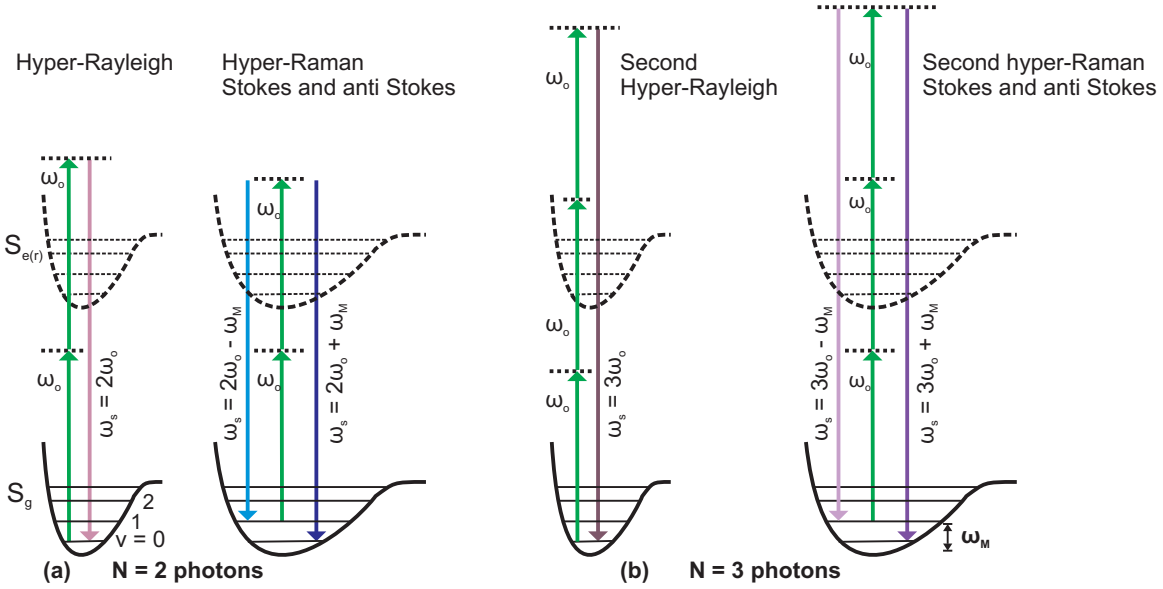


**Figure 2.4: Energy level diagram for hyper (a) and second hyper (b) Rayleigh and Raman scattering**.

## 2.2 Theoretical Formulation of Rayleigh and Raman Scattering

### 2.2.1 Macroscopic Treatment of Light Scattering

Nearly all light scattering phenomena are based on the classical description of electromagnetic radiation. The scattered light is considered to originate from various oscillating electric and magnetic multipole moments already existing or induced in the material system by photon-matter interaction. The electric dipole **P** is by several orders of magnitude the most important, followed by the magnetic dipole moment, the electric quadrupole moment, etc. Magnetic moments arise only as the result of moving charges and are usually neglected.
Let's consider a molecule charge distribution $\rho_i$ of radii vectors $\mathbf{r}_i$ from the molecular origin $O$. By definition, the first significant electric moments, the dipole moment **P**, and the quadrupole moment tensor $\tilde{Q}$ or equivalently the corresponding traceless tensor $\Theta$ are given

by

$$\mathbf{P} = \sum_i \rho_i \mathbf{r}_i \; ; \qquad \text{and} \qquad \tilde{Q}_{\rho\sigma} = \sum_i \rho_i \mathbf{r}_{i\rho} \mathbf{r}_{i\sigma} \qquad \text{or} \qquad \Theta_{\rho\sigma} = \frac{1}{2}\left(3\tilde{Q}_{\rho\sigma} - \tilde{Q}_{\tau\tau}\delta_{\rho\Sigma}\right). \tag{2.1}$$

The subscript symbols $\rho,\ \sigma\ \ldots = x\,y\,z$ , and summation over repeated subscripts is implied in each term and in all other expressions to follow. Let us first suppose the charge distribution at rest in an external electric field which we also consider to be static. A general treatment of the interaction with the field expresses the electric potential energy of interaction $W_e$ as the sum of the energies of, an equivalent point charge in a potential, a dipole in a uniform field, a quadrupole in a field gradient, an octopole in a second-field gradient and so on. In order to see this explicitly, it is helpful to introduce a Taylor series expansion, about the molecular origin "$O$", of the potential $\phi(\mathbf{r})$ created by the external field $\mathbf{E}$ at the positions of the charges $\rho_i$, in the definition of $W_e \triangleq \sum_i \rho_i \phi(\mathbf{r}_i)$.

$$W_e = \sum_i \rho_i \left[\phi_0 + \left(\frac{\partial\phi}{\partial r_\rho}\right)_O r_{i\rho} + \frac{1}{2}\left(\frac{\partial^2\phi}{\partial r_\rho \partial r_\sigma}\right)_O r_{i\rho} r_{i\sigma} + \frac{1}{6}\left(\frac{\partial^3\phi}{\partial r_\rho \partial r_\sigma \partial r_\tau}\right)_O r_{i\rho} r_{i\sigma} r_{i\tau} + \ldots\right]. \tag{2.2}$$

The subscript "$O$" implies that the corresponding terms are evaluated at the molecular origin. From the definition of $\mathbf{P}$ and $\Theta$ given by eqn (2.1), and knowing that the electric field is $\mathbf{E} = -\nabla\phi(\mathbf{r}) = \frac{\partial\phi}{\partial r}$, $W_e$ can be rewritten, limiting ourselves to the third term, as follows:

$$W_e = \rho_{tot}\phi_0 - P_\rho\left(E_\rho\right)_O - \frac{1}{3}\Theta_{\rho\sigma}\left(\tilde{E}_{\rho\sigma}\right)_O + \ldots, \tag{2.3}$$

where $\rho_{tot} = \sum_i \rho_i$ is the electric monopole and, $\left(\tilde{E}_{\rho\sigma}\right)_O = \left(\frac{\partial \mathbf{E}_\rho}{\partial r_\sigma}\right)_O$ represents the field gradient evaluated at the molecular origin. It then follows from eqn (2.3) that the dipole moment and the quadrupole moment tensor are equally expressed as follows:

$$P_\rho = -\frac{\partial W_e}{\partial (E_\rho)_O}\,; \qquad \text{and} \qquad \Theta_{\rho\sigma} = -3\frac{\partial W_e}{\partial\left(\tilde{E}_{\rho\sigma}\right)_O}. \tag{2.4}$$

Here again, $(E_\rho)_O$ is the $\rho$ component of the electric field at the molecular origin. The third term neglected in the series expansion of the electric potential, and subsequent higher order terms will introduce the electric octopole moment and other higher order moments respectively, which however do not practically contribute to light scattering. In addition, each moment involved in the expression of the potential energy is actually of two contributions; a permanent moment and an induced moment of increasing order as a result of the interaction with the field. If the interaction with the field is weak, this situation can be illustrated by expanding the electric potential energy $W_e$ in a Taylor series about the energy

$W_e^0$ in zero field strength $(\mathbf{E})_O$ and zero field gradient $(\tilde{E}_{\rho\sigma})_O$ at the molecular origin "$O$". Note that the notation "$O$" refers to molecular origin, while "0" refers to zero field strength or zero field gradient.

$$\begin{aligned} W_e\left((\mathbf{E})_O\,,(\tilde{E}_{\rho\sigma})_O\right) &= W_e^0 + (E_\rho)_O\left[\frac{\partial W_e}{\partial(E_\rho)_O}\right]_0 + \frac{1}{2}(E_\rho)_O(E_\sigma)_O\left[\frac{\partial^2 W_e}{\partial(E_\rho)_O\partial(E_\sigma)_O}\right]_0 \\ &+ \frac{1}{6}(E_\rho)_O(E_\sigma)_O(E_\tau)_O\left[\frac{\partial^3 W_e}{\partial(E_\rho)_O\partial(E_\sigma)_O\partial(E_\tau)_O}\right]_0 \\ &+ \frac{1}{24}(E_\rho)_O(E_\sigma)_O(E_\tau)_O(E_\nu)_O\left[\frac{\partial^4 W_e}{\partial(E_\rho)_O\partial(E_\sigma)_O\partial(E_\tau)_O\partial(E_\nu)_O}\right]_0 + \ldots \\ &+ (\tilde{E}_{\rho\sigma})_O\left[\frac{\partial W_e}{\partial(\tilde{E}_{\rho\sigma})_O}\right]_0 + \frac{1}{2}(\tilde{E}_{\rho\sigma})_O(\tilde{E}_{\tau\nu})_O\left[\frac{\partial^2 W_e}{\partial(\tilde{E}_{\rho\sigma})_O(\tilde{E}_{\tau\nu})_O}\right]_0 + \ldots \quad (2.5) \end{aligned}$$

where cross derivatives involving the field strength and field strength gradient have been left out. The dipole $P_\rho$ and quadrupole $\Theta_{\rho\sigma}$ defined in eqn (2.4) can now be explicitly derived from eqn (2.5).

The total dipole moment is obtained by differentiating the potential energy $W_e\left((\mathbf{E})_O\,,(\tilde{E}_{\rho\sigma})_O\right)$ with respect to the field strength $(E_\rho)_O$:

$$\mathbf{P} = \mathbf{P}^0 + \mathbf{P}^{(1)} + \mathbf{P}^{(2)} + \mathbf{P}^{(3)} + \cdots \equiv \mathbf{P}^0 + \alpha\cdot\mathbf{E} + \frac{1}{2}\beta\!:\mathbf{E} + \frac{1}{6}\gamma\!:\!\mathbf{E} + \cdots . \quad (2.6)$$

Here $\mathbf{P}^0 = -\left[\frac{\partial W_e}{\partial(\mathbf{E})_O}\right]_0$ and $\mathbf{P}^{ind} = \mathbf{P}^{(1)}+\mathbf{P}^{(2)}+\mathbf{P}^{(3)}+\cdots$ are the permanent and the total induced dipole moments of the molecule respectively. $\mathbf{P}^{(1)}$, $\mathbf{P}^{(2)}$, and $\mathbf{P}^{(3)}$ are first, second, and third order induced dipole moments determined respectively by the polarizability tensor $\alpha$, the hyper polarizability tensor $\beta$, and the second hyper polarizability tensor $\gamma$ expressed from eqns (2.5) and (2.6) as follows:

$$\begin{aligned} \alpha \equiv \alpha_{\rho\sigma} &= -\left[\frac{\partial^2 W_e}{\partial(E_\rho)_O\partial(E_\sigma)_O}\right]_0 \\ \beta \equiv \beta_{\rho\sigma\tau} &= -\left[\frac{\partial^3 W_e}{\partial(E_\rho)_O\partial(E_\sigma)_O\partial(E_\tau)_O}\right]_0 \\ \gamma \equiv \gamma_{\rho\sigma\tau\nu} &= -\left[\frac{\partial^4 W_e}{\partial(E_\rho)_O\partial(E_\sigma)_O\partial(E_\tau)_O\partial(E_\nu)_O}\right]_0 . \end{aligned}$$

Similarly, the total quadrupole moment is derived by differentiating the potential energy $W_e\left((\mathbf{E})_O\,,(\tilde{E}_{\rho\sigma})_O\right)$ with respect to the field strength gradient $\left(\tilde{E}_{\rho\sigma}\right)_O$:

$$\Theta_{\rho\sigma} = \Theta^0_{\rho\sigma} + \complement_{\rho\sigma,\tau\nu}\left(\tilde{E}_{\tau\nu}\right)_O \;:\quad \Theta^0_{\rho\sigma} = \left[\frac{\partial W_e}{\partial(\tilde{E}_{\rho\sigma})_0}\right]_0 \quad\text{and}\quad \complement_{\rho\sigma,\,\tau\nu} = \left[\frac{\partial^2 W_e}{\partial(\tilde{E}_{\rho\sigma})_0(\tilde{E}_{\tau\nu})_0}\right]_0 , \quad (2.7)$$

where $\Theta^0_{\rho\sigma}$ is the permanent quadrupole moment tensor and $\complement_{\rho\sigma,\,\tau\nu}$ the field gradient quadrupole polarizability tensor.

In the previous treatment we have considered a charge distribution fixed in space. However, in the real situation, charges are in perpetual motion. An analogous treatment of the interaction of the molecular system with a static magnetic field with magnetic induction **B** yields the total magnetic moment **m** expressed to the first order by the following relation;

$$\mathbf{m} = \mathbf{m}^0 + \Xi.\,\mathbf{B}\,; \quad \text{with} \quad \mathbf{m}^0 = -\left[\frac{\partial W_m}{\partial(\mathbf{B})_0}\right]_0 \quad \text{and} \quad \Xi \equiv \xi_{\rho\sigma} = -\left[\frac{\partial^2 W_m}{\partial(B_\rho)_0 \partial(B_\sigma)_0}\right]_0, \quad (2.8)$$

where the permanent magnetic moment $\mathbf{m}^0$ is the magnetic analog of the permanent electric dipole $\mathbf{P}^0$, and $\Xi$ is the magnetic susceptibility tensor, both related to the magnetic potential energy $W_m$ as shown in eqn (2.8).

So far, we have considered interacting fields to be static. For time dependent fields, the different multipole moments established above are also time dependent. Therefore, the interaction of the material system with an oscillating electromagnetic field will in the material system create an oscillating electric dipole moment, magnetic moment, electric quadrupole moment, etc, which then according to the principles of electrodynamics serve as sources of electromagnetic radiations within the material system. Both classical and quantum mechanical treatment of light scattering (e.g., elastic, linear and non linear Raman scattering) rely first of all upon such initial classical description of the relevant interaction moments as sources of electromagnetic radiations in material systems. The electric dipole is by several orders of magnitude the most significant. It is the only interaction moment considered in nearly all light scattering phenomena. The second important moment, the magnetic moment, is significant only in light scattering by chiral molecules. Therefore, in the treatment of Raman scattering, the interaction moments can be restricted to be of electric dipole in nature only.

The radiant intensity of an oscillating dipole with frequency $\omega_s$ along a particular direction $\theta$ to the dipole axis is given by

$$I_s = k'_\omega \omega_s^4 \mathbf{P}_0^2 \sin^2\theta \;\equiv\; k'_{\tilde{\nu}} \tilde{\nu}^4 \sin^2\theta \;;\quad k'_\omega = \frac{1}{32\pi^2 \epsilon_o C_o^2} \quad \text{or equivalently} \quad k'_{\tilde{\nu}} = \frac{\pi^2 C_o}{2\epsilon_o}. \quad (2.9)$$

Here $\mathbf{P}_0$ is the dipole moment amplitude, and $\tilde{\nu} = \omega_0/2\pi C_o = 1/\lambda$ is the wavenumber.

The goal of both classical and quantum mechanical treatment of light scattering is to find how the dipole moment frequency $\omega_s$ and amplitude $\mathbf{P}_0$ are related to the material properties and the exciting radiation ($\omega_0$). Once $\omega_s$ and $\mathbf{P}_0$ are known, the scattering intensity can be calculated from enq (2.9).

### 2.2.2 Classical Approach of Rayleigh and Raman Scattering

The classical approach of light scattering treats both the material system and the electromagnetic field classically. The incident and scatter radiation are considered as monochromatic plane waves totally characterized by their frequencies $\omega_0$ and $\omega_s$ respectively. A comprehensive classical study of vibrational scattering was developed earlier by Placzek.[31] More extended developments can be found in the literature.[31–34] In the framework of vibrational Raman scattering for which molecules are free to vibrate but do not rotate, the description is restrained to the case of the electric dipole moment.

As outlined in the previous section, the total dipole moment of a molecule interacting with the electric field $\mathbf{E} = \mathbf{E}_0 \cos \omega_0 t$ of the incident radiation is rewritten here for convenience.

$$\mathbf{P} = \mathbf{P}^0 + \mathbf{P}^{(1)} + \mathbf{P}^{(2)} + \mathbf{P}^{(3)} + \cdots \equiv \mathbf{P}^0 + \alpha \cdot \mathbf{E} + \frac{1}{2}\beta : \mathbf{E} + \frac{1}{6}\gamma \vdots \mathbf{E} + \cdots, \tag{2.10}$$

where $\mathbf{P}^0$ is any permanent dipole moment. The first order induced dipole $\mathbf{P}^{(1)}$ is linear in $\mathbf{E}$ and describes linear scattering processes, such as Raman and Rayleigh scattering, determined by the polarizability tensor $\alpha$. The second order induced dipole $\mathbf{P}^{(2)}$ is quadratic in $\mathbf{E}$ and describes non-linear second order processes, such as hyper Raman, hyper Rayleigh, second harmonic generation, etc, determined by the hyper polarizability tensor $\beta$. The third order induced dipole $\mathbf{P}^{(3)}$ is cubic in $\mathbf{E}$ and describes non-linear $\chi^3$ processes such coherent Raman (CARS, CSRS SRS), second hyper Raman and second hyper Rayleigh, etc, determined by the second hyper polarizability tensor $\gamma$. In order to elucidate the origin of the above mentioned scattering processes, the goal of the classical treatment is to find the frequency dependence of the dipole moment and identify characteristic frequency terms.

For pure vibrational scattering, the dipole moment and the different polarizability tensors depend on the vibrational modes only. For small nuclear displacements, $\mathbf{P}$, $\alpha$, $\beta$, and $\gamma$ can be expanded into Taylor series about the equilibrium configuration "O" in the normal coordinates $q_k$:

$$\mathbf{P}(\mathrm{q}_k) = \mathbf{P}(0) + \sum_{k=1}^{Q} \left(\frac{\partial \mathbf{P}}{\partial \mathrm{q}_k}\right)_0 \mathrm{q}_k + \frac{1}{2} \sum_{k,l=1}^{Q} \left(\frac{\partial^2 \mathbf{P}}{\partial \mathrm{q}_k \partial \mathrm{q}_l}\right)_0 \mathrm{q}_k \mathrm{q}_l \quad + \cdots \; ; \; \mathbf{P}(0) \equiv \mathbf{P}^0 \tag{2.11}$$

$$\alpha_{\rho\sigma}(\mathrm{q}_k) = \alpha_{\rho\sigma}(0) + \sum_{k=1}^{Q} \left(\frac{\partial \alpha_{\rho\sigma}}{\partial \mathrm{q}_k}\right)_0 \mathrm{q}_k + \frac{1}{2} \sum_{k,l=1}^{Q} \left(\frac{\partial^2 \alpha_{\rho\sigma}}{\partial \mathrm{q}_k \partial \mathrm{q}_l}\right)_0 \mathrm{q}_k \mathrm{q}_l + \cdots \; ; \; \alpha_{\rho\sigma}(0) \equiv \alpha_0 \tag{2.12}$$

$$\beta_{\rho\sigma\tau}(\mathrm{q}_k) = \beta_{\rho\sigma\tau}(0) + \sum_{k=1}^{Q} \left(\frac{\partial \beta_{\rho\sigma\tau}}{\partial \mathrm{q}_k}\right)_0 \mathrm{q}_k + \frac{1}{2} \sum_{k,l=1}^{Q} \left(\frac{\partial^2 \beta_{\rho\sigma\tau}}{\partial \mathrm{q}_k \partial \mathrm{q}_l}\right)_0 \mathrm{q}_k \mathrm{q}_l \quad + \cdots \; ; \; \beta_{\rho\sigma\tau}(0) \equiv \beta_0 \tag{2.13}$$

$$\gamma_{\rho\sigma\tau\nu}(q_k) = \gamma_{\rho\sigma\tau\nu}(0) + \sum_{k=1}^{Q}\left(\frac{\partial\gamma_{\rho\sigma\tau\nu}}{\partial q_k}\right)_0 q_k + \frac{1}{2}\sum_{k,l=1}^{Q}\left(\frac{\partial^2\gamma_{\rho\sigma\tau\nu}}{\partial q_k\partial q_l}\right)_0 q_k q_l + \cdots \;;\;\; \gamma_{\rho\sigma\tau\nu}(0) \equiv \gamma_0. \quad (2.14)$$

Here, the total number of vibrational modes for $N$ nuclei is $Q = 3N - 6$ (or $Q = 3N - 5$ for linear molecules). $\mathbf{P}(0) \equiv \mathbf{P}^0$ is the dipole moment at the equilibrium configuration, meaning any permanent dipole moment of the molecule. Similarly, $\alpha_0$, $\beta_0$, and $\gamma_0$ represent the equilibrium polarizability, hyper polarizability, and second hyper polarizability tensors, respectively. Their different derivatives with respect to the normal coordinates $q_k$ are as well understood as tensors of the same order respectively, and we may adopt a simple notation,

$$\text{for example} \quad \alpha'_k \equiv \alpha'_{\rho\sigma} = \left(\frac{\partial\alpha_{\rho\sigma}}{\partial q_k}\right)_0 \quad \beta'_k \equiv \beta'_{\rho\sigma\tau} = \left(\frac{\partial\beta_{\rho\sigma\tau}}{\partial q_k}\right)_0 \quad \gamma'_k \equiv \gamma'_{\rho\sigma\tau\nu} = \left(\frac{\partial\gamma_{\rho\sigma\tau\nu}}{\partial q_k}\right)_0$$

At this point two useful approximations are usually introduced, namely electrical harmonicity according to which only terms linear in $q_k$ in the above expansion are considered; and the simple harmonic motion approximation which expresses the displacement as follows;

$$q_k = q_{ko}\cos(\omega_k t + \varphi_k)\;, \qquad q_{ko} \text{ is the amplitude} \quad (2.15)$$

Let the electric field of the incident monochromatic plane wave have the simple form,

$$\mathbf{E} = \mathbf{E}_0\cos(\omega_0 t)\;; \qquad \mathbf{E}_0 \text{ is the amplitude.}$$

Using the notations introduced above and inserting eqns(2.11 - 2.15) into eqn(2.10), we can obtain the frequency dependence of the total electric dipole moment expressed after rearrangement of the various terms as follows;

$$\begin{aligned}
\mathbf{P} &= \mathbf{P}^0 + \frac{1}{4}\beta_0\!:\mathbf{E_0}\mathbf{E_0} + \sum_{k=1}^{Q}\left[\left(\frac{\partial\mathbf{P}}{\partial q_k}\right)_0 + \frac{1}{4}\beta'_k\!:\mathbf{E_0}\mathbf{E_0}\right] q_{ko}\cos(\omega_k t + \varphi_k) \\
&+ \left(\alpha_0\cdot\mathbf{E}_0 + \frac{3}{24}\gamma_0\vdots\mathbf{E_0}\mathbf{E_0}\mathbf{E_0}\right)\cos\omega_0 t \\
&+ \sum_{k=1}^{Q}\left\{\left(\frac{1}{2}\alpha'_k\cdot\mathbf{E}_0 + \frac{3}{48}\gamma'_k\vdots\mathbf{E_0}\mathbf{E_0}\mathbf{E_0}\right) q_{ko}\Big[\cos\left[(\omega_0-\omega_k)t-\varphi_k\right] + \cos\left[(\omega_0+\omega_k)t+\varphi_k\right]\Big]\right\} \\
&+ \frac{1}{4}\beta_0\!:\mathbf{E_0}\mathbf{E_0}\cos 2\omega_0 t \\
&+ \sum_{k=1}^{Q}\frac{1}{8}\beta'_k\!:\mathbf{E_0}\mathbf{E_0}q_{ko}\Big[\cos\left[(2\omega_0-\omega_k)t-\varphi_k\right] + \cos\left[(2\omega_0+\omega_k)t+\varphi_k\right]\Big]
\end{aligned}$$

$$
\begin{aligned}
&+ \quad \frac{1}{24}\gamma_0 \vdots \mathbf{E_0}\mathbf{E_0}\mathbf{E_0} \cos 3\omega_0 t \\
&+ \quad \sum_{k=1}^{Q} \frac{1}{48}\gamma'_k \vdots \mathbf{E_0}\mathbf{E_0}\mathbf{E_0}\mathrm{q}_{ko}\Big[ \cos\left[(3\omega_0 - \omega_k)t - \varphi_k\right] + \cos\left[(3\omega_0 + \omega_k)t + \varphi_k\right] \Big] \\
&+ \quad \cdots
\end{aligned}
\tag{2.16}
$$

In this expression, the first constant term has no frequency dependence and is irrelevant for optical spectroscopy. The second term involves only the frequency $\omega_k$ and does not correspond to light scattering. Instead, it describes infrared absorption: in this spectral range, the contribution from the hyper polarizability gradient $\beta'_k \equiv \beta'_{\rho\sigma\tau} = \left(\frac{\partial\beta_{\rho\sigma\tau}}{\partial \mathrm{q}_k}\right)_0$ and other higher order terms is negligible. Therefore, the selection rule of infrared absorption is fulfilled if the variation of the polarization with respect to molecular motion at the equilibrium configuration is not zero. All other subsequent terms are connected with frequency modulation of the incident photon $\hbar\omega_0$ and correspond to light scattering phenomena. So as already pointed out, terms of the dipole moment that oscillate at $\omega_0$ and at $\omega_0 \pm \omega_k$ describe Rayleigh, stokes $(\omega_0 - \omega_k)$ and ant-Stokes $(\omega_0 + \omega_k)$ Raman scattering. The moments vibrating at $2\omega_0$ and $2\omega_0 \pm \omega_k$ describe hyper Rayleigh and hyper Raman scattering, while terms at $3\omega_0$ and $3\omega_0 \pm \omega_k$ correspond to second hyper Rayleigh and second hyper Raman scattering respectively. Although it does appear that the equilibrium second hyper polarizability tensor $\gamma_0$ and its gradient $\gamma'_k = \left(\frac{\partial\gamma_{\rho\sigma\tau\nu}}{\partial \mathrm{q}_k}\right)_0$ could contribute respectively to Rayleigh and Raman scattering, in experimental conditions concerned with both types of scattering, these terms practically vanish. So Rayleigh and Raman scattering within electrical and mechanical harmonicity are totally described by the first order induced dipole moment $\mathbf{P}^{(1)}$ retrieved from eqn 2.16 as follows;

$$
\begin{aligned}
\mathbf{P}^{(1)} &\equiv \mathbf{P}^{(1)}(\omega_0) + \mathbf{P}^{(1)}(\omega_0 \pm \omega_k) \\
&= \alpha_0 \cdot \mathbf{E}_0 \cos\omega_0 t + \sum_{k=1}^{Q} \left\{ \frac{1}{2}\alpha'_k \cdot \mathbf{E}_0 \mathrm{q}_{ko} \Big[ \cos\left[(\omega_0 - \omega_k)t - \varphi_k\right] + \cos\left[(\omega_0 + \omega_k)t + \varphi_k\right] \Big] \right\}
\end{aligned}
\tag{2.17}
$$

Since every molecule is polarizable and has a non trivial equilibrium polarizability $\alpha_0$, Rayleigh scattering is always observed, while regarding Raman scattering which we will now consider specifically for further discussion, the selection rule for a given mode $\mathrm{q}_k$ requires that the net variation of the molecular polarizability, $\alpha'_k = \left(\frac{\partial\alpha_{\rho\sigma}}{\partial \mathrm{q}_k}\right)_0$, be non-zero at the equilibrium configuration. Hence, symmetric vibrations inactive in infrared absorption become very strong in Raman scattering. Eqn 2.17 clearly shows that Raman transitions

$E_i \longrightarrow E_f$ occur with $E_f - E_i = \Delta E = \pm\hbar\omega_k$, where the $\omega_k$ are normal vibrational frequencies of the molecule.

## Overtones and Combinations Tones Transitions

In the description presented so far, mechanical and electric harmonicity were introduced. However, the normal coordinate $q_k$ (eqn 2.15) generally includes anharmonic factors of the form $\cos(2\omega_k t + \varphi_{2k})$, $\cos(3\omega_k t + \varphi_{3k}), \ldots$ related to overtones, and $\cos(\omega_k t + \varphi_{kl})\cos(\omega_l t + \varphi_{lk})$ related to combination tones. So to the first order these new factors will introduce in each term of the total dipole moment (eqn 2.16) involving $q_k$ new frequency components of the form $2\omega_k$ and $(\omega_k \pm \omega_l)$ called overtones and combination tones, respectively. Since the anharmonic nature of $q_k$ does not affect the polarizability gradient $\alpha'_k$, the same selection rule applies for Raman over tones $(\omega_0 \pm 2\omega_k)$ and combination tones $(\omega_0 \pm (\omega_k \pm \omega_l))$. However, in case of electrical anharmonicity, third and higher order terms in the Taylor series expansion of the polarization and the various polarizability tensors (eqns 2.11 - 2.14) include factors of the form $q_k q_l \propto \cos(\omega_k t + \varphi_k)\cos(\omega_k t + \varphi_k)$, $k, l = 1, 2, \cdots Q$ and so on. They will equally introduce additional frequency components connected with overtones and combination tones involving new tensors. So Raman overtones and combination tones due to electrical anharmonicity follow a different selection rule since they involve, to the first order, a new tensor $\alpha''_{kl} = \left(\frac{\partial^2 \alpha_{\rho\sigma}}{\partial q_k \partial q_l}\right)_0$ ; $k, l = 1, 2 \cdots Q$. As a consequence these transitions can be Raman active even if the fundamental is not.

It follows from the classical approach just touched upon above that Raman intensity from one molecule depends on the phase $\varphi_k$ of the corresponding vibrational mode. Because $\varphi_k$ differs from one molecule to another in the exciting volume, the molecules involved behave as independent sources: the intensity from $N$ non-interacting molecules is $N$-times that from a single molecule and does not depend on the bulky structure of the molecular system. Consequently, Raman scattering is incoherent, unlike Rayleigh scattering, which strongly depends on the molecular system arrangement and can be coherent in some cases, such as in forward scattering. In addition, the classical approach is very suitable for qualitative characterization, since it yields the correct frequency dependence of the scattered radiation, including, fundamental modes, overtones, and combinations tones. It also predicts the dependence of the vibrational scattering tensors for both linear and non linear Raman spectroscopies on the different derived polarizability tensors $\alpha'$, $\beta'$, $\gamma'$, and so on. Meanwhile, the classical description cannot be applied to molecular rotations. It fails to show how $\alpha'$ is connected with molecular properties and does not consequently yield experimentally observed intensities. A quantum mechanical treatment is therefore needed for

both comprehensive qualitative and quantitative description of all light scattering phenomena in general and Raman scattering spectroscopies in particular.

### 2.2.3 Quantum Mechanical Approach of Raman Scattering

The motion of the molecule is quantized and the classical multipole moments are easily cast into operators. The electromagnetic field is regarded as introducing a perturbation in the molecular system. Using time-dependent perturbation theory, the generalized transition polarizability tensor describing Raman scattering is expressed as followed;

$$(\alpha_{\rho\sigma})_{fi} \equiv \langle f|\hat{\alpha}_{\rho\sigma}|i\rangle_{\mathbf{Raman}} = \frac{1}{\hbar}\sum_{r\neq i,f}\left\{\frac{\langle f|\hat{\mathbf{P}}_{\rho}|r\rangle\langle r|\hat{\mathbf{P}}_{\sigma}|i\rangle}{\omega_{ri}-\omega_0-\mathrm{i}\Gamma_r}+\frac{\langle f|\hat{\mathbf{P}}_{\sigma}|r\rangle\langle r|\hat{\mathbf{P}}_{\rho}|i\rangle}{\omega_{rf}+\omega_0+\mathrm{i}\Gamma_r}\right\} \tag{2.18}$$

The kets $|f\rangle$ and $|i\rangle$ are time-independent unperturbed wave functions related to the time-dependent ones by the exponential phase factors $\exp[-i(\omega - i\Gamma)t]$; the summation extends over all intermediate levels $r$ of the full bandwidth $\Gamma_r$. Within the Born Oppenheimer approximation and after introducing electrical and mechanical approximations in a treatment similar to equations [(2.2)-(2.4)], the contributions to Rayleigh and Raman scattering of the polarizability tensor operator are expressed for non degenerate vibrational states as follows;

$$(\alpha_{\rho\sigma})_{v^f v^i} = \langle v^f|\hat{\alpha}_{\rho\sigma}|v^i\rangle = \left\langle \prod_{k=1}^{Q} v_k^f \middle| \hat{\alpha}_{\rho\sigma} \middle| \prod_{k=1}^{Q} v_k^i \right\rangle = (\alpha_{\rho\sigma})^{Ray}_{v^i v^i} + (\alpha_{\rho\sigma})^{R}_{v^f v^i}$$

$$(\alpha_{\rho\sigma})^{Ray}_{v^i v^i} = (\alpha_{\rho\sigma})_0 \left\langle \prod_{k=1}^{Q} v_k^f \middle| \prod_{k=1}^{Q} v_k^i \right\rangle = (\alpha_{\rho\sigma})_0 \ , \qquad v_k^f = v_k^i \qquad ; \qquad \text{(Rayleigh)}$$

$$(\alpha_{\rho\sigma})^{R}_{v^f v^i} = \sum_{k=1}^{Q}\left(\frac{\partial\alpha_{\rho\sigma}}{\partial \mathrm{q}_k}\right)_0 \left\langle \prod_{k=1}^{Q} v_k^f \middle| \hat{\mathrm{q}}_k \middle| \prod_{k=1}^{Q} v_k^i \right\rangle = \begin{cases} \sum_k \left(\frac{\partial\alpha_{\rho\sigma}}{\partial \mathrm{q}_k}\right)_0 b_{v_k}(v_k^i+1)^{\frac{1}{2}}\,; & v_k^f = v_k^i + 1 \\ \sum_k \left(\frac{\partial\alpha_{\rho\sigma}}{\partial \mathrm{q}_k}\right)_0 b_{v_k}(v_k^i)^{\frac{1}{2}}\,; & v_k^f = v_k^i - 1 \end{cases} \tag{2.19}$$

where $b_{v_k} = \left(\frac{\hbar}{2\omega_k}\right)^{\frac{1}{2}}$. The molecule's total vibrational wave function $|v^i\rangle$ of the state "i" for example is the product of independent oscillator wave functions $|v_k^i\rangle$ containing each $v_k^i$ vibrational quanta: $E_k = \hbar\omega_k(v_k^i + \frac{1}{2})$. The number of vibrational quanta of the final state "f" for a given vibrational mode "k" is $v_k^f = v_k^i + 1$ (Stokes) or $v_k^f = v_k^i - 1$ (anti-Stokes). Therefore, the condition $\Delta v = v_k^f - v_k^i = \pm 1$ for permitted Raman transitions elucidates the same frequency dependence as in the classical approach. However, still, the basic parameter for Raman spectroscopy remains the polarizability gradient $\alpha'_{\rho\sigma} = \left(\frac{\partial\alpha_{\rho\sigma}}{\partial \mathrm{q}_k}\right)_0$ which should be non zero for a given mode $k$ to be Raman active. The classical approach assigns the same intensity for both Stokes and anti-Stokes bands; but the intensity actually depends on the

population density $N_i(E_i)$ in the initial level $i$, the excitation intensity $I_0$ and the Raman scattering cross section $\sigma_R(i \to f)$.

$$I_s = N_i(E_i)\sigma_R(i \to f)I_0$$

The population densities follow the Boltzmann distribution at thermal equilibrium; with comparable cross section, the anti-Stokes lines are several orders of magnitude lower than the Stokes lines since the initial state in the former case is an excited state. Consequently, only the Stokes part of the Raman spectrum is used in practice. The scattering cross section depends on the matrix elements (2.18) and can be calculated using the generalized polarizability tensor (2.20);

$$\sigma_R(i \to f) = \frac{8\pi\omega_s^4}{9\hbar c^4}\left|\sum_{r\neq i,f}\frac{\langle f|\hat{\mathbf{P}}_\rho|r\rangle\langle r|\hat{\mathbf{P}}_\sigma|i\rangle}{\omega_{ri}-\omega_0-\mathrm{i}\Gamma_r}+\frac{\langle f|\hat{\mathbf{P}}_\sigma|r\rangle\langle r|\hat{\mathbf{P}}_\rho|i\rangle}{\omega_{rf}+\omega_0+\mathrm{i}\Gamma_r}\right|^2 \tag{2.20}$$

where the elements $\langle\alpha_{\rho\sigma}\rangle_{ir} = \langle r|\hat{\mathbf{P}}_\sigma|i\rangle$ depend on the symmetrical properties of the molecular wave functions $\langle i|$ and $\langle f|$.

# 3. Raman Experimental Techniques and Biomedical Applications

## 3.1 Methods for Biological Investigation – The Raman Approach

### 3.1.1 Standard Tools – Advantages and Disadvantages

Most sophisticated methods for the investigation of tissue and cells or for diagnosis are a combination of several basic procedures together with visualization techniques. The most common basic procedures include staining, protein binding, and antigen expression or immunoassays, flow cytometry and cell count, fluorescence excitation, various separation techniques, such as protein extraction, just to list a few. Histology and immunoassays are commonly used for cancer diagnosis and grading. In this cases, staining using specific reagents helps to reveal the morphological structure of cells and tissue, that can be visualized under a microscope. For immunostaining, specific organelles or molecular groups can be stained to enhance the visualization and the diagnostic power. Most clinical diagnoses rely on direct and large scale visualization techniques using X-ray diffraction (X-ray radiology, CT scan, mammography and tomosynthesis, etc), nuclear magnetic resonance (MRI), ultrasound (sonography), or tracer agents (PET: positron emission tomography, and other nuclear medical imaging). Some of these visualization techniques are enhanced by the use of contrast agents for optimal 3D imaging of bodily structures. They help to diagnose several types of diseases. In the case of cancer, the tumor can be localized by a CT or a PET scan, for example. Then, a biopsy is taken for histology or immunoassay in order to determine the type and grade of the cancer and to decide about the treatment. Besides diagnosis, the understanding of the inherent complexity of biological systems requires information at the molecular level. Selective excitation of fluorescence from natural intrinsic chromophores, such the green fluorescence protein (GFP), within the cell or tissue, is widely exploited. These intrinsic chromophores are however limited, and many tissue

or cellular compounds yield overlapping fluorescence. Therefore, the use of extrinsic dyes is a common practice in biorecognition assays in order to image specific targets, biological functions, and to visualize the molecular basis of some key biological events. This is of particular interest in cancer research for the discovery of biomarkers that may help to understand the biomolecular basis of cancer transformation, tumor development, and the response to therapy. During flow cytometry, antigen recognition assays can be combined with FACScan analysis (fluorescence activated cell sorting) in order to separate cells with slight phenotypic differences. In brief, in order to probe biochemical mechanisms in detail, besides traditional methods, such as histology and immunostaining, the state of the art very effective technique is a direct optical observation combining the highly sensitive fluorescence imaging and indirect immunofluorescence with biorecognition methods.

### 3.1.2 Raman Techniques as Alternative or Complementary Tools

Although highly sensitive and rather efficient, the combined biorecognition with immunofluorescence and fluorescence imaging technique does suffer from some limitations. First of all, at the moment, this technique is in most cases restricted to the observation of already known and labeled markers only. In addition, the prior bio-conjugation required may, in some cases, influence the detailed biochemical makeup. Especially, this can be detrimental in the situation where very precise and specific, but rather small information is being looked for. Therefore, the ultimate achievement for the investigation of detailed biological processes would be to look for small variations without interfering with the cell too much or without destroying it. This situation justifies the search for noninvasive and nondestructive methods. Therefore, Raman spectroscopy has been introduced as powerful alternative or complementary tool for biomedical investigations, because it can provide direct fingerprint-like molecular information based on the vibrational contrast of molecules. In this context, the application of Raman spectroscopy usually refers to the implementation of the linear spontaneous Raman scattering. moreover, different variants of Raman techniques are applicable for biological investigations. The choice of a given Raman technique depends of the biological information of interest. Despite limitation due to low scattering cross section and fluorescence disturbance, spontaneous Raman scattering or simply Raman scattering is viewed as the most attractive potential candidate for its ability to render molecular-level information both *in situ* or *in vivo* and in a nondestructive and noninvasive way. As a key approach, it is important to first of all resolve specific Raman signatures of the potential but unknown reliable biomarkers associated with biological events, such as

cancer transformation, tumor development, phenotypes variation, and disease onset in general. In this context SERS can also be very helpful in enhancing the weak Raman signals in many situations. Once resolved and specific Raman fingerprints are known or suggested, current Raman techniques based on either linear Raman (spontaneous Raman, SERS, etc.) or nonlinear Raman (e.g. CARS, SRS, etc.) allow to couple this information with spatial information. In this respect, both SERS and nonlinear Raman techniques can offer sensitivity comparable to fluorescence in many cases.[21,26–30] At the same time, since they are still based on the Raman vibrational contrast, they can provide better biochemical specificity (as compared to fluorescence). Among nonlinear Raman techniques for bioimaging, coherent anti-Stokes Raman microscopy (CARS) and stimulated Raman loss microscopy (SRLS) are far more efficient than spontaneous Raman spectroscopy. They can provide high quality chemically-specific and spatially resolved images within seconds. However, benefiting from these advantages optimally is, for some nonlinear Raman techniques (e.g. CARS), at the cost of losing the hyperspectral information in the normal Raman spectrum. In the next sections, some aspects of the experimental Raman techniques are presented. The case of CARS or SRLS is only briefly summarized, with a few examples. Then, an overview of some biomedical applications of Raman scattering, that are in some respect related to the different projects carried out in the framework of this thesis, is presented.

## 3.2 Experimental Raman Scattering Techniques

### 3.2.1 Spontaneous Raman Scattering Experiment

A Raman scattering experiment consists of an excitation and signal collection unit, a signal analysis and detection unit, and alignment optics. Sample excitation requires a laser source (ideally tunable) of monochromatic line(s), that is coupled to the sample. Signal analysis consists of Rayleigh scattering rejection, followed by the dispersion of the Raman signal using a spectrometer equipped with a sensitive and low noise threshold detector. The direction of signal collection to that of the incident laser defines the scattering geometry, and the most common ones are the 180° (back scattering), 90°, and 0° (forward scattering) geometries. The point or area of signal collection may be chosen away from the focus of the incident laser on the sample, as is the case in a variant of Raman scattering called “spatially offset Raman scattering”. In all, the choice of the optics for beam alignment, focusing, and signal collection, helps to perform either macroRaman (lenses with long focal length or no focusing; mostly in a 90° scattering geometry) or microRaman (tight focusing using a microscope setup, mostly in a back scattering geometry). In confocal Raman, a pair of

adjustable pinholes are added in the beam paths of the exciting and scattered light. MicroRaman (usually in a confocal configuration) is the most popular technique for Raman investigations of biological samples (cells, tissue, and circulatory fluids). Raman setups used for the projects within this thesis are described in the next section.

### 3.2.2 MicroRaman

For most of the Raman experiments carried out in the framework of this thesis, an open Raman setup (self assembled) and a partially automated mainly commercial Raman system, both in the laboratory of Prof. Dr. Arnulf Materny at Jacobs University, Bremen, Germany, were used as described below. An illustration of the Raman setup is shown in Fig 3.1. Different excitation sources, with an argon ion laser (Inova 308, Coherent INC., USA) and a krypton ion laser (Inova 302, Coherent INC., USA) as the main sources, are configured to be simultaneously shared in two measurement setups. In the first setup, a self-built microscope equipped with four focusing objectives (100×, N.A. 0.90: Nikon, Japan; 50× LWD, N.A. 0.50: Zeiss, Germany; 40×, N.A. 0.65; and 10×, N.A. 0.20: Olympus, Germany) and a CCD camera for sample inspection is used to focus the laser onto the sample and to record the scattered light in a back scattering geometry. Then, Rayleigh scattering is filtered out by placing the appropriate holographic notch filter for the corresponding laser line before a 20 cm lens that focuses the Raman signal onto the slit of a spectrometer. A single monochromator (Triax 302, Jobin Yvon, France) with three interchangeable holographic gratings (600, 1200, and 2400 grooves/mm) is used to disperse the Raman signal. Finally, a liquid $N_2$ UV-enhanced cooled CCD detector (symphony 3500, Jobin Yvon, France) with optimal sensitivity in the green is used for the detection. The Triax spectrometer has two motorized slits, one at the front entrance and the other at the side entrance. It can also be used for macroRaman in the 90° scattering geometry for efficient measurement of liquid samples. The second setup includes a semi-compact commercial Raman system consisting of a spectrometer unit rigidly assembled with a microscope unit (for microRaman in the back scattering geometry), and a macro unit (for macroRaman in the 90°, or forward scattering geometries). Manually switchable mirrors help to operate the system either in the micro or macro mode. The microscope part consists of a semi-confocal microscope assembly equipped with four focusing objectives (100×, N.A. 0.90: Nikon, Japan; 50× LWD, N.A. 0.50: Zeiss, Germany; 40×, N.A. 0.65; and 10×, N.A. 0.20: Olympus, Germany), a color CCD camera for sample inspection, and an automatic raster XY scanning stage. The spectrometer part consists of a threefold-operational modes triple spectrometer (T64000, Jobin Yvon, France). In fact, this systems has there stages of gratings for either a triple additive mode, a double subtractive mode or a single mode. The first two stages have

a 1800 grooves/mm holographic grating each, and the last stage has two interchangeable holographic gratings (600, 1800 grooves/mm) for single mode. In the triple additive mode, light is dispersed at all three stages, in order to obtain highly resolved Raman spectra. In the subtractive mode, the first two stages are subtractive, *i.e.* light dispersed by the first stage is recombined by the second stage so that spatial separation of the spectral region of interest is efficiently achieved. This arrangement makes measurements very close to the laser position possible, without the use of a filter for Rayleigh rejection. In the single mode option, the first two stages are simple bypassed, and only the last stage is used as in a simple monochromator. In the triple additive and single modes, the systems has an inbuilt mount for inserting a filter for Rayleigh scattering rejection before the Raman signal enters the first or the last stage of the T64000 spectrometer. Finally, a liquid $N_2$ cooled front illuminated CCD detector more suitable in the red is attached to the T64000 spectrometer.

For some of the projects completed within the framework of this thesis, two more compact

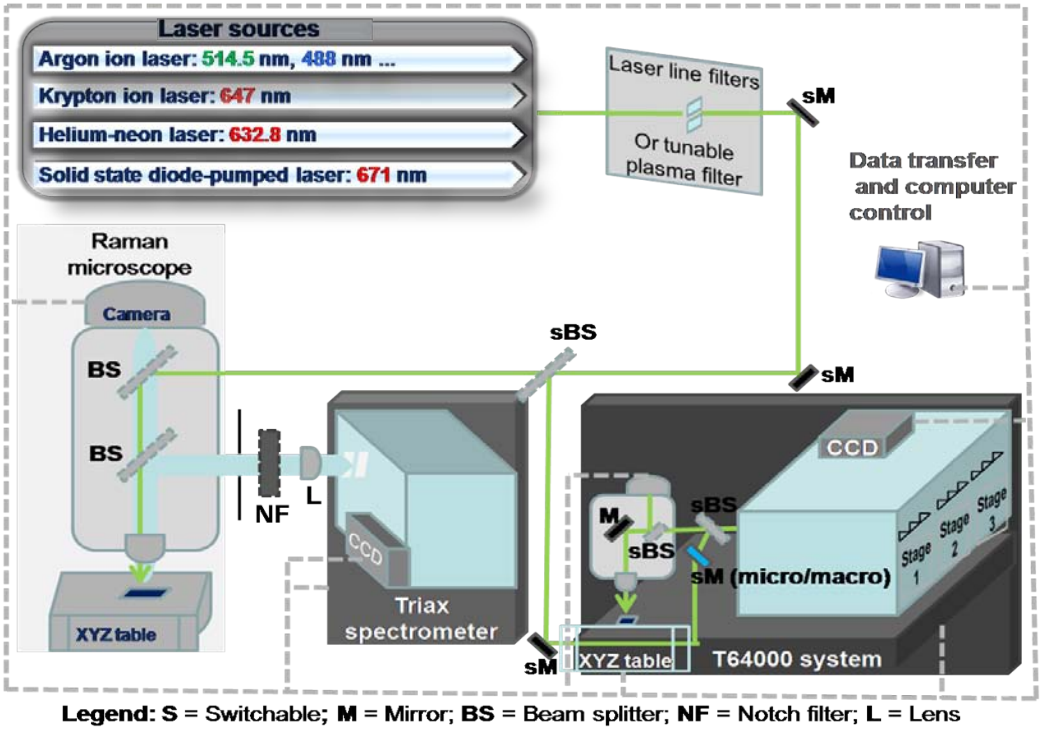


**Figure 3.1: Experimental setup**

commercial and automated Raman systems were made available to us in the laboratory of Prof. Jiming Hu at Wuhan University, Wuhan, China:

Of the two Raman systems, the first and main sytem used for the Raman experiments discussed in chapter 7 is a Horiba Jobin Yvon Raman microspectrometer (HR800 system, Horiba Jobin Yvon, Villeneuve dAscq, France). It is fully automated, with built-in laser

sources (*e.g.,* 632.8 nm HeNe laser, 785 nm diode laser, etc.), attenuation prisms and filters to control the power of the laser exposed on the sample. The microscope part has several focusing objectives including among others a 50× long-working-distance objective [numerical aperture (NA) 0.50, Olympus, Japan]. This system includes a stigmatic spectrometer with two motorized gratings (600 and 1200 grooves/mm). The other Raman system is a Renishaw RM1000 Raman system (Renishaw RM1000, Wotton-under-Edge, Gloucestershire, UK) equipped several lasers sources ($Ar^+$, 785-Diode, etc.), with similar characteristics as above. Both systems can be optimized for maximum throughput, detection sensitivity, and fluorescence suppression using a motorized confocal arrangement.

### 3.2.3 Surface Enhanced Raman Scattering (SERS) and SERS Probes

The Raman effect, as stated earlier, is an inefficient scattering process. Surface enhanced Raman scattering (SERS) has been one of the highlights of optical spectroscopic methods that has helped overcome efficiently the low scattering cross section of the spontaneous Raman effect. Experimentally, SERS just consists of a normal Raman experiment (in any desired configuration), in which the sample is brought in close contact with rough metal particles of nanometer size in order to obtain an enhanced Raman signal. When a molecule is absorbed on a nanometric scale rough metal surface, number of competitive effects enhance its spectroscopic features. The enhancement observed in SERS is usually attributed to two mechanisms: A field enhancement termed electromagnetic (EM) mechanism, and the chemical mechanism. The EM enhancement is mainly due the excitation of localized surface plasmons (LSP), but also to multiple reflections at the metal surface, and to the lightning rod effect, which is considerable at sharp-edged structures. The chemical enhancement is usually much smaller than the EM enhancement, and is caused by electron tunneling between the molecule and the metal surface, providing a way for resonant excitation, such as in resonant Raman. Therefore, except of direct overlap of molecular orbitals and electronic states in the metal, the most relevant mechanism of SERS is the EM enhancement of the molecular dipole moment by the strong size-dependent local field of the surface plasmon resonance in the metal particles and a non-negligible lightning rod effect for particle having sharp edges. Many works are reported, which efficiently describe theoretical models of these effects.[35–39] Using dye molecules absorbed on substrates of aggregated Au and Ag nanoparticles, Kneipp et al al.[17,19,40] and Nie and Emory[23] have reported large enhancements of [12–14] and [13–15] orders of magnitude respectively. Such giant enhancements are attributed to localized SP — hot spots[41] — formed by a cluster of nanoparticles concentrated in a small region. This aspect has allowed strong single-molecule SERS highly beneficial for biological applications, such as space-resolved

single-cell mapping.[25] In some situations, it is interesting to apply SERS active probes, such as colloid films, self-similar nanostructures, and self-assembled nanoparticles for enhancing spectroscopic differences that exist between healthy and unhealthy cells and tissue.

#### 3.2.3.1 Standard Preparation of SERS Substrates

Monitoring the mechanisms responsible for SERS is one of the most challenging tasks of SERS. It has been shown that self-assembled similar geometries can also provide nanoenvironments (hot spots) favorable for large field enhancements, comparable to random aggregates, the morphological properties of which cannot be controlled. Making use of different geometries, shapes and sizes, the parameter of the nanostructures can be flexibly set in order to tune the plasmon resonance for specific needs. Therefore, for biological investigations, noble metal colloids, as well as Au nanostructures can be used.

**Examples for Gold and Silver Colloids**

- **Gold colloid** can be prepared by diluting 0.1 ml of $HAuCL_4$ solution (4%, w/v) in 40 ml of triply distilled water, followed by a dropwise addition, with stirring, of 1 ml of trisodium citrate solution (1%,w/v). This mixture is then boiled for 5 min to obtain a colloidal solution of homogeneously distributed gold particles with plasmon resonance around 525 nm.

- **Silver colloid** can be produced as followed: 200 ml of 1 mM $AgNO_3$ aqueous solution is heated to boiling, then 4 ml of 1% trisodium citrate are added, keeping the mixture boiling for 1 h. A turbid gray, stable (for some months) colloid is then obtained showing a plasmon absorption maximum at $\sim$ 400 nm. Alternatively, silver colloid can also be prepared in a cold bath procedure, following an original procedure by Creighton *et al.*[42] Briefly, an ice-cold and $N_2$-saturated $NaBH_4$ solution is added to a certain amount of $AgNO_3$ solution in 1:3 ratio, under vigorous stirring of the $AgNO_3$ solution. The result is a yellowish colloid of silver nanoparticles with the plasmon abosorption at 392 nm. The conditions in the above preparation procedure can be adjusted to influence the size of the nanoparticles and the plasmon resonance frequency. In addition, many other simple procedures can be found in the literature.

- **Core-shell metal nanoparticles**: For biological applications gold is preferred. However, because silver exhibits the strongest SERS among noble metals, many applications make use of multi-shell metallic structures, with silver as the core. These multishells structures are usually obtained by reducing the salt of a given metal on top of

the nanoparticles seeds of another metal. In many cases for biological applications, a thin layer of gold is deposited on a silver core. This can be repeated alternately. This silver/gold bilayer structures help to tune the plasmon resonance to the red and provide stronger enhancement than silver or gold alone.

- **Self assembled nanoparticles**: Highly **aggregated sols** provide the best SERS-active substrates: Aggregated sols can be obtained when metal colloids are simply cast onto optically suitable substrates such as silicon, quartz, etc to form clusters and fractals. They can also be obtained during the preparation of metal colloids by inducing aggregation in solution via the addition of salts or surfactants. Since the morphological properties of randomly aggregated nanoparticles cannot be controlled, they are not reliable for quantitative analysis.

- **Self-assembled nanoparticles with defined and reproducible geometries** are also formed via the aggregation of individual particles, but with a certain degree of regularity. This can be achieved by controlling the aggregation in order to form special geometries, including nanoparticle networks, nanorods, and more interestingly, dimers, trimers, and so on. With sufficient care, these particles can be obtained with size distribution close to mono dispersion. Assembled particle dimers and trimers yield hot spots at the junction between individual particles or in micro interstices formed by the assembled particles. They are therefore very promising for biological applications. Good and recent examples for the production and characterization of self-assembled nanoparticles are reported in many works.[43–46] Within the framework of the present thesis, a simple procedure for the production of peanut-like nanoparticles is given later in chapter 8 “Synthesis of Gold Nanopeanuts from Gold-Silver Core-Shell Nanoparticles”

**Preparation of SERS Nanostructures**

- **Metal Films**: Thin metal islands (aggregated nanodots, nanoislands, etc) films can be prepared by vacuum deposition of the evaporated SERS-active medium on a suitably pre-conditioned substrate. They can also be prepared by electrochemical deposition. This is done by reducing an electrolyte containing the ions of the metal to be deposited onto a pre-conditioned substrate (*e.g.* through electropolishing and/or anodizing) placed at the cathode. These films are widely used as SERS substrates. The SERS signal critically depends on the film morphology; the deposition rate, the substrate condition (roughness, purity, etc), its temperature during deposition and the

mass thickness are key factors that need to be handled properly to control the film structure. Vacuum deposition is very convenient since it is applicable to any metal as active medium. However, similar to aggregated nanoparticles in solution, pre-defined film structures are rather hard to obtain with thin films in this way.

- **Self-Similar Au Nanostructures**: Metal nano arrays are very good reproducible pre-defined structures that can provide tunable nanoenvironments for the EM enhancement mechanism. They can be produced with different geometries, shapes and orientations, sizes, and variable grating constants, which can be controlled flexibly in order to tune the resonant frequencies of the surface plasmon. They can be prepared by vacuum or electrochemical deposition as well, but after a given mask or pattern has been applied or written on a substrate. Highly ordered nanostructures are commonly prepared by electron beam lithography techniques. The preparation of Au nanostructures is briefly described below as an example:
  First of all, a thin film (100-200 nm) of a polymeric e-beam resist is deposited by spin coating over a convenient pre-conditioned substrate such as silicon. Then, the desired structure is directly written using an e-beam gun, followed by the development in a soft solvent to remove the polymer resist from the written areas. Finally, a double Au/Ti layer is successively deposited by metal evaporation before a lift-off process in acetone, which dissolves the polymer, leaving only the Au nanodots resting on the written areas of the silicon substrate.

#### 3.2.3.2 SERS Tags for Biological Application

Silver/gold core-shell nanoparticles, self-assembled gold nanoparticles, such as dimers, trimers, etc., and simple gold nanoparticles are rather interesting for biological applications of SERS both due to the biocompatibility of gold and the efficient SERS enhancement of the self-assembled particles. Multilayer silver/gold core-shell spherical nanoparticles are very promising because, they can offer an combined benefit of high reproducibility and high SERS enhancement (comparable to self-assembles particles, better than silver or gold alone for red excitation). These nanoparticles can also be functionalized to form sensing probes based on SERS.

### 3.2.4 Raman Imaging

#### 3.2.4.1 MicroRaman Imaging – Potential and Limitation of Spontaneous Raman

Raman spectra from cells and tissue show prominent contributions from proteins, lipids, nucleic and amino acids. MicroRaman has the potential for imaging these macromolecules via the selection of the corresponding spectral signatures. It offers one of the most interesting multiplex imaging capabilities, because many macromolecules can be imaged simultaneously. The confocal arrangement helps to improve both spatial resolution and sensitivity. The use of intensified CCD detectors helps to further increase the sensitivity and reduce mapping acquisition times. Some researchers have demonstrated confocal Raman imaging of molecular profiles in the skin.[47] Other possible applications exist, where carotenoids content and lipid molecules on the subcutaneous layers are imaged. Another interesting example is "confocal cross-polarized imaging of skin cancers to potentially guide mohs micrographic surgery" by Rajadhyaksha *et al.*[48] Compared to nonlinear Raman techniques, spontaneous Raman is powerful for probing fine spectral details associated with slight molecular changes, such as in cancer. However, at the present, the low sensitively of spontaneous Raman hinders realistic practical imaging applications.

#### 3.2.4.2 Coherent Anti-Stokes Raman and Stimulated Raman Imaging

For the experimental implementation of CARS, the coherent interaction of two pump ($\omega_p$) laser pulses and a Stokes ($\omega_s$) laser pulse is required to produce an anti Stokes signal $2\omega_p - \omega_s$, which is also coherent and is directed according to the phase matching condition. For a resonant CARS signal (vibrational or Raman resonance), the frequency difference between the pump and the Stokes has to match the vibrational frequency "$\omega_M$" of a specific Raman mode ($\omega_p - \omega_s = \omega_M$) (*e.g.* corresponding to a specific molecular information of interest for imaging). In order to achieve the desired frequencies, (*e.g.* an optical parametric can be used to produce from a given fundamental laser (a Ti-Sapphire laser), laser outputs with tunable frequency. For the spatial overlap of the exciting beams, a folded BOXCARS geometry can be used as in Figure 2.3 (c) (macroCARS); it helps to spatially separate the CARS signal. However, for microscopy (microCARS), which is of particular interest for biological applications, a collinear arrangement of the beams is more convenient. The possibility to detect a CARS signal from tightly focused pump and Stokes beams opened the way to CARS microscopy, which gained new interest especially since 1999.[49] The CARS signal can then be collected either in transmission (forward CARS) or in a backscattering mode (epi-CARS). Epi-CARS detection has revolutionized CARS microscopy[49–51] and made CARS imaging of biological samples (cells and tissue) possible.

As a nonlinear Raman process, CARS relies on the use of strong field strengths obtainable with pulsed lasers. This results in intense CARS signals that can considerably reduce image acquisition time, for a much faster imaging capability as compared to spontaneous Raman imaging. Noteworthy, the CARS signal is generated only at the focus of the spatially coincident exciting beams. This results in a better image resolution than with spontaneous Raman and fluorescence imaging. The drawback of CARS compared to Raman is that the spectral information is only tuned to one Raman peak rather than acquiring the full Raman spectrum. The biggest problem in CARS microscopy is the non-resonant background contribution. Ideal CARS microscopy systems use picosecond tunable pulsed laser sources operating in the near infrared region. These systems provide a good compromise for safety (avoiding photodamage due to multi photons processes), spectral resolution, sensitivity, and speed, while minimizing the non-resonant contribution. Another nonlinear Raman technique, which is rather promising for biological application, is stimulated Raman loss (SRLS) microscopy, which is one the two types of stimulated Raman scattering (SRS: loss and gain). In a SRS experiment, a narrow pump pulse (a few picoseconds long) together with a white light super continuum as the Stokes pulse, are used in order to simultaneously record the full Raman spectrum. Therefore, SRS has the advantage of providing the complete spectral information as normal Raman (hyperspectral imaging with true Raman line shape) while also offering the same benefit as CARS, for the special case of SRLS. The non-resonant background contribution observed in CARS microscopy is less problematic is SRS microscopy. However, the white light continuum is the background in a SRS spectrum, and the difficulty to produce stable and flat white continua limits the sensitivity in SRS, as compared to CARS.

CARS imaging of many biological events have been successfully achieved in many examples. Despite the drawback that CARS is only tuned to one Raman peak rather than providing the full spectrum, CARS can still be used to acquire highly resolved images of many biological systems including the skin, brain, cells, and tumors, based on the strongly intense $CH_2$ stretch of lipids. Also in the fingerprint region of biological samples, CARS can be used to visualize mitochondria by tuning to the Raman CH stretch band. CARS has been used to image protein (collagen and elastin) and protein secondary structures (Alpha-helix proteins and beta-sheet proteins), DNA using the phosphate vibration, and deuterated molecules. A good record of the CARS experimentation and biological applications have been summarized by Evans *et al.*, and Downes *et al.*[52,53] Specific biological benefits of CARS have been demonstrated.[21,26,29,30,54,55] Stimulated Raman loss microscopy for label-free biomedical imaging with high sensitivity has also been shown. For example, SRLS images tuned to the vibrational frequency of dimethyl sulfoxide (DMSO), which is

a vehicle for drug transport through the skin have been acquired.[56] The main benefit of CARS is speed and spatial resolution for imaging, and the fact that it is fluorescence-free, whereas the benefit of Raman is the full and more detailed spectral information. Both techniques can be implemented together. However SRS holds more promising prospects for the future in biomedical imaging.

#### 3.2.4.3 Surface Enhanced Raman Imaging

SERS targeting probes are SERS-active complexes that can be used to address specific events or biomolecules within living cells. This approach is similar to biorecognition based on fluorescent labels. However, it has the advantage that the Raman or SERS label is portable and does not bleach. The same Raman label or Raman reporter can be used for different targeting events (here just the bio-linker needs to be changed to conjugate a different biomolecule). In addition, multiplex labeling are less problematic compared to fluorescent labels, because Raman reporters with clearly separated spectral signatures are plentifully available. Strong SERS images of cells incubated with silver nanoparticles labeled with cresyl violet acetate has been reported, where the authors[54] showed a clear distribution of the SERS-active complex inside the cell. Biologically active networks of gold-phages (Au-Phage)[57] consisting of bacteriophage (phage) directly assembled with gold nanoparticles have also been addressed as promising efficient signal reporters for many optical spectroscopies including SERS. In these example the signal originating from the Raman labels was monitored to gain biological information. However, another interesting aspect for SERS targeting is that the signal recorded does not necessarily have to be restricted to the scattering that originates from these Raman labels themselves (signal reporters). In fact – and that is also a concern in standard biorecognition assays – critical molecular events inside cells can only be probed when the binding of the labels to certain markers is known with high reliability. In the case of SERS, the microenvironment of potential biomarkers would be probed directly.

### 3.2.5 Potential Raman Tools for Deep *in situ* Interrogation

Raman scattering can be applied in a minimally invasive way using a fiber optic probe. Many applications, such Raman endoscopic probes and Raman colonoscopic probes have been proposed.[58] A Raman fiber optic probe can *e.g.* be helpful to guide surgery during tumor removal.

## 3.3 Raman Data Analysis & Chemometrics

Raman spectra from biological samples have very rich features in the region within [400-1800 $cm^{-1}$], which is usually referred to as the fingerprint region. In fact, this region contains nearly all spectral signatures of the main biological building blocks, including proteins, lipids, amino acids, nucleic acids, DNA and RNA, protein and DNA/RNA secondary structures, and other biological functional groups. Another interesting part of the spectrum is the region around the $CH_2$ stretching mode of lipids and proteins near 2880 $cm^{-1}$. Mainly because of the more complex fingerprint region, the evaluation of Raman spectra requires in many cases prior pre-processing and spectra correction. In the latter case the identification of the spectral features suitable for the correction is performed such that the intrinsic Raman fingerprint information from the cells or tissue can be retained.

### 3.3.1 Spectral Processing and Correction

Pre-processing of the Raman spectra of biological samples, including cells and tissue, usually can involve smoothing, baseline (fluorescence background) subtraction, spectral normalization, and band fitting. In this thesis, a linear Savitsky-Golay smoothing algorithm with a user-specified degree and size is used to filter spike noise from the Raman spectra. This commonly applied linear Savitsky-Golay smoothing method is based on the convolution approach which performs a least squares fit of polynomials. The larger the size value (9 being the highest) and the lower the degree (2 being the lowest) results in a higher smoothing effect. It is a rather convenient method since, even the highest smoothing effect achievable by a 2-degree 9-size linear Savitsky-Golay algorithm sill helps to retain the detailed spectral fine structures, while providing an optimum smoothing result. A 2-5 times, 4-degree 5-size or 2-degree 9-size linear Savitsky-Golay algorithm smoothing of the spectra is mostly applied in this thesis. Following this procedure, the spectra can be zeroed to the minimum intensity level in some cases. Baseline subtraction is done in very limited cases using a 5th degree user-defined polynomial fit. For most Raman spectra of biological cells and tissue, it appears more reliable and reproducible to approximate the baseline by a nonlinear first-order spline fit. In this case about 7-8 spline fitting nodes at approx. 477, 605, 692, 802, 865, 900, 1144, and 1780 $cm^{-1}$ in the first fingerprint region [450-1800 $cm^{-1}$] or about 3 fitting nodes at approx. 2700, 2820, and 3652 $cm^{-1}$ in the second region [2700 - 3700 $cm^{-1}$], can be manually or automatically set. These spline fitting nodes appear to be very suited for Raman spectra of different cells and tissue, but their exact position and number may be slightly adjusted depending on the specific sample being measured and on the experimental conditions. Finally, spectra normalization can be done using the

peak intensity or band area of the $CH_2$ def. mode at 1450 $cm^{-1}$. Only in limited examples is spectral pre-processing sufficient for the evaluation of the Raman spectra of biological samples. Actually, Raman spectra of fixed and adherent cells or of living adherent cells measured through the culture medium and of tissue sections mounted on substrates can be seriously affected by overwhelming contributions from the substrates and/or the embedding medium or buffer. Therefore, they require proper correction before they can be evaluated. This correction can be done either before or after baseline subtraction, depending on the case, *i.e.*, on the appearance and quality of the raw spectra. In general, it appears reasonable to perform baseline subtraction before spectra correction in order to remove unquantifiable background (*e.g.* fluorescence baseline) that might compromise spectra correction. The subtraction of a background spectrum from a composite spectrum can only be done easily, if it can be separately measured (*e.g.* solvent) and if in both spectra features can be identified, which are separate from the Raman bands of the sample. In practice, one has to deal with composite spectra, where the desired Raman signal might actually be extremely weak compared to other undesirable but feature-like Raman contributions. In order to extract the actual Raman signal it is required, not just to approximate unwanted component spectra – what most automatic correction software do – but to correctly estimate the ratio, in which the unwanted contributions are present in the composite Raman signal. It is shown in this thesis that, though most powerful spectra processing software only indirectly and approximately enable such corrections, this can actually be easily achieved in very simple algorithmic steps: The first step is estimating the correction factor using the top peak areas (not influenced by any background signal) of a given feature in the unwanted spectrum around a position where minimal Raman signal is expected from the sample. This is repeated for all overlapping contributions to the Raman signal (substrate, buffer, culture or mounting medium). For example, for fixed or living cells adherent on substrates and measured through the overlaying buffer or medium, the substrate spectrum is itself usually a composite signal mainly dominated by the embedding solution and the substrate. This spectrum should itself first of all be corrected with a pure solution spectrum recorded without the substrate to obtain the substrate's residual spectrum. The cell spectra are first corrected with the pure buffer or with the pure culture medium as described above, and then with the aforementioned substrate's residual spectrum. Via these careful corrections steps, Raman signals from single adherent cells can be well resolved. For single individual spectra this can be done by most Raman programs in a multi-click procedure (top integral computation, then scaling and correction, with the integral, simple math and correction tool, resp.). However, for raster maps of hundreds of spectra, the tool in many Raman softwares, for mapping

acquisition, provides an option to generate the mapping image with "average integral intensity minus background" (*i.e.*, top integral only), around a desired wavenumber position. Therefore, simply exporting the raw mapping file and the corresponding image file that can provide the correction factors (top areas in map spectra, around a given position, divided by the corresponding top area in the corrector spectrum) into worksheets, all spectra in the map can be scaled all at once and later corrected all at once with the Raman program. Finally, pre-processed and corrected Raman data are usually exported into different formats for further spectral analysis and for multivariate analysis. The spectral data can be grouped and averaged for general information about intrinsic molecular changes accompanying the biological events under study. In this process, spectral sorting for the separation of bad data from those that can be averaged in a given set can be facilitated by multivariate analysis.

### 3.3.2 Multivariate Analysis and Histopathological Assignment

In order to evidence the capability of Raman scattering for discrimination, especially when this is based on rather small spectroscopic differences, multivariate analysis tests, including principal component analysis (PCA) and clustering analysis, are applied. This helps to reduce the dimension of the Raman data and to group the data into different clusters for detailed and more specific average information. This information describes the specific molecular basis of the different spectral variations (now clustered) present in the Raman data. PCA is usually combined with non-assisted clustering analyses in order to better characterize the spectral variations of the large dataset of the Raman spectra. Besides evidencing the discriminative capability of Raman spectroscopy, PCA is very helpful for delineating unspecific but sometimes predominant spectral variations (associated with biomolecular fluctuations inherent to the living and changing cell for example) from specific and histopathologically relevant spectral changes.

#### 3.3.2.1 Clustering Analysis

In order to better visualize PCA results, PCA is usually combined with clustering analysis. For this purpose it is useful to perform a PCA first before clustering in order to make a realistic guess of the clusters number, and then after clustering in order to highlight data grouping according to the clustering variable. The most common clustering analysis is the $K$-means clustering. In this case, the data points $x_n$ are distributed among K random clusters with the cluster centroid $z_{ki}$ of the $k^{th}$ cluster for the i$^{th}$ dimension (coordinate) being simply defined as the average over all data points belonging to the $k^{th}$ cluster $\left(z_k i = 1/n_k \sum_{n=1}^{n=n_k} x_{ni}\right)$.

Any other data point $x$ is then assigned to the $k^{th}$ cluster if the distance to that cluster centroid $d(x, z_k)$ is the shortest. In practice, K-means clustering is an iterative algorithm; the clusters are first randomly formed by choosing the first $K$ points, assigning each subsequent point to the nearest of the $K$s, then calculating the centroid of each cluster. In this work two distance types were of interest, the Euclidean distance or the usual norm 2 distance in Cartesian coordinates $\left(d(x, z_k) = \sqrt{\sum_i (x_i - z_{ki})^2}\right)$, and the Kendall's (tau) distance, which is a non-parametric distance (metric) based on the count of the number of pair-wise disagreements between two orderings (here any pair of wavenumbers for example, with the corresponding Raman intensities as the ordering values). Clustering analysis helps to easily detect bad data clusters or deviating data clusters.
The clustering result is called the Sum of Distances (SOD) usually denoted by "¡Distance type¿-SOD" (e.g., Euclidean_SOD). The Sum of Distances (SOD) is the sum of the distance values of each data point to its respective cluster centroid, added-up over all 'K' clusters. For every single iteration of the algorithm and for each resulting batch of cluster-IDs (randomly assigned numerals), the SOD is calculated. Then, after all iterations, the solution with the least SOD is retained, and displayed in the data table as the clustering parameter or category variable which takes as value the cluster ID for each data point.

#### 3.3.2.2 Principal Component Analysis (PCA)

Principal component analysis is a factorization method that helps to reduce a multidimensional dataset into only few observables or principal components, which describe the most relevant variations within the data set, as depicted by the following equation,

$$TD = V^T D^T$$

where, TD is a matrix representing the transformed or final data set. $D^T$ is the original data set matrix transposed. $V^T$ is the feature eigenvectors matrix transposed containing only selected new dimensions or eigenvectors, arranged in rows with the most significant ones at the top. The new dimensions are the eigenvectors of the covariance matrix of the original data set containing preprocessed Raman data with X-variables and Y-variables. These X- and Y-variables are defined in the case of Raman spectroscopy by the pixels number of the CCD detector (wavenumbers) and the Raman intensities of the "Y" measured samples spectra, respectively.
The PCA overview yields very important results including the total explained variance (X-expl.) described by each computed principal component (PC), the residual variance plot against sample leverage, and especially, the PCA scores' scatter plot of any two PCs,

and the corresponding PCA loading plot (X-loadings). The PCA scores' scatter plot of every two principal components (PCs) displays the samples in a new frame defined by the two PCs as new axis (new dimensions). It is a two-dimensional coordinate system that displays the samples according to their component scores and provides natural sample grouping (*e.g.*, scatter plot for PC1 **vs.** PC2). The scatter plot also helps to detect outlying samples and bad data points. The loading plot for any selected PC displays the relative importance of the original variables (X-variables; equal to the Raman wavenumbers in the present case) for the plotted PC and helps to determine the chemical origin, *i.e.*, the histopathological assignment, of the variation described by that particular PC. It should be noted that variables with high positive or negative loadings are the most significant for the variation described by the corresponding PC, while variables with small loadings are insignificant. A simple non-assisted K-means clustering analysis performed together with PCA, provides results that can be used as category variables in order to highlight the grouping in the PCA analysis of the Raman data.

## 3.4 Outline of Biomedical Applications of Raman Spectroscopy – Case Studies

### 3.4.1 General Overview of Raman Scattering Applications

In the framework of biological investigations considered in this work, the interest in mainly focused on the implementation of linear Raman techniques. Although spontaneous Raman spectroscopy suffers from a low scattering cross section, it yields, for measurable signals, fingerprint patterns with better distinguishable features and only gives a low water scattering.

To date, Raman spectroscopy has gained considerable interest across a wide range of research activities and is being introduced among standard techniques in academic, industrial and analytical, pharmacotherapeutic and medical laboratories. In fact, the fingerprinting capability can be combined, very interestingly, with the ability to resolve slight molecular changes or denaturation in molecular systems in general. This is of particular interest for living cells/tissue and possibly many disease biomarkers. An indication for this is that Raman spectroscopy has been enjoying a new renaissance and has been widely spread among state-of-the-art spectroscopy techniques in biomedical sciences. Many diseases are related to biomolecular distortions such as enzymatic or hormonal impairments, DNA and/or RNA modifications and metabolic disorders or phenotypic variations. Diseases such as cancer are connected with the modification of the proteome nature and con-

tent of living bodies. *In vivo* diagnosis of cancer is among the present most challenging topics in biomedical sciences. Early detection of the onset of diseases in general and of cancer in particular is of paramount importance to reducing morbidity, mortality and monitoring disease evolution.[59,60,60–67]

Evidence on the application of Raman spectroscopy in biomedical science in general and for noninvasive and nondestructive diagnosis of many types of cancer in particular has been brought upon numerous reports and reviews.[58,61,66,68–83] These include noninvasive diagnosis of brain tumor,[84] breast cancer,[75,76] cervix cancer,[69] skin cancer,[47,48,66,77,78], bladder and prostate cancer,[80–83] gastrocarcinoma, normal and unhealthy cells, cells growth differentiation and single cell mapping using SERS,[74] and Raman imaging of subcellular components and of tumor cells/tissue.[47,48,85,86] However, in the case of cancer, only few works applying Raman scattering have reported histochemical assignments of the spectral differences between cancerous and healthy tissues[64,87,88] or cells. Much of the work done in this attractive field relies upon bulky investigations of tissues and cells that do not allow unambiguous assignment directly targeting biologically relevant disease markers. This drawback is due to the fact that those specific and reproducible markers for cancer in particular and for many other physiological changes are present at a very low concentration in cells and tissues. An overall increase of the nucleus-to-cytoplasm ratio, disordered chromatin, higher metabolic activity, and changes in lipid and protein levels in cancerous samples has been documented for example.[53] However, this observation has mostly been related only to collagen. Unambiguous assignment of spectra differences to sensitive, specific, and reproducible cancer biomarkers then appears as the ideal attainment that would open up the possibility for realistic *in vivo* nondestructive and noninvasive implementation of Raman spectroscopy for cancer diagnosis. In addition, despite the difficulty to handle living cells, Raman scattering has been applied for the characterization of stem cells.[89] In the case of cancer, the potential of Raman scattering for diagnosis is well acknowledged and established. As compared to fluorescence, the limitations of Raman scattering are also well known, as far as full imaging with high sensitivity and speed is concerned. However, regarding the molecular basis of disease occurrence, early detection, and disease development and therapy, Raman scattering is a very versatile tool that can provides a wealth of information.

The main focus of this work comprises the following: The understanding of the molecular basis of biological events including carcinogenesis, phenotypic variation, disease induction and disease therapy, hormonal changes as well as studying the behavior of simple biomolecules at metal surfaces. The understanding of detailed tumorigenicity steps and the elucidation of the underlying molecular basis of detailed phenotypic variations associated

with any disease in general, represent an ideal attainment that would help to monitor disease development with fundamental benefit for therapy.

### 3.4.2 Specific Examples Studied as Collaborative or Joint Projects

Concrete examples or case studies completed as separate projects within the framework of the present thesis include the following:

- Monitoring and understanding of the underlying mechanism of tumorigenicity-associated biomolecular transformation in skin carcinoma.
- Monitoring tumor development in a lymphoma mouse model used to study the risk of radiation exposure.
- Probing hormonal or pathological effects of short/long-day photoperiods in hamster tissues – A Raman spectroscopic approach for studying of biological rhythms *in-situ*.
- Raman implementation in immunology: Label-free cell-sublines discrimination for the understanding of the role of molecular chaperons in phenotypic variations in colon carcinoma sublines (CX- and CX+).
- Noninvasive Raman monitoring of drug response; as a joint research project.
- Fabrication of new types of nanoparticles; as a joint research project.
- SERS of a biological molecule: The interaction of the main important biological functional groups (carboxylic and amino) with metal surface in the case of glycine.

### 3.4.3 Instrumentation for All Collaborative and Joint Projects

The different projects described in this thesis involved many instruments that were operated by the author at the host institution (Jacobs University, Bremen, Germany) and/or at the guest institution (Wuhan University, Wuhan, China) during an exchange program for the joint research projects including “Noninvasive Raman monitoring of drug response” on the one hand, and “Fabrication of new types of nanoparticles” on the other hand. The main instruments are listed in the following.

For Raman measurements, the author operated the following Raman systems:

- A self assembled Raman setup (with a Horiba Jobin Yvon Triax spectrometer) and a Horiba Jobin Yvon T64000 system both supplied with many laser sources including ion gas lasers ($Ar^+$ and $Kr^+$: Inova 308, Coherent INC., USA) and installed in the laboratory of Prof. Dr. Arnulf Materny at Jacobs university (Bremen, Germany).

- Compact and fully automated confocal Raman systems including a Horiba Jobin Yvon LabRam HR800 system with in-built laser sources and a Renishaw RM1000 Raman system (Renishaw RM1000, UK) equipped several lasers sources ($Ar^+$ laser, 785 nm diode laser, etc.), both installed in the laboratory of Prof. Jiming Hu at Wuhan University (Wuhan, China).
  These Raman systems have been described earlier, in section 3.2.2 "MicroRaman".

- Instruments operated by the author for other characterization purposes include standard UV-VIS spectrometers (*e.g.*, a Varian Cary UV-VIS, a PharmaSpec Shimadzu UV-1700, etc.), a Zeiss EM 900 transmission electron microscope (TEM), and a standard X-ray diffraction spectrometer, all available at Jacobs University.
  For the joint project about the fabrication of novel metal nanoparticles described in chapter 8, besides the instruments available at the host institution, the author and collaborators have also operated a more advance TEM system, a JEOL JEM-100CXII microscope at Wuhan University (Wuhan, China), and with the help of the project leader **Dr. Wei Xie**, high resolution TEM images (HRTEM) obtained in China as a paid service on a modern and commercial JEOL JEM-2100 microscope for HRTEM. In addition, an energy-dispersive X-ray instrument EDX (FEI Quanta 200) and an inductively coupled plasma optical emission spectrometry instrument ICP-OES (Thermo Intrepid XSP Radial) were used by the Jiming group at Wuhan University, especially by **Dr. Wei Xie** for our joint project.

- A fluorescence activated cell sorting (FACS) instrument (FACSCalibur, BD, Heidelberg, Germany) was used by the Multhoff group at "Klinikum rechts der Isar", Technical University Munich (Munich, Germany) for the sorting of cell-sublines and their phenotypic characterization before Raman measurements.

# 4. Raman Study of a Skin Carcinoma Model – Monitoring Alterations Between Human Keratinocyte Line HaCaT and the Tumorigenic Derivative A5RT3

## Summary

In this chapter, it is shown that Raman scattering can help to obtain molecular information about biochemical differences between healthy and cancerous cells in a non-invasive and non-destructive fashion. For this purpose, we have monitored biochemical changes between the human skin keratinocyte cell line HaCaT and its cancerogenic counterpart A5RT3 at 514.5 and 647 nm excitations, with either fixed cell droplets or adherent fixed and living cells for repeated preparations over time in order to discriminate intrinsic characteristic changes. droplets of cells yielded average but rather reproducible information and helped to rapidly determine such changes. The Raman spectra show differences in the relative intensity ratios of the protein amide I band at 1656 $cm^{-1}$ and amide III bands around 1250 $cm^{-1}$ and of the phenylalanine ring mode at 1003.6 $cm^{-1}$ to the $CH_2$ deformation band at 1448 $cm^{-1}$, which are considerably greater for HaCaT cells than A5RT3 cells. Interestingly, these observations were accompanied by severe and consistent changes in the amide III region, and in the collagen marker region around 936 $cm^{-1}$, therefore providing an unambiguous evidence of protein degradation and changes in the essential amino acid phenylalanine and in the lipid components in tumorigenic A5RT3 cells. Ultimately, in the light of these intrinsic changes, the present findings are consistent with the passage number of the non-tumorigenic HaCaT cells, since low pass HaCaT showed less pronounced alterations than higher pass HaCaT, suggesting a correlation of tumorigenic transformation with primarily genetic instabilities in HaCaT cells. This work represents the first Raman spectroscopic discrimination of the skin carcinoma model cell lines, the non tumorigenic

HaCaT and the cancerous A5RT3 cells, addressing the importance of delineating non specific variations from intrinsic characteristic changes and giving a spectroscopic indication for the influence of the passage number of HaCaT cells on the tumorigenic development.
The work described in this chapter has been published in the following article[90] and in final form at http://onlinelibrary.wiley.com/doi/10.1002/jrs.2400/abstract:
Donfack, P., Rehders, M., Brix, K., Boukamp, P. and Materny, A. (2010), Micro Raman spectroscopy for monitoring alterations between human skin keratinocytes HaCaT and their tumorigenic derivatives A5RT3toward a Raman characterization of a skin carcinoma model. Journal of Raman Spectroscopy, 41: 1626. doi: 10.1002/jrs.2400

## 4.1 Introduction

Skin cancer is the most frequent cancer worldwide and the number is still increasing continuously. Basal cell carcinoma (BCC) and squamous cell carcinoma (SCC) are the two known types of skin cancer of which BCC is the most commonly diagnosed.[91,92] Their occurrence has increased due to excessive exposure to UV radiation as a result of an altered leisure behavior as well as an altered quality of UV radiation through the depleting ozone layer as a result of environmental pollution from the global mass industrialization.[91] Although skin carcinomas are supposed to be "easily" eliminated surgically, particularly in BCC patients the delimitation of tumor boundaries is a challenging and time-demanding task due to the difficulty in the detection of disseminated single tumor cells, which is traditionally carried out on sample biopsies via tedious immunostaining assays. Therefore, the search for rapid check and in-situ detection techniques has gained particular interest in skin cancer research. However, bigger living biological systems such as tissue are more complex and usually show variability triggered by a number of factors though still physiological but other than the investigated pathology. Due to this, studying smaller living organisms, *i.e.* normal and cancer cell lines, as model systems could provide more significant insights into the characteristic features of cancer development. Traditional detection methods of tumor cells rely on immunoblotting and are time-consuming. Furthermore, fluorescence imaging is restricted to the characterization of already known differentiation markers. Direct visualization by optical methods, on the other hand, has been proven much faster for diagnosis and accordingly Raman spectroscopy may offer new concepts in the achievement of an overall characterization of the tumorigenic state.
In this contribution, we demonstrate that Raman spectroscopy (RS)[1] may be a good alternative or addition to the already established characterization techniques. RS can yield fingerprint-like characterization of a specimen without the limitation to few molecules or

the necessity of a special preparation of the sample. However, because RS can be sensitive to even slight molecular changes, a correct assessment of the state of a sample subjected to Raman interrogation is required to facilitate the interpretation of the rather complex information contained in the Raman of biological specimen. As it is well known, unlike Rayleigh scattering or fluorescence emission, spontaneous Raman scattering is an inherently weak process, and its low scattering cross section is usually overcome via enhancement techniques, which include resonant Raman scattering[33] and surface enhanced Raman scattering (SERS).[17,23,35,38,93–96] Over the past two decades vibrational Raman spectroscopy, due to its fingerprint-like detection of molecular vibrations, has intensely been used to study biological systems[26,47,61,63,64,71,74,78,84,88,97–119] including tissue, cells and body fluids. Potential applications of Raman spectroscopy for cancer diagnosis have attracted particular interest.[61,63,64,71,78,84,88,99–104,108,111–113,116,118] The Raman signal from biological samples is usually weak. Recently, SERS has been successfully applied for single molecule detection with enhancement factors up to 14 orders of magnitude[17,23,96] and for Raman mapping of single cells.[26,74,97] Kneipp *et al.*[74] have reported ultra enhanced Raman spectra in cells fed with gold nanoparticles. However, since the biochemical markers of cancer development in most biological systems are only traces, the rather complex Raman spectra of most cell types show similar main features for healthy and cancerous states, and the histopathological assignment of the spectral differences is not always straightforward. Consequently, unless a specific biomarker is already known, which can be directly addressed, the use of SERS substrates (metal nanoparticles) in most previous works suffered from clustering,[74] which, though producing significant enhancements, led to considerable signal changes across the cells not necessarily connected to the phenotypic properties of interest. Therefore, we believe that by suitably adjusting experimental parameters, spontaneous Raman spectra provide the most significant average differences between healthy and cancerous cells. For the use of SERS, a suitable choice of SERS-substrates would help to selectively enhance these differences and improve their understanding.

In this work we used a model system for skin carcinogenesis, the spontaneously immortalized non-tumorigenic HaCaT keratinocytes[120] and a variant that upon introduction of the Harvey-ras oncogene and further *in vivo* propagation gained a malignant (metastatic) phenotype.[92] To better monitor this transformation we used in addition HaCaT cells at different passages. Having the same genetic background and accordingly many common genetic changes, these cells, the non-tumorigenic HaCaT and the metastatic A5RT3 cells, may in future provide an excellent model to determine the potential of either Raman or SERS interrogation under visible excitation as a probing technique for skin carcinomas. Cells can be presented to Raman interrogation in different ways of which drying cells on

a given substrate would be one of the simplest. For instance Schuster *et al.*[121] have been successful in obtaining multidimensional information on the chemical composition of single bacterial cells by confocal micro Raman spectroscopy just by drying cells on $CaF_2$ glass substrates. For diagnostic purposes, in which markers changes are usually traces, it is required to investigate the samples presented differently to the Raman interrogation with great care, since in this case most peak variations are not necessarily indicative of the investigated biomolecular change, and it would be judicious to expect Raman spectra of healthy and cancerous cells and tissue to show similar main features. While measuring fixed cell droplets or adherent fixed and living cells, we now show that HaCaT and A5RT3 cell suspensions simply dropped on $CaF_2$ glass substrates yield enriched Raman spectra that can be used not only to trace the Raman signature of the tumorigenic transformation from the HaCaT into A5RT3 cells, but also to delineate intrinsic changes from aberrant alterations for a better tentative assignment of the observed differences. Many studies have been reported to demonstrate the capability of Raman spectroscopy for both *in vivo* and *in vitro* skin characterization[47,78,99–101,107,112,116] in general, and for the diagnosis of skin cancer[78,99–101,116] in particular. However, from our literature research we found that the few reports on the direct distinction of BCC against surrounding healthy tissue showed some discrepancies in the observed spectral details. On the one hand, Choi *et al.*[99] showed Raman spectra of normal skin tissues where both lipid and protein bands (expected at approx. 1450 and 1658 $cm^{-1}$) were less prominent. Raman spectra of BCC were found to be drastically different from normal tissue and showed only few broad bands. The broadest feature in their BCC spectra extended over the positions of the amide I and $CH_2$ bands normally found well separated in almost all biological tissue and cells. On the other hand Nijssen *et al.*[78] and Gniadecka *et al.*[100] reported Raman spectra of BCC and surrounding healthy dermis showing similar main features in both according to the expectation. Moreover Gniadecka *et al.*[101] later on reported near-infrared Fourier transform Raman spectra of different skin lesions showing once again similar main features, with the histologically related lesions such as BCC and SCC (non melanoma skin cancers) exhibiting similar main changes as compared to normal skin. It should be noted that the only difference in sample preparation in these examples was reported to be that tissue sections were stored in liquid $N_2$ before the Raman measurement in the first case, while in the latter case they were either kept at 4°C for less than 30 min before the Raman measurement[100] or just snap frozen in liquid $N_2$ and then stored at -80°C until Raman interrogation.[78,101] These discrepancies justify the interest of studying models and simple systems that can be variably handled, and demonstrate that experimental results have to be treated with great care and prior knowledge of potential experimental observations has to be taken into consideration

for a correct interpretation of spectroscopic details. Especially, the influence of different sample preparation as well as possible systematic errors has to be investigated. For example, spectral broadening together with the disappearance of Raman bands assigned to the main biological building blocks is usually an indication of a molecular breakdown of the biological architecture. Ideally, a prior knowledge of Raman spectra of isolated intact cells from healthy skin and BCC or SCC samples would provide the most characteristic information related to skin carcinogenesis. Nonetheless, there are well established skin keratinocytes cell lines[91,92] and tumorigenic derivatives used in the prospect of a model skin carcinoma study. To the best of our knowledge, only two studies have been reported on the application of RS to these cells. In the first instance, using near-IR Fourier transform Raman spectroscopy for studying epidermal human keratinocytes, Gao *et al.*[106] reported Raman spectra of the Papilloma virus-immortalized non-tumorigenic human keratinocytes cell line HPK1A and its malignant ras transformed counterpart (HPK1A-ras). Interestingly, although these spectra show similar main features, the authors observed a very weak amide I band in both cell types in contrast to a relatively stronger band around 1600 $cm^{-1}$, which they have assigned to amino acids. This observation is surprising since a line assigned to phenylalanine (Phe) on the shoulder (approx. 1604 $cm^{-1}$) of the amide I band of proteins is hardly seen in the average Raman spectra of tissue and cells. The authors did not explain this peculiar observation since their work mainly focused on the study of the DNA structure modification following *in vitro* oncogenic transformation. In a second example, studying human keratinocytes treated with $HgCl_2$ by atomic force microscopy, Lastella *et al.*[122] also reported Raman spectra of the intact human keratinocyte cells line BSPRC20 (huke human keratinocytes). Although the authors rather aimed to reveal the cells' morphological changes due to exposure to chemical stress, the Raman spectra presented were dominated by stronger contributions from the main biological building blocks (proteins, lipids, carbohydrates) as expected, and agreed with the very detailed Raman spectra of healthy dermis tissue surrounding BCC or SCC reported by Ndijssen *et al.*[78] and Gniadecka *et al.*[100,101] In the following, we present a first Raman spectroscopic discrimination of the human keratinocyte cell line HaCaT and its cancerous counterpart A5RT3, which could in the future prove useful for a model study of skin carcinogenesis. We have used HaCaT cells at different passages for a relatively quantitative characterization of the tumorigenic transformation. Though our samples were understood to be prepared similarly we have put great effort into performing the experiments in such a way as to achieve an agreement between our data and the abundantly reported average Raman spectra of the main biological building blocks in general (tissue, cells, biomolecules)[64] and to some respect with the most reliable average Raman spectra of BCC or SCC reported by Nijssen *et al.*[78] and Gniadecka *et al.*[100,101]

We have accomplished this by as much as possible simplifying the sample preparation and manipulation, from adherent fixed or living cells substrates through simple cell droplets. Finally, we have performed a careful analysis of the spectral details in order to delineate spectral differences that were suspected to be due to factors other than cancer development, such as sample deterioration, laser power induced alteration and physical stress, or simply further alterations of the rather complex and unstable biological systems

## 4.2 Material, Methods, and Experimental Techniques

### 4.2.1 Cell Culture

The Raman experiments discussed in the following were performed on the human keratinocyte cell line HaCaT and its cancerous counterpart A5RT3.[92,120] The HaCaT and A5RT3 cells were separately cultured following similar procedures as described previously.[120] Both low passage number (P43) and high passage number (P60) HaCaT cells and A5RT3 (P41) were obtained from a patented source. Both cell types were grown in Dulbecco's modified eagle's medium (DMEM; Cambrex) supplemented with 10% FCS and/or with 20 mM Hepes in Petri dishes. The only practical difference in the culture of the two cell types is that HaCaT cells were split 1:4 ca. every 10 days while the fast growing and metastatic A5RT3 cells were split 1:10 ca. every 5 days. Petri dishes or cell culture flasks containing either HaCaT or A5RT3 cells were used to prepare fixed cell suspensions and adherent fixed or living cells substrates. Replica cell preparations were made over an extended study period with a considerable elapsing time between the different preparations and a slight adjustment of few parameters. Only four of such replica preparations will be discussed, which consisted of (i) fixed high passage number HaCaT and fixed A5RT3 cell suspensions (note that for this replica the two cell types samples were prepared on separate dates; the HaCaT first and the A5RT3 a week later), (ii) fixed high passage number HaCaT and fixed A5RT3 cell suspensions and cell substrates, (iii) fixed low passage number HaCaT cell substrates and living low passage number HaCaT cell substrates, (iv) fixed high passage number and low passage number HaCaT and fixed A5RT3 cell suspensions, fixed and living high passage number HaCaT and fixed and living A5RT cell substrates. For the preparation of cell droplets, the culture medium was first of all removed from the mostly confluent (or semi-confluent: replica 2) culture flasks, followed by a twofold washing in phosphate buffer saline (PBS). Cells were then scraped off in PBS using a cell scraper into 15 ml tubes and were collected by centrifugation @ 1000 rpm for 5 min (3 min @ 900 rpm for replica 2, leaving the cells intact). To fix the cells, the obtained cell pellet was carefully

re-suspended in 1 ml 4% (8% for replica 1) paraformaldehyde (PFA) in 200 mM Hepes and incubated on a rotator for 15 min (20 min for replica 1) at room temperature. A final threefold washing step through centrifugation (5 min @ 1000 rpm) followed each time by re-suspension in PBS was carried out, upon which the cell pellets were re-suspended in 100 - 200 l PBS to obtain final cell suspensions at different densities for each cell type (slightly dense: replica 1; dispersed: replica 2; thick or very dense: replica 4). For the preparation of fixed cell substrates, cells from confluent (or semi-confluent for replica 2) culture flasks were split onto the $CaF_2$ substrates and continued to grow until confluency (for about a week). Then, the DMEM was washed off three-fold in PBS and the cells were fixed in 4% PFA in 200 mM Hepes for 30 min (replica 2) or 15 min (replica 3, 4). PFA was subsequently washed off 3 times in PBS and finally the sample substrates were dipped/embedded in PBS until Raman interrogation (For replica 2, Hepes was used for washing and embedding an extra cell substrate). For the final preparation of living cell substrates, following the initial washing of the DMEM, fresh DMEM, without phenol red, supplemented with 200 mM Hepes for maintaining pH-neutrality, was added to the cells substrates (for replica 2, only Hepes was added to some of the substrates), and the samples were immediately returned into the incubator at 37°C shortly before Raman interrogation. For the micro Raman spectroscopic investigations, the samples have been placed on object slides made from high quality calcium fluoride ($CaF_2$) glass (LayerTec INC., Germany).

### 4.2.2 Raman Experiment and Instrumentation

For the Raman experiment we have used an argon ion laser (Inova 308, Coherent INC., USA) and a krypton ion laser (Inova 302, Coherent INC., USA) as excitation sources, which are configured to be simultaneously coupled to the two detections systems already described in chapter 3. The first system consists of a self-built microscope equipped with several focusing objectives (*e.g.*, 50× LWD, N.A. 0.50 and 40×, N.A. 0.65) and a CCD camera for sample inspection, a single monochromator (Triax 302, Jobin Yvon, France) with three interchangeable holographic gratings (600, 1200, and 2400 grooves/mm), and a liquid $N_2$ cooled UV-enhanced CCD detector (Symphony 3500, Jobin Yvon, France) with optimal sensitivity in the green. The second system consists of a semi-confocal microscope assembly equipped with several focusing objectives (*e.g.*, 50× LWD, N.A. 0.50 and 40×, N.A. 0.65), a color CCD camera for sample inspection, and an automatic raster XY scanning stage, rigidly mounted onto a threefold-operational modes triple spectrometer (T64000, Jobin Yvon, France) with its single mode option consisting of two interchangeable holographic gratings (600, 1800 grooves/mm), equipped with a liquid $N_2$ cooled front illuminated CCD detector more suitable in the red.

For the Raman measurement ~ 5 µl of PFA fixed cell droplets were cast onto $CaF_2$ and measured while slowly drying on the substrate. Dropped cell measurements from replica 1 were spread over about 2 weeks, during which the suspensions were kept at 4°C (*i.e.* droplets measured within the same day following the preparation, and droplets from stored suspensions measured 3 to 12 days later). Fixed cell substrates were measured either as washed and dried substrates (replica 2: substrates taken out of the embedding buffer, quickly dipped in DI water for clearing the salty buffer and in ethanol absolute for rapid dehydration) or directly through the embedding buffer (replica 3 and 4) without unnecessary delay following the preparation of the sample. Living cell substrates taken out of the incubator were measured immediately through the embedding culture medium as fast as possible. For Raman interrogation, the argon ion laser's green line at 514.5 nm and the krypton ion laser's red line at 647 nm were used to excite the specimen. For dropped cell measurement noise free spectra could be obtained at 514.5 nm excitation with less than 5 mW laser power at the sample and exposure times from approx. 20 to 120 s with 3 to 10 averaged accumulations. At an excitation wavelength of 647 nm, we found that good spectra of the droplets can be obtained with a laser power up to 50 mW in just 10 s exposure time and 3 averaged signal accumulations. Raman spectra of the fixed dropped cells were recorded from different points close to the center of identified cells for less dense droplets (replica 1 and 2 at 514.5 nm), and for very dense droplets (replica 4), in which isolated cells could not be identified, either from randomly selected points (at 514.5 nm) or along raster maps (at 647 nm) over a large area (~ 50 x 50 $\mu m^2$). For fixed and living cell substrates, all measured under 647 nm red excitation, we show that laser powers up to 90 mW were safe and facilitated the measurement of the single and rather very thin adherent cells onto the $CaF_2$ substrates in just 10 s exposure time with 3 averaged accumulations. Raster mapping acquisitions were performed either on specific cells or over a large area containing a huge number of cells (cell substrates were confluent). In all cases, in order to exclude any radiation induced sample deterioration, sample safety was confirmed by recording 4 to 5 consecutive spectra from the same point at increasing exposure times. In order to record the Raman spectra, the laser beam was coupled into the microscope, which focused it onto the sample using the appropriate objective: the 40× objective could be used to measure – dry – the fixed dropped cells at 5145 nm (replica 1) or to measure – immersed in the buffer or culture medium – the fixed and the living cell substrates (in replica 3 and 4). The 50× LWD objective was used to measure wash and dried fixed cell substrates (replica 2), fixed cell droplets and fixed and living cell substrates (replica 4) through the embedding solution. Both objectives delivered onto the sample a laser focus of about 1 - 2 µm spot . The signal was collected in a back scattering geometry using the

same objective. Rayleigh scattering was filtered out using an appropriate Notch filter for each excitation line before focusing the beam onto the spectrometer slit. Optimal spectral dispersion was achieved on the one hand, under 514.5 nm green excitation using the Triax monochromator's 1200 grooves/mm grating and a slit width of 100 μm, and on the other under 647 nm red excitation using the T64000 triple spectrometer's 600 grooves/mm grating and a slit width of 100 μm. For effective signal detection, the liquid $N_2$ cooled CCD detector with optimum performance in the blue/green was used with the Triax monochromator at full width (2048 × 1024 pixels) that covers the entire fingerprint region [475-1752 $cm^{-1}$] within a single spectral window, and the other CCD detector optimized for red sensitivity was used with the T64000 system equally at its full width (1024 × 512 pixels) covering the entire fingerprint region within a single spectral window [450 - 1770 $cm^{-1}$]. The Triax system yielded a spectral resolution of about 3 $cm^{-1}$ and a precision better than 1%. This high accuracy was confirmed through spectral calibration in the lower wavenumber region using the silicon phonon line at 520.7 $cm^{-1}$, and in the fingerprint region taking the spectrum of spectroscopic grade toluene where strong Raman lines at 521.7, 786.6, 1003.6, 1031, 1211, and 1604.5 $cm^{-1}$ could be simultaneously observed. Due to the long wavelenght red excitation line at 647 nm, the T64000 system yielded a relatively lower resolution (~ 5 $cm^{-1}$) but provided a very good compromise for rather fast spectral acquisition with very short exposure times. This system was equally calibrated by the Si and toluene lines as above and exhibited a highly stable calibration point. The calibration was in fact repeated once during and after each separate experiment and indicated that the systems remained very well calibrated throughout the experiments. As computer interface for instrument communication and spectral acquisition and pre-processing, commercial software (LabSpec, Jobin Yvon, France) was used.

### 4.2.3 Spectra Correction and Data Analysis

All spectra were first of all 5 times smoothed with a 2-degree 9-size Savitsky-Golay fit and zeroed to the minimum intensity level. Only in the experiment with replica 1 (fixed high passage number HaCaT and fixed A5RT3 cell droplets) were the spectra baseline corrected with a $5^{th}$ degree polynomial fit (non automatic, but with identical user defined characteristic fitting points for all the spectra) and normalized to the peak intensity of the $CH_2$ def. mode at 1448 $cm^{-1}$. In all the subsequent experiments with other replicas, firstly a spectral correction for buffers, culture medium, or glass substrate contribution was performed when required. Then, all the spectra were baseline corrected with a non-linear but simple first order spline interpolation with only 8 fitting nodes manually set in

the spectral regions near 470, 605, 686, 798, 1020, 1143, 1508, and 1770 $cm^{-1}$ in order to assure that all background signal was completely and identically removed within each of the wavenumber broadband regions defined by the fitting nodes. The spectra were finally normalized to the integral intensity [1438 - 1458 $cm^{-1}$] of the $CH_2$ def. mode. Only spectra of cells adherent to substrates required prior correction before baseline correction. In fact, the high quality $CaF_2$ substrate shows a practically flat background in the fingerprint region when compare to the Raman signal from cell droplets, but in single cell measurement such as in the case of adherent cell substrates, cells are so flattened onto the substrates (just a couple of microns thick) that the excitation cylinder extends into the substrates beneath the sample and the signal is dominated by the substrate background and seems not to exhibit at first glance any feature-like information. However, because the $CaF_2$ itself yielded a rather featureless background contribution in the fingerprint region, except for an extremely broad and weak feature in the lower wavenumber region, the dried, fixed cell substrates (replica 2) were automatically corrected for glass at 590 $cm^{-1}$ where almost no Raman signal arising from the cells is observed, using the Labspec program corrector module. In complex spectra, where the desired Raman signal is actually extremely weak compared to other undesirable but feature-like Raman contributions, in order to extract the actual Raman signal it is required not just to approximate unwanted component spectra – what most automatic correction software do – but to correctly estimate the ratio, in which the correction spectrum is present in the composite Raman signal. Upon few trials we realized that though most powerful spectra processing software only indirectly and approximately enable such corrections, this can actually be easily achieved in very simple algorithmic steps by estimating the correction factor using the top areas (not influenced by the background signal) of a given feature in the corrector spectrum around a position where minimal Raman signal is expected from the sample. For fixed and living cell substrates measured through the overlaying buffer or medium, the corrector spectrum (focus moved to an area onto the glass not containing any cell) was itself a composite signal mainly dominated by the embedding solution and the glass, and was not directly used for correction as described above. Instead, this spectrum was itself first of all corrected with a pure solution spectrum recorded very far above the substrate to obtain the substrate's residual spectrum. Then, the cells spectra were first corrected with the pure buffer (top area around 996 $cm^{-1}$) or with the pure DMEM (top area around 1045.66 $cm^{-1}$) as described above. Finally, only the fixed cell substrates measured through the buffer were further corrected with the aforementioned substrate's residual spectrum. Via these careful corrections steps, we have revealed sensitive Raman signal from single adherent cells by the spontaneous Raman excitation. For single individual spectra this was done by our powerful Labspec program in a multi-click

step (top integral computation, then scaling and correction, with the integral, simple math and correction tool, resp.). However, for raster maps of a huge number of spectra (up to 300 spectra), the Labspec mapping acquisition tool provides an option to generate the mapping image with ”average intensity minus background”, around a desired wavenumber position. Therefore, simply exporting the mapping file and the corresponding image file that could provide the correction factors into origin worksheets, all spectra in the map were scaled all at once and later corrected all at once with the Labspec program. Finally, all corrected data were exported in different formats for further spectral data analysis in Origin (Origin 2007, Origin Lab cooperation) and for multivariate analysis (The Unscrambler 9.7, CAMO ASA). Spectral data corresponding to the different-replica experiments were grouped separately and carefully analyzed for a discriminative judgment of the spectral variation. Except for replica 1, average spectra within each replica and each sample category consisted of at least a few tens (in case of randomly selected individual cells or mapping around the center of cells) to hundreds individual spectra (mostly in raster mapping over large cell areas). Intrinsic molecular changes accompanying tumorigenic transformation from HaCaT to A5RT3 were assessed via the comparison of average spectra for both cell types, defined as the average of the fixed cell droplets, the average of dried fixed-cell substrates, for the different replicas and excitation wavelengths, the average of wet fixed cell and living cells substrates under 647 nm excitation. Spectral sorting for the rejection of bad data in each average data set was facilitated by multivariate analysis results.
Principal component analysis combined with non-assisted clustering analysis was performed in order to evaluate how well the cells could still be specifically discriminated, even after the *in situ* tumorigenic changes had been overlaid by further molecular changes (which could be caused by fixation, storage, dropping or drying, or just physical distortions without the biomaterial being necessarily damaged).

## 4.3 Results and Discussion

### 4.3.1 Reliable Raman Fingerprints of Intrinsic Tumorigenic Changes

In our experiments, we first aimed at addressing the capability of the Raman measurements to discriminate the HaCaT cells from their tumorigenic counterparts A5RT3 while evaluating the reproducibility and reliability of such a discrimination for both cell types measured in the form of fixed droplets that were dried on $CaF_2$ or in the form of adherent fixed or living single cells on $CaF_2$. In fact, the HaCaT cells show in-vitro instability as they represent the spontaneously immortalized keratinocyte line. However, despite some defined

genetic aberrations, the HaCaT cells are still very similar in their differentiation potential to normal keratinocytes and are non-tumorigenic.[120,123] Therefore, they may represent a very early stage of skin carcinoma. The HaCaT cells became tumorigenic upon introduction of the Harvey-ras oncogene,[124] culture stress,[92] elevated temperature,[125] and UV-A exposure.[126] The highly invasive and metastatic A5RT3 cells were generated from benign tumorigenic ras oncogene transduced HaCaT cells, which were further selected by serial *in vivo* passaging.[92,124] Therefore, one has to take into consideration the possible formation of a mixed population in transformed A5RT3 cells and in – not necessarily transformed – HaCaT cells with different genetic aberrations.

Figure 4.1 shows from left to right some phase contrast micrographs of less dense dried fixed-cell droplets, very dense dried fixed-cell droplets, adherent dried fixed-cells and adherent living cells on $CaF_2$. The cells had an average diameter less than 10 μm and were mostly elongated and/or polygonal in shape when attached to the $CaF_2$ substrate. Dropped cells when discernable from each other (dispersed cell suspensions) were mostly round and had shrunken. As already described in the material and methods section, repetitive measurement were conducted on the different replica sample preparations; Raman spectra were recorded from the points marked in the images (those are just for some of the spectra) either as random or raster mapping acquisitions over a single cell or an extended area of numerous cells. In other cases (*e.g.* at 514.5 nm excitation with the Triax system not benefiting from the use of the motorized XY stage) few individual spectra were simply taken about the center of some selected cells by a manual XY scan.[120,123] Figure 4.2 displays the average and normalized Raman spectra of the HaCaT (any color except red) and A5RT3 (red) cells measured in the form of fixed and dried droplets at 514.5 and 647 nm excitation [panels (A), (B), (C) and (D) of all shown replicas, 2 to 4], dried fixed-cell substrates [Replica 2: panel (E)] and living (unfixed) cell substrates [Replica 4/3: panel (F)] at 647 nm excitation. All shown spectra have been normalized to the integral intensity [1438 - 1458 $cm^{-1}$] about the $CH_2$ def. mode. Data from the last four of our replica experiments have been analyzed and compared. The data from the first of those replica experiments (less dense fixed cell droplets at 514.5 nm excitation) have not been included in Figure 4.2. On the one hand, this is due to the fact that the determined reproducible spectra agreed relatively well with the spectra in replica 2 [panel (A)]. On the other hand, the corresponding number of cells (or spectra) was rather limited ($\leq 8$), since many spectra were rejected because of bigger but uncorrelated variations, which then justified the importance of duplicate experiments of the HaCaT and A5RT3 cells under different physical environments. Figure 4.2 demonstrates how well Raman scattering discriminated HaCaT from A5RT3 while highlighting eventual variations. These are either a result of a non-ideal sample handling or also of inherent features of the

HaCaT cells themselves. In order to achieve this, the data from all replica measurements have been carefully analyzed and compared with one another and within the same replica for different measuring parameters. A close inspection of all available spectra showed among other eventual variations that characteristic differences can be identified, which included but were not limited to the characteristic ratios $R_1 = I_{1658}$ (amide I)$/I_{1448}$ ($CH_2$) and $R_2 = I_{1308}/I_{1339}$, $R_3 = I_{1308}/I_{1260}$ (amide III), the relative intensities at about $I_{1582}$, $I_{1339}$, $I_{1308}$, $I_{[1240-1270]}$ (amide III), $I_{1126}$, $I_{1003}$ (phenylalanine ring mode), $I_{936}$, and $I_{957}$. These can be related to intrinsic tumorigenic changes and to the suggested spectral signatures associated with such changes. The different Raman bands involved in these characteristic spectral fingerprints are due to proteins, lipids, nucleic acids, and amino acids, and the corresponding changes observed can be attributed to the modification in the proteins distribution and secondary structure ($R_1, R_2, R_3, I_{936}$ and $I_{957}$), lipid/proteins profile ($R_1, R_2, I_{1126}$), cellular nuclear activity ($R_2 = I_{1308}/I_{1339}$) and the intracellular chemical environment ($I_{1003}$). The ratio $R_1$ is greater in HaCaT cells than in A5RT3 cells. Our observations are consistent with the results reported by Nijssen *et al.*,[78] Gniadecka *et al.*[100,101], and Lastella *et al.*,[122] who investigated BCC and surrounding healthy dermis, BCC and also distinctive molecular abnormalities in benign and malignant skin lesions, and the human keratinocytes cell line BSPRC20 and transformed HUKE-ras cells, respectively. The inspection of panels (A) to (F) of Figure 4.2 shows that the spectral characteristics suggested to represent intrinsic tumorigenic transformation appear to be specific and reproducible within and across the different replica measurements, although they might have been differently modulated in some situations depending on how the cells were interrogated, as will be discussed later.

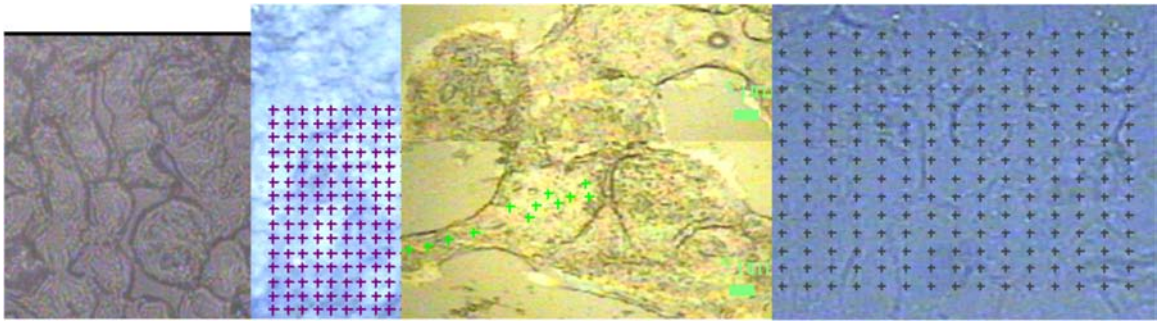

**Figure 4.1: Phase contrast micrographs of (left to right) less dense dried fixed-cell droplets, very dense dried fixed-cell droplets, adherent dried fixed cells and adherent living cells on $CaF_2$.**

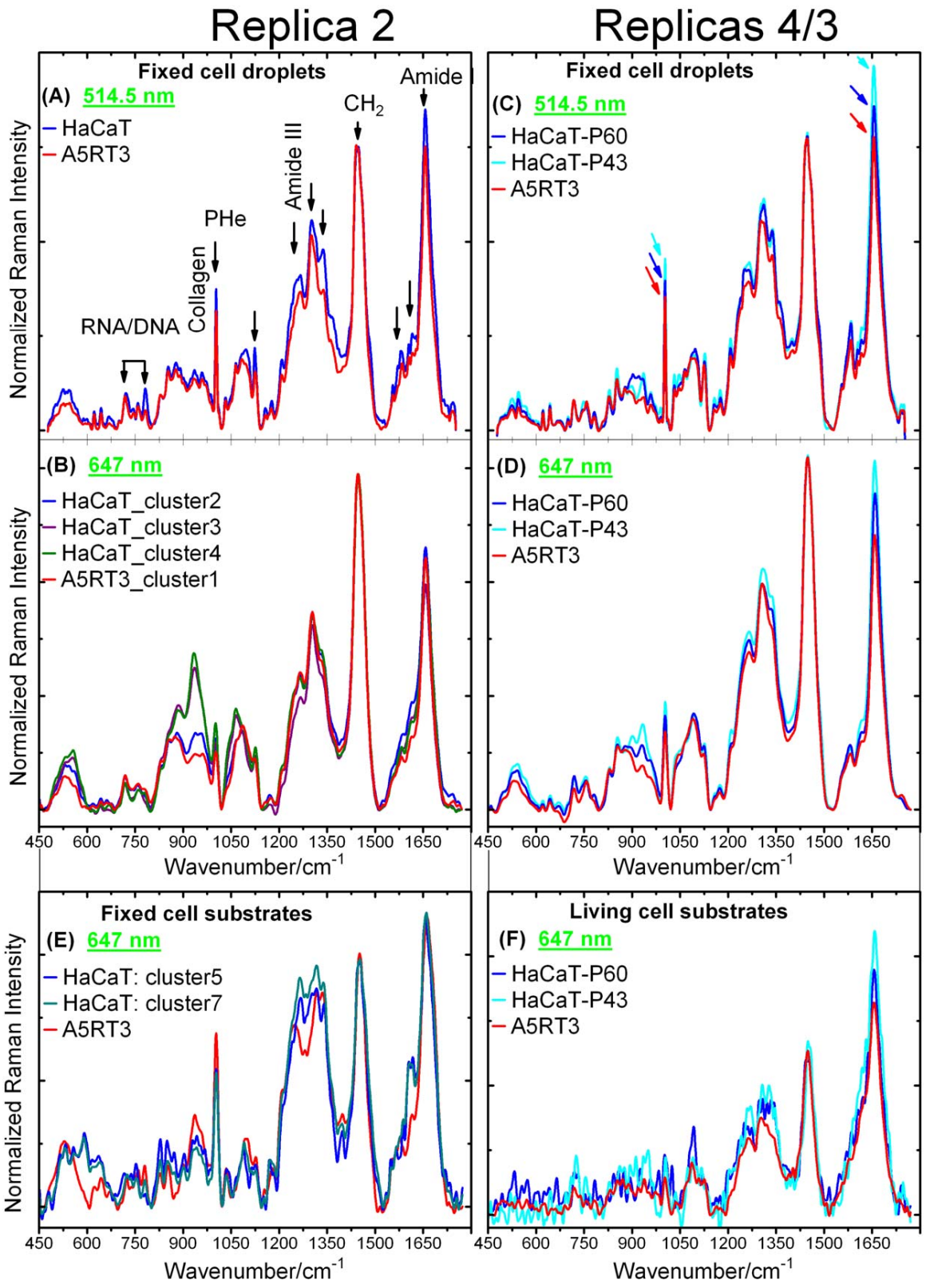


**Figure 4.2: Average Raman spectra of HaCaT and A5RT3 cells for all replica experiments.**

### 4.3.2 Spectral Variation and Differentiation Distribution in HaCaT Population

When addressing spectra variation for both HaCaT and A5RT3 cells we considered as a rule that spectra for both cell types should show similar main features for the main biological building blocks, such as proteins and/or lipids that exhibit pronounced well-known characteristic Raman bands (amide I, amide III, $CH_2$ def., C=C str. vibrations). Any drastic change of a spectral feature assigned to the main macromolecules was regarded as artifact due to physical distortions having nothing to do with the intrinsic phenotypic changes between the two cell lines (damage of the biomaterial via drying, fixation, or loss of biomaterial via lysis, or simply destroyed cells in the living cells samples). Therefore, spectra showing such behavior were identified and simply disregarded. For example it was noticed for dried cell droplets mostly in the first replica experiment where the cells suspensions were much dispersed (*i.e.* less dense droplets), that many cells selected on the $CaF_2$ substrate showed a drastic decrease of the ratio $R_1$ and an overall signal intensity drop in the amide I, amide III, and $CH_2$ bands with sometimes a corresponding signal increase in the spectral region [800-1000 $cm^{-1}$]. For that particular experiment (replica 1), starting initially with many cells, spectra from only a few cells (5-8) were found reliable enough to be averaged in order to look for the tumorigenic spectral signatures between the two cell types (data for replica 1 not shown in Figure 4.2). In replica 2 the representative spectra of fixed cell droplets for both HaCaT and A5RT3 at 514.5 nm excitation [panel (A) of Figure 4.2] are the averages of 14 and 17 cell spectra out of 20 selected cells in total, respectively. We have realized that more bad spectra had to be rejected for HaCaT than for A5RT3. This suggests that the HaCaT cells either suffered more easily from physical distortions than the A5RT3 or were most probably mixed populations with some cells containing many other pronounced biomolecular variations (whether with tumorigenic similarity or not). At 647 nm excitation [Replica 2, panel (B)] a bigger number of spectra were taken (mainly from HaCaT cells), and after rejection of obviously bad data (outliers) the A5RT3 cells grouped into a single cluster while the HaCaT formed 3 clusters, 2 of which [green and violet traces in panel (B) of Figure 4.2] showed bigger deviations, which were however not necessarily uncorrelated. Also for replica 2, the bottom panel (E) shows the spectra of dried, fixed HaCaT (211 spectra) and A5RT3 (190 spectra) on $CaF_2$. The adherent fixed cell substrates were taken out of the embedding PBS buffer and quickly dipped-washed in DI water and then in ethanol for dehydration. Though, these additional steps appear to possibly induce further molecular changes overlaying the original ones (tumorigenic or any other biochemical changes), they represented a gentle chemical treatment. More importantly, the single

adherent cells now homogeneously dried on the substrates. This minimized the uncontrollable physical distortions of the cells, since only very few bad data had to be rejected and the number of clusters in the HaCaT samples had reduced. We would like to point out, that again all the 167 (out of 190) reliable spectra from the A5RT3 formed a single cluster in the evaluation while the about 211 HaCaT cells formed 2 clusters with 89 and 99 reproducible spectra, respectively [cluster 5 shown as blue trace, and cluster 7 as dark green trace in panel (E) of Figure 4.2]. The fact that the cluster traces were similar and did not display any drastic variations even with respect to the trace representing the tumorigenic A5RT3 definitely proved that additional variations existed in the HaCaT population, for which physical distortions due to sample handling and treatment could not be blamed. Unlike the dried fixed-cell substrates and the fixed cell droplets, the wet fixed-cell substrates measured directly through the PBS exhibited serious other distorted features (data not shown in Figure 4.2), which complicated the analysis of the distribution of the cell population differentiation in that case. Nonetheless, it was expected that the variations within the HaCaT population would also average out in a less distinguishable cell preparation, since the HaCaT cells are of course much more similar with one another than they would be to their cancerous counterparts, the A5RT3 cells. In fact, in the replica experiment 4 shown in panels (C) and (D) of Figure 4.2, the fixed cell droplets, obtained for lower passage number HaCaT, in addition to the high passage number HaCaT (same as in the precedent replicas 1 to 2) and A5RT3 cells, were very dense and looked gel-like; no cell contour could be distinguished. Therefore, the Raman spectra in panels (C) and (D) of Figure 4.2 represent the average of about 12 lower pass HaCaT, 15 high pass HaCaT and 27 A5RT individual spectra randomly recorded from certain points over the gel-like looking dried fixed-cell droplets at 514.5 nm excitation and the average of about 215 lower pass HaCaT, 265 high pass HaCaT and ~ 1200 A5RT3 individual spectra recorded as raster mapping acquisitions from many areas over the dried droplets at 647 nm excitation. Because the droplets were very thick above the $CaF_2$ substrates, the spectra collected over the droplets did not show any serious distortions, and all the spectra were highly reproducible and averaged very well as a single cluster for each cell preparation. Therefore, as suggested earlier, only the variations representing intrinsic tumorigenic changes between the HaCaT and the A5RT3 cells have remained and have become even much clearer, agreeing very well with the observations made for the precedent replica experiments [compare *e.g.* the blue and red traces in panels (A), (B), (C) and (D) in Figure 4.2 for both excitation wavelengths]. More importantly, the reproducibility of these intrinsic changes is further evidenced by the fact that the tumorigenic transformation showed a linear agreement with the passage number of the HaCaT cells [compare the green trace with the blue and red traces in panel (C) and

(D) of Figure 4.2]. This interesting result agrees well with the assertion that because of the genetic instability of the spontaneously immortalized keratinocytes HaCaT (*in vitro*), late passed (higher passage number) HaCaT can acquire malignant properties.[120] It is well known that cancer development occurs via multiple differentiation steps until the final stage where the tumor has lost any differentiation ability, just as it would most likely be the case of the highly invasive and metastatic A5RT4 tumor cells. The Raman scattering measurement therefore not only is capable of discriminating HaCaT from the tumorigenic A5RT3, but also can predict different differentiation situations for the HaCaT cells and discriminate them. Furthermore, HaCaT cells with different passage numbers can be distinguished.

### 4.3.3 Exogenous Variations and Histopathological Assignment of Intrinsic Changes

In the previous section we have demonstrated that Raman fingerprints can be used with sufficient reproducibility to identify actual tumorigeninc changes in the transformed A5RT3 cells in comparison to the non-tumorigenic analogs HaCaT. The correct histopathological interpretation of the observed changes depends however on the exogenous (external) variation coupled to the original variation in the samples, and these can only be addressed together. Such external variations include, but are not limited to the sample treatment and even the probe used to extract the hidden information (*e.g.* laser excitation in the present case). For example, the characteristic ratio $R_1$ ($R_1(\text{HaCaT}) \gg R_1(\text{A5RT3})$) is greater than unity at 514.5 nm and less than unity at 647 nm excitation. This situation is simply attributed to resonance conditions affecting the Raman band at 1448 $\text{cm}^{-1}$. This band is assigned to the $CH_2$ def. mode. A tentative assignment of the Raman bands observed in the spectra of HaCaT and A5RT3 is given in Table 4.1. In most biological systems both proteins ($CH_2/CH_3$) and lipids ($CH_2$) competitively yield overlapping contributions to the deformation modes of the $CH_2/CH_3$ groups.[61] However, the spectra of dried fixed-cell substrates at 647 nm shown in panel (E) of Figure 4.2 are similar to the spectra taken with 514.5 nm [see panels (A) and (C) of Figure 4.2]. The reason is that because, for the purpose of dehydration, the substrates were washed in ethanol, which affected and decreased the lipid components. This incidentally also shows that the resonance excitation of the $CH_2$ def. band involved mainly the lipid contributions to this band. Meanwhile, the similarity of the spectra of living cells at 647 nm [panel (F) of Figure 4.2] to the spectra taken at 514.5 nm [panels (A) and (C) of Figure 4.2] is due to the broad water contributions $\left(\sim\ [1500 - 1750\ \text{cm}^{-1}]\right)$ near the position of the amide I band, which have led to the increase of the signal intensity at this position. Therefore, the Raman spectra of both cell

types are dominated mainly by protein and lipid contributions. It is well described in literature that cancer development is accompanied by the modification of proteins and lipids in tissue or cells.[61,63,64,71,78,84,88,99–104,108,111–113,116,118] The changes in the characteristic ratios can be attributed to the modification in the proteins distribution and secondary structure ($R_1$, $R_2$, $R_3$, $I_{[1240-1270]}$ (amide III), $I_{936}$ and $I_{957}$), lipid/proteins profile ($R_1$, $R_2$, $I_{1126}$), cellular nuclear activity ($R_2 = I_{1308}/I_{1339}$) and the intracellular chemical environment ($I_{1003}$). In fact, the protein secondary structure variation is reflected in the relative intensity and the shape of the amide I and amide III bands. HaCaT cells show a stronger and sharper amide I band at 1656 $cm^{-1}$ and stronger amide III bands (with 2 though poorly resolved amide III bands), which is consistent with a highly ordered α-helical structure of proteins.[71,110] In addition, the HaCaT cells, more than the A5RT3 cells, show stronger intracellular collagenous proteins content represented by typical bands at 855.5 and 936 $cm^{-1}$; these bands are assigned to the ring breathing modes of tyrosine and C-C stretching vibrations of hydroxyproline, an α-helical marker of the proteins' backbone (proline/glycogen),[84,88,100,107,109–112] respectively. This further points to more ordered protein secondary structures (*e.g.* collagen, keratin) in HaCaT cells, and a disordered and degraded protein architecture in A5RT3. Furthermore, the Raman band at 1126 $cm^{-1}$ partly assigned to the C-C mode of lipids from trans segments[107] is better resolved and more intense in HaCaT cells. Together with the ratios $R_1$ and $R_2$, this points to a relative decrease of lipid components in A5RT3 cells. Moreover, the Raman bands at 622, 644, and 1003 $cm^{-1}$ can be assigned to the skeletal modes of phenylalanine (Phe)[84,110,118] and tyrosine (Tyr),[84,110,118] and the symmetric ring breathing mode of Phe,[107,109–111] respectively. The phenylalanine ring breathing mode at 1003 $cm^{-1}$ is very sensitive to the chemical environment of the cell, and the changes observed in the tumorigenic A5RT3 cells for the relative intensity $I_{1003}$ [panels (A), (B), (C), and (D) of Figure 4.2] are indicative of the changes in the chemical environment of the phenylalanine molecule, which is an essential amino acid. In addition, in the spectra of the dried fixed-cell substrates [panel (E) of Figure 4.2], where the lipid bands had decreased due to the additional treatment (washing in DI water and dehydration in ethanol), the phenylalanine band had considerably changed, suggesting that the change in the chemical environment could be related to the changes in the lipid profile in the tumorigenic A5RT3 cells. Finally, in the lower wavenumber region, the Raman bands at 783 and 1170 $cm^{-1}$ can be assigned to the ring breathing modes of the RNA nucleotides (U,C,T) and DNA[110,118] and the C-H in-plane bending mode of tyrosine,[84] respectively. The bands at 758 and 833 $cm^{-1}$ can be assigned to the symmetric ring breathing mode of tryptophan (Trp)[118] and the O-P-O vibration of the backbone,[84,110,111,117,118] or the out-of-plane ring breathing mode of tyrosine, respectively. These bands showed only small changes within the cell population, mainly

for HaCaT, but were not reproducible between the two cell types. Therefore, these changes could be related to the reported genetic aberrations within the HaCaT cells. Summarizing these results, making use of the ratios $R_1 = I_{1656}$ (amide I)$/I_{1448}$ ($CH_2$), $R_2 = I_{1308}/I_{1339}$, the proteins' amide III bands, some characteristic lipid bands, and the phenylalanine ring breathing band, differences in the Raman spectra of HaCaT and A5RT3 cells can be assigned to characteristic features on the biomolecular level.

**Table 4.1:** Tentative assignment of Raman lines observed in HaCaT an A5RT3 cells

| HaCaT | A5RT3 | Band assignment and remarks |
|---|---|---|
| 1745 ; 1738 | 1745 ; 1738 | >C=O str. ester, C=O str. lipid;[103,111] — |
| 1726; — | 1726; 1717.6 | — ; >C=O str. of ester, protonated carboxyland carbonyl groups[61] |
| — | 1700 ,1685, 1677 | Found in A5RT3 (not assigned) |
| 1656 | - | Amide I: α-helix[71,110] (collagen); random coil |
| | 1659, 1670 | (collagen, elastin),[103,113] β-pleated sheet motion[114,115] |
| 1616 | 1612, 1617, 1625 | C=C str.: Tyr, Trp[118] |
| 1604 (very weak) | 1604 | C=C in-plane bend: Phe, Tyr[118] |
| 1582 | 1579 | Ring Str.: G, A[100,118] |
| 1555 | 1555 | Trp[84,100,118,119] |
| — | 1457; 1484 | —; G[119] |
| 1448 | 1448 | $CH_2$ def (protein) & $CH_2CH_3$ def (lipid)[61,71,100] |
| 1302 | —- | CH2 twist of phospholipids[71] & collagen |
| 1308 / 1339 | 1308 / 1339 | $CH_3CH_2$ wag (protein, collagen)[61,63,118] & poly- nucleotide chain (DNA-purine bases)[103] / Amide III, hydrated α-helix N-H and C-N, and desmosine or isodesmosine (elastin) (A and G of DNA/RNA) vibrations[61,63,84,88,103,109–111,118] |
| 1248, 1270 | 1247 | Amide III: proline rich, proline poor collagen[88] (mainly α-helical conformation); elastin[88] |
| 1238; 1209 | 1238; 1209 | Cytosine; $C - C_6H_5$ mode of Trp and Phe[118] |
| 1176.6 | 1176.6 | C-H in-plane bend of Tyr[84,118,119] |
| 1126 | 1126 | C-C str. of lipids from trans-segments[107] / protein C-N str.[88,118] |
| 1096; 1085 | 1096; 1085 | Sym str. DNA: Back bone O-P-O-[61]; C-N str. of proteins, and lipid (to a lesser degree), C-C and C-O of phospholipids[71,110], $PO_2^-$ of DNA/RNA[61]. |
| 1065.8 | 1065.8 | C-O, C-O-C str. of phospholipid[61] |
| — | 1048 | C-O str. of carbohydrates[110] |
| 1032, 1003 | 1032, 1003 | Phe: CH3- str. , ring breathing[84,107,110,111] |
| 936 | 936 | C-C str.: proline/valine, α-helical marker of proteins backbone /glycogen, collagen[84,88,100,107,109–112] |
| 855.5 | 855.5 | Ring breathing of Tyr and C-C str. of hydroxyproline ring specific to collagen[84,110,111] |
| 782 | 783.4 | Ring breathing of DNA /RNA nucleotides (U,C,T)[110] |
| — | 670 | C-S stretching mode of cysteine[118,127] |
| 622 / 644 | 622, 644 | Skeletal mode (CC twisting) of Phe and Tyr[84,118] / Tyr[117] |

### 4.3.4 Principal Component and Clustering Analysis of HaCaT & A5RT3 Raman Data

Multivariate analysis was carried out as described in chapter 3, section "Principal Component Analysis (PCA)". The original dataset for PCA analysis contains preprocessed Raman data with X = 2048 dimensions or independent variables, in our case defined by the pixels of the CCD detector. In order to further evidence the ability of Raman scattering in discriminating HaCaT from A5RT3 cells, PCA was applied in combination with clustering analysis in order to reduce the dimension of the Raman data and to group them into different clusters for average information. First of all, a simple non-assisted clustering analysis was performed and the results were used as category variables in order to highlight the grouping of the Raman data. Figure 4.3 shows as example the PCA scores of the dried fixed cell substrates discussed earlier based on the results presented in panel (E) of Figure 4.2. The PCA not only successfully discriminated HaCaT cells from their tumorigenic counterparts A5RT3 cells, but also provided conclusive insights into the differentiation distribution of the cell population. Figure 4.3 clearly shows how the HaCaT cells formed two sub-populations while the A5RT3 cells formed a single population, pointing to additional intrinsic variations within the HaCaT cells population that may not necessarily be directly connected to the final tumorigenic changes observed in A5RT3 cells. The spectra from each cluster were therefore averaged, as discussed earlier.

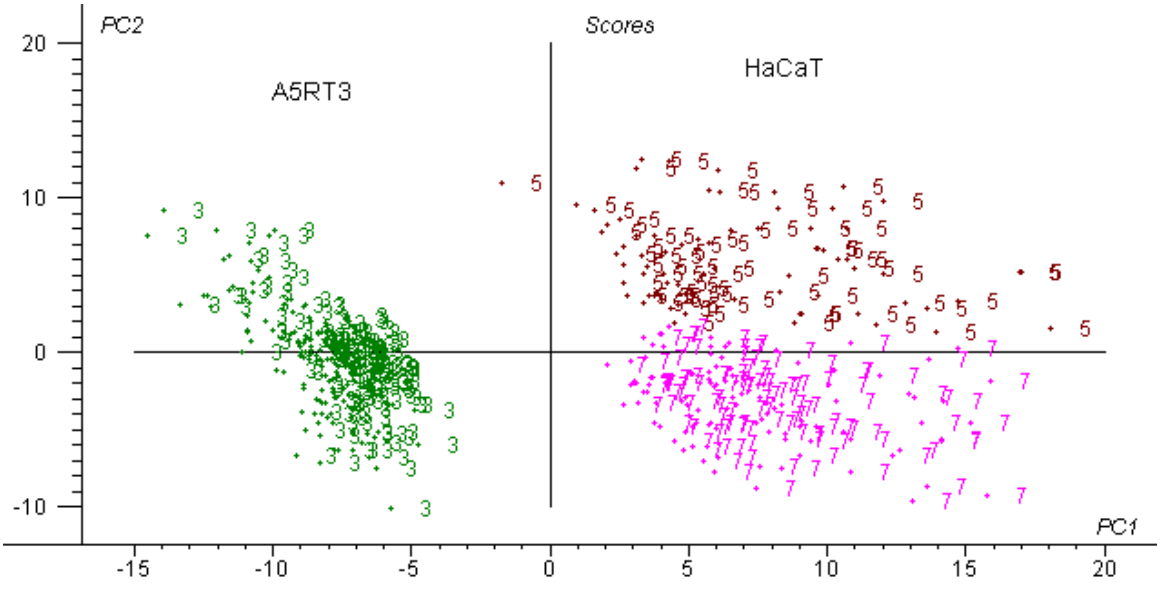


**Figure 4.3: PCA score and clustering of the Raman data of dried fixed-cells substrates of HaCaT and A5RT3**: The numbers 7, 5 and 3 are the clusters names obtained from the clustering analysis and represent the average distance of each data to its clusters center.

## 4.4 Conclusions

In this contribution, we have shown that Raman scattering is capable of differentiating the non-tumorigenic human HaCaT keratinocyte cell line from its tumorigenic counterpart A5RT3. Additionally, different differentiation situations for the HaCaT cells can be distinguished. The Raman data further show that a discrimination of HaCaT cells with different passage numbers is possible. A clear linear dependence of the tumorigenic changes on the passage number of the HaCaT cells has been observed. We have confirmed that late pass HaCaT cells are more likely to acquire benign to premalignant capabilities, suggesting a correlation of tumorigenic transformation with primarily genetic instabilities in HaCaT cells. From our Raman spectra, we have concluded that HaCaT cells have higher lipid content and contain mainly proteins in $\alpha$-helical conformation (like *e.g.* histone, keratin and collagen). On the contrary, the tumorigenic A5RT3 cells have more disordered proteins, which are partially deregulated and degraded. In addition, from the Raman data we could conclude that the HaCaT cells, already reported to exhibit genetic aberrations, most likely exist in culture as mixed populations with a certain differentiation distribution. In summary, we have demonstrated that differences in the Raman spectra of HaCaT and A5RT3 cells can be assigned to characteristic features on the biomolecular level. These Raman fingerprints can provide characteristic and distinguishing information about the two cell types, which may well prove in future to be useful for skin carcinoma characterization.

# 5. Nondestructive Probing of Cancer in Predisposed Lymphoma/Leukemia Mice Used in Radiation Risk Assessment and of Daylight-Induced Biological Rhythm

## Main Summary

Within the scope of this chapter, the common point of the Raman investigations of key biological events has to do with animal models of interest in epidemiological or histological studies of the influence of Radiation on physiological determinants.

Recent research has been focusing on the elucidation of potential side effects of the exposure to electromagnetic fields (EMFs) on the incidence of lymphoma in humans. For this purpose lymphoma development in the AKR/J mouse model predisposed to this disease is monitored while the mice are exposed to EMF radiations. On the other hand, endogenously generated biological rhythms, which can be entrained by external cues such as daylight exposure, allow organisms to anticipate and adequately prepare for regular environmental changes. The photoperiod is one of the most important Zeitgebers (interval timers) of biological rhythms in mammals, which regulates the cyclical patterns of physiological functions or activities. For instance hamsters are well established models for studying the influence of long day and short day photoperiods on the biological rhythms. They exhibit specific photoperiod-induced changes associated with hormonal regulation, fur color and reproductive activities.

Therefore, the works presented in this chapter cover the two main aspects just described above. These include on the one hand the noninvasive probing of cancer in predisposed lymphoma/leukemia AKR/J mice and on the second hand the noninvasive Probing of Biological Rhythm-associated changes in hamster tissues (liver and testes), induced by seasonal variation of daylight exposure.

## 5.1 Nondestructive Probing of Cancer in the AKR/J Mice predisposed to Lymphoma/Leukemia


### Summary

In the first part of this chapter, it is demonstrated that Raman scattering can be applied for monitoring lymphoma development. This is done by discriminating lymphoma infiltration in the spleen, while highlighting the importance of different excitation profiles. Under green excitation, fluorescence bleaching can affect some important features. Nonetheless, as far as lymphoma discrimination is concerned, healthy and cancerous spleen showed notable changes. These changes include different amide III bands, big variations in intensity at the position of the phenylalanine (Phe) band, and especially, stronger nucleic acid bands in tumors (*e.g.* DNA backbone: 1085 $cm^{-1}$ and DNA bases: 780 $cm^{-1}$), and more importantly the fine structured doublet (1606/1639 $cm^{-1}$) specifically correlated with tumorigenesis. In this respect, the intensity ratio $I_{1672}$(amide-I)/$I_{1450}$($CH_2$) exhibits also slight changes. Under red excitation, lipids are more resonantly excited; this helps to reveal eventual changes in the lipid components as well, which in some cases can blur potential changes in DNA/RNA backbone around 1085 $cm^{-1}$. Rather significant changes observed under red excitation include notable intensity variations at the position of the Phe band, changes in the amide III mode, and specific changes on the high frequency wing of the amide I mode (revealing more pronounced beta sheet or random coils secondary structures of proteins in tumor or diseased tissue). These changes were used to discriminate healthy spleens from histological subtypes of lymphoma infiltration in the spleens of AKR/J mice.


### 5.1.1 Introduction to Lymphoma/Leukemia Modeling and Monitoring in Subjects at Risk

AKR/J mice are viremic from birth and carry the AKV retrovirus that predisposes them to spontaneous lymphoma or leukemia development within one year.[128–130] Because of their high lymphoma incidence (60 - 100%),[131] the AKR/J mice are widely used for cancer research. Mice of this train most commonly develop the lymphoblastic lymphoma type. In fact, a virus-induced cancer is generally restricted to a single histopathological type. However, the induced lymphoma can be influenced by the age of the mice or by animal

manipulation in a given experiment. Lymphoma is in some cases similar to leukemia, sharing a few common symptoms, causes, and/or responding to similar treatment. Actually, like leukemia, lymphoma is a blood cancer, and both are cancers of the immune system. They are associated with the proliferation of anomalous white blood cells (WBCs) (affected cells are lymphocytes for lymphoma, and mainly WBCs in general for leukemia). The primary difference between leukemia and lymphoma has to do with the disease's location: Leukemia begins in the bone marrow where blood cells are formed, with the production of leukemic cells. But it does not usually form any solid tumor. Instead the cancerous cells enter the circulatory system and become the dominant type of cells in the blood, outliving healthy (apoptotic) blood cells. Usually when leukemic cells are detected in the blood, the condition is referred to as leukemia. On the contrary, lymphoma starts in the lymphatic system and begins with anomalous lymphocytes proliferation resulting in tumor growth usually in a lymph node, or in any other lymphoid organ such as the spleen, the thymus, the tonsils, etc. Because lymphoid tissue can easily diffuse throughout the body, lymphoma can easily spread throughout and out of the lymphatic system, or eventually occur in any organ in the body. Subjects affected by lymphoma/leukemia can become vulnerable to many other infections. If not diagnosed early, lymphoma/leukemia patients will potentially experience disease complications and suffer a degenerative condition as in AIDS patients. Lymphoma or leukemia tend to affect more often people of all age groups in the upper hemisphere. Lymphoma/leukemia is the most abundant of all cancer cases in children, with the most aggressive type, lymphoblastic lymphoma/leukemia, representing about 79% of lymphoma or leukemia cases Although the exact cause of lymphoma or leukemia is not known, many risk factors and some case-specific causes exist. Known causes include natural and artificial ionizing radiations, some chemicals (*e.g.*, benzene), and a few viruses and bacteria. For example, the Epstein-Barr virus (EBV) causes Burkitt lymphoma, while the Human T-cell lymphotropic virus-I (HTLV-I) is the known human retrovirus that causes a type of T-cell lymphoma/leukemia in adults (Human T-cell or adult T-cell lymphoma/leukemia: ATL). The bacterium Helicobacter pylori which causes ulcers in the stomach is associated with the development of mucosa-associated lymphoid tissue (malt) lymphoma in the stomach wall. These viremic causes are however demonstrated only in patients from specific geographical regions. In fact individuals from other regions who develop the corresponding histopathological type of the disease do not carry the associated virus, which itself is sometimes also incriminated for many other pathologies. Other medical conditions that can increase the risk of lymphoma or leukemia, include infection with HIV, hepatitis B or C; autoimmune disease (*e.g.*, lupus); diseases requiring immuno-suppressing therapies, and any other immunodeficiency disease. Lymphoma and leukemia can also result from a

genetic predisposition inherited from family members. In addition, certain inherited gene defects (abnormal chromosomes) are known that predispose human carriers to develop cancer later in life,[132] as observed in viremic rodents that develop lymphoma with high rate within their lifespan. For example people with down syndrome are rather likely to develop some forms of acute leukemia. Finally, despite ionizing radiations, the role of non-ionizing non-thermal radiations is rather controversial.
Given the genetic predisposition and the other risk factors associated with known chromosomal abnormalities, the possible role of environmental factors on the incidence or development of cancer in subjects at risk is very important and of vital significance. Therefore, with the advent of private mobile telecommunication, public concerns have been raised about the eventual health hazards such as cancer-promoting effects of non ionizing overwhelming high frequency electromagnetic fields (EMFs) originating from mobile phones and base stations. Growing public concerns are noticed as the so-called third generation mobile telecommunication technology, including GSM (Global System for Mobile Communication) and UMTS (Universal Mobile Telecommunication System), is spreading. In response to this, as in some other countries, the German Federal Ministry for Environment, Natural Conservation and Nuclear Safety (BMU) and the German Federal Office for Radiation Protection initiated a joined program called German Mobile Telecommunication Research Program (Deutsches Mobilfunk Forschungsprogramm, DMF). The DMF covers about 50 research projects in many fields including biology, dosimetry, epidemiology, and risk communication. Among DMF projects are carcinogenicity studies in rodents with the aim to provide research findings about eventual carcinogenic effects of EMFs modulated according to the GSM and UMTS standards.

The present work is related to several works by Summer *et al.*[133–135] which are within the scope of the DMF program: They focus on tumorigenesis studies about possible cancer-promoting effects of power line frequency and high frequency EMFs modulated according to the GSM and UMTS standards in AKR/J mice that are predisposed to lymphoma development within approx. 1 year of age. In general, several mouse models have been used to monitor the incidence of lymphoma under chronic exposure to EMFs. Some physiological differences do exist between humans and rodents. However, good correlation between known or assumed human carcinogens and test counterparts in rodents have been demonstrated in previous studies: Sometimes the same organ is affected in humans as in rodents. Especially, the AKR/J mice strain has been shown to be a reliable model for humans.[136] Therefore, the results of the several studies on lymphoma development in AKR/J mice

under chronic exposure to power line frequency, and GSM- or UMTS-modulated high frequency EMFs[133–135] have helped to evaluate eventual health hazards of power lines and mobile phones. These studies take long (at least a year in most cases) and require long term exposure to simulate daily conditions for humans exposed to power lines or mobile phones. During the studies, mice are sacrificed and examined histologically and/or immunologically for lymphoma incidence. This is done after the appearance of first clinical symptoms (abnormal leukocytes count, swollen lymph nodes, protruded eyes, ruffled fur, etc.) or after about one year of age. As concluded by Sommer *et al.* and other authors, nearly all recent results obtained so far do not confirm the hypothesis on any cancer promoting effects of EMFs on lymphoma incidence, although they cannot rule out that exposure to non-ionizing non-thermal EMFs may be risk factors for other neoplastic development.[133–135] However, the many histological/immunological studies still fail to provide valuable information about the kinetic or the onset of lymphoma not only in AKR/J mice but also in other mice strains examined by other authors. To gain such information, mice would have to be sacrificed and examined at given fixed times irrespective whether clinical symptoms of the disease are present or not. This is practically costly due to limited animal resources, and hence not feasible using invasive and destructive methods, such as histological examination. Therefore, besides the traditional histological examinations, it would be of great relevance to introduce investigation methods that can provide nondestructive molecular level information. If feasible, this may in return help to detect early signs of molecular distortion associated with lymphoma incidence and development.

Therefore, the specific aim of the present work was to first of all find out whether Raman spectroscopy can be applied to noninvasively and nondestructively monitor lymphoma infiltration in the spleen tissue of the AKR/J mice that were chronically exposed to EMFs. Therefore, as already mentioned, this work follows the works by Sommer *et al.* (within the DMF scope) and exhibits further interests. The hypothesis whether chronic EMFs exposure may be a risk factor for Lymphoma incidence in AKR/J mice was already tested using histological examinations. Hence, the additional interest in this work deals with the discrimination of lymphoma infiltration in the AKR/J mice using Raman scattering.

The choice of the Raman technique as additional method is encouraged by the fact that Raman spectroscopy has proved efficient in discriminating other neoplasms. Raman scattering can provide molecular fingerprints, which are based on the vibrational contrast in the spectra, and thereby characteristic of even slight molecular distortions. However, because Raman scattering is an inherently weak process, it can be disturbed by the overwhelming autofluorescence from biological tissue. Raman studies do not normally require complicated sample manipulation, such as the tedious histological tissue processing. However,

due to the time requirement for these DMF studies by Sommer *et al.*, the Raman experiments had to be done on histological samples that were prepared according to guidelines for histology and immunology. Therefore, in this work the effect of tissue processing and of the bleaching of fluorescence, in part due to the tissue itself but also due to the histological processing of the tissue sections, are also discussed. Then lymphoma development in the spleen is monitored using different excitation wavelengths. It is attempted to detect inseminated tumor domains in the spleen, with different histological types.

## 5.1.2 Material, Methods, and Experimental Techniques

### 5.1.2.1 Animal Model – The AKR/J Mice

The mice of interest in this work are female AKR/J mice, a lymphoma mouse model, obtained from the Jackson Laboratory (Bar Harbor, ME, USA), at an age of about 5-7 weeks and used by Sommer *et al.* in the mentioned studies[133–135] on which this work is based, as mentioned above. Namely, the corresponding studies started in 2004 and continued through 2007; in these studies, the mice were used to test the hypothesis whether power line frequency, GSM and UMTS modulated high frequency EMFs have any influence on lymphoma incidence or development. The animal handling and the follow-up of their survival have been described as already reported.[134,135] Briefly, upon arrival, the about 360 female mice in each of the studies were randomly distributed between sham exposed and control groups. Then they were housed in groups of about 6 mice, unrestrained, in wooden-wall cages adequately designed for optimal exposure to EMFs, free mobility, and free access to standard food pellets and proper aeration. The mice were checked daily and palpated weekly for signs of disease. Starting at about 6 months of age, blood samples were taken once or twice monthly for blood test (leukocytes count). Here, we focus on the samples obtained after histological examinations and in particular, on the AKR/J mice spleen samples, which were later used for Raman spectroscopy investigations.

### 5.1.2.2 Histological Sections, Clinical Picture, and Sample Preparation for Raman Analysis

The female AKR/J mice rapidly developed lymphoma. Upon the appearance of first evident signs of disease (changes in differential leukocytes count, palpable lymph nodes, ruffled fur, respiratory distress, etc.), or at about 43 or 46 weeks of age, the mice were sacrificed humanly by $CO_2$ inhalation. Then a gross necropsy was performed, focusing on the main lymphatic tissue of disease involvement (spleen, thymus, and lymph nodes) and

tumor infiltration (liver, lung, brain). For histology, the tissues had to be immersion-fixed in Bouin's solution for up to 24 h immersion and subsequently in ethanol (70%), embedded in paraffin and sectioned at 5 μm. Blood smears were stained with Pappenheim's stain. Tissue slices were stained using hematoxylin and eosin or with an FITC (fluorescein isothiocyanate)-conjugated anti-mouse/rat Thy-1 antibody. In all of the studies, nearly all ill or dead AKR/J mice were diagnosed with lymphoblastic lymphoma. Exceptions were a few animals that became ill or died because of rectal eczema (about 3 animals in each study), unclear findings (about 1 animal), or other pathological conditions related to, *e.g.*, protruded vaginae (2 animal in one of the studies). The spleen of the AKR/J mice were later considered for Raman spectroscopy investigations. The samples discussed in the present work are divided into two batches. The first batch of samples are mostly from the mice in the first study,[133] and include cancerous mice (irrespective of the lymphoma type) and a few mice that were still alive and healthy at the end of the study. The second batch of samples are from the mice in the second study[133] mainly: They include mice diagnosed with lymphoma that were further subdivided into the two histological subtypes, large lymphoblastic lymphoma (LB) and small lymphoblastic lymphoma (LL), mice that died of causes other than lymphoma (*e.g.* eczema) and termed here as "other", and mice that were still alive and healthy (N) at the end of the study. It is noteworthy to mention that, while large lymphoblastic lymphoma is very common in lymphoma mice, small lymphoblastic lymphoma is a rare spleen insult. This was also the case for the spleen tissue of the AKR/J mice. The diagnosed LB and LL in the AKR/J mice were directly related to the size of the lymphocytes (large or a mixture of large plus small lymphocytes for LB, and small lymphocytes for LL). Because lymphoma infiltration to the spleen is usually accompanied by splenomegaly, a record of spleen sizes was made: the sizes ranged from the "smallest" size denoted "1/2A" or "a" (mostly in healthy mice only) through "small" denoted "A", "large" denoted "B" and the "largest" denoted "C" (exclusively for LB mice). The mice selected for Raman investigation were chosen to be representative of all histological determinants (large, large + small, or small lymphocytes; for LB and LL, and normal tissue "N"), and of all spleen sizes (1/2A to C) as summarized in Table 5.1

**Table 5.1:** Histological record of lymphoma AKR/J mice used for Raman investigation following EMF assessment on lymphoma incidence

| Number of Mice | Number of samples | Lymphocytes morphology | Spleen size range | Histology/ diagnosis | Spleen size label in order | |
|---|---|---|---|---|---|---|
| | | | | | 1 : 1/2A or a<br>2 : A | smallest<br>small |
| 10 | 50 | large, large/small | 1/2A - C | LB | 3 : AB | : |
| 08 | 40 | small (mainly) | 1/2A - B | LL | 4 : B | : |
| 06 | 27 | normal tissue | 1/2A | N | 5 : BC | : |
| 01 | 08 | normal tissue | 1/2A | Eczema | 6 : C | biggest |

### Histological Spleen Section Treatment for Raman Study: Systematic de-Waxing and Washing

Raman investigations of the spleen tissue were planned after completion of the histopathological and other immunological examinations. The histologically fixed (Bouin's fixed) tissue blocks and the remaining paraffin embedded Bouin's fixed tissues blocks were conserved either in the Bouin's solution and in the fridge, respectively, until the time of Raman measurement. Before Raman measurements, all tissue blocks (all paraffin-mounted at this stage) were sliced with different thickness (5, 10 or 20 μm), and mounted on different substrates, including mainly normal microscope glass slides (super frost glass plates), but also special $CaF_2$ glass. The sections from all the samples in the second batch were all mounted on the super frost glass plates only, as they were supposed to be all measured the same way. The histologically prepared spleen tissue sections (except that they were unstained) were first measured directly, and showed disturbing signals, both from the embedding paraffin wax and from the fixative Bouin's solution. For these reasons the sections had to be further treated through de-waxing and removal of the excess colorful Bouin's fixation under systematic washing.

For de-waxing, the sections were efficiently deparaffinated using a combination of either n-hexane or xylene with methyl-ketone, based on already reported procedures.[137,138] Briefly, the Bouin's fixed paraffin-embedded sections were immersed in a series of solutions consisting of two baths of xylene or n-hexane for 5 min and 4 min, respectively, two baths of ethanol absolute for 3 min and 2 min, and a final bath of industrial methylated spirits 95% for 1 min. Xylene was preferred whenever the sections could easily de-waxed, otherwise hexane was used. When necessary the sections were left sitting in xylene or hexane (mainly) to remove residual wax. (All of these reagents were of histological grade: Sigma Aldrich, Germany).

The fixative Bouin's solution, which is yellow in color, is a powerful fixative for retaining tissue 3D structure and for long term conservation. However, it strongly stains the tissue, causing a rather strong disturbing background signal, besides the already existing fluorescence due to the fixing process itself (cross-linking) and the tissue autofluorescence. The Bouin's solution gives rise to strong overlapping Raman lines. For these reasons the sections had to be washed after de-waxing. For this purpose, the sections were immersed in ethanol baths of decreasing concentrations, consisting of ethanol absolute (99.99%), 90%, 80%, 70%, 60%, and 50% ethanol, for 3-5 min. The washing

step leads to tissue hydration! Therefore, the sections were immersed in a second series of ethanol baths in increasing concentration order for dehydration.

#### 5.1.2.3 Raman Experiment and Instrumentation

For Raman investigations, the 514.5 nm line of an argon ion laser (Innova 308, Coherent INC., USA) and the 647 nm line of a krypton ion laser (Innova 302, Coherent INC., USA) were used for excitation, to search for different diagnostic information. For this comparison only the samples from the first batch (*i.e.*, cancerous mice irrespective of the histopathological subtype *vs.* healthy mice) that were measured will be discussed. Besides that, tissue sections excited at 514.5 nm had to be measured either on the special $CaF_2$ substrates or on Al-foil (for this purpose tissue was scrapped off the glass plates and deposited on the Al foil or on $CaF_2$; some sections were already mounted on $CaF_2$ as mentioned above). Moreover, the samples used for the comparison between the different excitation wavelengths were measured under 647 nm excitation the same way (*i.e.*, on the same substrate: either on $CaF_2$ or on Al foil). Due to the strong fluorescence, large scale measurements were done under 647 nm red excitation only, and involved the samples from the second batch that covered the available histological types or subtypes as described in the previous section. In this case the sections were directly measured on the super frost glass plates.
The lasers were simultaneously coupled to two detection systems. The first system consists of a self-built microscope equipped with two focusing objectives (x40, N.A. 0.65 and x10, N.A. 0.20; Olympus, Germany) and a CCD camera for sample inspection, a single monochromator (Triax 302, Jobin Yvon, France) with three interchangeable holographic gratings (600, 1200, and 2400 grooves/mm), and a liquid $N_2$ cooled CCD detector (CCD 3500, Jobin Yvon, France) with optimal sensitivity in the green. For the second system, a semi-confocal microscope, equipped with three focusing objectives (x40, N.A. 0.65; x50 LWD, N.A. 0.50; and x10, N.A. 0.20), a color CCD camera for sample inspection, and an automatic raster XY scanning stage, is rigidly attached to a threefold-operational modes spectrometer (T64000, Jobin Yvon, France) having two interchangeable holographic gratings (600, 1800 grooves/mm) in its single mode option, and equipped with a liquid $N_2$ cooled front illuminated CCD detector more suitable in the red. The tissue sections were excited in a back scattering geometry using the x40 (for green excitation) and/or the x50 (for red excitation) objectives, which both produced a spot of about 2-3 μm on the sample. The scattered light, collected with the same objective, was Rayleigh filtered using the appropriate holographic Notch filer for each laser wavelength.
Under 514.5 nm green excitation, optimal spectral dispersion was achieved using the Triax monochromator's 1200 grooves/mm grating and a slit width of 100 μm, and the Raman

signal was detected by the liquid $N_2$ cooled CCD detector with optimum performance in the blue/green. This yielded a spectra resolution of about 3 $cm^{-1}$ and a precision better than 1%. Under 647 nm red excitation, spectral analysis was done using the T64000 triple spectrometer's 600 grooves/mm grating and a slit width of 100 μm, and the signal was detected by the other CCD detector optimized for red sensitivity. With the red excitation line at 647 nm, the T64000 system yielded a relatively lower resolution ( 5 $cm^{-1}$) but provided a very good compromise for rather fast spectral acquisition within short exposure times. User interface for instruments communication and spectral acquisition and pre-processing was provided by a commercial software (LabSpec, Jobin Yvon, France).
All Raman spectral were pre-processed through 2-degree 9-size Savitsky-Golay smoothing filter for spike noise removal. The fluorescence background was approximated by a $3^{rd}$ order (under 647 nm excitation) or at least a $8^{th}$ order (under 514,5 nm excitation) polynomial fit. Whenever necessary, spectral normalization was performed by normalizing the respective spectra to the peak intensity of the $CH_2$ mode peaking within 1449-1451 $cm^{-1}$.

## 5.1.3 Results and Discussion

### 5.1.3.1 Effect of the Histological Tissue Processing on Raman Spectra

Some studies have discussed the influence of the processing of biological samples such as tissue on their Raman investigation. For instance Raman spectra of frozen tissue sections differ in some respects (mainly in the protein secondary structure) from those of fresh or fixed tissue. Fixation helps to maintain main biochemical determinants in tissue for later or extended interrogation. Carrying out Raman investigations side by side with histology is a key approach to test the capability of Raman spectroscopy for retrieving diagnostic information from fixed tissue. It is therefore important to understand how tissue processing, which is sophisticated and delicate for histology or immunology, affects the Raman spectra in return. This is specific to the tissue processing procedure applied in a given experiment. The histological preparation of tissue sections in this work included fixing and mounting on normal glass, which both complicated Raman measurement in one way or the other.
In Fig. 5.1, Raman spectra of substrates made of gold or aluminium foil, measured at 514.5 nm, are compared with those of different glass types including special $CaF_2$, quartz and normal borosilicate glass. The background spectra of the Au substrate and $CaF_2$ glass are not necessarily flat, but rather weak and featureless in the fingerprint region [400 - 3800 $cm^{-1}$]. This makes Au and $CaF_2$ the best options (among the substrates shown) for Raman investigation. These substrates are however expensive. Al foil provides a very good

compromise because of its nearly flat background spectrum and the fact that it is extremely inexpensive. However, it cannot be used directly for mounting tissue sections. At 514.5 nm, normal glass and quartz glass show rather disturbing overlapping bands in the first and important fingerprint region [400 - 1800 $cm^{-1}$] (perturbing glass bands are marked by full black rectangles in Fig. 5.1 (**a**)). This complicates the recording of the inherently weak Raman signal from biological samples, such as histological tissue sections that are mounted on normal glass slides. Under red excitation (*e.g.* at 647 nm, see Fig. 5.1 (**d**)), glass becomes fluorescent, but its broad Raman bands diminish sensibly. This can be helpful in some cases, provided that fluorescence suppression in the red is good enough to allow the retrieval of weak Raman signals of thin tissue slices.

In Fig. 5.2, 514.5 nm excited Raman spectra of the main tissue fixatives, including Bouin's solution, paraformaldehyde, and acetone, and of the tissue embedding paraffin wax, are shown in the region [500 - 3700 $cm^{-1}$]. Paraformaldehyde provides a quick fixing solution, and except from the OH vibrational region around 3400 $cm^{-1}$, it shows only weaker Raman bands in the first fingerprint region. In addition, it easily evaporates after fixing, leaving no trace in the Raman spectra of fixed tissue. The same is true for tissue fixed with acetone or ethanol to a great extend. However, the choice of tissue fixative depends on the intended analysis. Bouin's solution is a rather good fixative that preserves well the 3D structure of tissue, for long term conservation and/or measurement as in the present situation. The efficient fixation has drawbacks for Raman measurements in return: First, it leads to increased tissue autofluorescence as a result of cross-linking. In addition, the Bouin's solution is yellow and stains the tissue during fixing (this is actually beneficial for histology, since in some cases, additional staining, such as H&E, may not be required to view tissue 3D structure). Therefore, a rather intense Raman spectrum (Fig. 5.2) results, which can be very disturbing in the first and very important fingerprint region. The most disturbing bands of Bouin's solution have been marked by "#" in Fig. 5.2 **a**. Paraffin, which is the most commonly used material to mount tissue slices on substrates, shows rather perturbing Raman bands marked by "$*$" in Fig. 5.2 **c**.

In Fig. 5.3, the effects of the processing of AKR/J mice spleen tissue sections for this work is recapitulated. The results obtained after further treatment of the histological sections for good Raman measurements have also been included. As an illustration, Fig. 5.3 shows 5 representative Raman spectra recorded at 514.5 nm from the spleen sections (**S1**, **S2**, **S3**, **S4**, and **S5**) that were either untreated, partially treated, or treated. Histological sections mounted on glass (**S1**) without further treatment exhibits strong fluorescence (signal recording possible only after partial bleaching) and are dominated by disturbing bands from the Bouin's solution (#), paraffin wax ($*$), and glass (black rectangles). Wax interfering

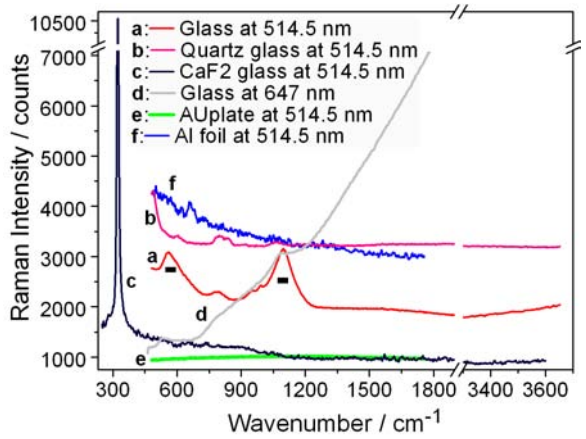


**Figure 5.1: Raman spectra of normal glass (a and d), quartz glass (b), special $CaF_2$ glass (c), gold plate (e) and aluminium foil (f):** Spectra measured at 514.5 nm and also at 647 nm for normal glass.

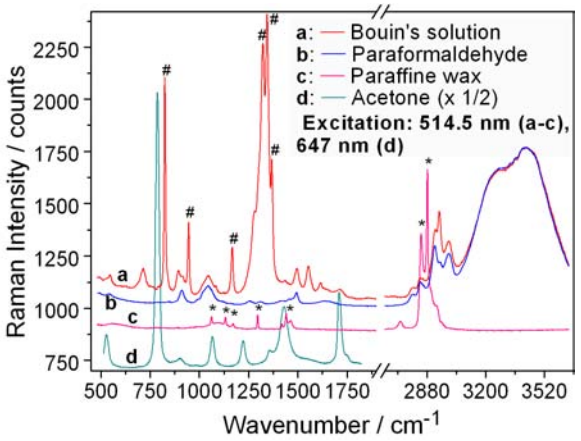


**Figure 5.2: Raman spectra of tissue fixing media Bouin's solution (a), paraformaldehyde (b), or acetone (d), and of the mounting paraffin wax (c)**: Spectra measured at 514.5 nm and 647 nm

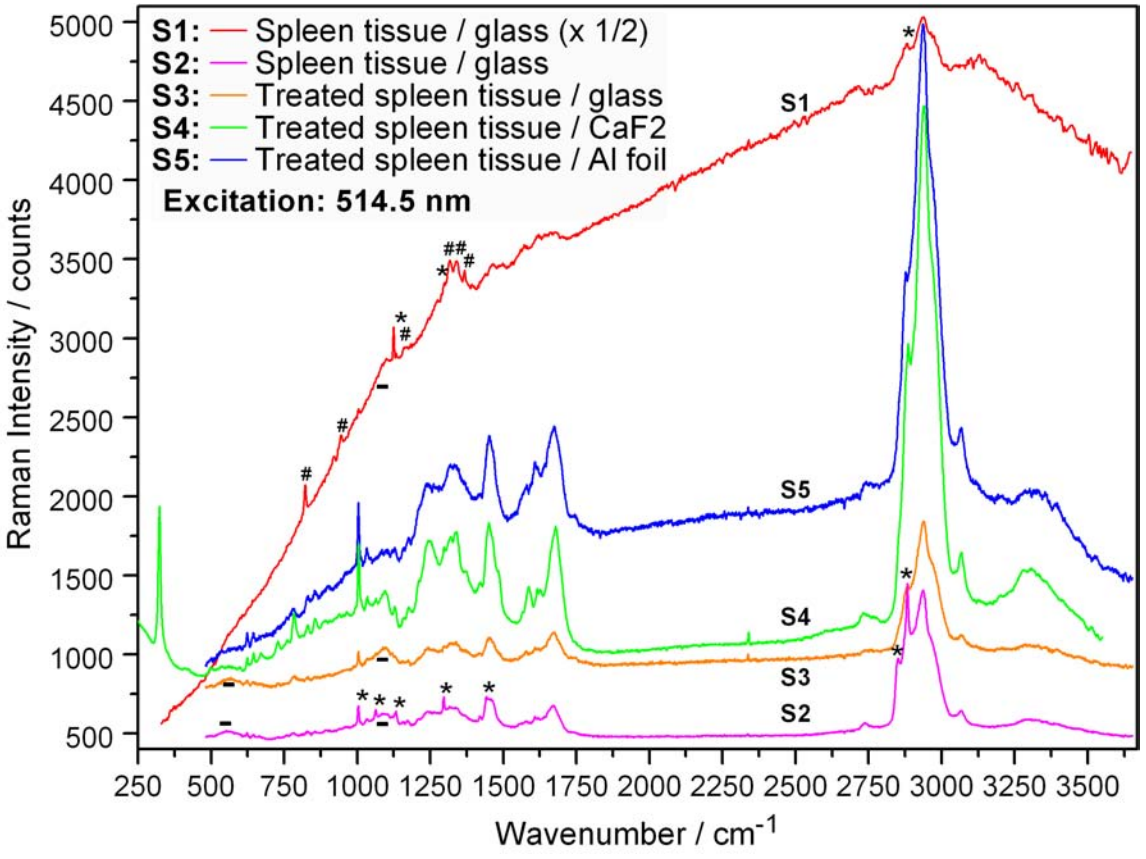


**Figure 5.3: Tissue processing (fixing and mounting) interfering effects on the Raman spectra of AKR/J mouse spleen**. As prepared histological sections on glass measured with the strong inherent fluorescence (**S1**) or bleached fluorescence (**S2**): Note the marked spectra interferences from the Bouin's solution (#), paraffin wax (∗), and glass (black rectangles). Also shown are deparaffinated and washed sections measured on glass (**S3**), and on $CaF_2$ glass (**S4**) or Al foil (**S5**)

bands (∗) are clearly seen on a partially treated histological section (**S2**) that was washed

in ethanol to remove excess Bouin's solution but leaving most of the wax. Therefore, complete treatment of histological sections had to involve de-waxing and systematic washing in ethanol baths as described in section 5.1.2.2 "Histological Spleen Section Treatment for Raman Study: Systematic de-Waxing and Washing". Treated histological sections do still suffer from broad Raman features from glass (**S3**). On the contrary, sections mounted on the special $CaF_2$ glass before treatment (**S4**) and treated histological sections scrapped off the normal glass and deposited on Al foil substrates (**S5**) yield highest quality Raman spectra at 514.5 nm, as shown in Fig. 5.3 (**S4**) and (**S5**). The $CaF_2$ glass is a very good substrate for Raman measurement. However, tissue sections do not stick well on this glass. In addition, it is rather costly. Although tissue does not even stick on Al foil at all, for point by point measurement, the Al foil provided the best option (intense and highest quality signal, extremely inexpensive) for AKR/J spleen tissue sections measurements. This especially applies to Raman measurements at 514.5 nm green excitation, but also at 647 nm red excitation. Therefore, for 514.5 nm excitation, only spectra measured on Al foil substrates will be discussed in the later sections. In Fig. 5.3, it is important to note that the spectra with a nearly flat fluorescence background (**S2**) or only minimal fluorescence background (**S3**, **S4**, **S5**) corresponded to situations where the tissue sections have bleached long enough under the laser at a moderate laser powers ($\leq$ 4 mW). The effect of bleaching will be assessed and described in the next section.

### 5.1.3.2 Effect of Fluorescence Bleaching

Tissue autofluorescence is obviously a serious concern for Raman interrogation with high energy visible excitation (*e.g.* green laser at 514.5 nm). Although the treatment of the original histological spleen tissue sections as discussed above helps to reduce fluorescence, overwhelming tissue autofluorescence is still present. The sections therefore have to bleach sufficiently long enough before decent and noise free Raman spectra can be recorded. This requires long bleaching time at low power to maintain tissue integrity. however, even with these measures, bleaching can affect certain Raman features, and it is important to check if this situation influences discriminative characterization.

The effect of fluorescence bleaching is depicted in Fig. 5.4 for AKR/J mice spleen sections measured under 514.5 nm excitation on Al foil substrates. For this purpose, many spectra were taken repeatedly at successive bleaching time intervals. As an illustration, Fig. 5.4 shows just two raw spectra for an early and a longer bleaching times (left panel of Fig. 5.4) and the fluorescence background-free (subtracted) spectra for two early bleaching times $t_1$ and $t_2$ (Fig. 5.4 right panel, top: $t_1 < t_2$) and for two much longer bleaching times $t_3$ and $t_4$ (Fig. 5.4 right panel, bottom: $t_3 < t_4$). The fluorescence background was approximated

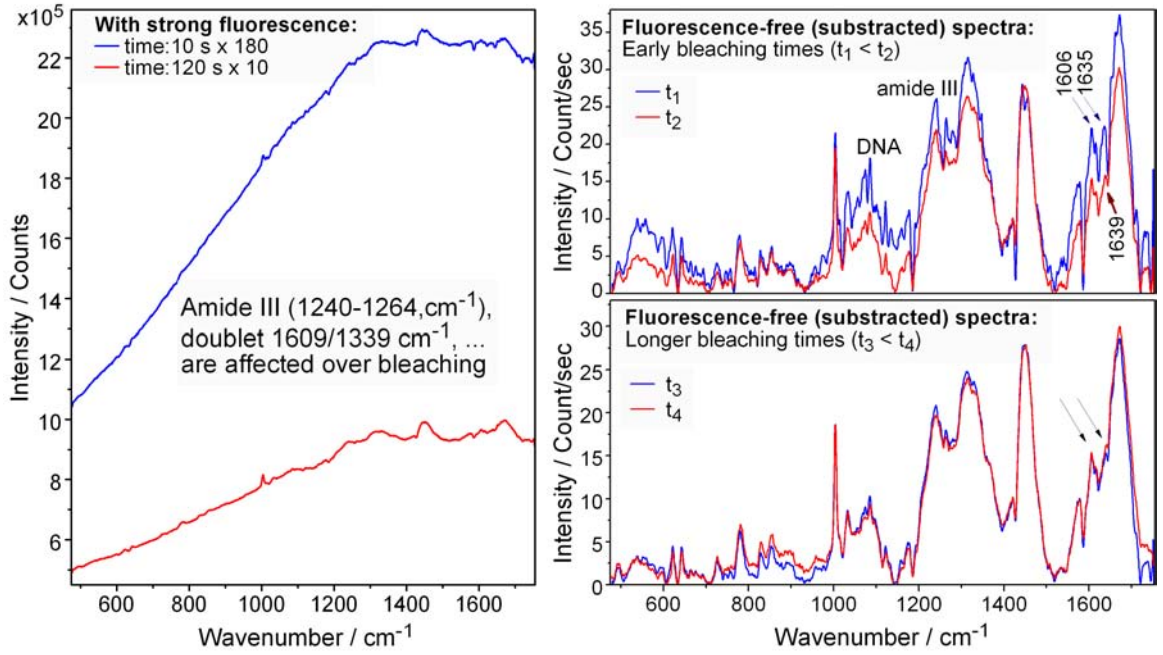


**Figure 5.4: Effect of fluorescence bleaching on the Raman spectra of AKR/J mouse spleen.** Spleen sections were measured nm on Al-foil substrates, after consecutive bleaching times: $t_1 < t_2 < t_3 < t_4$.

by $8^{th}$ order polynomial fit. Only very short exposure times are possible at early bleaching times due to strong fluorescence. Therefore the corresponding subtracted spectra are not noise free. This situation is detrimental for the following-up of slight spectral changes during bleaching. In order to minimize the noise in this case, several signal accumulations (120 to 180) were averaged for each spectrum acquisition. The inspection of the subtracted spectra in Fig. 5.4 reveals that some important features, including the amide III band region and the doublet formed by the bands 1606 and 1635 $cm^{-1}$, are affected. Especially, the 1606/1635 doublet drops in intensity over bleaching while the amide I band seems to broaden slightly toward the lower frequency side. This leads to the loss of fine structure resolution of the 1606/1635 doublet. As will be noticed later, these spectral features can be crucial for diagnostic analysis when a 514.5 nm excitation is used.

#### 5.1.3.3 Discrimination of AKR/J Mouse Histological Condition by Raman Monitoring of Lymphoma Infiltration in the Spleen

As mentioned earlier in section 5.1.2.2 "**Histological Sections, Clinical Picture, and Sample Preparation for Raman Analysis**", the spleen tissues measured in this work are from the AKR/J lymphoma mouse model used in three studies on which the present work is based.[133–135] These AKR/J mice were used to test the hypothesis whether EMFs exposure

has cancer promoting effects, by studying their lymphoma incidence under chronic exposure to either power line frequency (first study),[133] GMS modulated (second study),[134] or UMTS modulated (third study)[135] EMFs. This hypothesis was rejected after histological and immunological examinations: most mice died of lymphoma while a few were still alive or healthy and the end of the studies. The histological spleen tissue sections were then later considered for Raman spectroscopy monitoring of lymphoma infiltration in the spleen using both green (514.5 nm) and red (647 nm) excitation. One batch of samples contains spleen sections mostly from the mice in the first study,[133] and involve cancerous mice (irrespective of the lymphoma type) and a few mice that were still alive and healthy at the end of the study. Only the measurements done with this sample batch will be discussed for green excitation and for the comparison with red excitation. The last batch of samples contains spleen sections from the mice in the second study[133] mainly: They include mice diagnosed with lymphoma that were further subdivided into the two histological subtypes, large lymphoblastic lymphoma (LB) and small lymphoblastic lymphoma (LL), mice that died of other causes (O: other), and a few mice that were still alive and healthy (N) at the end of the study. Only the measurements done with this sample batch will discussed for robust and large scale Raman interrogation under red excitation at 647 nm.

### Monitoring of Lymphoma Infiltration in the Spleen under Green and Red Excitation

Figure 5.5 shows normalized mean Raman spectra of high quality from cancerous and healthy spleen tissue of the AKR/J mice, excited at 514.5 nm on Al foil substrates. The original histological sections were treated and then scrapped off the glass and deposited on Al foil. The samples were allowed to bleach only moderately, and the spectra were corrected (fluorescence background subtraction). Prominent Raman bands are detected at 514.5 nm. The most important bands include, but are not limited to the 622 and 643 $cm^{-1}$ doublet, the bands at 780, 828, and 854 $cm^{-1}$ (DNA/RNA bases and protein), the 1004 $cm^{-1}$ band (phenylalanine), the 1085 $cm^{-1}$ band (DNA/RNA, or lipid), the bands around 1240 and 1264 $cm^{-1}$ (amide III bands), the 1450 band ($CH_2$/$CH_3$ def. bands of proteins and lipids), the doublet at 1606 and 1638 $cm^{-1}$ (amino acid and H-bonding vibration), and the amide I band peaking at 1671 $cm^{-1}$. Under green excitation, healthy and cancerous spleen showed notable changes for different amide III bands, reduced intensity of the phenylalanine (Phe) band, and especially stronger nucleic acid (*e.g.* DNA band at 1085 $cm^{-1}$) bands in tumors and a double fine structure at 1606 and 1639 $cm^{-1}$ in different aspect ratios. The intensity ratio I(1672)/I(1450) of the amide I peak to the $CH_2$ def. band exhibits slight changes as well. For comparison, Fig. 5.6 shows corresponding normalized mean Raman spectra of cancerous *vs* healthy spleen tissue of the AKR/J mice, for the same sections as in

Fig. 5.5, but excited at 647 nm on Al foil substrates as well. The signal to noise ratio is not as good as with the excitation at 514.5 nm. Some characteristic spectral features, such as the amide III bands and the 1606/1638 double fine structure accessible under green excitation, were only poorly resolved at 647 nm (only the band at 1605 $cm^{-1}$ is observed on the lower frequency side of the amide I mode). The non-resolution of the amide III bands and of the 1638 $cm^{-1}$ band (which is usually part of the broad amide I band) is probably due to the lower spectral resolution achievable at this wavelength with the measuring system (see "Material and Methods"). The overall poor resolution is due to the low signal to noise ratio achievable with 647 nm excitation of the sections on Al foil, for the sample batch concerned. However, many main details were retained even upon averaging of as many as 305 individual spectra (1003 $cm^{-1}$ Phe band, protein, DNA bases, and amino acids bands; new details appeared showing an apparent shift of the amide I band in tumors). Under red excitation, the intensity of the Phe band changes notably in tumors and could be used for both differentiation and grading.

Despite strong fluorescence under green excitation, many reproducible features were detected. Besides the protein band structure, the relative intensity of the Phe band can be used in a binary plot to quickly characterize lymphoma development in AKR/J mice. More importantly, the 1606/1638 doublet exited at 514.5 nm appears to be consistently different (the relative intensity ratio of the two sub-bands) between healthy and lymphoma AKR/J mice spleen. This suggests that this doublet may be specific for cancer transformation and lymphoma infiltration in the spleen.

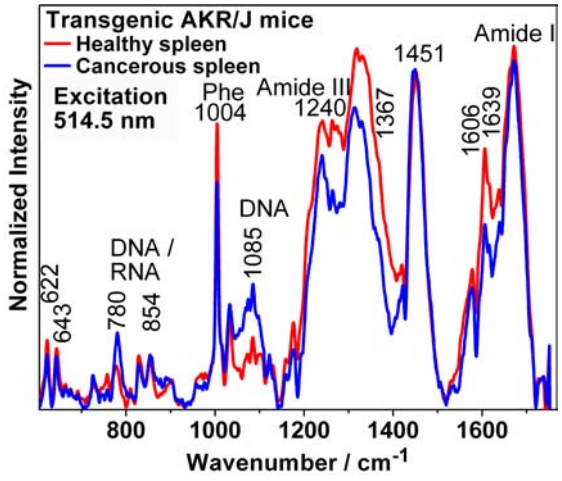


**Figure 5.5: Raman spectra of healthy *vs.* cancerous AKR/J mouse spleen tissue sections under 514.5 nm excitation**: Sections on Al-foil substrates.

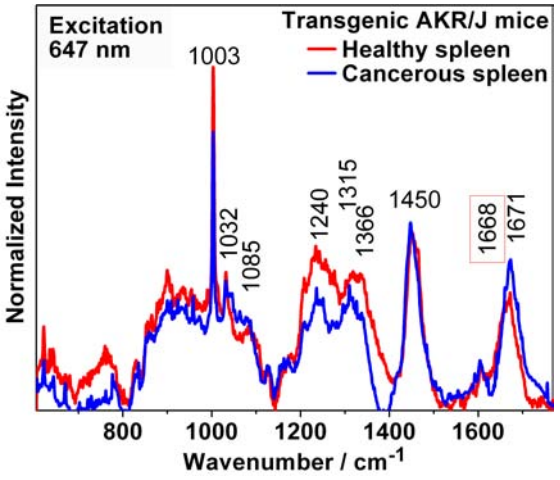


**Figure 5.6: Raman spectra of healthy *vs.* cancerous AKR/J mouse spleen tissue sections under 647 nm excitation**: Sections on Al-foil substrates.

### Statistical Discrimination of Lymphoma Histological Subtypes in AKR/J Mouse Spleen Tissues

Due to overwhelming autofluorescence of the spleen tissue measured in this present work, large scale measurements are very complicated with excitation at 514.5 nm. In order to perform robust analysis with a greater statistical significance, the T64000 triple spectrometer offered a very good alternative with the excitation at 647 nm. The use of the long wavelength helped to reduce tissue autofluorescence and to apply higher powers ($\leq$ 10 mW at the sample) for quick recording of decent Raman signals within short exposure times (5 to 10 s) (actually, up to 30 mW at the sample was safe over this time). This satisfactory situation is however just a coincidence. Actually, despite the reduced tissue autofluorescence, at red excitation (647 nm), normal glass substrates show strong fluorescence, which restricts signal acquisition to short exposure times only (less than 20s). However, fortunately, the glass fluorescence was a constant background during the complete integration time (e.g. 10 s x 3 accumulations = 30 s, or longer). Therefore, it does not add noise to the intrinsic Raman signals. As mentioned above, another batch of spleen tissue samples was used for the robust Raman investigations. The mice concerned in this case were from two of the studies by Sommer *et al.* on which the present work is based, mainly that described in ref. [134] and that introduced in ref. [135]. The spleen samples in this batch were well organized. They were chosen to cover all lymphoma subtypes and histological determinants provided by histological or immunological assays of the AKR/J mice. Namely, a large number of Raman spectra were recorded from 125 spleen samples distributed among 40 small lymphoblastic lymphoma (LL), 50 large lymphoblastic lymphoma (LB), 27 normal spleen sections (N), and 8 "others" (O), from 8, 10, 6, and 1 animal(s) (or subjects), respectively. This sample repartition has also been summarized in Table 5.1. The treatment (de-waxing and systematic washing in ethanol) of the histological sections in this sample batch was done altogether. The sections were similarly measured while still mounted on the normal glass slides as pointed out earlier. With these careful considerations, as many as possible good Raman spectra could be recorded for reliable statistical analysis. A total of 418 of all recorded Raman spectra were analyzed.

Figure 5.7 shows high quality representative mean Raman spectra of the AKR/J mice spleen for the different histological types, including healthy spleens (N), the two lymphoma histological subtypes (LL and LB ), and spleen with other pathological condition (O). The mean spectra were calculated as the average of all individual processed spectra within each histological group: the selection of individual spectra to be averaged was facilitated by criteria to retain good signal quality. The quality judgment was made from the relative intensity of the protein amide I band together with the overall signal intensity in the region

comprising both the $CH_2$ def mode and the protein amide I band [100-1800 $cm^{-1}$]. This helped to easily reject a few obviously distorted spectra. Except from the slightly reduced spectral resolution (*e.g.*, amide III region and the 1638 $cm^{-1}$ not resolved from the amide I mode), the spectra measured at 647 nm are rich and as good as those measured under 514.5 nm excitation and presented earlier. They are dominated by protein, amino acid, and nucleic acid vibrations. Many Raman features for which the AKR/J mice spleen condition differs can be easily noticed by comparing the four mean spectra. Among the important spectral features are the doublet of the 622 and 643 $cm^{-1}$ bands, the bands at 728 and 780 $cm^{-1}$ (DNA/RNA bases), the 828 and 854 $cm^{-1}$ bands (DNA/RNA or protein), the 935 $cm^{-1}$ alpha-helical marker band (collagen), the 1004 $cm^{-1}$ band (phenylalanine), the 1091 $cm^{-1}$ band (DNA/RNA backbone marker or lipid), the band at around 1240 $cm^{-1}$ (amide III bands), the 1450 $cm^{-1}$ band ($CH_2$/$CH_3$ def. mode of proteins and lipids), the band at 1606 $cm^{-1}$ (amino acid), and the amide I complex band structure. Some of the most important discriminative Raman features are highlighted by arrowed marks in Fig. 5.7. These include the bands at 780, 935, 1003.6, 1091, 1236, 1658, and 1671 $cm^{-1}$, attributed to the DNA pyrimidine ring breathing (C,T,U), the alpha-helical marker in collagenous protein, phenylalanine (or a hidden protein skeletal modes: 1001 $cm^{-1}$), the DNA/RNA backbone vibration, the amide III mode, the amide I alpha-helical secondary structure and the amide I beta sheet or disordered secondary structure. The complex secondary structure of the amide I band clearly shows that beta sheet or disordered secondary structures contributions (1671 $cm^{-1}$) are specifically more pronounced in all histological types except the healthy type. This also agrees with the assignment and the behavior of the alpha-helical marker band at 936 $cm^{-1}$, which is also a measure of order. It is usually very difficult to characterize the variation of individual spectra from one another within a large dataset of Raman spectra from biological samples, because many other variations can be present. The implementation of a multivariate test is very helpful in this case.

### Statistical Discrimination Models for Normal, Lymphoma and Other Histological Types in AKR/J Mice

Based of the mean Raman spectra of AKR/J mice spleen tissue discussed above, many Raman spectral signatures can serve as fingerprints for lymphoma infiltration with different histological subtypes in the spleen tissue of this lymphoma mouse model. Multivariate analysis can help to describe more specifically the variation within the dataset of the spleen spectra both in term of individual spectral variation and cluster variation. Therefore, multivariate analysis was a key approach to evaluate the relative distance between the different histological conditions in the spleen tissue of the AKR/J mice. For this purpose,

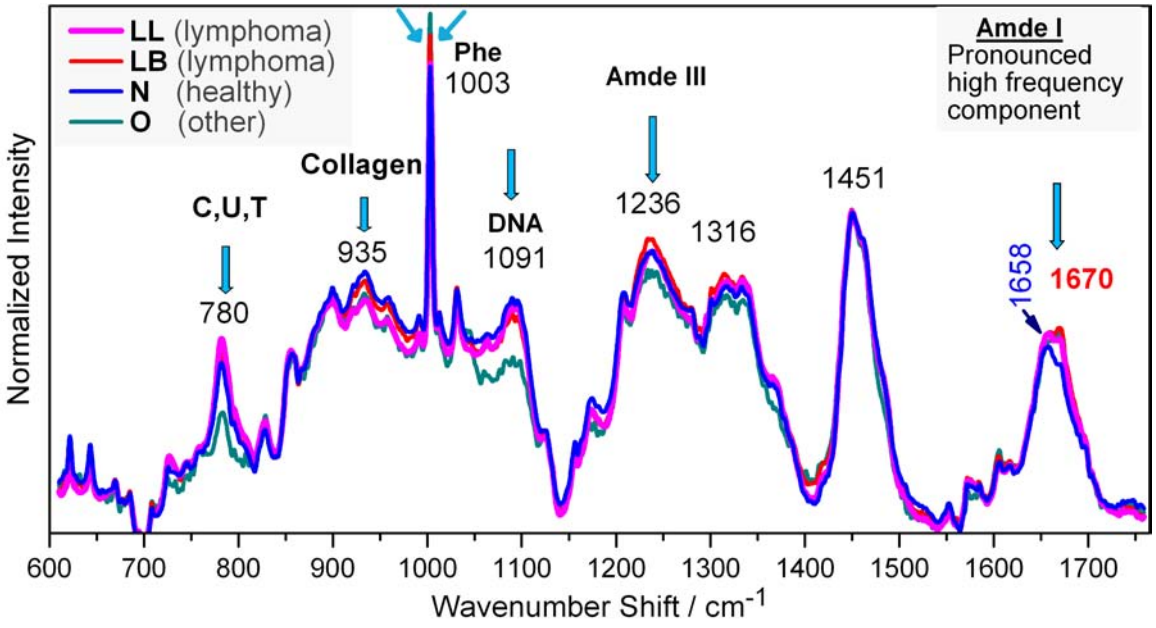


**Figure 5.7: Statistically significant mean Raman spectra of healthy spleen (N), spleen with lymphoma histological subtypes (LL, and LB ), and spleen with other pathological condition (O) from AKR/J mice**: Spectra measured at 647 nm from tissue sections mounted on glass substrates.

statistical tests including principal component analysis (PCA) and multi curve regression analysis (MCR) were performed with the 418 individual Raman spectra obtained from the AKR/J mouse spleen tissues. The first calculations revealed that individual data points of the AKR/J mouse spleen sections formed several clusters, but were more or less randomly distributed with respect to the different histological types. This points to mixed variations in part due to the high heterogeneity across the spleen section. In addition, lymphoma usually affects different regions of the spleen unequally or selectively, resulting in tumor insemination within healthy tissue.

In order to easily estimate an average statistical distance between the different histological conditions (LL, LB, or N), two simplified PCA sub-models were reconstructed. First, each subject was represented by one average spectrum (subject mean) using all corresponding spectra, to form a new and reduced dataset. For the two PCA models, the new dataset was completed by 6 more data points associated with two mean values for each histological type (histological MEAN, twice for LL, LB, or N) computed as follows: Model 1 is the histological MEAN of all corresponding individual spectra, while Model 2 is the histological MEAN of subject means where each subject mean in this case is the average of only corresponding spectra with non-trivial intensity on the 780 $cm^{-1}$ band.

Figure 5.8 shows the results of the PCA analysis on the dataset comprising all subject means plus histological means (two for LL, LB and N) (top panels **(a)**-**(d)**) and the corresponding histological mean Raman spectra for LL, LB and N (bottom panels). As can

be seen in the PCA scores scatter plot in Fig. 5.8 (panel (a)), mice diagnosed with the same histological condition (normal spleen: N; lymphoma: LL, LB) now tend to group together with their respective histological means. The X-loading plot of a given principal component (PC) provides information about the original variables that are significant for the plotted PC. The X-loadings displayed in panel (b) of Fig. 5.8 show the relative importance of the original variables (Raman shifts) to the PCs (PC3 and PC4) accounting for the discrimination shown in panel (a). Significant variables marked by the arrows (728, 780, 935, 1001, 1091, 1236, 1415, 1658, and 1671 $cm^{-1}$) comprise among others the main Raman spectral features discussed at the precedent section. The different histological means (LL, LB, N, two mean values for each) were again separately classified to estimate their average statistical distance from one another, as shown in the second PCA scores scatter plot in Fig. 5.8 (panel (c)). It is important to recall that the two ways of computing the means differ only by the rejection of individual spectra with very small intensities for the 780 $cm^{-1}$ band in one case (Model 2). As shown in panel (c) of Fig. 5.8, the histological means are well separated from one another, as was already noticed from the averaged Raman spectra discussed earlier. However, they differ very little with respect to the different ways of computing the means (model 1 and 2). This can also be seen by comparing the set of the corresponding mean Raman spectra in panel (e) to those in panel (f) of Fig. 5.8. This implies that the information carried by the 780 $cm^{-1}$ band is less significant along the direction of at least one of the main discrimination components (the PCs) within the dataset. Significant X-variables for PC1 and PC2, which both describe the distribution of the histological means shown in panel (c), have also been marked in the loading plots shown in panel (d) of Fig. 5.8. On the one hand, the set of significant Raman features marked for along PC2 (PC2 trace in panel (d)) or PC4 (PC4 trace in panel (b)), do not include the 780 $cm^{-1}$ band (it has zero or negligible X-loadings). They are specifically significant for the separation of LB from both LL and N (note the distribution along PC2 or PC4 in the scatter plots in panels (c) and (a) of Fig. 5.8, respectively). On the other hand, the set of other important variables marked for PC1 (PC1 trace in panel (d)) or PC3 (PC3 trace in panel (b)) now include the 780 $cm^{-1}$ band, which however has rather small X-loadings for PC1 (PC1 trace in panel (c)). These Raman features are significant for the discrimination between the 3 histological types. However, the difference is weaker since the corresponding loadings are small. Therefore withing the datasets, the discriminative components (PCs in panels (a), (b), (c), and (d) of Fig. 5.8) lie in the direction of specific or of less specific variations. The interesting conclusion derived from this detailed analysis is that LB differs significantly from LL and N. This is consistent with the fact that large lymphoblastic lymphoma (LB) is a common spleen insult with well differentiated large lymphoma cells,

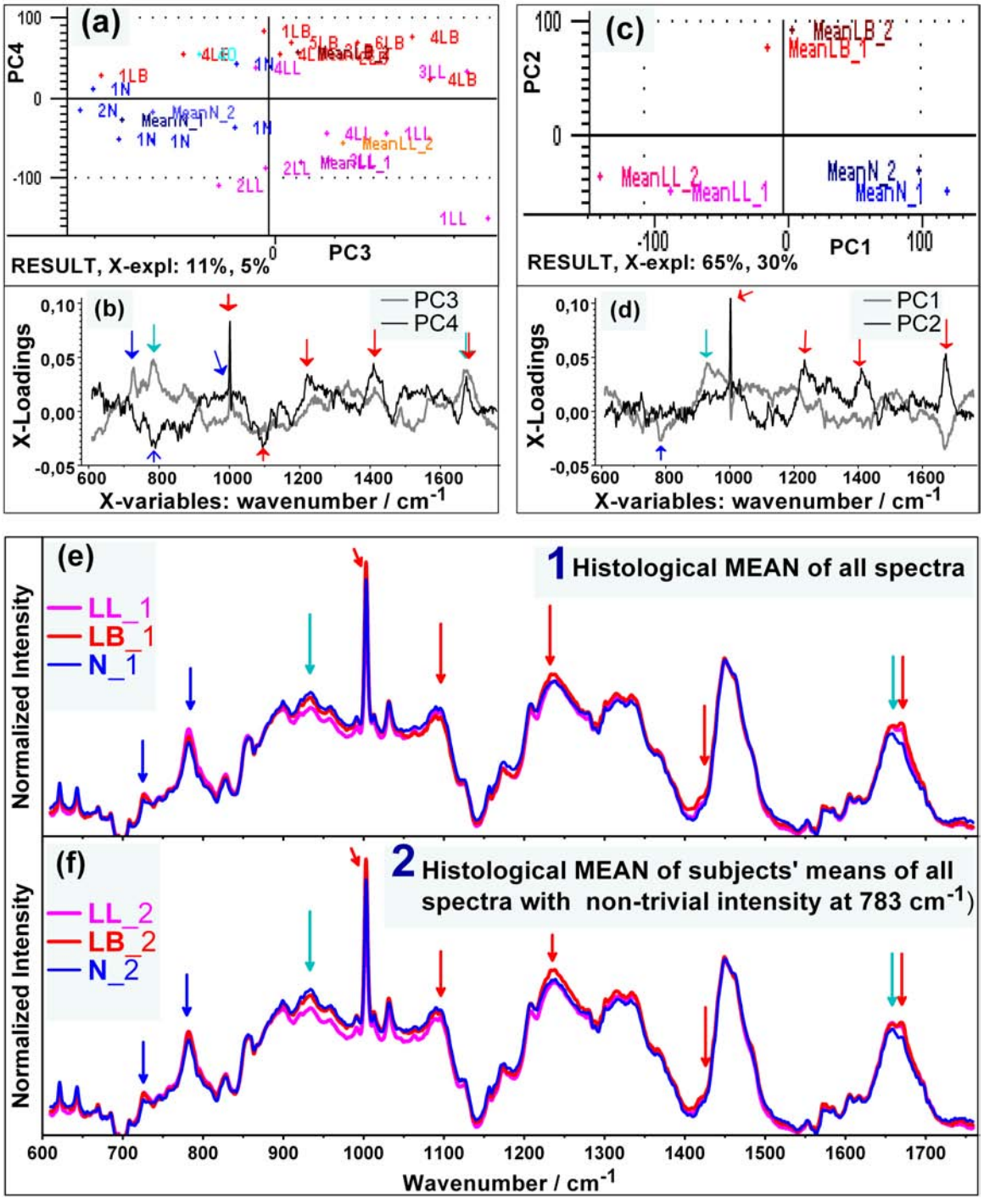


**Figure 5.8: PCA models (scores and loadings) and the corresponding histological mean Raman spectra of AKR/J mouse spleen tissues**: (a)-(b) PCA analysis on subjects means plus histological means (LL, LB, N, O) in the dataset. The histological mean is either the average of all corresponding individual spectra (model 1) or the average of subjects means where each subject mean consists of only individual spectra having non-vanishing 783 $cm^{-1}$ intensity (model 2). (c)-(d) extracted PCA scores and loadings for the histological means in the two models. (e)-(f) comparison of the different histological means for the two models respectively.

different from normal lymphocytes. On the contrary, small lymphoblastic lymphoma (LL) is a rare spleen insult with small lymphocytes, similar to normal lymphocytes that cannot

be differentiated from normal tissue without delicate immunoassay.

### 5.1.4 Conclusions

The general focus in this chapter is the implementation of noninvasive and nondestructive methods to gain molecular-level information from biological systems, associated with cancer transformation. Such an information is crucial regarding the prospects toward the understanding of early signs of cancer incidence and development in subjects at risk. In this respect, the specific aim of the work presented in this chapter was to test whether Raman spectroscopy can be applied as a noninvasive and nondestructive technique for monitoring lymphoma infiltration in the spleen tissue of the AKR/J lymphoma mouse model. Despite difficulties caused by histological processing of tissue, several experimental and analytical procedures considered have helped to perform Raman scattering measurements on histological spleen sections.

Characteristic differences, which depend partly on the excitation wavelength, can be observed between the Raman spectra of normal and lymphoma infiltrated spleen tissue of AKR/J mice. Important Raman spectral changes include significant variations in intensity at the positions of the phenylalanine (Phe) band and different amide III bands, and changes in the spectral region around the alpha-helical maker band of protein, in the amide I mode, and in nucleic acid and amino acid bands. Besides these changes, the use of two excitation wavelengths helped to selectively reveal certain spectral features. Under green excitation, nucleic acid bands (*e.g.* DNA backbone band at 1085 $cm^{-1}$) were significantly stronger in tumors. In addition, the relative intensity of the double bands at 1606 and 1638 $cm^{-1}$ was specifically different between normal spleen and lymphoma infiltrated spleen, where the second band at 1638 $cm^{-1}$ was accessible only with the excitation at 514.5 nm. Even clearer additional characteristic changes, some of which are associated with the complex secondary structure of protein, were observed with the excitation at 647 nm. Especially, at this wavelength, significant changes (increase in intensity) observed on the high frequency wing of the amide I mode were more pronounced in all diseased and tumorigenic tissue, but not in healthy tissue. These changes are indicative of beta sheet or random coil secondary structures of proteins in tumor or diseased tissue. Noteworthy, besides the characteristic Raman fingerprints that could be obtained, rapid interrogation under red excitation was feasible. Ultimately, the characteristic changes, observed with the excitation at 647 nm, were used to discriminate between healthy spleen and the histological subtypes of lymphoma infiltration in the spleen tissue of AKR/J mice.

The results discussed in the above completed part of this chapter have been submitted for publication in the following article:
Patrice Donfack, Karen Grote, Alexander Lerchl and Arnulf Materny; Probing Lymphoma Infiltration in the Spleens of AKR/J Lymphoma Mice Chronically Exposed in Risk Assessment Studies to Electromagnetic Fields, Toward Raman Spectroscopic Discrimination and Modeling of Cancer Incidence; *Physical Biology*, **2011**.

## 5.2 Probing Hormonal or Pathological Effects of Short/Long-Day Photoperiods in Hamster Tissues – A Raman Spectroscopic Approach for *in-situ* Biological Rhythm Study

### Summary

In this part, Raman spectroscopic investigations of several organs from hamsters subjected to different day and night ratios are recapitulated. These investigations highlight within the PhD research the Raman spectroscopic approach in the study of biological rhythms which depend on seasonal modulations in the light-regulated nocturnal production of the tryptophan derivative neurohormone melatonin in the pineal. The change in the nocturnal duration of pineal melatonin rise is a passive signal that regulates reproductive behaviors in breeding mammals. The main goal of this work was to probe, via Raman spectroscopy, changes in the testes of male Djungarian hamsters maintained under short-day photoperiods with 8 hours light and 16 hours darkness (SD, 8L:16D) *vs.* a control group under long-day photoperiods with 16 hours light and 8 hours darkness (LD, 16L:8D). Since melatonin is mainly metabolized in the liver, liver tissues were initially investigated in a control study. After three months under such well-defined light conditions, hamsters in the two photoperiod groups exhibited drastic reproductive changes including androgen suppression and testicular regression and other changes in body weight and in fur color. Previous studies on the testicular and androgen producing leydig cells showed that short-day photoperiods are associated with the depletion of lipid droplets that provide essential lipid components for the synthesis of testosterone. Despite the high heterogeneity of the livers, Raman spectral signatures of the liver tissues of short-day *vs.* long-day Djungarian hamsters are overall very similar. However, minor spectral changes for the livers of short-day hamsters seemed to appear in the C=C str. mode of tryptophan/tyrosine. Moreover, testis Raman spectra of short-day non-responsive (large testes) *vs.* long-day hamsters are very similar. Interestingly, the short-day responsive (reduced testes) hamsters exhibit, among other spectral differences, marked changes in specific lipid bands (*e.g.*, phospholipds, etc.), in the tryptophan residue bands, and in the main tyrosine bands. These results demonstrate the potential for non-invasive probing of the rhythmic molecular changes governed by the biological clock in response to changing photoperiods for Djungarian hamsters.

### 5.2.1 Introduction – Seasonal Hormonal Effects of Photoperiods in Hamster Tissues

Hamsters respond drastically different to natural occurring seasonal changes in the length of daylight exposure. The pineal gland and its tryptophan derivative hormone melatonin are associated with the seasonal variation in the reproductive activity of breeding mammals.[139] In all species, pineal melatonin synthesis is controlled by light, showing a clear rhythm with a minimal level during the day and an elevated level during the night. Therefore, melatonin produced by the pineal gland is known as the night marker and the duration of the nocturnal pineal melatonin pulse (*i.e.*, the melatonin rise also termed melatonin message) is a direct measure of the day and night length. As universally ascertained and summarized in a recent review by Reiter *et al.*,[139] the seasonal involution and recrudescence of the gonads of photoperiodically sensitive mammals, including both long-day and short-day breeders, depend on the annual fluctuations in day and night lengths which determine the interval of the nocturnal melatonin pulse. The physiological mechanisms of the rhythmic production of melatonin are well established. Briefly, highly specialized retinal ganglion cells containing a unique photopigment called melanopsin[140] function as the photoreceptors that mediate the precisely timed reproductive events. These photoreceptors convey the information about day and night length, via the retinohypothalamic tract, to the suprachiasmatic nuclei (SCN) known as the biological clock located in the anterior hypothalamus.[141,142] Then, central and peripheral sympathetic neurons, which ensure the communication from the SCN to the pineal gland,[143,144] regulate the nocturnal elevation in melatonin production[139] by releasing norepinephrine to the pinealocytes on a nightly basis. The changing duration of the nocturnal melatonin message constitutes a passive signal that provides the neuroendocrine-reproductive axis (this designates the functional activity of the hypothalamus-pituitary-gonadal axis) with the information about the time of year (*i.e.*, information about seasonal calendar). It is believed that the reproductive axis uses this information to adjust gonadal (testicular and ovarian) physiology accordingly, by regulating the secretion of pituitary gonadotropins luteinizing hormone (LH) and follicle stimulating hormone (FSH) and pituitary prolactin. The detailed cellular and molecular mechanisms whereby melatonin intervenes to modulate the secretion of pituitary gonadotropins and prolactin are rather delicate and complex.[139,145,146] It is however apparent that melatonin acts at the three different levels of the reproductive axis (hypothalamus-pituitary-gonadal), including hypothalamic, adenohypophyseal, and end-organ sites. The main end or target organs here are the gonads (*e.g.*, testis and ovary). It is however important to note that the liver is the primary site for the metabolism of melatonin.

As described above, the absolute duration of the nocturnal melatonin pulse has widely been demonstrated to be the major, if not the only, determining and relevant signal for the induction of sexual activity and quiescence.[139,147] For example, in long-day breeders, such as the Djungarian hamsters widely studied by Lerchl and collaborators[148–151] and considered in the present work, short nights with a relatively compressed nocturnal melatonin synthesis exert a stimulatory effect on the reproductive system, while long nights with prolonged overnight melatonin production exerts an inhibitory effect associated with reduced testosterone levels and involuted testes. Other short-day photoperiod-induced changes in the Djungarian hamsters include reduced body weight and fur color change. These changes have been exhaustively studied using both tissue and special cells of the reproductive organs in order to describe the influence of the photoperiod length at the biomolecular level. Especially, the testicular leydig cells are known for their major if not only role in the production of androgens (*e.g.*, testosterone). Noteworthy, C. J. Gravis[152] showed that, lipid droplets commonly detected in the leydig cells of long-day (short-night) hamsters are depleted in the inactivated or involuted leydig cells of blinded hamsters (short-day or long-night). Phospholipids and cholesterol found among major components of the lipid droplets are the main precursors of testosterone synthesis, and it was also shown that leydig cell inactivation or involution is the cause for the decline of testosterone during short-day photoperiods (in long-day breeders).[152] In general, lipid metabolism and androgens (or estrogens in females) are in several aspects related to insure normal reproductive functions.[153–155] Usually, delicate biochemical methods, which are complex and time consuming are required for the study of the biological rhythm and to gain insights into the associated biomolecular information of the photoperiod-mediated regulation of the reproductive system.

However, as supported with many other examples in this thesis, Raman spectroscopy is capable of providing biomolecular insights in a noninvasive way. In a recent work, we have shown that Raman spectroscopy might be useful for monitoring the influence of short-day photoperiods on bone composition of Djungarian hamsters.[156] Therefore, in the present work, a Raman spectroscopic approach is adopted for the study of photoperiod-mediated biological rhythm. In particular, Raman spectroscopy was used to probe molecular changes in the testes of male Djungarian hamsters maintained under short-day photoperiods with 8 hours light and 16 hours darkness (SD, 8L:16D) *vs.* a control group under long-day photoperiods with 16 hours light and 8 hours darkness (LD, 16L:8D). Since the liver is the primary site of pineal melatonin metabolism, liver tissue samples of Djungarian hamsters were initially investigated in a control experiment. The results obtained in the present

work show that Raman spectroscopy might provide a rather interesting complementary or alternative approach for studying biological rhythms *in situ*.

## 5.2.2 Material, Methods, and Experimental Techniques

### 5.2.2.1 Animal Model – Short-Day Photoperiod Response in Male Djungarian Hamsters (Phodopus Sungorus)

The mouse model for this study was created in the animal laboratory of Prof. Dr. A. Lerchl using twenty adult male Djungarian hamsters (Phodopus Sungorus), six months of age at the time of experiment. Experimental handling of the hamsters followed the guiding principles in the "Care and Use of Animals" regulation and were in compliance with recommendations and policies of the German "Law on Animal Protection". All hamsters were housed in groups of two in standard polycarbonate cages (21 × 26 × 14 cm) with temperature regulation about 21 ± 2°C, humidity control (50-70%), and with free access to tap water and standard chow (Altromin, Lage, Germany). The hamsters' diet was supplemented with vitamine D3 pellets. Light was provided artificially on a daily basis to mimic the sommer-like long-day photoperiod with 16 hours of light and 8 hours of darkness (16L:8D); lights were on from 6 a.m. to 10 p.m. In the initial phase of the model creation, all animals were acclimated under the long-day photoperiod. Then, for the experiment, ten hamsters were transferred to the winter-like short-day photoperiod with 8 hours of light and 16 hours of darkness (8L:16D); lights were on from 8 a.m. to 4 p.m. The short-day model was successfully established after three months, with the appearance of short-day patterns in the short-day group (SD), while the other hamsters, which remained in the long-day photoperiod formed the long-day group (LD). The experimental conditions were applied according to detailed methods well established earlier.[149] Several such models (completed within different time spans) were regularly reproduced in Prof. Lerchl's animal laboratory. Following the creation of the model (*i.e.* three months after the transfer of half of the hamsters to the short-day photoperiod), the animals were deeply anesthetized with $CO_2$ and perfused with 0.9% physiological saline. Then, different organs, including testes, livers, etc., from both short-day photoperiod responsive and non-responsive subjects in the short group and from the long-day control group were collected for Raman investigations. All collected tissues were briefly washed with 0.9% physiological saline and were immediately either fixed or snapp-frozen and stored until Raman investgations.

### 5.2.2.2 Hamster Tissue Sampling for Raman Experiments

The liver tissues were obtained from a model created shortly before Raman experiments were planned, and were immediately fixed upon removal in paraformaldehyde and embedded in paraffin blocks. These formalin fixed paraffin processed (FFPP) liver sections can be indefinitely kept for measurements that are planned only latter. Given the short-day characteristically marked changes in the case of hamster testes, the model creation was planned together with Raman investigations. Each pair of testes were removed from the hamsters. After rinsing with 0.9% physiological saline, the testes were immediately wrapped in Al-foil, snap-frozen in liquid $N_2$ and then kept at - 80°C until Raman interrogation.
Liver tissue slices of 20 μm thickness were sectioned using a standard microtome at room temperature and mounted on $CaF_2$. Since paraformaldehyde was used as the fixative, no tricky washing of the liver sections was needed, as it was the case for the histological spleen sections discussed in the first part of this chapter (see section 5.1.2.2 "Histological Spleen Section Treatment for Raman Study: Systematic de-Waxing and Washing"). Instead, the thicker liver sections (for avoiding substrate background) were only gently de-waxed, following a similar procedure as described in section 5.1.2.2. Excessive de-waxing was avoided because the liver itself is very heterogeneous and soft, and might be seriously affected by prolonged de-waxing.
The frozen testis tissues were mounted with the water soluble tissue freezing medium OCT and slices of 20 μm thickness were sectioned using a microtome in a cryostat station at -20°C. Given their elongated shape, the testis tissue slices were cut either transversally across the testis (cross section denoted by "h") or longitudinally along the testis (longitudinal section denoted by "v"). The fresh frozen testis sections were mounted on either $CaF_2$ or Al foil substrates. They were finally thawed at room temperature and Raman measurements were immediately taken without further processing. However, since many sections were cut from each testis, for the sake of comparative evaluation and data reproducibility, another set of the frozen testis sections mounted on the $CaF_2$ were immediately fixed in acetone and were also investigated by Raman spectroscopy.

### 5.2.2.3 Raman Experimental Settings for the Hamster Tissues

For all Raman experiments, the scattering geometry was the same as before (back scattering) and the Raman systems used were also the same as already described in the first part of this chapter, namely in section 5.1.2.3 "Raman Experiment and Instrumentation". However the experimental settings were different in some aspects. Briefly, the liver tissues, measured with the Triax Raman setup, were efficiently and sensitively excited using

the 488 nm line of the argon ion laser (Innova 308, Coherent INC., USA). The laser was focused on the sample using an ULWD 50× objective. After Rayleigh scattering rejection using the appropriate holographic notch filter for 488 nm, the Raman signal was analyzed in the Triax monochromator with a slit width of 100 μm using a 1200 grooves/mm diffraction grating and detected on the liquid $N_2$ cooled CCD detector. Only the argon ion laser system was available at the time of the liver tissue measurements. Nevertheless, the above settings helped to record a decent number of intense Raman spectra despite the overlapping fluorescence, which was however less disturbing as compared to the Raman investigation of the spleen tissue under green excitation discussed in the first part of this chapter. However at 488 nm, the fragile liver tissues can be easily damaged. Therefore the laser power was kept to the lowest value ($\leq$ 2-3 mW at the sample) that still allowed the recording of good spectra and the exposure time was about 120 s with 5 times averaged signal acquisitions.
Given the characteristic changes in the hamster testes, which are associated with the variation in the photoperiod length, it was necessary to use a laser excitation that could help to characterize such changes based on a large number of Raman data (for this reason, the collection of hamster testes was delayed and done only later in a separate batch of another established short/long-day hamster model). Therefore, all frozen testis tissue sections were measured using the later installed T64000 Raman setup, where the specimens were excited using the the 647 nm line of the krypton ion laser (Innova 302, Coherent INC., USA). The laser power was about 10 mW at the sample. For these frozen testis sections, the highest numerical aperture 100× objective (100×, N.A. 0.90: Nikon, Japan) could be used, which helped to achieve efficient signal collection for intense scattered light and enhanced signal quality, with only minimal fluorescence. Following Rayleigh scattering rejection through the appropriate holographic notch filter for 647 nm, spectral analysis was done using the T64000 triple spectrometer's 600 grooves/mm grating and a slit width of 100 μm, and the signal was detected by the red-optimized liquid $N_2$ cooled CCD detector. The other settings and system characteristic were as summarized in section 5.1.2.3.

#### 5.2.2.4 Spectral Analysis of the Hamster Tissues

For the filtering of spike noise, all Raman spectra were pre-processed through a 5 times 2-degree 9-size (for liver tissues) or a 3 times 4-degree 5-size (for testis tissues) linear Savitsky-Golay smoothing filter. The smoothing effect was higher for liver tissues because of the relatively higher spike noise mainly due to the stronger fluorescence under 488 nm excitation in the corresponding spectra. Since the Raman spectra of the Hamster tissue sections ($\sim$ 20 μm thick) did not suffer from any substrate background, the only spectral

correction performed was the baseline subtraction, which included the fluorescence background. The complete baseline was simply approximated by a $4^{th}$ order polynomial fit in the case of the liver tissues (measured at 488 nm). For the testis tissues (measured at 647 nm), the complete baseline was simply and more reproducibly approximated by a nonlinear first order spline fit with 8 fitting nodes placed approximately at these wavenumber positions; 460, 600, 695, 798, 905, 983, 1022, 1143, 1192, 1515, and 1755 $cm^{-1}$. Data normalization was also performed. The liver tissue spectra were normalized to the peak intensity of the $CH_2$ mode at about 1449 $cm^{-1}$. The testis tissue spectra were normalized to the integral intensity within a very narrow window containing the peak position of the $CH_2$ mode for all spectra, namely, within [1448-1452.6 $cm^{-1}$].

## 5.2.3 Results and Discussion of Hamsters' Rhythm Study

### 5.2.3.1 Physiological Picture of the Long/Short-Day Hamster Model

After the three months during which the experimental animals were continuously subjected to different day/night ratios termed long-day (LD) and short-day (SD), the average body weight of the hamsters in the LD group was 45 g, while in the SD group it was 38 g. Hence, the SD Djungarian hamsters exhibited a body weight loss of 16% ($P \leq 0.05$). The LD hamsters exhibited an agouti pelage color and large testes, while hamsters in the SD group had a predominantly white pelage and small testes except for two animals. Gonadal regression is a characteristic pattern for short-day photoperiods in Djungarian hamsters. Therefore, in the SD group, the two hamsters which had large testes (as in the LD group) despite being mantained under the same SD conditions were nonresponsive to SD photoperiods, while the other hamsters with invuluted testes were responsive. These observations were totally consistent with the already reported phenomena in hamsters[149–151] and indicated the successful establishment of the model. Several such models were reproduced wihtin different time spans as mentioned above in section 5.2.2.1 "Short-Day Photoperiod Response in Male Djungarian Hamsters (Phodopus Sungorus)". In one of the models, the livers of LD and SD hamsters were harvested. In a later model, testes from LD and from both SD photoperiod responsive and nonresponsive hamsters were carefully harvested. All these tissues were investigated via Raman spectroscopy in several ways.

### 5.2.3.2 Raman Spectroscopic Results with Hamster Livers and Testes

The most studied physiological activity in Djungarian hamsters, for which the internal biological clock can be influenced by seasonal changes in the photoperiod length, is their

reproductive activity as indicated by the regulation of the size of the gonads. In this respect, Djungarian hamster testes are the main target organs that can be considered in the Raman approach for the study of the biological rhythm in situ. Actually, depending on the environmental conditions, many organisms regulate their internal clock as an adaptive process. During winter, for many species such as short-day photoperiod responsive hamsters, finite energy stores is reallocated from less critical functions such reproduction and immunity to functions critical for immediate survival such as thermoregulation. In this respect, the liver is among the major sites of energy stores. Moreover, the liver is the primary site for the metabolism of melatonin. For the reasons, liver tissues of the LD and SD Djungarian hamsters were initially investigated by Raman spectroscopy.

### Raman Characterization of the Short-Day and Long-Day Djungarian Hamster Livers

Figure 5.9 shows normalized mean Raman spectra of FFPP liver sections from long-day (LD: green) and short-day (SD: purple) Djungarian hamsters. The spectra were measured under 488 nm excitation on $CaF_2$ substrates and normalized to the peak intensity of the $CH_2$ def. mode at 1449 $cm^{-1}$. Note that residual wax was still present in the de-waxed liver sections. This was because thick sections ($\sim$ 20 $\mu$m) were used. Given the fragility of the liver tissue, complete wax removal from thick sections would have required excessive washing and many prolonged de-waxing cycles and would not have been done without undermining tissue integrity of the livers. Therefore the liver sections were only gently de-waxed (in only one or two de-waxing cycles in xylene) as mentioned in the previous section. The corresponding Raman spectra in Fig. 5.9 are overlaid on the (background) Raman spectrum of the embedding paraffin wax (gray trace) in order to highlight residual wax bands. Fig. 5.9 shows that the 488 nm excited Raman spectra of the Djungarian hamster liver tissues are very rich and dominated by prominent contributions from lipids, proteins and amino acids, with practically no contribution from nucleic acid (DNA/RNA), except for a few weak bands that might be due to some nucleobases (*e.g.*, 1585 $cm^{-1}$: G, $A^{[100]}$). The livers appeared very heterogeneous and point-to-point single spectra often varied greatly. Spectral variation sometimes appeared drastically pronounced for the data in the SD group, but this was the case for about two individual spectra only, and could not be reproduced. Based on a large number of individual data points, reproducible spectra were rather similar on average, as depicted in Fig. 5.9. This suggests that the liver tissue did not deffer significantly between the hamsters in the short-day photoperiod as compared to the control group in the long-day photoperiod. Especially, there is no net change in the lipid and protein content (note that lipids are interesting for the present study since they play a crucial role in the synthesis of androgens). Nevertheless, small changes seem to appear in a

specific lipid band (1127 $cm^{-1}$) and in fine features assignable to tryptophan residues (low frequency side of the amide I band). However, disturbing residual wax bands (marked by "*" in Fig. 5.9) also led to some small differences at certain positions; and the change in the 1127 $cm^{-1}$ band might just be due to the stronger overlapping residual wax band for LD. The band at ~ 1127 $cm^{-1}$ is assigned to the C-C str. of lipids in trans-segments or to protein C-N str.[88] On the low frequency side of the amide I band, the fine feature at ~ 1555 $cm^{-1}$ and the higher frequency component of the 1605/1616 $cm^{-1}$ double fine structure are due to tryptophan residues.[100] At this stage, the few minor changes were hardly significant (except, maybe, for the changes in tryptophan residues) and cannot be directly associated with the photoperiod-induced modulation of the internal biological clock of the hamster reproductive functions. In the following, the investigation of the hamster testes is discussed.

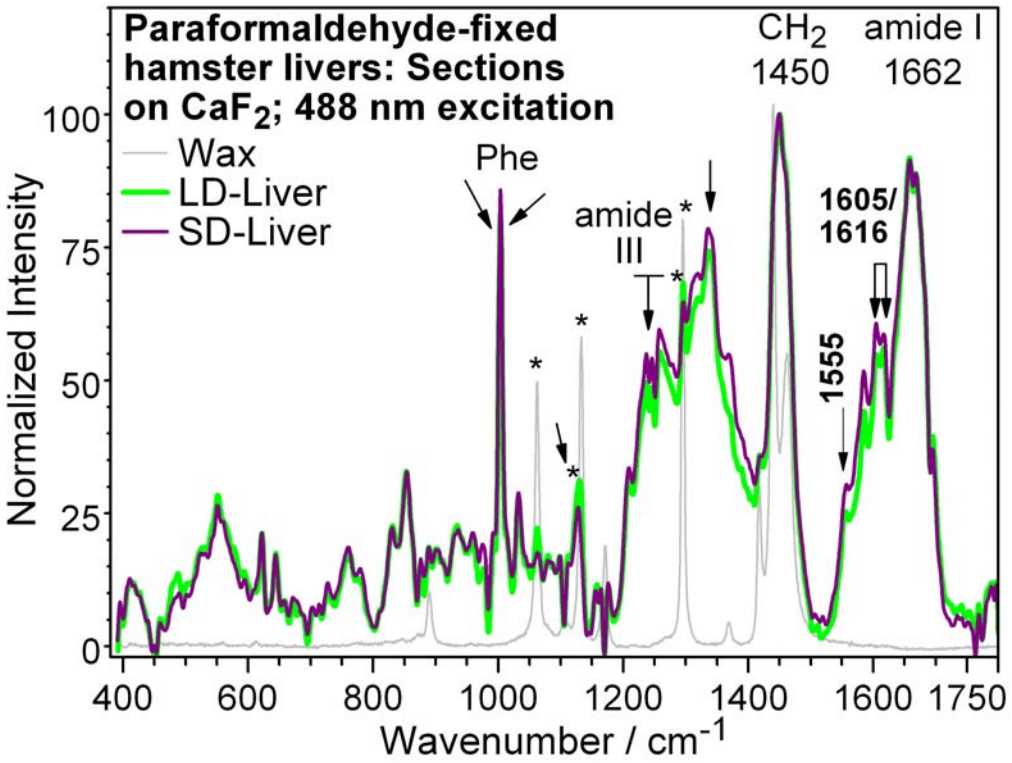


**Figure 5.9: Raman spectra of long-day (LD: green) and short-day (SD: purple) fixed hamster liver tissues overlaid on the (background) Raman spectrum of the embedding paraffin wax (gray)**: The sections were measured at 488 nm on $CaF_2$ substrates.

### Raman Characterization of the Short-Day and Long-Day Djungarian Hamster Testes

In order to probe the *in vivo* intrinsic photoperiod-induced molecular changes in the testes, fresh frozen testis sections were measured after they gradually thawed to room temperature.

In addition, since plenty of sections were cut from the freshly frozen testes, for the sake of comparison and data reproducibility, some of these sections were immediately fixed in acetone and also measured. Since the testes had elongated shapes and each hamster's pair of testes were removed, both cross sections (denoted "h") of one testis in the pair and longitudinal sections (denoted "v") of the other testis were cut and measured. Testes from both SD photoperiod nonresponsive and responsive hamsters in the SD group and from hamsters the LD group have been investigated. The results of the *in situ* Raman spectroscopic investigations of the Djungarian hamster testes are depicted in Figs. 5.10, 5.11, and 5.12, as mean data normalized to the $CH_2$ def. mode integral intensity within [1448-1452.6 $cm^{-1}$]. Figure 5.10 shows mean normalized Raman spectra of long-day (LD: green and cyan curves) and photoperiod nonresponsive short-day (SD: purple curve) fresh frozen hamster testes that were fixed in acetone after sectioning. Spectra of both cross (h) and longitudinal (v: *e.g.* long-day) sections were measured at 647 nm on $CaF_2$ substrates. Figures 5.11 and 5.12 show mean normalized Raman spectra of long-day (LD: green and cyan curves), photoperiod nonresponsive short-day (SD: purple and violet curves), and photoperiod responsive short-day (SD: red and pink curves) fresh frozen hamster testes measured at 647 nm, on either $CaF_2$ or Al foil substrates, respectively. These spectra were also taken from both cross sections (h: top panels) and longitudinal testis sections (v: bottom panels) cut from the testes obtained from the different groups of hamsters (LD group and photoperiod nonresponsive and responsive SD group).

As can be seen in Figures 5.10, 5.11, and 5.12, the 647 nm excited Raman spectra of the Djungarian hamster testis tissues are dominated by prominent contributions from lipids mainly, and from proteins and amino acids, with practically no noticeable contribution from nucleic acids (DNA/RNA), except for a few weak bands that might be attributed to some nucleobases (*e.g.*, 1581 $cm^{-1}$: G, A[100]). Many features point to the strong lipid contribution in the spectra of the hamster testes. For example, noticeable bands of specific lipid components dominate the spectral regions [600 - 960 $cm^{-1}$] (phospholipid head, cholesterol) and [ 1040 - 1130 $cm^{-1}$] (phospholipids; skeletal C-C str. and C-O str. of lipids). In addition, the $CH_2$ def. mode is very intense as compared to a less intense and rather sharp band at the position common to the lipid C=C str. and the protein amide I modes (the $CH_2$ def. mode is much stronger in lipids than in proteins and the lipid C=C str. is less intense and much narrower than the protein amide I mode). Furthermore, the amide III region within 1240-1265 $cm^{-1}$, which is usually assigned to the C-N str. mode of proteins indicating mainly $\alpha$-helix conformations, appears poorly resolved. This is probably due to an overlapping lipid contribution, since the unique and pronounced band at 1265 $cm^{-1}$ can be assigned to the =C-H in plane bending of lipids. Other overlapping lipid bands are present

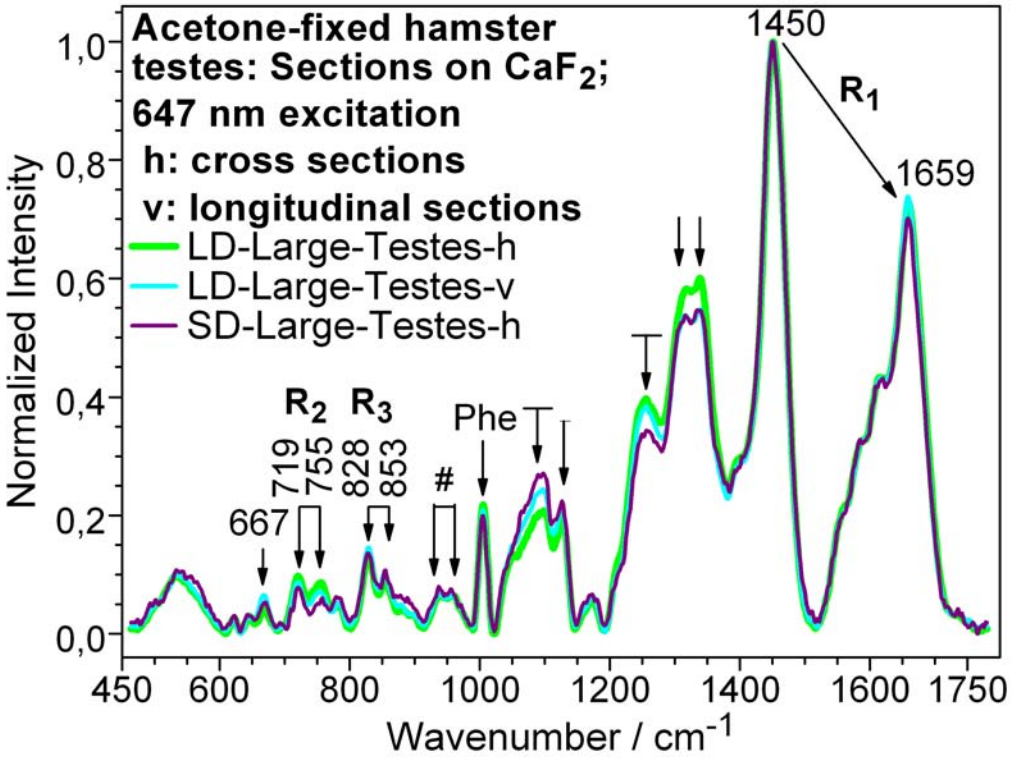


**Figure 5.10: Raman spectra of long-day (LD: green and cyan curves) and photoperiod nonresponsive short-day (SD: purple curve) fresh frozen hamster testes fixed in acetone after sectioning**: Both cross (h) and longitudinal (v: *e.g.* long-day) sections were measured at 647 nm on $CaF_2$ substrates.

in the region from ~ 1295 to 1340 $cm^{-1}$. Namely, the non-resolved shoulder band at 1300 $cm^{-1}$ is due to the lipid $CH_2$ twisting mode, while the double bands at 1318 and 1335 $cm^{-1}$ have got contributions from $CH_3/CH_2$ twisting mode of collagen/lipids and $CH_3/CH_2$ wagging mode of collagen and polynucleotide chain (DNApurine bases), respectively.[61,113,118] Besides amino acid bands, the detection of the Raman signatures of specific lipid components, such as phospholipds and cholesterol, is rather interesting because these molecules play a crucial role in the synthesis of key hormones (*e.g.* testosterone) that determine reproductive functions and behavior. In this respect, the most likely 'characteristic and relevant' spectral features among the marked (double arrows, arrows or #) spectral signatures in Figures 5.10, 5.11, and 5.12 include the ratio $R_2$ ($I_{719}/I_{755}$ in LD and SD-Large-Testes or $I_{721}/I_{750}$ in SD-Small-Testes) of the relative intensities of a phospholipid band and the the main tryptophan band, the ratio $R_3$ ($I_{828}/I_{853}$) of the relative intensities of the main tyrosine modes, the intensity ratio $R_1$ ($I_{1659}/I_{1448}$) of the protein amide I resp. lipid C=C str. modes to the $CH_2$ def. mode of lipid and protein, the doublet labeled "#" and formed by the bands at 932 $cm^{-1}$ (collagen) and 953 $cm^{-1}$ (cholesterol among others), the band at 1126 $cm^{-1}$ (lipids: C-C str.), the region containing the bands 1552, 1616 $cm^{-1}$, etc. (tryptophan residues, etc.), and the region around 1065 $cm^{-1}$ (lipid C-C and C-O str.).

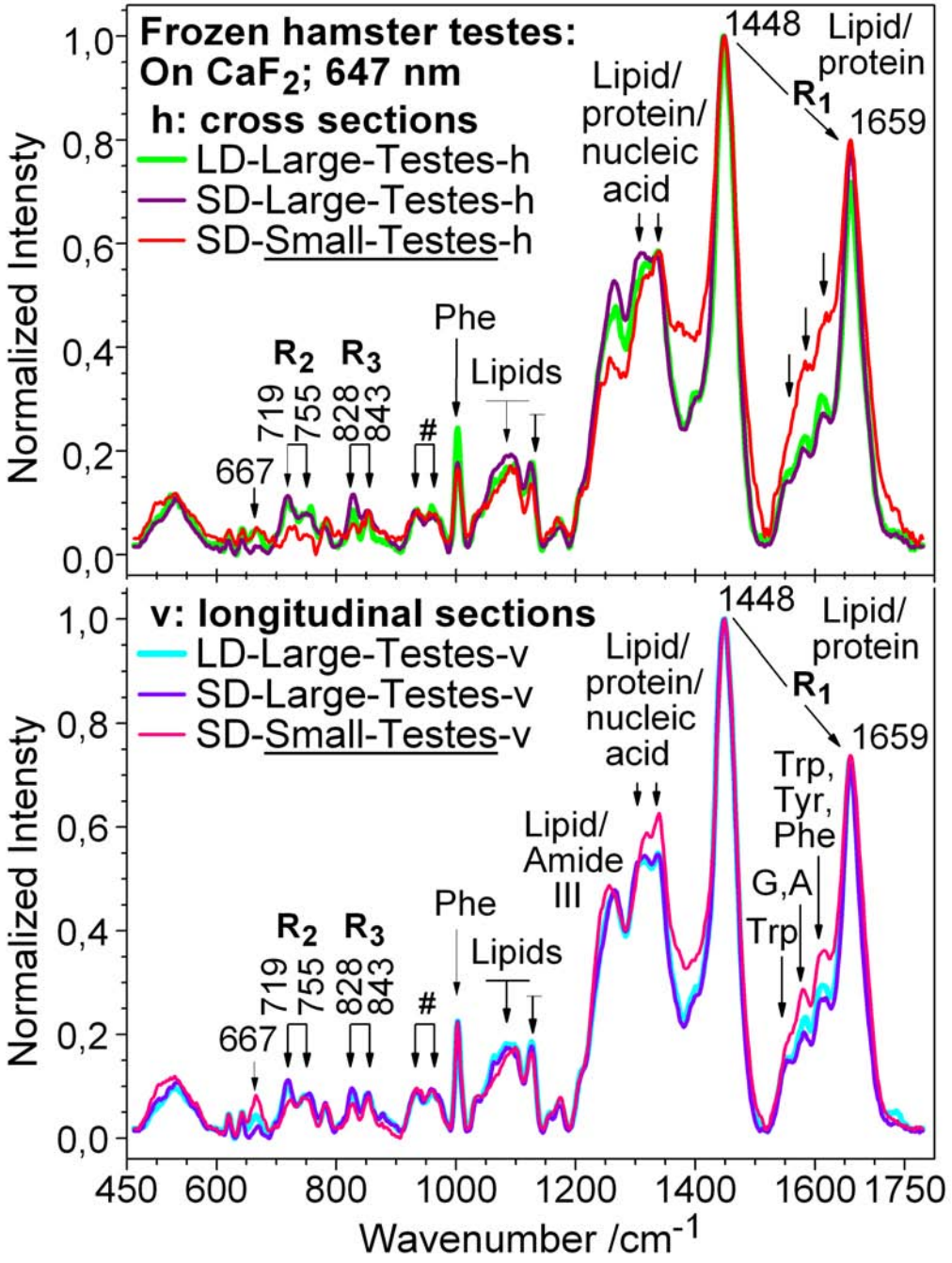


**Figure 5.11: Raman spectra of long-day (LD: green and cyan curves), photoperiod nonresponsive short-day (SD: purple and violet curves), and photoperiod responsive short-day (SD: red and light pink curves) fresh frozen hamster testes measured at 647 nm on $CaF_2$:** The spectra were taken from either cross sections (h: top panel) or longitudinal sections (v: bottom panel).

It is important to recall that that the photoperiod nonresponsive SD hamsters had large testes as the indication of their negative response to the change in the photoperiod length. Looking first at the mean Raman spectra of the fresh frozen and fixed hamster testes in Fig. 5.10, it appears that the photoperiod nonresponsive SD hamsters also exhibited characteristic

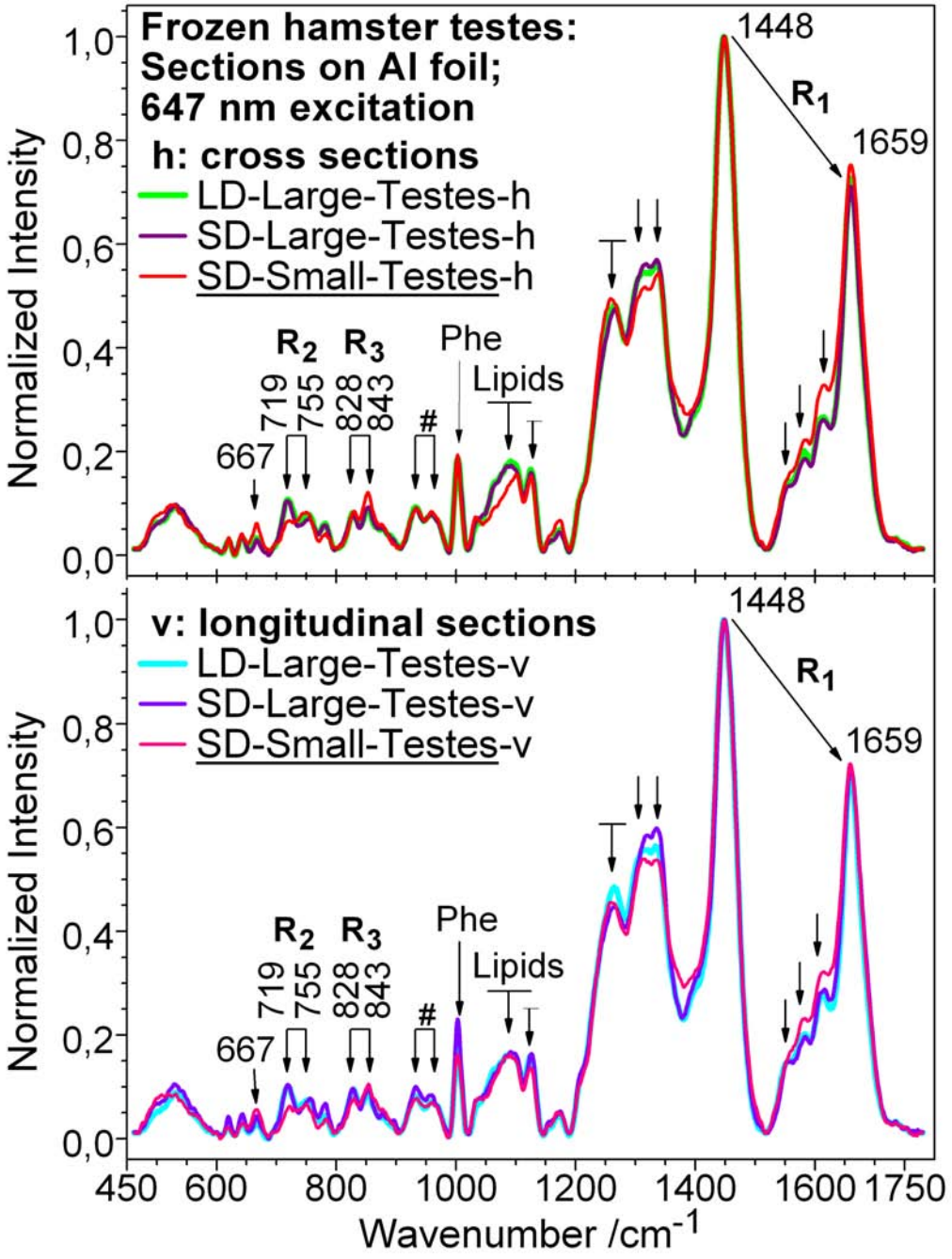


**Figure 5.12: Raman spectra of long-day (LD: green and cyan curves), photoperiod nonresponsive short-day (SD: purple and violet curves), and photoperiod responsive short-day (SD: red and light pink curves) fresh frozen hamster testes measured at 647 nm on Al foil**: The spectra were taken from either cross sections (h: top panel) or longitudinal sections (v: bottom panel).

features of the LD group, associated with the accumulation of lipid droplets (see later explanation). This observation is evidenced by the similarity of the spectra in Fig. 5.10. In fact the spectrum for the photoperiod nonresponsive SD (SD-Large-Testes-h: purple curve) overlap throughout the entire spectral range with the LD spectrum for either cross

or longitudinal testis sections. Although some variations appear in the amide III region and in the region containing the double band 1317/1335 $cm^{-1}$, as can also be noticed in the spectra in Figures 5.11 and 5.12, these variations were often seen with the different ways of sectioning the testes (*i.e.*, cross or longitudinal sections) and were not necessarily photoperiod specific. Nevertheless, the mean spectrum for SD hamster testes (named "SD-Large-Testes-h" in Fig. 5.10) shows a slight decrease in $R_1$ [ratio $I_{(\text{amide I + lipid C=C str.})}/I_{(CH_2)}$] and an intensity increase within the region [1020 - 1150 $cm^{-1}$] (peaking at $\sim$ 1096 $cm^{-1}$), suggesting that the photoperiod nonresponsive SD relatively accumulated even more lipids overall. This is just another supporting hint to the above conclusion that, with respect to the applied photoperiods, the nonresponsive SD hamsters were similar to the LD group and exhibited the same characteristic response. This is a rather consistent result and it would be interesting to resolve Raman signatures of the photoperiod-induced molecular changes associated with the change in the internal biological clock of the photoperiod responsive hamsters in the SD group.

As already noticed in the spectra in Fig. 5.10, Figures 5.11 and 5.12 show that testis cross (h) and longitudinal (v) sections tended to exhibit in some cases noticeable differences in the amide III region and in the region containing the double band 1317/1335 $cm^{-1}$. However these variations seemed to reduce for the sections measured on Al foil substrates which allowed the highest spectral quality (more intense spectra could be recorded on Al foil). Nevertheless, the observation that the two different ways of cutting testis sections (cross or longitudinal) exhibited differences, apparently not correlated with the change in the photoperiod length, indicates either local heterogeneities in the testis tissue sections or just exogenous and unspecific variations. Therefore, the investigation of the freshly frozen testis sections in different ways, such as the use of fixed and non-fixed sections, cross and longitudinal sections, and of both $CaF_2$ and Al foil substrates, has helped to address other eventual spectral variations on the one hand and reproducible spectral changes associated with the biological rhythm under study on the other hand. Hence, as already pointed out for the spectra in Fig. 5.10, Figures 5.11 and 5.12 also confirms that the photoperiod non-responsive SD hamsters (*i.e.*, having large testes) show similar Raman spectra as compared to the LD control group (compare the purple and violet curves named SD-Large-Testes-h and SD-Large-Testes-v with the corresponding green or cyan curves for LD hamsters). Interestingly, a detailed inspection of the spectra in Figures 5.11 and 5.12 reveals that the photoperiod responsive hamsters in the SD group (*i.e.*, having small testes: red and pink curves in Figures 5.11 and 5.12) exhibit significant and reproducible changes for most of the aforementioned and listed 'characteristic and relevant' spectral features, including the ratios $R_2$, $R_3$ and $R_1$, the 1126, 1552, and 1616 $cm^{-1}$ bands, but also the region around

the 1065 $cm^{-1}$ band. These significant and reproducible changes therefore appear in specific lipid bands including phospholipds (719 and 1126 $cm^{-1}$), in tryptophan residues (755, 1552 and 1616 $cm^{-1}$) and in tyrosine residues (828, 853, and 1616 $cm^{-1}$). Firstly, the 719 and 1126 $cm^{-1}$ can be assigned to the C-N str. of membrane phospholipid heads and the lipid C-C str. mode in *trans* segments, respectively. Secondly, the 755, 1552 and 1616 $cm^{-1}$ bands can be assigned to the ring breathing and ring str. modes of tryptophan and the C=C str. mode of tryptophan and tyrosine, respectively. Finally, the 828 and 853 $cm^{-1}$ bands can be assigned to the out of plane ring breathing of tyrosine and O-P-O str. of DNA, and the ring breathing mode of tyrosine and C-C str. of proline ring, respectively. The marked decrease in the relative intensity of the 719 $cm^{-1}$ band and the slight decrease of the 1126 $cm^{-1}$ band point to the down-regulation of specific lipid components (*e.g.*, phospholipids, etc.) in the photoperiod responsive SD hamsters. In addition, considering the ratio $R_1$ $[I_{(\text{amide I + lipid C=C str.})}/I_{(CH_2)}]$, it is clear that the overall lipid content did not change significantly for SD hamsters as compared to LD hamsters, but the slight increase in $R_1$ for photoperiod responsive SD hamsters points to a small decrease in lipid content overall. The above changes in lipids are well consistent with the previously reported observations that lipid droplets usually present in the leydig cells of long-day hamster testes are depleted in the involuting leydig cells of the photoperiod responsive SD hamster testes. It is important to note that phospholipids and cholesterol, also found among the major components of the lipid droplet, are the main precursors of testosterone synthesis. In addition, the main function of the testis's leydig cells is the synthesis of androgens (*e.g.*, testosterone in the male Djungarian hamsters) and it is well established that the inactivation of leydig cells (involuting leydig cells) is responsible for the declined testosterone levels observed in the LD breeding mammals during winter time (SD day-like photoperiod). Moreover, the neurohormone melatonin, which is called the night marker, *i.e.* the maker of the day length, derives from the amino acid tryptophan. Yet, reproducible Raman spectral changes in specific lipid components including phospholipds and in the important amino acids including tryptophan and tyrosine have been observed in the photoperiod responsive hamsters in the short-day group.

Therefore, the above discussed 'characteristic and relevant' spectral features represent the Raman signatures of the photoperiod-induced molecular changes. These changes are associated with the rhythmic switch in the internal biological clock resulting in seasonal regulation of male reproductive functions in short-day responsive Djungarian hamsters.

### 5.2.4 Conclusions

As has been demonstrated in the present work, Raman spectroscopy has helped to detect, besides amino acid bands, specific lipid components, such as phospholipds and cholesterol. This possibility makes the Raman spectroscopic approach rather interesting for the study of biological rhythm because these molecules play a crucial role in the regulation of key hormones (*e.g.* testosterone) that determine male reproductive functions and behavior. It has been shown that Raman spectra of the liver tissues for short-day *vs.* long-day male Djungarian hamsters are mostly similar. Moreover, Raman spectra of the testis tissues for short-day non-responsive (large testes) *vs.* long-day hamsters are also practically the same, confirming that the short-day non-responsive (large testes) male Djungarian hamsters showed the same characteristics response as the long-day control group to the applied photoperiods. Interestingly, the short-day responsive (reduced testes) hamsters exhibit, among other spectral differences, marked and reproducible changes mainly in specific lipid bands including phospholipds (719 and 1126 $cm^{-1}$), in tryptophan residues (755, 1552 and 1616 $cm^{-1}$) and in tyrosine residues (828, 853, and 1616 $cm^{-1}$).

Therefore, 'Characteristic and relevant' spectral features have been revealed, which represent the Raman signatures of the photoperiodically induced molecular changes in the gonads of male hamsters. These molecular changes are associated with the rhythmic switch in the internal biological clock resulting in seasonal regulation of the reproductive functions in short-day responsive male Djungarian hamsters. These results demonstrate the capability of Raman spectroscopy as a rather interesting complementary or alternative approach for the study of biological rhythms.

The results discussed in the above completed second part of this chapter have been submitted for publication in the following article:

Patrice Donfack, Karen Grote, Alexander Lerchl and Arnulf Materny; Raman Spectroscopic Approach for *in-situ* Biological Rhythm Studies in Light-Sensitive Mammals - Probing Physiological Response of Short/Long Day Photoperiods in Hamster Tissues; *Physical Biology*, **2011**, submitted.

# 6. Raman Potential in Immunology — Label-Free Discrimination of Colon Carcinoma Sublines with Insights into their Differential Expression of the Hsp70 Chaperone

## Summary

In this chapter, it is demonstrated that Raman scattering provides a noninvasive discrimination tool for Hsp70-associated sublines of human colon carcinoma *in vivo* and helps to reveal biomolecular insights on an intracellular level. Hsp70 is biologically relevant for its chaperon functions. CX- and CX+ sublines derive from parental CX2 and are very similar. They are reported specifically different only in Hsp70 membrane expression associated with immunostimulatory effects. CX-/CX+ have been phenotypically characterized by immunofluorescence studies and Raman spectroscopy combined with robust clustering and multivariate analysis. In the case of Raman spectroscopy, we address the potential of overall characterization, for CX-/CX+ discrimination and probing molecular insights into Hsp70 differential expression. Due to their strong resemblance, CX- and CX+ show similar mean Raman spectra, looking indiscernible at first. Interestingly, their rather protein-dominated Raman spectra reveal, besides changes in protein and amino acids, very specific changes in DNA/RNA nucleotides involving pyrimidine ring Raman hypochromic effects. Therefore, discriminating CX- from CX+ is ultimately achieved based on principal component scores. Because CX-/CX+ are associated with the same lipid-marker, changes in proteins may support lipid interaction with regulatory proteins. More importantly, changes observed in nucleobases, indicative of DNA-RNA/protein binding interactions, suggest transcription deregulations as participating precursor onsets of different transport mech-

anisms leading to Hsp70 differential expression and the associated phenotypic variation. Besides immunofluorescence, this work highlights a combined Raman spectroscopy and multivariate-analysis study of Hsp70-specific sublines within the autologous CX2 tumor system. Especially, the results obtained demonstrate the Raman spectroscopic potential for label-free nondestructive cell-subline discrimination, providing, to our knowledge, the first overall phenotypic monitoring with insights into the Hsp70 differential expression responsible for the expansion of many individual tumor lines into sublines. This might prove in future useful for label-free Raman cell-sorting of the CX-/CX+ sublines.

The works exhaustively described this chapter have been concisely presented in the following article, which has been accepted for publication in final form in CHEMBIOCHEM (a European Journal of Chemical Biology) at http://dx.doi.org/10.1002/cbic.201000653:
Patrice Donfack; Gabriele Multhoff and Arnulf Materny; Label-Free Nondestructive Discrimination of Colon Carcinoma Sublines and Biomolecular Insights into Their Differential Hsp70 Expression - DNA/RNA Nucleobase Specific Changes; ChemBioChem, 2011, Accepted, in press.

## 6.1 Introduction

Efforts to probe slight variations within a single tumor line or cell-type in general by breaking it into sublines (if possible) have helped to discover molecular chaperons, which shed light onto the pathways of the immune response. Molecular chaperones are diverse structural proteins, which interact with various non-native polypeptides and aid in the acquisition of their native conformation without being associated with their natively folded and functional center structure. They also aid in protein degradation if refolding is not possible, such as in case of stress (*e.g.*, heat shock). Some chaperones exhibit stress resistance, but also anti-cancer immune response. Colon cancer can be efficiently diagnosed via colonoscopy, which can help to detect the formation of and eventually remove polyps that indicate early signs of the disease.[157] However, patients are usually unaware of the disease onset, until a very advanced stage, where complications often might compromise therapy, and a combination of multiple treatments such as laser therapy and immunotherapy might be required. Therefore, research on the molecular basis of disease development and disease therapy in general is at the spotlight of biomedical sciences, and colorectal cancer in particular has been widely addressed since many decades. In the fight against cancer, besides cancer staging which is obviously an important step that helps to determine a suitable therapy for a patient, the idea to break down a single tumor cell line into sublines can help to understand how the tumor would behave in different physiological situations

and how the immune system could be tailored to efficiently recognize tumor cells. Lipid components of the lipid rafts can interact with proteins that play an important role in the regulation of cellular functions, such as cell growth, differentiation and cell survival respectively apoptosis.[158,159] Hence, tumor cells, unlike healthy cells, exhibit changes in the lipid raft composition associated with their immortality capability and the increase of the tumorigenicity.[160,161] On the one hand, it has been shown that the plasma membrane of primary colon adenocarcinoma cells and their metastasis overexpresses the lipid component globoyltriaosylceramid (Gb3), which is found only in tumor cells but never in healthy cells with the exception of B-cells.[60] Gb3 is a characteristic component of tumor associated lipid rafts. On the other hand, Multhoff *et al.* showed earlier that the major stress-inducible protein, the heat shock protein (Hsp70), is expressed on the cell surface of cancerous cells but not healthy cells.[162] Later on, Multhoff and collaborators found that the tumor-specific heat shock protein Hsp70 is combined with Gb3 on the plasma membrane of tumor cells,[163,164] providing the explanation why membrane-bound Hsp70, which may interact with other lipid partners,[164] is found only in tumors. In an effort to visualize the detailed tumorigenic properties of the colon carcinoma CX2 cell line for the prospect of developing specific antibodies, Multhoff *et al.* showed that this normally cytoplasmically localized heat shock protein is expressed on the plasma membrane of the CX2 tumor cells, with an average of Hsp70 positive cells of 60%.[165] In that study it was demonstrated that the CX2 tumor cells can therefore be sorted according to their membrane localization protein expression (Hsp70), expanding the CX2 tumor system into the sub-cell-lines with high Hsp70 expression of >90% Hsp70-positive cells (CX+) and low Hsp70 expression of <20% Hsp70-positive cells (CX-).[165] Interestingly, the membrane-bound Hsp70 has been found to correlate with the ability of the NK-cells (natural killer cells) to recognize the tumor cells.[165–168] Therefore, this brought evidence that the study of the sublines CX- and CX+ helped to reveal immunostimulatory functions associated with tumor cell membrane localization protein Hsp70; which then counts among essential molecular chaperones.
In fact, chaperone functions are not restricted to assisting protein folding and assembling, that essentially involve iterative cycles of binding and release of a client until it has reached its final active conformation, or has entered the proteolytic pathway.[169] Chaperones can also regulate molecular epitopes or behave in such a way that the associated immune response is not only protective for the host but also helps the host to recognize the danger. In this respect molecular chaperones can be helpful for both diagnosis (*e.g.*, cancer) and therapy control.[165,166,168] Hsp70 is the major heat-inducible protein of the heat shock protein family. Molecular chaperones of the Hsp70 family were for a long time suspected to be essential in autoregulation of the heat shock response, since they facilitate protein folding via

the stabilization of intermediate folded states of nascent proteins, thereby preventing non-native irreversible, and nonspecific aggregation.[170] It is now established that the Hsp70 chaperone plays a crucial role in regulating cellular processes, including protein synthesis, folding and degradation. Hsp70 is also known as a nucleotide recycling and exchange protein. More importantly, under stressful conditions (*e.g.*, heat shock) in practically all living organisms, Hsp70 is upregulated and is essential for transcription regulation for cellular survival and the development of thermotolerance. In this case, heat shock transcription factors (HSF) that co-localize with Hsp70 are released, because heat shock proteins need to be recruited throughout the cell to assist in the refolding or disposal of partly degraded proteins due to stress. Released HSFs undergo conformational changes and acquire DNA binding activity to the Hsp70 specific gene domain called Hsp70 element (HSE) having a 5'-flanking 5-basepair DNA motif "NGAAN", where N is any other nucleotide. This triggers transcription regulation leading to protein synthesis including mainly Hsp70s. It is a loop of self balanced processes which can restore the initial state upon return of normal physiological conditions (stress removal), if no irreversible damage or change has occurred. All of the chaperone properties and associated benefits of the Hsp70 have been carefully studied using standard and efficient biochemical methods, as evidenced by the abundant literature.[166,170–182] Besides the regulation of intracellular processes, the membrane bound Hsp70 on the cell surface of tumor cells provides recognizable structures for the natural defense of the host system: This was demonstrated by Multhoff *et al.* using first the human colon carcinoma autologous CX2 tumor system that could be expanded into the sublines CX- and CX+,[165] and secondly other tumor lines.[168] These immunostimulatory effects therefore elicit potential anti-cancer immune response mediated by either the adaptive or innate immune system.[167] As a matter of fact, immunostimulatory properties of the membrane-bound Hsp70 have been attracting particular interest in the understanding of NK-mediated and stress-induced apoptosis, or even in the screening of mammalian or mouse cancer, and in directed therapy.[163,165,166,168,183–187] Hsp70 and its members can also bind to RNA motifs, and are involved in mRNA stability (degradation and/or translation).[188–190] Therefore, in the differential CX-/CX+ sublines, mRNAs are differentially regulated, without being expressed at the cell surface. However, since cytosolic Hsp70 content is comparable between the two CX- and CX+ tumor sublines, it is not completely clear why, upon stress, some cells of the same tumor line express Hsp70 on their membrane and others do not. Differences in transport mechanisms leading to the association of the heat shock protein Hsp70 with tumor specific lipid raft components and accordingly its differential expression at the tumor cell surface are not fully understood yet.

Therefore, this work points to the fact that the detailed Hsp70 associated tumorigenic phenotype of the CX- and CX+ sublines has been of particular interest so far.[164–167,191,192] It has been hypothesized that different transport pathways and other reaction-partners of the heat shock protein family interacting with the tumor specific lipid marker Gb3 respectively other lipid rafts components might exist. A better understanding of the different mechanisms associated with the phenotypic variation between CX- and CX+ would provide detailed explanations about the unique features of the CX2 tumor system with the underlining therapy related benefits. For this purpose, a direct optical observation combining the highly sensitive fluorescence imaging and indirect immunofluorescence with biorecognition methods is the state of the art and offers a very effective technique.[164–167,191,192] This technique was first of all applied for the phenotypic characterization of established CX-/CX+ sublines in this work. However, although highly sensitive and rather efficient, this technique makes use of labels that have to fulfill stringent requirements, including specificity, biocompatibility and availability. In addition, the observation is restricted to the already known and labeled markers only. Moreover, the required prior bio-conjugation may in some cases compromise the reliability of the final observations by influencing the detailed biochemical makeup. This especially applies to the present particular case where detailed and very specific but small phenotypic information is of interest within the same tumor system of CX- and CX+. It would be interesting to look for such small variations without interfering with the cell too much or without destroying it. Finally and more importantly, the combined immunofluorescence & FACScan analysis technique helps to directly sort the CX2 cells' sublines (CX- and CX+) efficiently based on their differential Hsp70 membrane expression. However, it does not provide straightforward insights into Hsp70 differential expression resulting in the original cell line subdividing into two sublines following heat shock treatment. The focus of the PhD work described in the present chapter was not to try to detect Hsp70 on the cell surface (other Raman techniques and fluorescence can do this very efficiently). Instead, the focus was to probe overall biomolecular changes that can be correlated with the CX-/CX+ Hsp70 specific phenotypic variation. As extensively studied earlier by Multhoff and collaborators,[164–167,191,192] the CX-/CX+ sublines have so far been reported identical with respect to most of their membrane makers expression patterns. Hsp70s operate efficiently when in concert with other co-chaperones. Recent immunoprecipitation studies[192] not only pointed to an eventual association of Hsp70 and the co-chaperone Hsp40, but also confirmed the colocalization of Hsp70 with Bag-4, a protein known as the "silencer of the dead domain": It was shown that the colocalized Bag-4 exhibited differential membrane expression in CX-/CX+ sublines as well, under physiological conditions. However, in contrast to Hsp70, neither Bag-4 nor Hsp40 shows affinity to

NK-mediated cytosolic attack. Several other heat shock protein antibodies and membrane adhesive molecules tested so far did not differ. Therefore, the CX-/CX+ differ significantly only in Hsp70 membrane expression. Nevertheless, it is believed that key intracellular mechanisms exist that influence the transport pathways of Hsp70, resulting in the differential cell surface expression patterns.

One of the main goals of this work is to demonstrate the potential for label-free cell-subline discrimination within the autologous CX-/CX+ tumor system. More importantly, we at the same time wanted to search for the molecular basis of such discrimination in order to gain insights on an intracellular level into the differential Hsp70 membrane expression. In this respect, Raman spectroscopy is an interesting tool, since it can allow a noninvasive and nondestructive observation of the overall phenotypic state of CX- and CX+ sublines.

For the above reason, Raman spectroscopy has been introduced in the present work as an additional tool for the characterization of the CX- and CX+ sublines. To the best of our knowledge, this represents the first attempt of applying Raman scattering in order to interrogate intracellular biomolecular details that might be correlated to the Hsp70-specific phenotypic difference within an autologous tumor system (*e.g.*, the CX2 tumor line). Raman spectroscopy can provide specific molecular fingerprints and has been addressed over the last decades as a potential alternative and complementary technique for probing biological systems. Raman scattering has proven to efficiently characterize biological cells and tissues and to discriminate normal biological systems from cancerous or other pathological counterparts.[61,64,88,90,100,118,119,193–196] Disease grading in general is also possible and has been shown in many examples.[61,118,193–195] Recent progress in flow cytometry focuses on single cell analysis.[197,198] Unlike the broad emission of the florescence labels, narrow spectral features that provide better chemical contrasts are making Raman spectroscopic techniques the tools of preference in flow cytometry research.[55,199,200] However, since Raman scattering is an inherently week process, Raman spectroscopic investigations of biological systems cannot always be performed without difficulties. The delineation of the inherent variations within living cells can be sometimes demanding as was exhaustively discussed in chapter 4 (see also ref. 90). The study of detailed differentiation steps of tumorigenicity is a challenging task, since the related specific variations in the Raman spectra have to be separated from other big variations due to naturally occurring fluctuations within the cells or to ambient fluctuations.

In the following, immunofluorescence and FACScan analysis are used to characterize the CX2 line and the derived CX-/CX+. Then we demonstrate that Raman spectroscopy can be applied within the autologous CX2 tumor system. Based on this, the reliability and the potential both for nondestructive label-free phenotypic cell-subline discrimination and for gaining overall biomolecular insights into the differential Hsp70 expression are carefully assessed. We show that a careful and detailed analysis of the variations in the Raman spectra, in combination with multivariate analysis (clustering and principal component analysis, PCA) can be used not only for a quick phenotypic discrimination between the very similar CX- and CX+ sublines, but also for revealing intracellular insights into their Hsp70 specific phenotypic difference.

## 6.2 Material, Methods, and Experimental Techniques

### 6.2.1 Derivation of the CX- and CX+ Cells: Heat Shock Treatment

In the first part of the current work, the patented CX-/CX+ sublines were first of all exclusively established and phenotypically characterized at the "Klinikum rechts der Isar" of the Technical University Munich, Germany, in the department of Radiooncology. Then they were shipped to Jacobs University Bremen, Germany, for repetitive Raman measurements. As described earlier,[164–167,191,192] the CX- and CX+ cells are generated after heat shock treatment from their parental human colon carcinoma cell line CX2 (Tumorbank DKFZ, Heidelberg, Germany) cultured in RPMI 1640 medium (Life Technologies, Eggenstein, Germany) supplemented with 10% heat-inactivated FCS (fetal calf serum). Briefly, a non lethal heat treatment at 41.8°Cin a temperature-controlled water bath was applied to exponentially growing CX2 tumor cells for 2 h, followed by 12 h incubation at 37°Cfor recovery. As determined by trypan blue exclusion and propidium iodide staining, the viability of the heat-treated cell was always >95%.

### 6.2.2 Phenotypic Characterization: Flow Cytometry, Indirect Immunofluorescence, FACScan Analysis and Cell Sorting

The work described in this section was done in the group of Prof. Multhoff at the Klinikum rechts der Isar, Munich.

For phenotypic characterization, indirect immunofluorescence analysis with Hsp70-specific mAb (monoclonal antibody) and a suitable chromophore (FITC: fluorescein isothiocyanate), followed by FACScan analysis ("Fluorescence Activated Cell Sorting"; FACSCalibur, BD,

Heidelberg, Germany) were carried out in order to quantify Hsp70 expression on the cell surface of the CX2 and the derived sublines CX- and CX+. The flow cytometry studies and the cell sorting experiments of CX2 tumor cells were performed with exponentially growing cells and at comparable cell densities following a procedure similar to protocols described in ref. 165. Living CX2 tumor cells and the later derived CX-/CX+ were first incubated with Hsp70 specific Abs (RPN1197 or 3A3) at a final concentration of 1 to 5 μg per 0.5 to 1 $\times$ $10^6$ cells for 30 min at 4°C, supplemented with 0.1% sodium azide. After incubation with the above primary Abs, the cells were washed twice with PBS/10% FCS buffer and re-incubated with a second FITC-conjugated rabbit anti-mouse immunoglobulin (Ig) for 30 min at 4°C. On the FACScan instrument, the proportion of Hsp70 positively stained cells was defined as the difference between the number of specifically stained living cells and the number of cells stained with an isotype-matched control (IgG1).

For cell sorting, 5 $\times$ $10^6$ CX2 cells were stained with the Hsp70-specific mAbs (RPNI 197, 3A3) and rabbit anti-mouse FITC as described above for flow cytometry. On the FACSCalibur instrument, cells that did not express Hsp70 on their surface were separated from the cells that yielded Hsp70 expression, thereby FACS-sorting the original CX2 tumor line into a high (CX+) and low (CX-) Hsp70 expressing subline. The generated CX- and CX+ sublines were separately cultured in RPMI 1640 medium supplemented with 10% heat-inactivated FCS and antibiotics; these cells grow in small colonies in cell culture flasks. Established and stably expressing CX- and CX+ cells were maintained in culture in two cell cultures flasks, which were then carefully packed and transferred from Munich to Bremen for replicated Raman experiments.

### 6.2.3 CX- and CX+ Cells Culture for Raman Experiment

For the Raman measurement, viable, stably Hsp70 expressing CX- and CX+ tumor sublines (confirmed at the source) were shipped from Munich in a different culture medium, a phenol-free RPMI 1640 medium suitable for Raman interrogation, together with sterilized reagents (trypsin/EDTA, additional culture medium, and PBS), sterilized additional cell culture flasks and transfer-wares. All reagents were regularly kept at 4°Cand aliquots were taken when needed. In the pre-experiment phase, following a simple and routine procedure for cell splitting, immediately after receipt, the cell samples were gently trypsinized and split into new culture flasks, with about 5 ml of culture medium supplemented with FCS above the cells (this procedure helps to get rid of cells, which have died of were stressed *e.g.* during the travel). The two cell populations normally and rapidly recovered and multiplied into small colonies within cell culture flasks in just a couple of hours while in culture

inside a 5% $CO_2$ incubator, with a doubling time of 20 h. They could be repeatedly split at a dilution of 1:4 every 3–4 days into new sterilized culture flasks provided, for many weeks in order to perform replicate Raman measurements. For every third to fourth splitting, a few cells of each cell type were equally split onto 2–3 special $CaF_2$ substrates (*i.e.* 2–3 $CaF_2$ cell substrate samples for each cell type) for a set or group of Raman experiments, as summarized in Table 6.1. The $CaF_2$ cell substrate samples were left resting with the same medium composition inside separate cell wells of a sterilized cell well flask that was also kept in the same incubator as the cell culture flasks until Raman interrogation. Figure 6.1 shows the whitelight screen capture images (under the Raman microscope) of adherent CX-/CX+ cell colonies on $CaF_2$ substrates. The CX- and CX+ cells on the $CaF_2$ glass substrates grew in colonies as well and formed many separated colonies within 3–4 days. However, on the fourth day or beyond, they can formed many and much larger separated colonies with loss of single cell contour differentiation (a normal feature of the CX- and CX+ tumor cells' confluent colonies on glass substrates: see also the right picture in Fig. 6.1). Given the stability of the two cell-sublines, the splitting and incubation was not restricted in time, and could be continued as long as Raman replicate-experiments were needed. Therefore, as can be see in Table 6.1, a total of seventeen cell splittings, five of which were for sample preparations for Raman experiments, were performed (first four preparations every third to fourth splitting, and the fifth one at the last splitting). The passable number of the CX- and CX+ cells increases by $\sim 1$ for every cell splitting. Of all five cell splittings for Raman experimental groups, the last three were labeled A , B, C and are discussed (the first two splittings were used only for test experiments in order to adjust the Raman system for safe measurements: Laser power, integration time per point, etc.).

**Table 6.1:** Groups of replicate Raman experiments with the corresponding cell splitting order

| Cell splitting order on $CaF_2$ substrates | Replica labels in experiments | Passage number (same for CX-/CX+) | Remarks |
|---|---|---|---|
| - - | - - | 0 ➔ 1 | Cells trypsinized and split upon arrival |
| 1 | - - | 1 | |
| 4 | - - | 4 | |
| 7 | A | 7 | |
| 10 | B | 10 | |
| 17 | C | 17 | |

## 6.2.4 Raman Experiment and Instrumentation

As excitation source for Raman experiments, a krypton ion laser (Innova 302, Coherent INC, USA) coupled a Raman system described in detail in chapter 3 was used. Briefly,

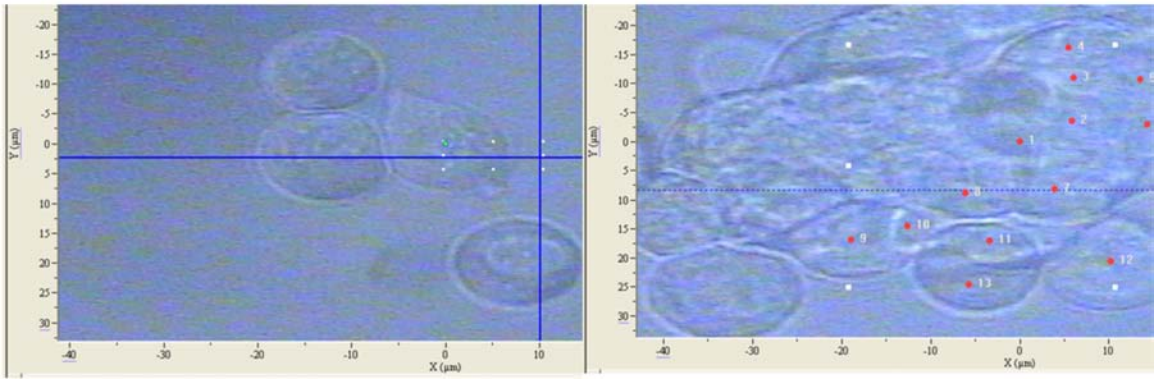

**Figure 6.1: White light images of the CX-/CX+ cells attached on $CaF_2$**: Isolated single cells (left) and cell colony (right)

this Raman setup is an assembly of a semi-confocal microscope mounted with 40× and 10× objectives, a color CCD camera for sample inspection, and a motorized XY scanning stage, rigidly attached to a triple spectrometer (T64000, Jobin Yvon, France). The latter is equipped with two interchangeable holographic gratings (600 and 1800 grooves/mm) in the final stage, and a liquid $N_2$-cooled, front-illuminated CCD detector (symphony 3000, 1024 × 512 pixels; Jobin Yvon, France) optimized for signal detection in the red.

For Raman interrogation, substrates of viable and adherent CX- and CX+ cell colonies resting in the cell well flask were taken out of the incubator one at a time and directly measured after transferring the substrate into a single standalone cell well, rinsing it once or twice with fresh culture medium, and filling in fresh medium. In this respect, the krypton laser line at 647 nm was used to excite the cells through the embedding culture medium. Raman spectra were recorded in a backscattering geometry. In this arrangement, the laser was coupled through the microscope which focused it to a ∼ 2 µm laser spot on the sample through a 40× objective immersed in the culture medium. The scattered light was then collected through the same objective. The laser power at the sample was kept below 10 mW, in order to avoid sample damage. This was checked in test measurements by recording 4 to 5 consecutive spectra from the same point of a cell at increasing exposure times. Individual spectra were recorded with 10 to 20 s exposure time and 3-5 averaged signal accumulations. Before and during Raman interrogation, the CX- and CX+ cell colonies were visually investigated with a long working distance (WD = 20 mm) 10 objective. For smaller colonies (less in number), 5 to 10 mapping points were recorded from selected spot centers of less differentiated cells. In general, CX- and CX+ form large colonies on the $CaF_2$ glass substrates. Consequently, much bigger raster scans with a larger number of spectra were recorded, with a scan step of 1–3 m and in just 10 s of exposure time with

2 signal accumulations per spectrum. Finally, the generated signal was filtered using an appropriate Notch filter for the 647 nm excitation in order to block the elastic Rayleigh scattering before a 10 cm biconcave lens that focused the resulting Raman signal onto the spectrometer slit. Then, setting the slit width to 100 μm, optimal spectral dispersion was achieved at 647 nm excitation using the T64000 triple spectrometer's 600 grooves/mm grating. The signal was detected using the liquid $N_2$ cooled CCD detector in two distinct fingerprint regions, [450 - 1780 $cm^{-1}$] and [2700 - 3680 $cm^{-1}$]. A resolution of 5 $cm^{-1}$ was achieved, which constituted a very good compromise between spectral details and a fast spectral mapping acquisition with rather short exposure times. Raman spectra were calibrated by recording the spectrum of spectroscopic grade toluene, where strong Raman lines were observed at 522, 786, 1004, 1031, 1211, and 1604 $cm^{-1}$ and at 2919 and 3056 $cm^{-1}$ in the first and second fingerprint regions of the cell spectra, respectively. Computer interface for instrument communication and spectral acquisition and pre-processing was provided by commercial software (LabSpec, Jobin Yvon, France).

### 6.2.5 Spectral Analysis and Multivariate Analysis

All spectra were 5 times smoothed with a 2-degree 9-size Savitsky-Golay algorithm. The composite Raman spectra of the cells recorded through the embedding medium, and background signals were first baseline corrected with a non-linear first-order spline fit with 8 or 3 fitting nodes in the first [450 - 1780 $cm^{-1}$] and second [2700 - 3650 $cm^{-1}$] fingerprint region, respectively. Then, for a systematic and more reliable spectral correction, the neat composite background contribution can be correctly estimated at those wavenumber positions where the samples show minimal to no overlapping intrinsic Raman bands, as shown earlier in chapter 4 (see also ref. 90). Therefore, the neat background contributions in the signal were estimated by scaling the raw background spectra by the ratio of the area around 1525 $cm^{-1}$ (within [1513 - 1540 $cm^{-1}$]) or within [3400 - 3450 $cm^{-1}$] in the background spectra to the corresponding area in the signal for the two regions, respectively. Multivariate analysis, including principal component analysis combined with *K*-means clustering analyses was performed in order to visualize how well the CX- and CX+ cell-sublines could be specifically discriminated, even when the *in situ* phenotypic changes may have been overlaid by further unspecific, but predominant molecular changes inherent to the living and changing cell. An exhaustive description of spectral correction can be found earlier in this thesis and also under section 6.5 "Supporting Spectral Analysis Information"

## 6.3 Results and Discussion

### 6.3.1 Immunofluorescence and FACScan Analysis: Phenotypic Makeup of the CX- and CX+ Cells

Following heat shock treatment at 41.8°C(non-lethal), CX- and CX+ sublines were FACS-sorted from their parental CX2. To this end, CX2 cells at the exponential growing stage were treated with Hsp70-specific monoclonal antibodies (mAbs) (RPN1197, 3A3) and anti-mouse FITC (fluorescein isothiocyanate). Then, Hsp70 on the cell surface was quantified by indirect immunofluorescence and FACScan analysis. Fig. 6.2 depicts FACS histograms for the CX2 line and the derived sublines CX- and CX+, showing (horizontal axes) $10^4$ accumulated FITC fluorescence events (in log fluorescence count) for cells stained with Hsp70-specific mAb (solid histograms) or with an isotype-matched immunoglobulin control (open histogram). The horizontal line M1 in the solid histogram (positive experiment) is a gate that separates specifically positive fluorescence events from the control: *i.e.*, the percentage of positive cells corresponds to the area under the curve delimited in the solid histogram by the M1 line. In the present study, 49% of CX2 tumor cells constantly expressed Hsp70 on their surface under physiologic condition. The specificity of the Hsp70 mAbs was shown previously.[164–167,191,192] CX2 tumor cells were then FACS-sorted into

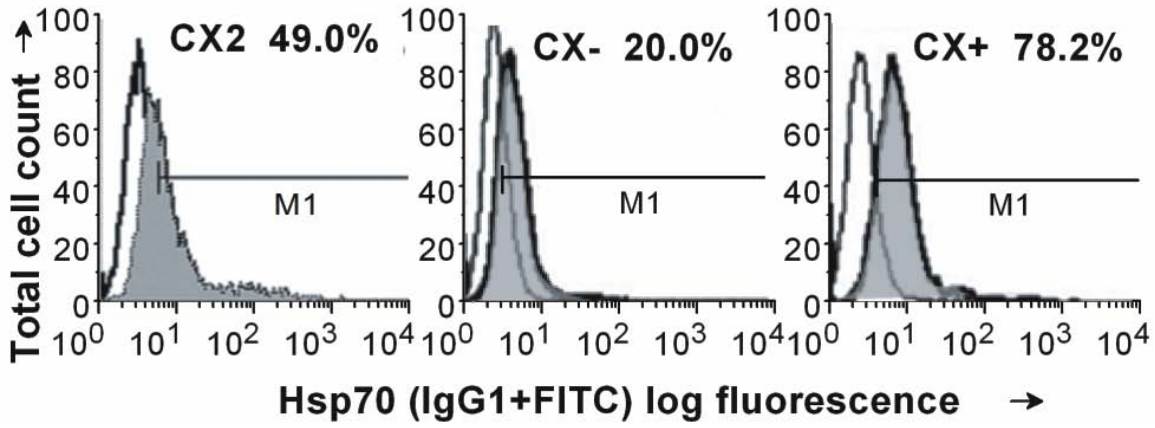


**Figure 6.2: FACScan histograms of the colon carcinoma line CX2 and the sublines CX- and CX+**, for cells stained with Hsp70-specific mAb (solid histogram) or an isotope-matched Igb control (open histogram)

Hsp70 low (CX-) and high (CX+) expressing sublines, which were separately cultured. The CX- and CX+ were also phenotypically characterized (quantification of Hsp70 cell surface expression) following the same protocol for flow cytometry, immunofluorescence and FACScan analysis with Hsp70 specific Abs and FITC as aforementioned. As depicted in Fig. 6.2, FACScan analysis showed 20% (CX-) and 78.2% (CX+) Hsp70 positive expressing cells of the total cell count in each case, respectively. The results presented for

FACScan analysis were mean values of at least four independent experiments. As established by Multhoff *et al.* and as has been observed so far,[164–167,191,192] the CX- subline expressed Hsp70 on ~ 20% of the cells, not immediately after cell sorting, but after cell passaging and stably on all further passages, and even after further re-sorting cycles. This observation has been so far been attributed to antigen (Ag) capping effect.[165] In their 1997 pioneer study, Multhoff et al could only report that the CX-/CX+ phenotype was stable for at last 30 passages, because they only worked with cells up to passage 30 following FACS-sorting. Nowadays, it is possible to work with the CX/CX+ sublines with more than 100 and up to 200 passages, without disruption their membrane-bound Hsp70 associated phenotype. The above phenotypical characterization was completed at a clinical institute with long term expertise and the patent for the establishment of the CX-/CX+ sublines. After this step, fresh cell populations of newly resorted and stably Hsp70 expressing CX- and CX+ were considered for replicated Raman measurement (note that the passage number resets to 0 upon resorting). For this purpose, the cell-sublines were only repeatedly split in culture, as described in the section "CX- and CX+ cells culture for Raman experiment".

### 6.3.2 Raman Characterization and Multivariate Analysis

In an effort to answer the question whether Raman spectroscopy can at all provide any discriminative information within the autologous human colon carcinoma CX2 system, the Raman scattering technique has been applied in combination with multivariate analysis to probe potential biochemical changes in the differential tumorigenic CX- and CX+ sublines. Grouped Raman experiments, labeled A, B, C and discussed in this work, corresponded each to the same round of cell splitting from cell cultures onto $CaF_2$ substrates for Raman interrogation. The cells increased by ~ 1 for every cell splitting as also mentioned in the section "CX- and CX+ cell culture for Raman experiment". Therefore, the Raman experiments were grouped as mentioned above to ensure that both cell sublines were measured under the same conditions. In fact, apart from the passage number, small fluctuations between the different split samples cannot be excluded. The Raman data from the different groups of experiments were treated separately (*i.e.* within each group) and the results were further compared between the different groups. Fig. 6.3 shows mean Raman spectra of CX- and CX+ cells for each group of experiments in the two fingerprint regions, [450 - 1780 $cm^{-1}$] on the left and [2700 - 3650 $cm^{-1}$] on the right. The mean spectra are first shown as the average absolute intensity counts per second ($cnt.s^{-1}$) (top three panels in each spectral window in Fig. 6.3). Then, they are shown using a normalized intensity scale (bottom panels of Fig. 6.3: All individual spectra were normalized to the peak intensity of the $CH_2$ def. (deformation) mode at 1450 $cm^{-1}$). This procedure helps to highlight two

types of variations, overall (*i.e.* content of marker biomolecules, *e.g.* those correlated with Hsp70 expression) and relative biomolecular changes. The raw preprocessed spectra to be averaged were selected according to several criteria including the overall spectral quality and a qualitative judgment of the ratio $R_1$ of the intensities $I_{1660}$ and $I_{1450}$ as described in the following.

In order to assess the reliability of the observed Raman fingerprints, we followed a detailed spectral analysis procedure as described in section 6.5 "Supporting Spectral Analysis Information". In particular, we have established as a rule that reliable spectra should agree in their overall appearance with well known Raman spectra of the main biological building blocks (*e.g.* proteins, amino acids, nucleic acids, etc.).[61,88,110] In general, obviously distorted spectra showing uncorrelated broadening and drastic variations (sometimes with new bands) are usually signs of artifact or biomolecular breakdown and should be disregarded. In the present study, within the data of each group of experiments, only a very few spectra distorted due to high noise were rejected. A moderate broadening affecting the region [1530 - 1780 $cm^{-1}$] (protein amide I region) was due to Raman scattering from water molecules, since the cells were measured with a short working distance 40 objective directly immersed in the embedding culture medium. This water contribution is part of the overall composite background signal that also includes an additional broad feature poorly resolved from the water band (see Fig. 6.6 in section 6.5 "Supporting Spectral Analysis Information"). It especially could not be neglected since slight defocusing can occur during extended and long-lasting mapping acquisitions. In addition, the background interference was big when very small cell colonies or separated single cells were occasionally measured on the $CaF_2$ substrates (although this was rarely the case in our experiments, since the CX-/CX+ sublines formed as usual relatively big colonies on substrates). Therefore, the spectra were carefully background corrected as mentioned in the experimental section. After this step, poor spectra were first left out from the set of averaged spectra (heavily background-affected raw spectra on the one hand or noisy ones on the other can become noisier or distorted, respectively, after background correction). In addition, the ratio $R_1$ is a characteristic fingerprint. However, its value can be seriously influenced by both exogenous and intrinsic variations. Given the strong similarity of both sublines, big variations in $R_1$ were considered with caution. Therefore, a few spectra although rather good but showing reversed $R_1$ values (*i.e.* $R_1$ ł 1) in contrary to the majority of spectra were first of all left out and assigned to a separate data set. This was simply achieved by inspecting the corrected spectra, without explicitly calculating $R_1$, since we only wanted to put aside those spectra showing an obvious deviation. For this particular case however, multivariate

analysis will later show that moderate variations in $R_1$ may indicate other eventual intrinsic changes. Therefore, the mean spectra displayed in Fig. 6.3 are the averages of all spectra (except for a very few showing R1 deviations) in groups C, or some of the good spectra in groups A and B. At least 50 CX+ to 167 CX- (in groups A and B) or hundreds ( 350 for each subline in group C) of individual spectra were averaged. Note that only 81 and 69 spectra in total were recorded from CX+ cells in groups A and B, respectively. Large maps of CX- spectra acquired in group A (mainly) and B were very noisy and not included in the means. Therefore, the total number of averaged spectra varied between the different groups because they had different numbers of noisy or poor data; the cause of the noise is discussed later in the multivariate analysis section.

### 6.3.3 Main Raman Fingerprints Observed in CX-/CX+ — Tentative Biomolecular Basis

It is worth mentioning again that, although the CX- and CX+ sublines exhibit a clear phenotypic variation associated with their differential Hsp70 membrane expression levels, they remain very similar with respect to their overall tumorigenic makeup, being associated with the same tumor-specific lipid component Gb3.[165,166] As can be seen in Fig. 6.3, the Raman spectra of the CX- and CX+ sublines are very rich in features. The different Raman bands or vibrational modes observed and their tentative biomolecular assignment are summarized in Table 6.2. The assignment is based on the literature about Raman spectra of the main biological building blocks (protein, lipid, DNA, RNA, carbohydrates), cells, tissue etc.[61,64,71,88,100,101] While CX- and CX+ are associated with a tumor-specific lipid marker, their Raman spectra depicted in Fig. 6.3 are dominated by amino acids, nucleic acids, and specifically proteins. The main fingerprints at $\sim$ 939, 1249, 1316, 1450, 1660, and 2935 $cm^{-1}$ are attributed to prominent contributions from collagenous proteins (C-C str. (stretching) mode in proline/valine, $\alpha$-helical marker of proteins), and the protein amide III (with overlapping pyrimidine base contributions sensitive to base stacking), protein $CH_3CH_2$ wag (collagen, and polynucleotide chain: DNA-purine bases), protein $CH_2$ deformation (with small lipid contribution in the present case), amide I and protein C–H str. vibrational modes, respectively. Other prominent bands mainly due to important biomolecules such as nucleic and amino acids or to biochemical functional groups were clearly observed at $\sim$ 720 (C–N of membrane phospholipid head, or nucleotide peak, *e.g.*, A),[118] 784 (C, U, T), 854 (Trp), 1003 (Phe), and 1095 $cm^{-1}$ (-O-P-O-). The resolved band at 1003 $cm^{-1}$ is usually due to the amino acid phenylalanine (Phe) in this region, but might contain, in the case of the CX-/CX+ under study, a much greater contribution from protein skeletal vibrations. The

other main bands at 854 and 784 $cm^{-1}$ arise from prominent contributions from tyrosine (ring breathing) mainly or hydroxyproline ring vibration (C–C str., specific to collagen), and ring breathing of DNA/RNA nucleotides (U, C, T),[61,88,118,119] respectively. The overall lipid contribution in the Raman spectra of CX- and CX+ tumor sublines is rather weak, and besides this observation, lipid bands from biological systems (cells, tissue, fat) in the vicinity of the 1095 $cm^{-1}$ band region are usually much weaker. Therefore, the 1095 $cm^{-1}$ band can exclusively be attributed to the DNA backbone vibration in CX-/CX+, and the remarkable strength of this band is indicative of high DNA content associated with the high nucleus/cytoplasm ratios in tumors cells. In addition, the 784 $cm^{-1}$ is overwhelmed in the Raman spectra of oligonucleotides which in the case of biological cells include the natural oligonucleotides DNA and RNA. It follows that the strong 784 $cm^{-1}$ is readily assigned to the pyrimidine ring breathing in the Raman spectra of cells and tissue,[61] especially when the DNA backbone marker bands around 1095 and 830 $cm^{-1}$ are detectable. In general, DNA bands are easily detectable in cancer cells due to their high DNA content. In addition, in microorganisms with up to 44% protein content, the Raman spectra are dominated by DNA contributions, because DNA is a stronger Raman scatterer than protein.[61] The above tentative biochemical assignment of the Raman spectroscopic signatures of the CX-/CX+ tumor sublines in the fingerprint regions [450 - 1780 $cm^{-1}$] and [2700 - 3650 $cm^{-1}$] has been recapitulated in Table 6.2. In addition, further remarks have also been included in Table 6.2 about the Raman band behavior that can be considered for discriminative characterization of the phenotypic variation between CX- and CX+.

Overall, the mean Raman spectra of the CX- and CX+ sublines are rather similar. Two important types of spectral changes between CX- and CX+ tumor sublines can be analyzed: Firstly, the average signal counts per second for the main bands(2935, 1660, 1450, 1249, 1003, 939, 853, and 784 $cm^{-1}$)show small absolute changes between CX- and for CX+. This may be indicative of an overall change in the content of key biomolecules, mainly nucleic acids and protein (and some amino acids) that might be (anti)-correlated with Hsp70 expression. However, some of these absolute variations do not seem to reproduce, and may be random fluctuations. The feature, which seems at first glance to best reproduce, is the band at 784 $cm^{-1}$. Secondly, relative biomolecular changes, small as evidenced by the strong similarity of the normalized mean spectra displayed in Fig. 6.3 (bottom panel), may also be present in the main Raman fingerprints. Taking the $CH_2$ def. band (1450 $cm^{-1}$) used for normalization as the reference, relative features can be noted. They include the relative intensities ($I_{1314}$ and $I_{1340}$), the protein amide III shape and relative intensities ( $I_{1249}$ and $I_{1269}$), and more importantly, the relative intensity of the ring breathing vibrations

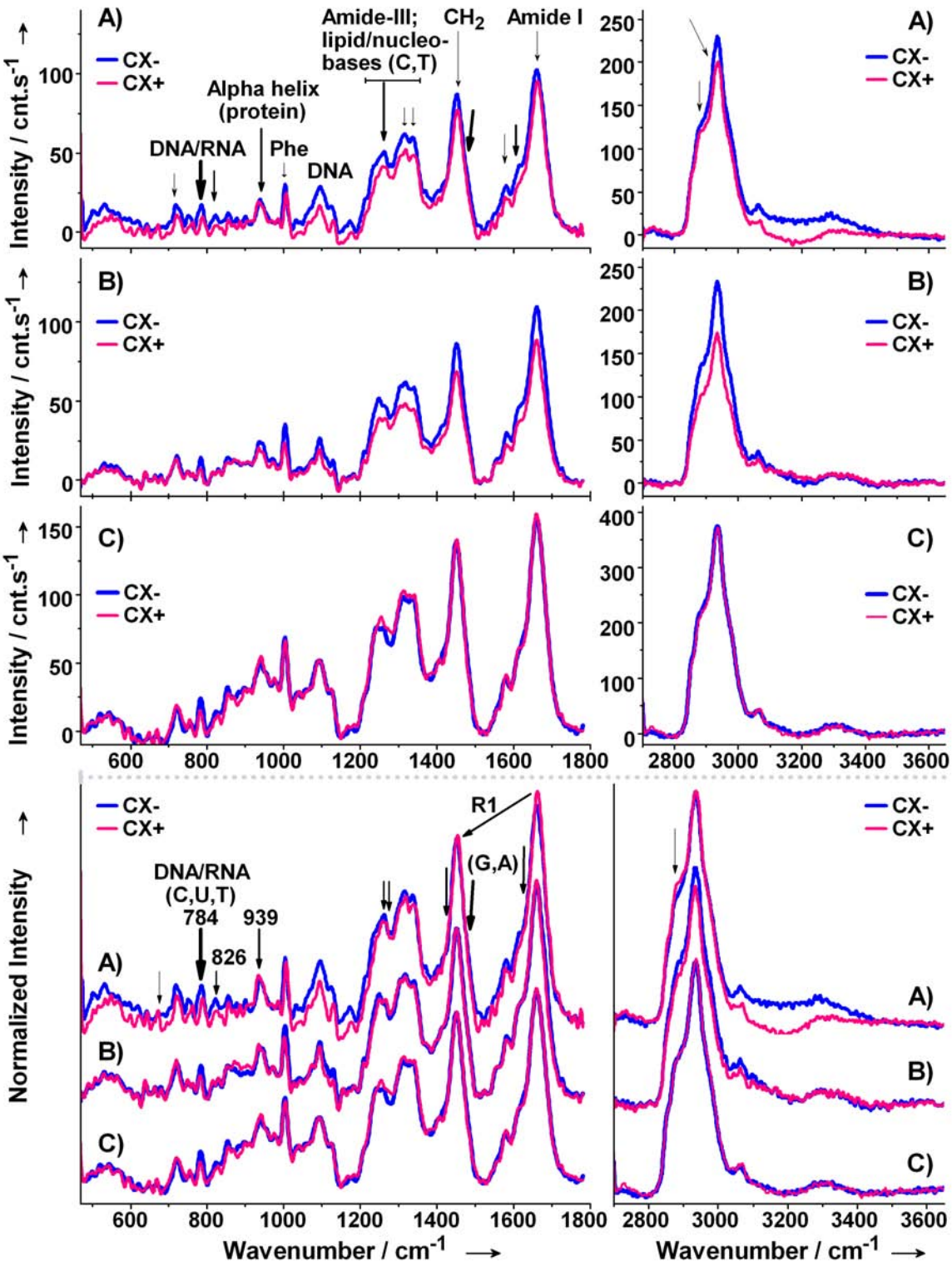


**Figure 6.3: Mean Raman spectra of CX- and CX+ tumor sublines**, for each group of experiments (A, B, C) in the two fingerprint regions [450 - 1780 $cm^{-1}$] (left) and [2700 - 3650 $cm^{-1}$] (right), displayed as the averaged absolute intensity counts per second (upper panels) and normalized mean spectra (bottom panel).

of RNA/DNA nucleotides (pyrimidine ring) at 784 $cm^{-1}$, very consistent in all groups

of experiments. Of all these absolute and relative changes, reproducible ones (*e.g.*, at 784 $cm^{-1}$) can provide insights into the different biochemical events (DNA/RNA/protein interactions) promoting different transport mechanisms of Hsp70 leading to the phenotypic variation in differential Hsp70 expression of the CX-/CX+ sublines since the latter is the only unambiguously well established tumorigenic phenotype of the two sublines (see again later argumentative sections for more details). In addition, they can also be attributed to other eventual biomolecular interactions (interaction involving key proteins, such as the Hsp70 family and/or tumor-specific lipid molecules). Reproducible changes can be exploited through an algorithmic scheme for direct phenotypic cell-classification of the CX- and CX+ sublines in a noninvasive (label-free) and nondestructive way. Peak intensity ratios for the 784 $cm^{-1}$ band ($I_{784}/I_{1450}$), and for the protein amide I (ratio $R_1$: $I_{1660}/I_{1450}$) and C-H (ratio $R_2$: $I_{2935}/I_{1450}$) are plotted in Fig. 6.4. As evidence, in Fig. 6.4 (top panel), the changes associated with the DNA/RNA pyrimidine ring mode were reproducible. In addition, the protein amide I ratio $R_1$ and C-H ratio $R_2$ plotted in Fig. 6.4 (bottom panel) evidence that the overall relative variation in proteins remained unchanged. Besides the

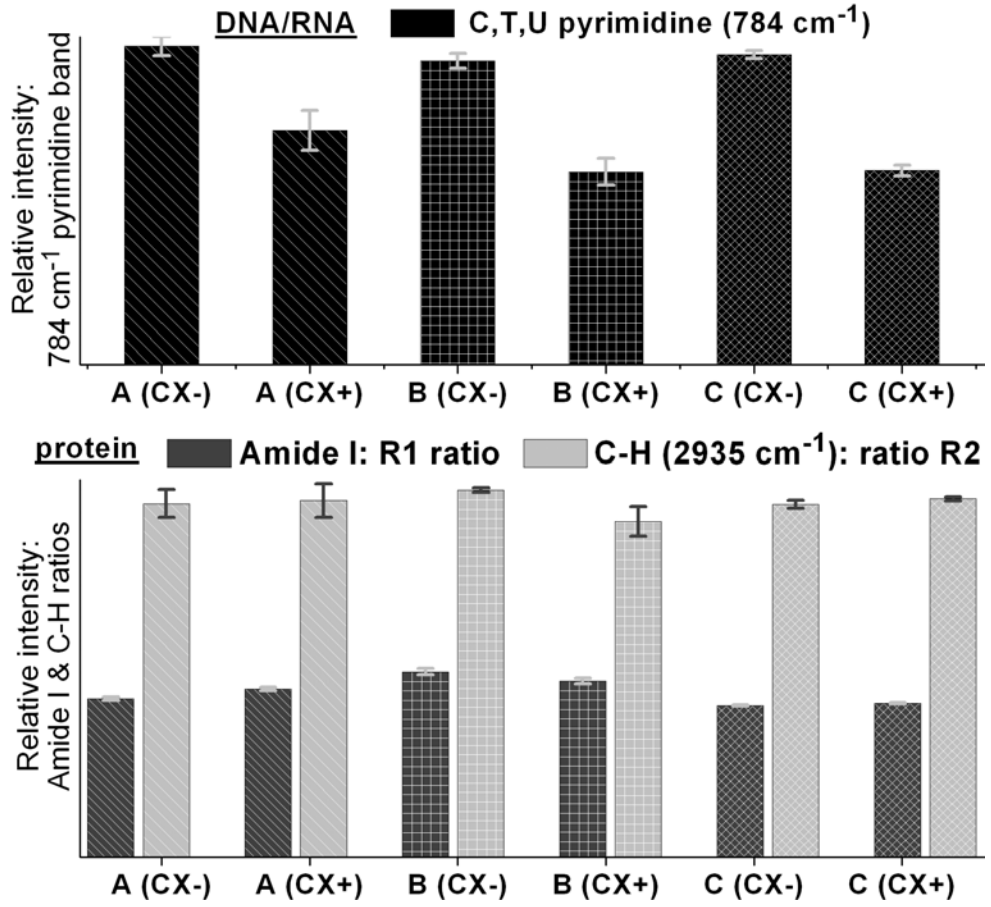


**Figure 6.4: Mean peak intensity ratios of the main protein bands and the pyrimidine ring mode relative to the $CH_2$ def. mode** for each subline CX- and CX+ and each group of Raman experiments (A, B, C).

aforementioned small changes, big variations in band intensities were not necessarily reproducible. This situation is not surprising and reflects the strong similarity of the CX- and CX+ tumor sublines within the same autologous CX2 tumor system. It is so-called because from the tumorigenic viewpoint, the CX-/CX+ are identical with respect to practically all tumor-specific cell surface markers expression patterns, except for their phenotypic variation in Hsp70 membrane expression. Moreover, as revealed by immunofluorescence and FACScan results discussed in the corresponding previous section, the CX-/CX+ tumor sublines in the present study exhibited a narrower gap regarding cell count positivity to Hsp70 (20% and 78.2% Hsp70 positive cells for FACS-sorted CX- and CX+, respectively). Therefore, unlike significant spectroscopic differences between healthy and cancerous states or cancer grades, the difference between CX- and CX+ tumor sublines can be thought of as being very small, especially, as far as the inherently insensitive Raman scattering is concerned. The very small difference between CX- and CX+ may be further overlaid by exogenous and/or other intrinsic variations due to physiological fluctuations, the dynamic and changing behavior of the living cell. This is the reason, why the few spectra showing drastic $R_1$ deviation ($R_1$ ł 1) were first left out of the set of the averaged spectra for both cell-sublines. Therefore, it is important to further analyze all possible variations in the Raman data thoroughly. Before Raman spectroscopy can be applied for the phenotypic analysis of specific systems, such as *e.g.* the implementation of Raman label-free cell-sorting in future, firstly the characteristic features have to be identified based on a statistically meaningful number of spectra. For the present study, between several hundreds to more than one thousand spectra were recorded within each group of experiments (see later). As demonstrated above (Fig. 6.3 and Fig. 6.4) slight but recurrent differences between CX- and CX+ were observed in the protein and more importantly in the RNA/DNA nucleotides bands, in the first fingerprint region. While the analysis of the different Raman bands observed in the spectra of the CX-/CX+ sublines can give some basic information, the complexity of the spectral information cannot be grasped entirely by a simple comparison of the mean spectra. A systematic analysis of the spectral variation can help to understand not only the significant changes, but also specific as well as all other eventual variations and their biomolecular basis.

Therefore, for all Raman spectra recorded within each group of experiments and for all replicated groups, all changes observed in the CX- and CX+ have been subjected to multivariate analysis. For this purpose, all individual spectra are analyzed. As will be discussed in the following section, this statistical approach eases the spectra sorting and grouping according to the trends of potential variations (whether spectral deviation, specific or unspecific variations) present in the data. Reproducible Raman signatures can be

validated. Hence, the discrimination between the CX- and CX+ tumor sublines based on the rather slight changes observed in their Raman spectra can be judged, while seeking for biomolecular insights into key mechanisms leading to different transport pathways of the Hsp70 chaperone. This ultimately might be useful for a potential noninvasive and nondestructive sorting of these cell-sublines in future.

**Table 6.2:** Tentative biomolecular assignment of the vibrational bands observed in the Raman spectra of CX- and CX+ sublines

| CX- | CX+ | Band assignment and remarks |
|---|---|---|
| 2935 | 2935 | C-H str.: Very strong, and show protein contributions mainly |
| 1660 | 1660 | Amide I: α-helix; random coil (collagen, elastin):[71,110] The ratio $R_1$ = $I_{1660}$/ $I_{1450}$ is comparable between CX- and CX+ |
| 1615 | 1618 | C-C str. Tyr, Trp:[100] **Stronger, but poorly resolved in CX+** |
| 1580 | 1580 | Ring Str. G, A:[100] Stronger and better resolved in CX- |
| 1555 | 1555 | Trp:[100] Weak in both cases |
| 1450 | 1450 | $CH_2$ def (lipid) & $CH_2CH_3$ def (protein):[61,71,100] **Strong** |
| 1303 | - | $CH_2$ twist, phospholipids & collagen:[71] Weak, unresolved in CX+ |
| 1316/1339 | 1316/1339 | $CH_3CH_2$ twist/wag, collagen & polynucleotide chain (DNA/RNA-purine bases A, G); G ring/$CH_3CH_2$ wag: desmosine, isodesmosine (elastin); Amide III, hydrated α-helix $\delta$(N-H) & $\nu$(C-N):[61,71,88] |
| 1249/1263 | 1249/1263 | Amide III, proline rich/proline poor collagen (mainly α-helical); elastin:[88] **Ratio $I_{1249}$/$I_{1263}$ greater in CX-: the 1263 cm$^{-1}$ mode is nearly absent or shifted in CX-.** |
| 1209 | 1209 | C-$C_6H_5$ mode of Trp and Phe[100] |
| 1177 | 1177 | C-H in-plane bend of Tyr[100] |
| 1129 | 1129 | C-C str. of lipids in trans-segments / protein C-N str.[88] |
| 1093 | 1093 | Sym str. of DNA back bone (O-P-0-);[61] C-N str. of proteins and lipid (to a lesser degree), and (C-C) and (C-O) of phospholipids:[88] (all negligible here): **Here, strong DNA back bone signature; comparable in both CX- and CX+.** |
| 1065 ··· | 1065 ··· | C-O, C-O-C str. of phospholipid:[61] Very weak signs appear in CX+ |
| 1042 | 1042 | C-O str. of carbohydrates:[110,127] Very weak |
| 1003 | 1003 | Phe ring breathing, protein C-C skeletal str.:[71,88,90,118] Strong |
| 973 | 973 | $\delta$(=CH) wagging:[61] **Weak but nearly absent in CX-** |
| 939/944 | 939/944 | C-C str. proline, valine, α-helix marker (protein backbone), collagen, glycogen:[71,88,100] **Strong/weak; ratio $I_{936}/I_{944}$ greater in CX-** |
| 854 | 854 | Ring breathing of Tyr and C.C str. of hydroxyproline ring specific to collagen:[61,88,118] Slightly greater in CX- (but insignificantly) |
| 830 | 830 | **DNA backbone marker for B-form DNA**:[61,88,118] |
| 784 | 784 | Ring breathing of DNA/RNA nucleotides (U,C,T):[61,88,118,119,201–203] **Strong, consistently and specifically greater in CX- than in CX+** |
| 720 | 722 | C-N str. of membrane phospholipid head or nucleotide peak:[118,127] strong (comparable) |
| - | 670 | C-S str. of cystine:[90,118,127] Nearly absent or broad & shifted in CX- |
| 622 / 644 | 622 / 644 | Skeletal mode (C-C twist) of Phe and Tyr[84,118] |

### 6.3.4 Multivariate Analysis of the Raman Fingerprints and CX- *vs.* CX+ Discrimination

As introduced in the previous section, in order to further evidence the capability of Raman scattering in discriminating the sublines CX- and CX+ of the human colon carcinoma CX2 system, based on their rather small spectroscopic differences, PCA combined with *K*-means clustering analysis, was carried out. PCA helps to reduce the dimension of the Raman data and to classify them into different subsets for detailed and more specific average information. This information describes the specific molecular basis of the different spectral variations (now clustered) present in the Raman data. The PCA overview yields very important results including the total explained variance (X-expl.) described by each computed principal component (PC) and, especially, the PCA scores' scatter plot of any two PCs, and the corresponding PCA loading plot (X-loadings). The PCA scores' scatter plot is a two-dimensional coordinate system that displays the samples according to their component scores and provides natural sample grouping (*e.g.* scatter plot for PC2 *vs.* PC1). The loading plot for any selected PC displays the relative importance of the original variables (X-variables; equal to the Raman wavenumbers in the present case) for the plotted PC and helps to determine the chemical origin of the variation described by that particular PC. For the sake of clarity, it should be noted that variables with high positive or negative loadings are the most significant for the variation described by the corresponding PC, while variables with small loadings are insignificant. A simple non-assisted *K*-means clustering analysis was performed and the results were used as category variables in order to highlight the grouping of the Raman data. For *K*-means clustering, two distance computation types were performed: In all cases, *K*-means clustering based on the Euclidean distance was performed. The Euclidean distance is the "natural" and intuitive way of computing a distance between two samples. It accounts for the difference directly based on the magnitude of changes. When needed, *K*-means clustering based on the Kendall's (tau) distance was initially run. The Kendall's (tau) distance is helpful in identifying samples with a huge deviation in a given data set. In general, the result of *K*-means clustering is presented as the sum of distances of the data points to their respective cluster centroid. The smaller the sum of distances, the better the clustering is. Not only spectra judiciously selected to compute the representative mean Raman spectra discussed in the previous section, but all recorded individual spectra were analyzed via PCA and clustering, in order to intuitively assess and delineate all other variations and noise from intrinsic changes. Kendall's (tau) *K*-means clustering helped to distribute data in two random clusters. Data points with drastic deviations (obviously distorted spectra) fell in one of the clusters and were removed (*i.e.*, ~ 36 spectra in group A, 2 in group B and 0 out of 1106 spectra in group C). It should be

noted that the cause of drastically distorted spectra is not deterministic (cell culture with minor cell debris on substrates cannot be excluded). In addition, spectra initially present in the dataset of group A, which were very poor and too noisy, mainly due to defocusing during large mapping acquisitions of a lot of spectra, were sorted out via clustering and disregarded, in order to obtain a starting set of about 408 spectra for the final analysis (note that not all noisy spectra could be directly removed, since noise assessment was itself part of the analysis). In group B, since the initial total number of spectra was only 320, all data (except a very few obviously distorted data rejected) were analyzed. Ultimately, a final Euclidean *K*-means clustering of the data (408 in A, 318 in B and 1106 in C) was performed, followed by PCA that used the clustering result as a category variable (a test PCA was performed beforehand to set the number of clusters).

Figure 6.5 shows the PCA results for the different groups of experiments A, B, and C, respectively. The PCA model for each group was computed with centered data and for 8 components (PCs). To display the results, a blue/red color code is applied to the two cell-sublines CX-/CX+ respectively. For each group (A, B, C), first the scatter plot PC2 *vs.* PC1 and the corresponding X-loadings are plotted (see Fig. 6.5 **Ai**,**j**; **Bi**,**j**; and **Ci**,**j**; the inserts in **Aj**, **Bj**, and **Cj** are explained later). Then, by screening the next components in each PCA model, the most significant and specific PC is found and the scatter plot for the PCs that best discriminate the CX-/CX+ sublines and the corresponding X-loadings are plotted (see Fig. 6.5 **Ak**,**l**; and **Ck**,**l**; discriminative scatter plot resp. X-loading not shown for group B, since the situation was not better than that of **Ak**,**l**; see later explanation). As revealed by Fig. 6.5, the scatter plot PC2 *vs.* PC1, which describes the biggest variations within the data, accounts for ~ 77 up to 94% total explained variance by both PCs in each group, while the discriminative scatter plots account for much less variation (~ 1-2%). The explained variance is denoted as "X-expl." Before any interpretation, one should recall that the components in a PCA model are ordered. PC1 is the most relevant one lying along the direction of the biggest variation in the dataset, followed by PC2, and so on. However, because, variations in multidimensional datasets can be of different nature, the relevance of a PC does not necessarily imply the significance and specificity of the variation it describes. That is why the X-loadings are important to judge both the scatter plot and the kind of variations it contains.

#### 6.3.4.1 About CX- and CX+ Similarity

As expected and as already exhaustively discussed in the previous section, the scatter plots of PC2 *vs.* PC1 in all 'groups of experiments A, B, and C show that CX- and CX+ remain indiscernible by the two first principal components PC1 and PC2 due to their strong similarity (even for very good and noise free spectra as in the experiments group C). This means that the difference between the two sublines is too small to overcome the biggest variations within the data, which are described mainly by PC1, but are non-specific to the phenotypic variation under study. The distribution observed is however not necessarily random and may reflect among others, natural bigger fluctuations. The corresponding loading plots for the main component PC1 appear to be nearly the same trace as the Raman spectra shown in the previous section. It is worth mentioning that the analyzed data represent individual spectra scaled to the average absolute signal count per second. Therefore, the X-loadings reflect absolute fluctuations in the Raman spectra. Their close match with the shape of the mean Raman spectra discussed in the previous section indicates that all X-variables (Raman shifts) linearly and positively correlate with the variation described by PC1 (*i.e.*, with the same weight as in the raw spectra). In other words, Raman shifts with zero or weak Raman intensity also have zero or small X-loadings for PC1, and important variables are just all the Raman bands themselves. Therefore, the sample distribution along PC1 in the scatter plots simply describes the overall intensity fluctuation of all the main Raman bands in the spectra of the cells, and this of course is not specific to the cell-subline, but simply reflects point to point variations. However, as aforementioned, the discussed X-loadings represent differences within the data based on their magnitude of changes. In order to determine the relative variation of spectra from one another and therefore to clarify the molecular origin of the biggest variation described by PC1 (up to 82%), the data tables corresponding to all individual spectra that were normalized to the intensity of the $CH_2$ def. mode at 1450 cm−1 were used. For normalized individual spectra, the X-loadings for PC1 in the different groups A, B, and C have been plotted as inserts in Fig. 6.5 **Aj**, **Bj**, and **Cj**, respectively, which reveal that the most important variables accounting for the biggest relative fluctuations (*i.e.*, within the normalized datasets) are nearly exclusively represented by two broad features comprising a water band (the bump from 800 to 1150 $cm^{-1}$ is in part due to an internal baseline as usually seen in the Raman spectra of many cells/tissue as a result of band overlapping). This demonstrates that the data relatively varied with respect to a residual background, and explains why CX- and CX+ remained indiscernible with respect to the PC2 *vs.* PC1 scatter plots.

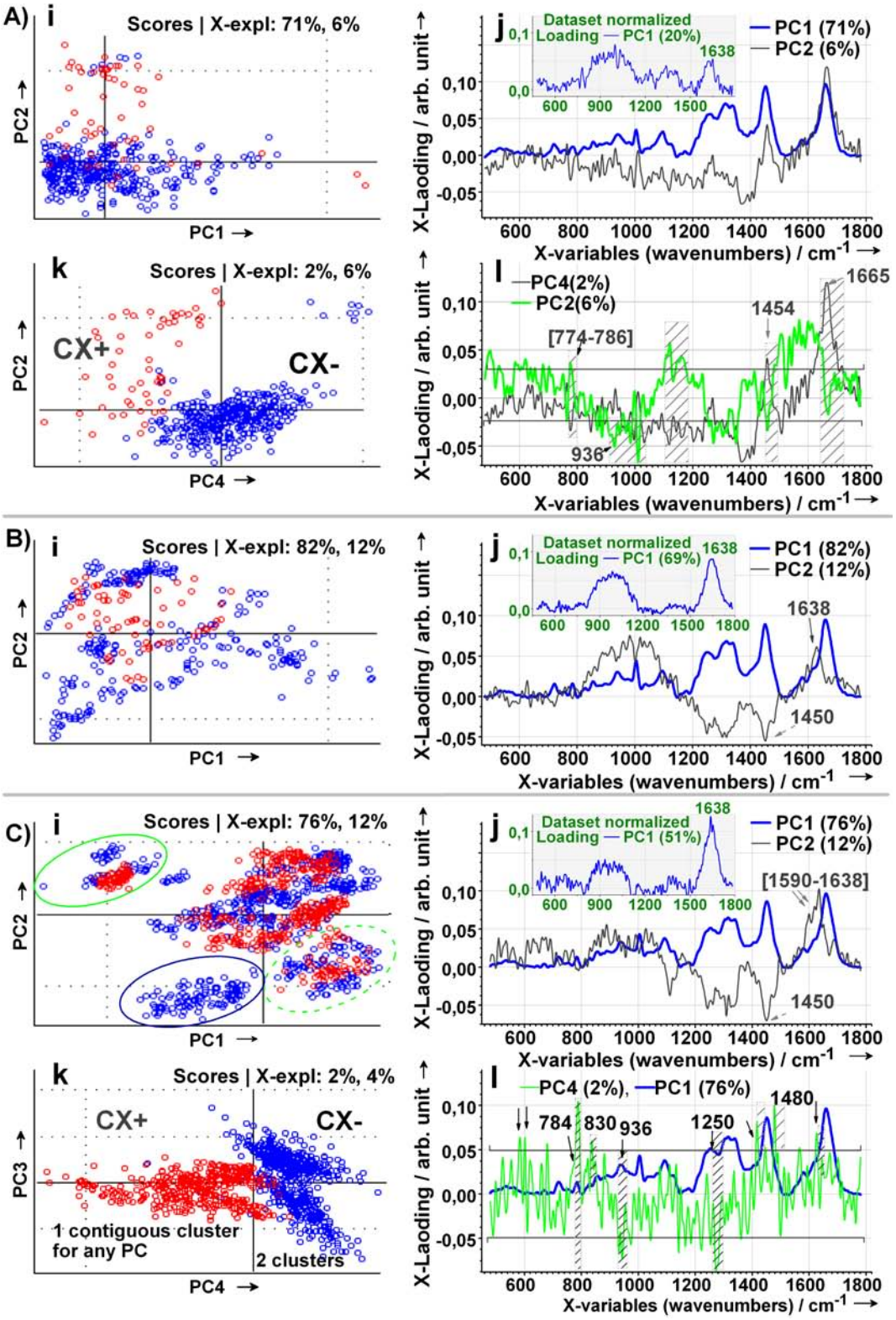


**Figure 6.5: PCA: Score plots (left) and X-loadings (right) of the CX-/CX+ Raman data for the groups of experiments A, B, and C, respectively**. First, PC1 and PC2 are plotted (upper panels **i** and **j**), followed by the components that best discriminate CX- from CX+ (lower panels **k** and **l**; discriminative plots for group B not shown). The inserts in **Aj Bj**, and **Cj** are X-loadings for PC1 with normalized datasets.

#### 6.3.4.2 The CX- *vs.* CX+ Discrimination Specifically Established

As mentioned, we will now look for the next PCs in the PCA models that best discriminate the two CX-/CX+ sublines, since the main components PC1 and PC2 described big but less specific variations between CX- and CX+: As depicted by the PCA scatter plots and corresponding X-loadings for the groups of experiments A and C displayed in Fig. 6.5 **Ak**,**l** and **Ck**,**l**, the discrimination (not so optimal for group A as for group C) can be achieved, despite the rather small phenotypic variations. The PC that best discriminated CX- from CX+ was PC4 mainly in group A (main PC in Fig. 6.5 **Ak**) and only PC4 in group C (see Fig. 6.5 **Ck**), accounting for 2% total explained variance only. These observations demonstrate that the phenotypic variation between the two tumor sublines was approx. 2% of the total sample variation. Using the statistical approach, these small variations that we have pointed out in the Raman spectra are clearly accessible even in the presence of rather prominent (PC1 X-expl. up to 82 %) other endogenous or exogenous variations. However, the discrimination in group A is less optimal, but better than in group B (data not shown), since only residual noise was left in group A, while high noise due background was present in group B.

In fact, for normalized data, the biggest but unspecific relative variations which are described by PC1 (see, *e.g.*, insert in Fig. 6.5 **Bj**) and are mostly associated with background signals, account for up to 69% total variation in group B. The PC2 *vs*. PC1 scatter plot in Fig. 6.5 **Bi** also shows PC2 background interferences, since the highest X-loadings for PC2 in group B include both the broad bump within [ 800 - 1200 $cm^{-1}$] and the broad peak around 1638 $cm^{-1}$. Hence data points with high positive or negative PC2 scores in Fig. 6.5 **Bj** were heavily background affected (*i.e.*, nearly half of the data in group B). The presence of noise, mainly in the dataset for group B, insured that all possible variations due to the background were present, and as just discussed above, we have carefully considered this situation in order to delineate unspecific spectral variations and to better judge the spectral quality overall, even in group C. As described above, systematically disregarding most of the noisiest data from the analysis did lead to a discrimination between CX- and CX- as shown for group A in Fig. 6.5 **Ai,k**. Doing the same for group B led to just a few final good spectra (~ 50 only for each subline; see also the above discussion about PC2) since the starting total number of spectra in this group was much smaller (only 320), and group B is not shown any longer. Despite the lower spectral quality in group A as compared to group C, the corresponding loadings show that important X-variables (wavenumbers) for the separation include, among others, some of the Raman fingerprints discussed earlier

(hatched variable intervals in the loading plots in Fig. 6.5 **Al** bounded by the horizontal lines at ~ 50% of the maximum loading value, on the PC4 and PC2 loading traces).

In group C, a total of about 1106 individual spectra were recorded. As was mentioned in the experimental section, since there was a long time gap between both groups of experiments A and B and group C, we could look at the data in groups A and B to realize that extended mapping acquisition with too many points contained very noisy spectra. Hence, in group C, more care was taken in a sense that, for all 1106 spectra, a big number of large, but separated cell colonies were sequentially measured, while avoiding extended raster mapping acquisition. These spectra were all free of noise, with only a very few spectra showing a minor residual background contribution, which grouped together within one cluster, delimited by the green and closed-up solid line in the scatter plot in Fig. 6.5 **Ci**. Interestingly, although additional intrinsic variations (not due to the embedding medium background signal) may exist among the CX-/CX+ data (mainly for CX-) and despite their very similar Raman spectra (see Fig 6.3, C), the CX- and CX+ sublines could be clearly discriminated. This is evidenced by the scatter plot in Fig. 6.5 **Ck**. The total phenotypic variation is completely described by only one principal component, PC4, representing a total of only 2% (or less) phenotypic-specific variance of the overall variation within the cells. The corresponding X-loading is plotted in Fig. 6.5 **Cl**. The PC1' X-loading shown by **Cj**, which strongly resembles the mean Raman spectrum itself as explained earlier, is again overlaid on top of PC4' X-loading in **Cl**. Therefore,the graph in Fig. 6.5 **Cl** helps to highlight the variable intervals of the most significant and more specific X-variables (Raman wavenumbers) for the phenotypic discrimination of the CX-/CX+ (hatched variable intervals bounded by the horizontal lines at ~ 50% of the maximum loading value). As can be clearly seen, the most significant variables contain all characteristic Raman fingerprints introduced in the previous section. This includes, in the order of specificity and significance, the bands or lines around 784 (RNA/DNA nucleotides pyrimidine ring breathing vibrations: U, C, T), ~ 1480 (shoulder band to the 1450 $cm^{-1}$ $CH_2$ def. mode, which may be assigned to the purine bases guanine and adenine in nucleic acids), 1260 (amide III vibration characteristic of proline-poor polar regions of collagen, or eventually overlapping contribution from the nucleobases C and T),[61] 1420 (unassigned for the moment), 939 (C-C str. in proline/valine, and an α-helical marker of proteins backbone: glycogen/collagen),[61,118] 1625 (C-C str. Tyr, Trp), 830 (DNA backbone marker for B-form DNA),[61,88,118] 1446 (a shoulder line to the lower frequency side of the $CH_2$ def. mode, usually indicative of protein extraction),[61] and 974 $cm^{-1}$ just to name the most important Raman fingerprints that account for more than 5% of the intrinsic phenotypic variation.

To sum up, using the multivariate analysis of the Raman data, three main results are confirmed as pointed out from the analysis of mean Raman spectra in the previous section. First of all, the CX- and CX+ sublines are successfully discriminated as evidenced in Fig. 6.5 **Cl**. As a matter of fact, this result may well prove useful in future for a directly label-free sorting the CX- and CX+ cell-sublines according to their component scores based on the small but phenotype-specific changes observed in their Raman fingerprints, without necessary understanding the complex structure of the Raman spectra (*e.g.* by a non expert). Secondly, the delineation of specific spectral changes from unspecific variations with their corresponding biomolecular basis provides insights into nucleic acid base interactions (see below) for the detailed understanding of the differential Hsp70 associated phenotypic variation between CX- and CX+. Finally, the delineation of other potential changes is indicative of the overall phenotypic state monitoring potential with Raman spectroscopy.

## 6.3.5 Discussion of Overall Phenotypic Monitoring – Insights into Biochemical Mechanisms and Relevance of the Label-Free Raman Cell-Subline Discrimination

### 6.3.5.1 Emphasis on the Nucleobase Specific Changes

As also described in previous studies,[164–167,191,192] for the characterization of the Hsp70-specific phenotypic variation and the sorting of the CX- and CX+ sublines from the original CX2 according to their Hsp70 membrane expression profiles (see Fig. 6.2), the very efficient and standard indirect immunofluorescence technique combined with FACScan analysis is usually applied. This requires the use of fluorescing labels, involving detailed flow cytometry assays. In some cases, fixation of the cells might also be necessary. Interestingly, as demonstrated by the Raman spectra presented and supported by their component analysis, the capability of Raman spectroscopy to discriminate the very similar CX- and CX+ sublines within the autologous CX2 tumor system may well prove useful in future for a label-free Raman cell sorting. Recent reports have evidenced the introduction of variants of the Raman technique in flow cytometry.[55,199] Differential Hsp70 expression is the unambiguously clear difference between the sublines CX- and CX+ as discussed in the introductory part. Therefore, the Raman bands and associated changes, which are found in the present work to be characteristically significant and specific for the noninvasive discrimination between CX- and CX+ sublines, represent the Raman signatures of the phenotypic variation associated with biochemical events leading to the differential Hsp70 expression patterns of the colon carcinoma sublines CX- and CX+. The significance of the

most interesting of these Raman signatures is further discussed in the following.

First of all, as pointed out, it is possible for a nonexpert to use the Raman technique for noninvasive discrimination of the CX-/CX+ sublines based on component scores without necessarily understanding the Raman spectra themselves. Actually, more insightful biomolecular information can be gained by a detailed analysis of the molecular basis of the observed changes in the Raman spectra, as demonstrated by the multivariate analysis test. As evidenced by the X-loadings in Fig. 6.5 **Cl**, the most significant and discrimination-specific Raman spectroscopic changes involve the 784 $cm^{-1}$ band, which is assigned to the pyrimidine ring breathing vibrations of the nucleic acids (DNA and RNA) nucleotides (C, U, T). This observation demonstrates that the phenotypic variation between CX- and CX+ is accompanied by specific changes or interactions in DNA/RNA nucleotides and suggests that eventual transcription deregulations may participate as precursor onsets of different transport mechanisms leading to differential Hsp70 cell surface expression patterns. It is worth mentioning again that, via a number of transport mechanisms, the normally cytoplasmically localized Hsp70 is expressed by tumor cells at the cellular membrane where it is combined with the lipid raft component Gb3.[163,164] The differential CX-/CX+ Hsp70 expression patterns have been attributed to differences in transport mechanisms of Hsp70 not yet fully understood or described.[164–167,191,192] Noteworthy, as mentioned in the introduction, classical biochemical methods have established that, the nucleotides cycling activity of the Hsp70, which involves nucleotide exchange is a characteristic property of the Hsp70 chaperone. More importantly, the participation of Hsp70 in transcription regulation involving DNA binding/replication of Hsp70-specific gene (HSE: –GAAG–) and mRNA regulation has been demonstrated.[166,170–182] This correlates with the fact that we see nucleobase-specific changes. Moreover, from the spectroscopic viewpoint, the physical basis of the well known Raman hypochromism[202] of the pyrimidine ring vibration at 784 $cm^{-1}$ is pyrimidine ring interaction upon base stacking:[204,205] The intensity of this band decreases with increased base stacking or equivalently, it increases with base destacking. Base stacking (C, T, A, U) provides the basis for thermal stability of nucleic acids. As exhaustively described in previous studies, base destacking in nucleic acids (DNA, RNA, packed DNA within chromosome or within cells)[61] but also in synthetic oligonucleotides occurs with elevated temperature.[202–206] Alternatively, in the case of DNA, base destacking also occurs when the DNA molecule binds to a protein or enzyme.[201] Therefore, besides the fact that the 784 $cm^{-1}$ band is found in the present work to be the most significant and specific for discriminating CX- from CX+, the Raman hypochromism observed around this band is indicative of changes in pyrimidine bases stacking. In DNA olygomers, base

destacking upon temperature increase has however been shown to be reversible (upon cooling) within a wide temperature range.[202,206] The CX- and CX+ sublines resulting from heat shock treatment of the original line CX2 maintain a stable profile in culture, even after several passages as mentioned in the introduction. Therefore, the suggested changes in base stacking are irreversible and are suspected to arise upon specific binding interactions (DNA/RNA/protein, etc.), which are however initiated or activated only upon heat shock treatment of the original CX2 cells that leads to their expansion into the sublines CX- and CX+. This explanation, which is based on the changes in base stacking upon DNA/RNA/protein binding interactions, is consistent with the reported Hsp70 nucleotide cycling capability[181] and the established Hsp70 transcriptional regulation involving DNA binding and mRNA regulation,[166,170–182] as just mentioned above. This strongly suggests that different transport mechanisms leading to differential Hsp70 expression and accordingly the expansion of the original CX2 line into the CX-/CX+ sublines upon heat shock treatment may, at least in part, be caused by disruption during the Hsp70 transcription regulation process, what could be termed as transcription deregulation.

Furthermore, with respect to their tumorigenic makeup, CX- and CX+ are associated to the same tumor-specific lipid marker (Gb3), with Hsp70 being associated with Gb3 or other eventual lipid partners at the cell surface within lipid rafts.[163,164] Therefore, the changes observed in the protein bands (polar regions of collagen, protein C-H str. and protein amide I and amide III secondary structures to a minor extent: eventual overlapping pyrimidine base vibrations in the amide III region, due to strong DNA contributions to the spectra) may support the assumption that tumor-specific lipid markers interact differently with key protein components, such as the heat shock protein family through different reaction pathways. Changes in lipid markers are then translated into changes in important protein components that play a key role in cellular functions, such as the cell growth regulation. However, unlike the clearly distinguishable pyrimidine ring mode around 784 $cm^{-1}$, it is important to note that nucleobase contributions, sensitive to bases stacking and also base pairing interactions, overlap with the strong protein contributions in the region from $\sim$ 1200 to 1700 $cm^{-1}$. Assignment of small molecular changes in this region is therefore not unequivocal. Especially pyrimidine base contributions that also exhibit Raman hypochromic effects are also expected within [1225-1250 $cm^{-1}$] (overlap with amide III).[61] Nonetheless, purine bases show contributions around 1480 $cm^{-1}$ (G, A) and 1580 $cm^{-1}$ (A).[61,119] As evidenced by the loading plot in Fig. 6.5 **Cl**,the changes in the 1480 $cm^{-1}$ shoulder band (G, A) are also specific to some extent (actually second most specific signatures), and are indicative of nucleobase interactions (*e.g.* basepairing) that can also arise from binding

interactions (DNA/RNA/protein etc.).

Finally, it is important to note that the information contained in the Raman spectra is not restricted to a specific marker molecule. The changes discussed above are not necessarily characteristic of the Raman spectrum of Hsp70 (Raman is too weak to detect a single protein on the cell surface), but describe the overall cell biochemical basis of the Hsp70-specific phenotypic difference of the CX- and CX+ sublines as well as eventual exogenous or other endogenous variations. As an example, we have carefully investigated the behavior of the Raman fingerprints represented by the ratio termed $R_1 = I_{1660}/I_{1450}$ (intensity ratio of the protein amide I mode to the $CH_2$ def mode). Changes near the amide I band region may in part be attributed to changes in nucleic acid base C=O vibrations sensitive to basepairing interactions,[61,203] but only to a rather minor extent in this region. In fact, unlike isolated bases or nucleotides, the C=O contribution in the Raman spectra of cellular DNA/RNA in this region is rather weak compared to the protein amide I. As reported in our work in chapter 4, the ratio $R_1$ can be seriously affected by a tumorigenic transformation (*i.e.* from non-cancerous to cancerous state), but in the present work, we are not differentiating a healthy cell from a cancerous one. However, a linear variation in $R_1$ may also be correlated with the degree of tumorigenicity, since a consistent decrease in $R_1$ could be observed as a function of the passage number of the cells that differ by $\sim 17$, in our study in chapter 4 (see also ref. 90). As already mentioned, the present experiments were spread over a long period of time during which the cells were regularly split and the passage number of the CX-/CX+ increased for every cell splitting by $\sim 1$ (from 0 to 17). It should be noted that the passage number of the cells had increased by 17 for group C, while it was comparable for the groups B and A (10 and 7), but the difference with group C is only 7-10, and we do not expect this to play a big role. The inspection of the normalized mean Raman spectra in Fig. 6.3 and the $R_1$ ratio plotted in Fig. 6.4 reveals that the ratio $R_1$ did not decrease linearly. On average, it practically remained constant throughout the groups of experiments, from group A to group C (*i.e.* after 17 splittings). This does not support any change in the tumorigenicity degree for both CX- and CX+ tumor sublines in culture after 17 passages only. The protein C-H str. ratio $R_2$ ($I_{2935}/I_{1450}$: intensity ratio of the protein C-H str. mode to the $CH_2$ def. mode) plotted in Fig. 6.4 did not change throughout the experiments either, and agrees with the behavior of the amide I. Moreover, multivariate analysis results can give more detailed information. Regarding the biomolecular information carried by PC2, it appears that PC2 provides some hints about background interference, but also contains insights about the variation in $R_1$. This can be seen in the X-loadings for PC2, showing that the variables accounting the sample distribution along PC2 (in groups A, B, and C)

include, besides some broad variable range (within [900 - 1200 cm 1] only in group B), the peaks at 1450 $cm^{-1}$ ($CH_2$ def.) and 1638 $cm^{-1}$ (water band close to the amide I). Therefore, the data cluster with small negative PC2 scores (*i.e.* cluster marked by the green and closed-up dashed line in the scatter plot in Fig. 6.5 **Ci**) contained spectra data exhibiting a moderate decrease in the $R_1$ ratio. This suggests that, small changes in $R_1$ might still be correlated with some intrinsic variation (cell's water contribution to the spectral), but this was not statistically significant (*i.e.*, these minor fluctuations appeared only in a very limited number of cells). However, the cluster with high negative PC2 scores (*e.g.*, marked by the blue and closed-up dotted line in the scatter plot in Fig. 6.5 **Ci**) contained data that actually were qualitatively good spectra, but exhibited a clear $R_1$ deviation (*i.e.* $R_1$ becoming less than unity) and which, therefore, were previously left out of the sets of averaged spectra as mentioned earlier. This deviation, as evidenced by PC2's loadings in Fig. 6.5 **Cl** (high loading for water band), was caused by the background correction that relatively overestimated the water contribution next to the amide I band in these spectra leading to the reduction of the corrected signal intensity at that position. Finally, other endogenous changes might still exist within the data, as illustrated by the discriminative scatter plot PC3 *vs.* PC4 in Fig. 6.5 **Ck**. It can be seen that, unlike the CX+, the CX- form two clusters, with comparable numbers of data points, and which are not correlated to the $R_1$ behavior.

The key changes observed between CX- and CX+ pave the way to more exhaustive biological studies. Especially, regarding the actual biochemical nature of the changes associated with DNA/RNA nucleobases, intracellular mechanisms affecting base cycling, base stacking, and probably also base pairing may be among precursor mechanisms at the onset of Hsp70 differential transport pathways, what brings the motivation for further elaborate biological studies. The present work represents an illustration in the case of the autologous CX2 tumor system. For realistic Raman label-free phenotypic cell sorting in a near future, more studies in other autologous cellular systems should be conducted and simpler algorithm schemes for the conversion of the Raman spectra into readable scores need to be developed.

A recent Raman study of metastasis of isogenic tumor cells also points to rather interesting prospects with Raman spectroscopy for interrogating or discriminating cell-sublines in general.[207]

## 6.4 Conclusions

The CX-/CX+ sublines are equal with respect to most of their cell surface expression patterns except their phenotypic variation in Hsp70 expression, making the present Raman investigation a rather challenging task. Firstly, their Hsp70 associated phenotype was characterized using the immunofluorescence technique combined with FACScan analysis ("Fluorescence Activated Cell Sorting"). 49% of the Hsp70 expressing CX2 cells were FACS-sorted into the low CX- (20%) and high CX+ (78.2%) Hsp70 positive sublines. Secondly, we have demonstrated the capability of Raman spectroscopy combined with statistical multivariate data evaluation techniques (principal component and cluster analysis) to discriminatively characterize the phenotypic variation between CX- and CX+. Based on the rather small spectroscopic signatures associated with Hsp70 specific phenotypic changes between CX- and CX+ (only 2% of the total variation within the cells), a differentiation could be achieved. This may be useful for label-free Raman cell-sorting in the future. The 2% of the spectral variations specific for the phenotypic variation associated with the differential Hsp70 cell surface expression patterns of the CX-/CX+ cells had to compete with up to 94% of the more prominent natural variations in the cells. These prominent variations represent both exogenous eventual other intrinsic variations. The strong similarity between CX- and CX+ was reflected by mean Raman spectra showing small but specific differences. This was confirmed by multivariate analysis showing that CX- and CX+ remained indiscernible by the two first principal components (PC1 and PC2). These PCs mainly described the natural fluctuations within the cells (up to 94%). For the discrimination, other PCs were screened to find those that best showed a separation of the cell-sublines. It has been shown for very good quality Raman spectra, that this discrimination can be achieved with only one PC, based on component scores. This implies that the foreseen label-free Raman cell-sorting can be automated via simpler algorithms.

Reproducible Raman signatures of Hsp70-specific phenotypic variation between CX- and CX+ have been proposed. The most significant ones involve essentially changes in ring breathing vibrations of DNA/RNA nucleotides sensitive to base destacking (pyrimidine bases exhibiting the so-called Raman hypochromism). In general, changes observed in protein bands of the protein-dominated Raman spectra of the CX-/CX+ sublines associated with a common tumor-specific lipid marker may support the assumption that lipid markers interact with key signaling proteins. Proteins, such as the Hsp70 family in the present case are critical for tumor progression. It is very interesting, that the changes in the DNA/RNA pyrimidine ring modes, due to base destacking indicative of DNA/RAN/protein

binding interactions, are found to be the most relevant and specific for the Hsp70 associated phenotypic variation between the CX- and CX+ sublines: This strongly suggests that different precursor transcription mechanisms may be among key biological events at the onset of the different transport pathways leading to the CX-/CX+ cellular membrane differential Hsp70 expression patterns.

Finally, besides demonstrating the potential of Raman spectroscopy for noninvasive and nondestructive monitoring of the Hsp70-associated phenotypic variation between CX- and CX+, we have also shown that, via careful and systematic data analysis, intrinsic variations can be resolved and delineated from prominent but unspecific other endogenous or exogenous variations.

To our knowledge, this work represents the first application of Raman spectroscopy for the characterization of the chaperone Hsp70 associated phenotypic variation within the autologous CX2 tumor system of very similar sublines. DNA/RNA nucleobase specific insights into the Hsp70-associated phenotypic variation in CX-/CX+ have been obtained and encourage further research. These results demonstrate Raman spectroscopy as a more versatile tool for the noninvasive and nondestructive characterization of tumor specific phenotypic variations in particular, and for the monitoring of the overall and detailed tumorigenicity steps at a biomolecular level in general.

## 6.5 Supporting Spectral Analysis Information

### Spectral Analysis, Background Correction, and Multivariate Analysis

Earlier in chapter 4, section 4.2.3 “Spectra Correction and Data Analysis”, we have demonstrated that the processing of the Raman spectra is a crucial step that requires great care and also experience in order to correctly extract reliable data.[90] Since the raw spectra without correction cannot be easily exploited in some cases, in the following we give a detailed description of the procedures applied making clear that simple automated background removal software etc. are definitely not sufficient for the treatment of such rather complex spectra.

Pre-processing of the Raman data in the present work consisted of the smoothing, scaling, and correction of the spectra using the LabSpec software tools. The spectra were 5 times smoothed with a 2-degree 9-size Savitsky-Golay algorithm. Because the Raman spectra were recorded through the embedding medium, they were in many cases composite spectra

that needed proper correction, which can be systematically and more accurately done via a correct estimation of the composite background contribution at those wavenumber positions where the samples show no overlapping Raman bands, as demonstrated earlier in chapter 4 (see also ref. 90). The cells formed colonies on the substrates. The used $CaF_2$ glass only had a featureless contribution in the fingerprint regions, which simplified the analysis. However the overall background signal (see light gray traces in Fig. 6.6) showed in the fingerprint region [450-1780 $cm^{-1}$] for example two broad features extending from 1444 to 1780 $cm^{-1}$ due to the culture medium with a non negligible water contribution overlapping in this region with the rather rich Raman spectral features from the cells. Since the cell culture medium did not show any resolved feature separated from the Raman signal of the cells, the removal of the composite background contribution was thoroughly and carefully assessed.

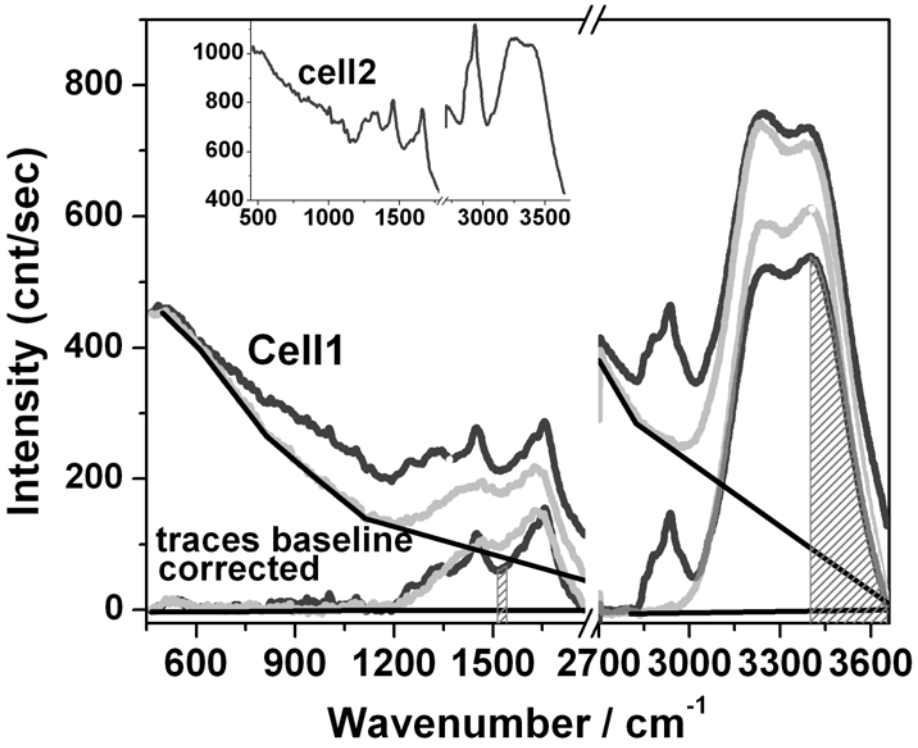


**Figure 6.6: Illustration of spectral correction in the fingerprint regions**: Note in [450 - 1780 $cm^{-1}$] and [2700 - 3650 $cm^{-1}$], the composite background (light grey) and a background-affected cell signal (Cell1: dark grey), both baseline-corrected (spline fit in black). The insert (Cell2) is a cell signal nearly not affected by the background signal

For an optimum correction of the spectra a careful inspection of a significant number of Raman spectra from the cells (especially when measuring living cells) was necessary in order to find general trends before a decision about the appropriate correction procedure

could be made. In the present case, three important observations were made: (i) apart from the broad region [1444 - 1780 $cm^{-1}$], the composite background signal was completely featureless anywhere else across the first fingerprint region and could simply be flattened (see light gray traces in Fig. 6.6); (ii) only an internal background (*e.g.* due to minimal fluorescence) is present between the $CH_2$ deformation band region and the amide I band region, in particular around 1525 $cm^{-1}$; (iii) the composite background signal showed in the second fingerprint region [2700-3650 $cm^{-1}$] only a strong and broad band around 3400 $cm^{-1}$, which however cannot be distinguished from a similar contribution from the cells because it is almost exclusively due to the strong water scattering at this position (see light gray traces in Fig. 6.6, for the second fingerprint region).
Therefore, as illustrated in Fig. 6.6, the composite cell spectra (*e.g.* gray trace labeled Cell1 in Fig. 6.6) and background (light gray trace in Fig. 6.6) signals were first baseline corrected with a non-linear first-order spline fit with 8 fitting nodes at 477, 605, 692, 802, 865, 900, 1144, and 1780 $cm^{-1}$ in the first fingerprint region (black trace in Fig. 6.6) so that the spectral region before the broad features of a neat correction background signal became flat. Then, the neat correction background contribution in the signal was better estimated by the area ratio around 1525 $cm^{-1}$ (within [1513- 1540 $cm^{-1}$]) and subtracted. In the second fingerprint region [2700 - 3650 $cm^{-1}$], all spectra including the composite background signal were also first baseline corrected (non-linear first-order spline fit) with 3 fitting nodes at 2700, 2820, and 3650 $cm^{-1}$ (black trace in Fig. 6.6). Then, the cells spectra in this region could only be corrected by removing the total water contribution estimated by the area ratio in the interval [3400 - 3650 $cm^{-1}$]. After the identification of the appropriate procedure and spectral features suitable for the correction such that the intrinsic Raman fingerprint information from the cells could be retained, following the above described baseline subtraction spectral correction automatically performed using built-in correction tools of the LabSpec software.

Moreover, we have tried to approach spectral correction on a rather general basis, *i.e.* from poor and highly background affected spectra to rather good and minimally background affected spectra. For example, the insert labeled “Cell2” in Fig. 6.6 displays a Raman spectrum nearly unaffected by the composite background signal, in contrast to the spectrum labeled “Cell1” showing a notably affected signal. Spectra recorded from smaller cell colonies were superimposed to the composite background signal. Strongly affected spectra were those recorded from very small cell colonies or isolated single cells (rare in this case) on the substrates or were often the result of gradual defocusing during longtime mapping acquisition. This was also purposely done to find out what poor, very poor, or

obviously distorted spectra looked like. In general, spectra recorded from the more abundant bigger and therefore dense cells colonies were only minimally to nearly not at all affected by the composite background signal. Finally, normalized versions of all scaled and corrected Raman data were formed, and all corrected Raman data were converted into appropriate formats for further data analysis with Origin (Origin 2007, Origin Lab cooperation) and for multivariate analyses (The Unscrambler 9.7, CAMO ASA).

Raman experiments corresponding to the repeated cell splitting events were regrouped according to the order cells were split as shown in Table 6.1. Spectral data from each experiments group labeled A, B, C in Table 6.1 were separately analyzed for a discriminative judgment of the spectral variation and for the phenotypic spectral characterization of the CX- and CX+ tumor sublines. Intrinsic biomolecular changes accompanying phenotypic variation respectively different biomolecular interactions between CX- and CX+ cell sublines were assessed by the comparison of average spectra for both cell sublines. The average spectrum for each group of experiments was defined as the overall average of all data (except for obviously distorted spectra or very poor spectra). The implementation of the combined clustering and principal component analysis (PCA) facilitated reliable spectral sorting for the rejection of bad data and spectra grouping into sets of similar data.

As described in chapter 3, section “Principal Component Analysis (PCA)”, principal component analysis was performed. The original dataset contains preprocessed and corrected Raman data with X-variables and Y-variables, defined by the pixels number of the CCD detector (wavenumbers) for each of the detectors used, and the corresponding Raman intensities of the “Y” measured sample spectra. PCA was combined with non-assisted Kendall’s and Euclidean clustering to highlight PCA grouping. This multivariate analysis helped to evaluate how well the CX- and CX+ sublines could be specifically sorted according to their spectral variation, and still be ultimately differentiated, even when the *in situ* phenotypic changes had been overlaid by further unspecific, but predominant molecular changes (inherent to the living and changing cell, or just due fluctuation in physiological conditions since the measurements were done at room temperature).

# 7. Noninvasive Raman Monitoring of Drug Response

## Summary

In this chapter, micro-Raman spectroscopy (MRS) was used to evaluate the effect of indole-3-carbinol (I3C) on acute alcoholic liver injury *in vivo*. *In vivo* Raman interrogation of tissue sections yielded distinct spectra that can be used to distinguish alcoholic liver injury as well as ethanol-induced liver fibrosis from the normal state. Using the Raman spectroscopic technique in conjunction with biomedical assay, sixteen mice with liver diseases including acute liver injury and chronic liver fibrosis, and eight mice with normal liver tissues, and eight remedial mice were studied. As a result of liver injury/fibrosis, the biochemical changes in mouse liver tissue such as the loss of reduced glutathione (GSH) and the increase of collagen (alpha-helix protein) were observed by MRS. Exploiting the intensity ratio of two Raman peaks ($I_{1450}/I_{666}$) in combination with statistical analysis of the entire Raman spectrum offered the capability for classifying liver tissues with different pathological features. Therefore, Raman spectroscopy is an important versatile tool for a nondestructive *in vivo* monitoring of the effect of drug treatment on liver disease, which potentially reduces the time-consuming clinical trials

The results presented in this chapter have been published in the following article[208] and in final form at http://onlinelibrary.wiley.com/doi/10.1002/jrs.2163/abstract:

Shen, A., Zhang, B., Ping, J., Xie, W., Donfack, P., Baek, S.-J., Zhou, X., Wang, H., Materny, A. and Hu, J. (2009), In vivo study on the protection of indole-3-carbinol (I3C) against the mouse acute alcoholic liver injury by micro-Raman spectroscopy. Journal of Raman Spectroscopy, 40: 550555. doi: 10.1002/jrs.2163

## 7.1 Introduction

Liver fibrosis is among medical problems with significant morbidity and mortality. The primary causes of liver fibrosis worldwide have been associated with hepatitis viral infections, including hepatitis B and hepatitis C. However, in many countries chronic ethanol consumption [alcohol liver disease (ALD)] is the leading cause.[209] If left untreated, fibrosis can progress to cirrhosis, an end stage complication of fibrosis, ultimately leading to liver failure and possible death. However, as has been demonstrated in the 1990s,[210] even advanced liver fibrosis is potentially reversible. Hence, besides continuous clinical trials, biopharmaceutical companies and researchers have been showing growing interest in developing antifibrotic programs. Noteworthy, the most efficient therapy for treating hepatic fibrosis to date relies on the use of medicine treatment.[211] Some drugs, such as reninangiotensin system blockers and antioxidants, have proven capable of reducing the accumulation of scar tissue in experimental models of chronic liver injury, although their efficacy has not been tested in humans. Clinical trials in humans are lacking because of the requirement for long follow-up studies and of the fact that liver biopsy, an invasive procedure, remains the standard method for assessing liver histology, disease activity, and liver fibrosis.[212] As shown in this chapter, the current effort to develop a reliable, simple, and nondestructive technique to rapidly assess liver fibrosis is expected to assist clinical trials and facilitate their design.

Indole-3-carbinol (I3C) is actually a nutritional supplement since it is found in high concentrations in Brassica family vegetables, including broccoli, cauliflower, Brussels sprouts, and cabbage. In this respect, I3C has attracted particular interest since many years as a promising preventive and treatment agent for breast and other types of cancers,[213] and may have a beneficial effect in the inhibition of liver disease. Preliminary studies have examined the efficacy of I3C in the protection against ethanol-induced hepatotoxicity and liver fibrosis on precision-cut liver slices[214,215] and cellular level,[216] respectively. In principle, standard biochemical assays are capable of identifying molecular changes associated with collagen, extracellular matrix (ECM) protein, etc. in the process of acute liver injury.[217] However, the application of these techniques in animal studies after intragastric administration of I3C did not show the expected results related to ethanol-induced liver injury, suggesting that other sensitive methods have to be employed for the investigation of the action of I3C.

Here, Raman spectroscopy is introduced as a fast and reliable method for the characterization of liver tissue. As already described in previous chapters (chapter 1 – 3), Raman spectra are depicted by plotting the intensity of the inelastically scattered photons as a function of the wavenumber shift. The Raman spectra reflect structural and electronic properties of molecules and their surroundings and can be considered to be "fingerprints" of the specific molecular species. This accounts for the wide spread biomedical applications of Raman spectroscopy. Most biologic molecules are Raman-active and their Raman spectra usually exhibit sharp spectral features that are characteristic for specific molecular structures and conformations of tissue,[218,219] thus providing more specific molecular information about a given tissue or disease state. In recent years, Raman techniques have been widely applied in the investigation of biomedical issues including quantitative histochemical analysis of human arteries,[220] disease diagnosis especially for cancer,[108,221] characterization of pterygium,[222] imaging of cells,[223] and analysis of the stratum corneum in human skin in relation to administration of therapeutic agents.[224] As for the 'hepatology', also the feasibility of confocal Raman spectroscopy (CRS) to monitor the molecular changes of hepatic stellate cells (HSCs) *in vitro* as well as *in vivo* activation.[225] In this work, we successfully developed a mouse model of ethanol-induced chronic liver fibrosis and acute alcoholic liver injury. For the present investigation, micro-Raman spectroscopy (MRS) was utilized to identifying spectral differences between normal mouse liver tissue and tissue affected by acute alcoholic liver injury and fibrosis *in vivo*. Comparing the Raman data with various pathological attributes, a tentative Raman criterion was established to sensitively distinguish liver damage from normal tissues. On this basis, we now have for the first time investigated the protection of the liver by I3C against acute alcoholic liver damage.We suggest MRS being a rapid and precise way to screen liver-protecting drugs.

## 7.2 Material, Methods, and Experimental Techniques

### 7.2.1 Animal Model and Tissue Specimen

The alcoholic acute liver injury model and ethanol-induced chronic liver fibrosis model animals employed Kunmin male mice weighing 18–22 g, which were purchased from the Experimental Center of Medical Scientific Academy of Hubei (China). Thirty-two mice were divided into four groups of eight: (1) normal control, (2) acute liver injury, (3) ethanol-induced chronic liver fibrosis, and (4) I3C treated on liver injury (40 mg/kg). Following acclimatization for 1 week after arrival, group (4) received intragastric administration of I3C, dissolved in olive oil, at doses of 40 mg/kg for 2 weeks. The acute liver injury model

control groups were intragastrically treated with olive oil; 50% ethanol (0.2 ml/10 g/day) was administered orally 1 h after the last dose of I3C. The ethanol-induced chronic liver fibrosis control mice were fed with 40% ethanol (0.2 ml/10 g/day) for 3 months. Normal control mice received a normal diet and free access to water. Mice were killed at the end of the $3^{rd}$ month and livers were excised. The right lobes of the livers were divided into two parts, one was fixed in 0.4 $mgl^{-1}$ paraformaldehyde solution, embedded in paraffin and then processed for light microscopy, and the other was snap-frozen in liquid nitrogen and stored at -80°C until use. Blood samples were obtained immediately before the mice were sacrificed.

### 7.2.2 Biochemical Assays of the Mouse Liver Tissue

Protein concentrations in liver were determined by the Lowry method using bovine serum albumin (BSA) as standard. The content of liver hydroxyproline was analyzed by standard spectrophotomeric methods using commercial test reagents. Hydroxyproline levels were analyzed separately for each liver, and the unit was microgram per gram liver weight. Glutathione S-Transferases (GST) activity in liver tissue was measured with 1-Chloro-2,4-dinitrobenzene (CDNB) as described by Ping *et al.*[226] In brief, the reaction of 1 mM CDNB with 1 mM glutathione (GSH) in the diluted human liver S-9 protein (1 mg) was monitored spectrophotometrically by recording the increase in absorbance at 340 nm. The final concentration of ethanol in the incubation mixture was 1%(v/v). A correction for the spontaneous reaction between GSH and CDNB in the absence of enzyme was made.
All the descriptions about animal models and corresponding biochemical assay results are listed in Table 7.1.

**Table 7.1:** Description of model animal and results of biochemical assays

| No. | Group | Total number of mice | Total number of spectra | Total protein[a] (g/L) | Hyp[a] (µg/g liver) | GST[a] (mmol/min mg) |
|---|---|---|---|---|---|---|
| 1 | Normal | 8 | 38 | 0.995 ± 0.093 | 89.30 ± 9 | 296.35 ± 33 |
| 2 | Injure | 8 | 42 | 1.121 ± 0.005** | | |
| 3 | Fibrosis | 8 | 45 | | 111.6 ± 18* | 231.77 ± 56** |
| 4 | Remedial | 8 | 42 | 0.691 ± 0.039*** | | |
| Total number | | 32 | 167 | | | |

[a] The results were expressed as mean ± SD.
* $P \leq 0.05$,
** $P \leq 0.01$ versus normal,
*** $P \leq 0.01$ versus injury.

### 7.2.3 Raman Experiment and Instrumentation

The automated Horiba Jobin Yvon Raman system (system HR800, Horiba Jobin Yvon, Villeneuve dAscq, France) described in "chapter 3, section 3.2.2: MicroRaman" was for the Raman measurement of the liver tissues in the present chapter. This system was optimized for maximum throughput, detection sensitivity, and fluorescence suppression. The built-in HeNe laser source with 13.6 mW power at 632.8 nm was used for excitation. After attenuation through prisms and filters, the power of the laser exposed on the samples was only about 1 mW, which makes it almost impossible for the laser to lead to degradation of the tissues. Spectra were measured from tissues with a 50x long-working-distance objective [numerical aperture (NA) 0.50, Olympus, Japan], and the signal was integrated for 4 x 60 s and measured over a spectral range of 600–1700 $cm^{-1}$ with respect to the excitation wavenumber. Of the two motorized gratings within the stigmatic spectrometer of the Raman system, the 600 grooves/mm grating was used to provide a spectral resolution of about 5 $cm^{-1}$ at an entrance slit width of 50 μm. The calibration of the wavenumber position and the instrumental response was performed using the silicon phonon line at 520 $cm^{-1}$. Cryosections (25 μm in thickness) were placed on a $CaF_2$ slides for Raman investigation. During the measurement, the liver tissue section was thawed to reach room temperature in air. From each mouse one to two tissue sections (two to three points per section) were selected and measured. In total, 167 Raman spectra (as shown in Table 7.1) were recorded and processed (for smoothing, baseline subtraction, and peak detection) by means of a simple background elimination method developed by our group.[227] The peak intensities of selected Raman lines were extracted from all spectra and exported automatically using a self-made program.

### 7.2.4 Principal Component & Logistic Regression Analysis

In the calibration stage, a total of 122 Raman spectra collected from 34 mice (except from the 'Fibrosis' group) formed a calibration set. The data in this set were analyzed using principal component analysis (PCA) to extract the principal components and their associated scores. The scores were then fed into a logistic regression (LR) algorithm to optimally differentiate the liver injury tissue from the normal and remedial ones.

## 7.3 Results and Discussion

### 7.3.1 Spectral Differences Among Raman Spectra of the Mouse Liver Tissues Including Normal, Injured, and Fibrotic Livers

The above-mentioned approach was applied to pre-processed Raman spectra of liver tissue. The background eliminated mean Raman spectra of normal, liver injury, and liver fibrosis tissues are shown in Fig. 7.1(A). From a visual inspection of the result, it is obvious that the background eliminated spectra preserved well defined Raman peaks in the 1700600 $cm^{-1}$ region. From these, height and position could easily be accessed, which were used to further assess the stage of liver disease.[228]

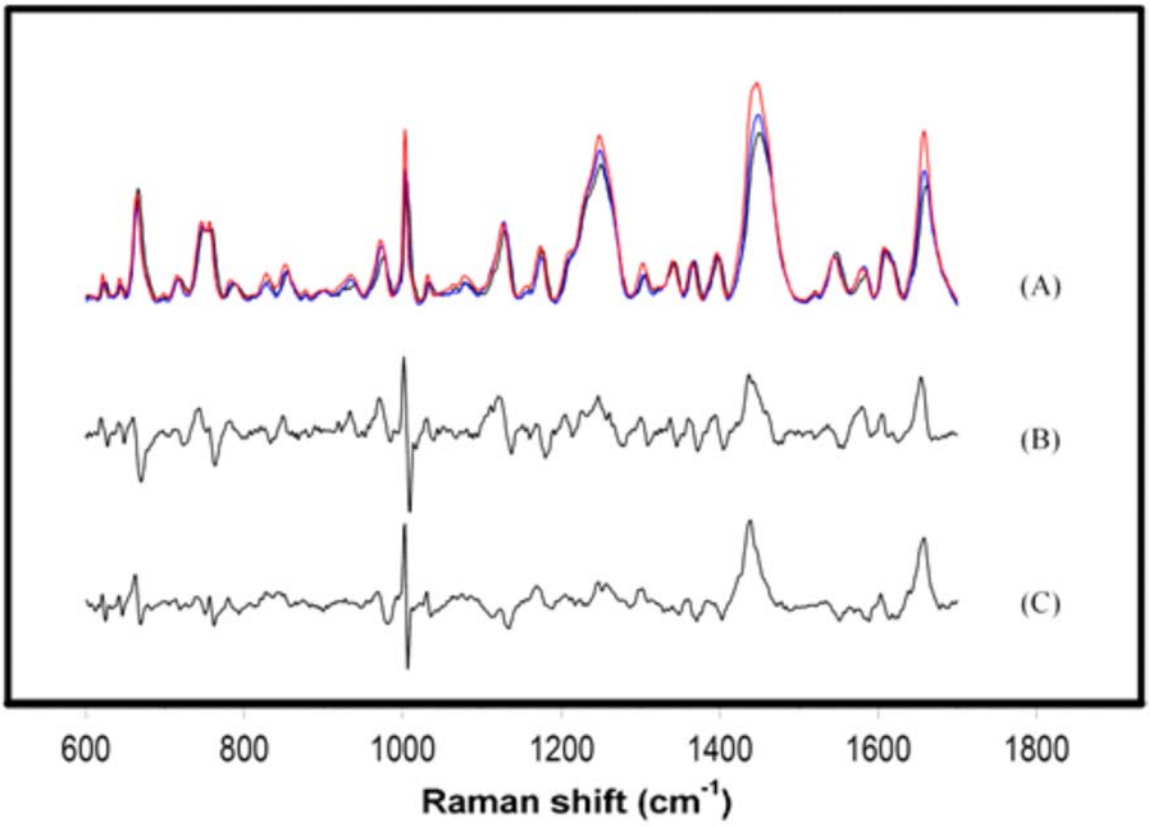


**Figure 7.1: Raman spectra of liver tissue after background elimination**. The mean Raman spectra of normal (black), liver injury (blue) and liver fibrosis (red) tissue after pre-processing are shown in panel (A). The difference between the mean Raman spectra of liver injury and normal tissue (injurynormal) and between liver fibrosis and normal tissue (fibrosisnormal) are displayed in panels (B) and (C), respectively.

From Fig. 7.1(A) it becomes obvious that Raman spectra of normal liver tissue are very similar to those of liver injury and liver fibrosis tissues. However, there are significant differences in the relative intensities of most bands. Primary Raman peaks at 666, 932, 938, 1005, 1033, 1083, 1123, 1170, 1248, 1303, 1340, 1450, 1546, 1579, and 1660 $cm^{-1}$ can

be consistently observed in all the tissues, with the strongest signals at 1005, 1248, 1450, and 1660 $cm^{-1}$. The normalized intensities of Raman peaks at 623, 644, 756, 853, 1004, 1033, 1083, 1303, 1248, and 1660 $cm^{-1}$ are greater for liver fibrosis tissue than that of normal tissue, even more than that of injury tissue, while for the Raman band at 666 $cm^{-1}$ an inverse behavior occurs. These normalized intensity differences can be viewed more clearly on the difference spectra between liver injury and normal tissue, and liver fibrosis and normal tissue in Fig. 7.1(B) and (C), respectively.

Mostly, the bands corresponded to vibrational modes of biomolecules, such as proteins, lipids, and nucleic acids, which may be altered in quantity with the extent of liver damage (Fig. 7.1(A)). To better understand the molecular basis for the observed Raman spectra of liver tissue, Table 7.2 lists the wavenumbers and tentative assignments in detail, according to literature data.[61,103,229,230] Thus, distinctive Raman features and intensity differences for liver fibrosis versus liver injury and normal liver tissue can reflect molecular and cellular changes associated with the aggravation of liver injury. From the difference spectra as shown in Fig. 7.1(B) and (C), some Raman bands at 1660, 1450, 1340, 1303, and 1248 $cm^{-1}$ typically assigned to vibrational modes of collagen molecules,[103] exhibited an obvious upward trend for their normalized intensity.

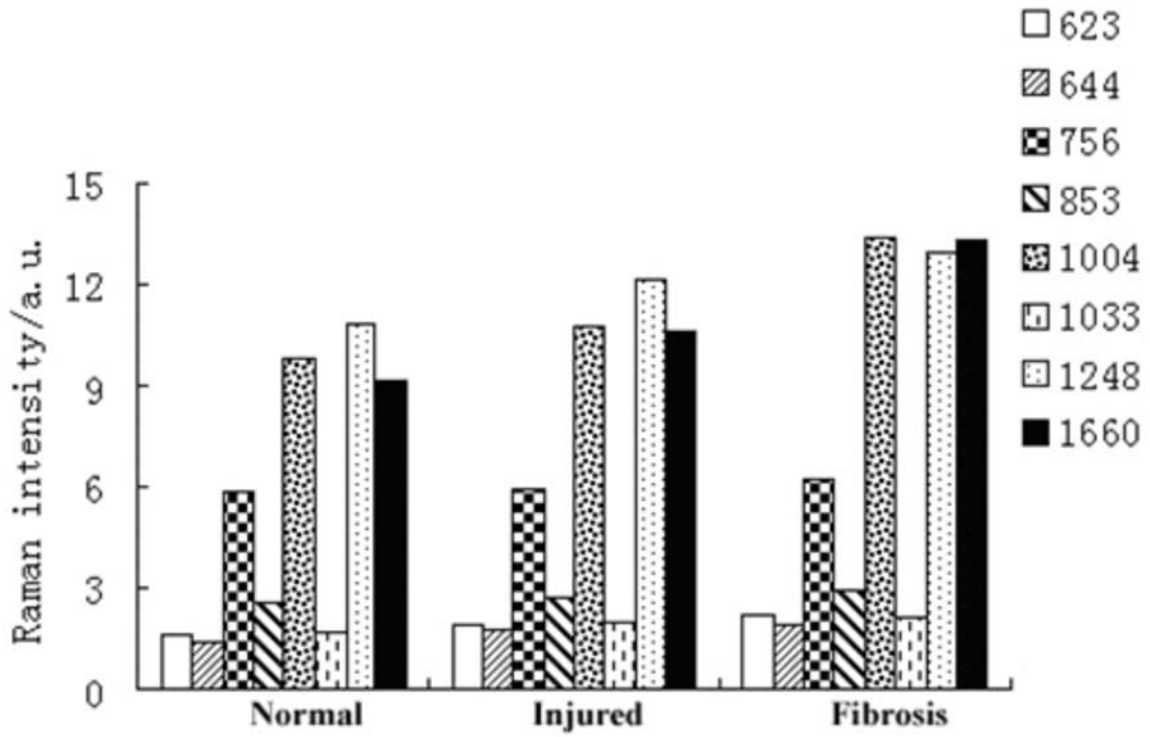


**Figure 7.2: Amplitudes of selected Raman peak intensities assigned to protein & amino acid vibrations in normal, injured, and fibrotic liver tissues**. The line positions are in $cm^{-1}$.

In Fig. 7.2, we have illustrated the changes in Raman peak intensities for some protein and

amino acid bands by displaying the intensities for normal, liver injury, and fibrosis material. The Raman spectrum of the normal tissue was weaker in intensity than that of the liver injury tissue and the intensity of the peaks increases with increasing degree of damage, liver fibrosis having the highest intensity, normal liver possessing the minimum, and acute liver injury lying in between (Fig. 7.1(A)). The increase in intensity of the $\nu$(C=O), $\delta(CH_2)$, and $\nu$(CN) peaks suggests changes in the proteins especial for collagen contents. Mahadevan-Jansen and Richards-Kortum[61] have summarized the features and interpretation of Raman spectra of proteins, DNA, and membrane in complex biological system. This review confirms these assignments and also points out that the protein secondary structure should mainly be described by an α-helix form. Actually, liver injury and also fibrosis can

**Table 7.2:** Peak positions and tentative assignments of major vibrational bands observed in the Raman spectra of normal, alcohol-injured, and fibrosis liver tissue

| Peak position ($cm^{-1}$) | Protein assignments | Lipid assignments | Others |
|---|---|---|---|
| 1660 vs | $\nu$(C=O) amide I, α-helix, collagen | | |
| 1610 m | Tryptophan | | |
| 1579 w | $\delta$(C=C) phenylalanine | | |
| 1546 m | $\nu$(C=C) tryptophan / $\nu$(C=C) porphyrin | | |
| 1450 vs | $\delta(CH_2)$, $\delta(CH_3)$, collagen | $\delta(CH_2)$ scissoring, phospholipids | |
| 1399 w | Hemoglobin | | |
| 1369 w | Unassigned | | |
| 1340 w | $CH_2/CH_3$ wagging collagen | | $CH_2$ $CH_3$ wagging nucleic acids |
| 1303 w | $\delta(CH_2)$ twisting, wagging collagen | $\delta(CH_2)$ twisting, wagging phospholipids | |
| 1248 vs | $\nu$(CN), $\delta$(NH) amide III, α-helix, collagen, trytophan | | |
| 1170 m | $\delta$(C-H), tyrosine | | |
| 1123 s | $\nu$(C-N), proteins | | |
| 1083 w | | $\nu$(C-C) or $\nu$(C-O), phospholipids | $PO_2^-$ nucleic acid skeleton |
| 1033 w, sh | $\delta$(C-H), phenylalanine | | |
| 1005 vs | C-C symmetric ring breathing, phenylalanine | | |
| 972 m | Unassigned | | |
| 938 w | C-C skeleton, proteins | | |
| 932 w | $\nu$(C-C), α-helix, praline, valine | | |
| 853 w | $\nu$(C-C), proline $\delta$(CCH) ring breathing, tyrosine | | Polysaccaride |
| 848 w | Trytophan | | |
| 784 w | $PO_2^-$ , cytosine, uracil, thymine | | |
| 716 w | Tyrosine/Adenine | | |
| 666 s | $\nu$(C-S), cysteine | | |
| 644 w | C-C, wagging tyrosine | | |
| 623 w | Adenine | | |

$\nu$: stretching mode; $\delta$: bending mode; v: very; s: strong; m: medium; w: weak; sh: shoulder.

be regarded as a wound-healing response to a variety of chronic/acute stimuli, *e.g.* alcohol. It is characterized by an excessive deposition of ECM proteins, in which collagen is included as a main component.[217] Additionally, our previous Raman investigations have also demonstrated that the major function of activated HSCs in liver injury induced by an other acute stimuli ($CCl_4$) was to secrete ECM containing fibril-forming collagen. Table 7.1 lists the content of hydroxyproline of different types of liver tissue, which could reflect the increase of collagen (hydroxyproline is only attributed to collagen) when the alcohol-induced liver fibrosis occurs. However, for alcoholic acute liver injury, there is no direct evidence to prove the increase of collagen here besides the total amount of protein. On the other hand, not all Raman peak intensities showed a consistent increase, for example the Raman band at 666 $cm^{-1}$, which can be assigned to the stretching vibration of the C-S bond of cysteine[229] (compare difference spectra given in Fig. 7.1(B) and (C)). This information from comparative Raman spectroscopy is very important for understanding the mechanism of acute liver injury. Generally, ethanol is largely dehydrogenated by alcohol dehydrogenase after its intake by the body, which would result in an obstruction of the tricarboxylic acid cycle and a decrease of fatty acid oxidation, and further results in a deposit of abundant lipids in hepatocytes. The Raman data point to the abnormality of the lipometabolism in the liver injury tissue (data not shown). Moreover, ethanol could activate oxygen molecules into oxygen derived free radicals, which induced lipid peroxidation of the liver membrane and decrease of reduced GSH.[231] It should be pointed out that the main amino acid molecule of GSH is cysteine, which is indeed reduced under alcoholic hepatic injury.

### 7.3.2 Monitoring the Effect of I3C Treatment on Acute Alcoholic Liver Injury

Simple, but effective diagnostic algorithms have been proposed on the basis of the empirical analysis of Raman spectra in terms of peak intensity or peak intensity ratio measurements and have been applied to a number of organ types. For example, the ratio of intensities at 1455 and 1655 $cm^{-1}$ has been used to classify tumor versus normal tissue in the brain, breast, colon, and cervix, since both bands are sensitive to histological abnormalities.[232] Considering the aforementioned spectral differences between normal and liver injury tissues, the intensity ratio between bands at 1450 and 666 $cm^{-1}$ ($I_{1450}/I_{666}$) was found to be a potential Raman criterion for assessing the histology of liver tissue, and as such can also be used to evaluate the effect of I3C treatment on acute alcoholic liver injury. Figure 7.3 displays the ratios ($I_{1450}/I_{666}$) for 122 Raman spectra of normal, liver injury, and I3C-remedial

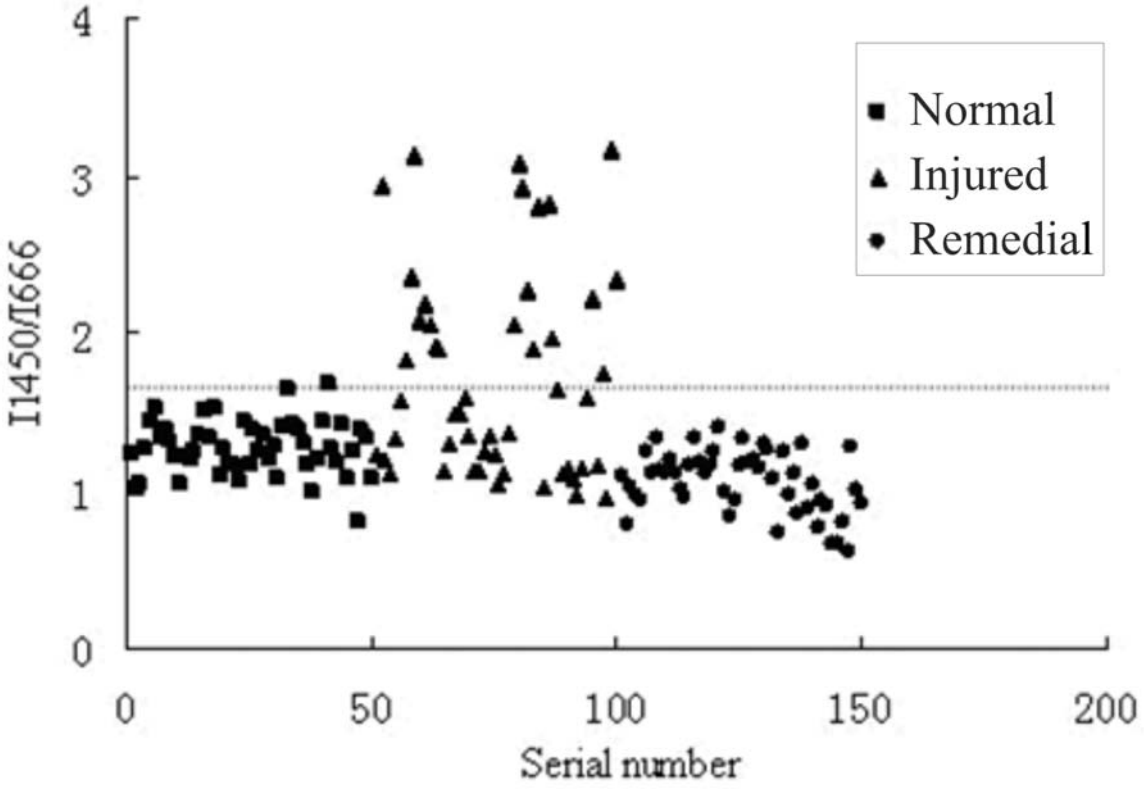


**Figure 7.3: Distribution of ratios between Raman peaks intensities at 1450 and 666 cm$^{-1}$ of normal, injured, and I3C-treated liver tissues**, taking serial number of spectra as abscissa.

tissues. As it becomes obvious from Fig. 7.3, the $I_{1450}/I_{666}$ values of normal liver tissue have a similar distribution as those obtained from the remedial group; nearly all are accumulated between 1 and 1.5. On the other hand, the injured group's values are dispersed over a larger range from 1 to 3.5. Thus, the ratio $I_{1450}/I_{666}$ can be considered to be a simple screening tool indicating possible acute liver injury. It can also be seen that I3C serves as a drug having perceptible efficacy reversing the alcoholic liver injury.
To analyze the effect of an I3C treatment on the injury model with an even higher reliability, the ratios of several Raman peaks can be used for data analysis. Figure 7.4 shows that the intensities of selected Raman peaks assigned to proteins show regular changes when going from "Normal" to "Remedial" groups, which is consistent with biochemical assay results as shown in Table 7.1.

In view of the wealth of information available in the Raman spectra and the biochemical complexity of liver lesions, a method of analysis that utilizes the entire Raman spectrum rather than only few peak height ratios is an optimum method to distinguish between normal and liver injury tissue.[108] Therefore, a multivariate statistical analysis (here PCA),

which utilized the entire spectrum and automatically determines the most diagnostically significant features (factors), should improve the efficiency of the tissue analysis and classification. For this, we have applied PCA and LR algorithms on the complete database. We find that the two-score combination PC1, PC2 gives the best differentiation between the three types of tissues (as shown in Fig. 7.5). Further studies and progress would help to achieve improvement and facilitate the perspective application in clinic routine.

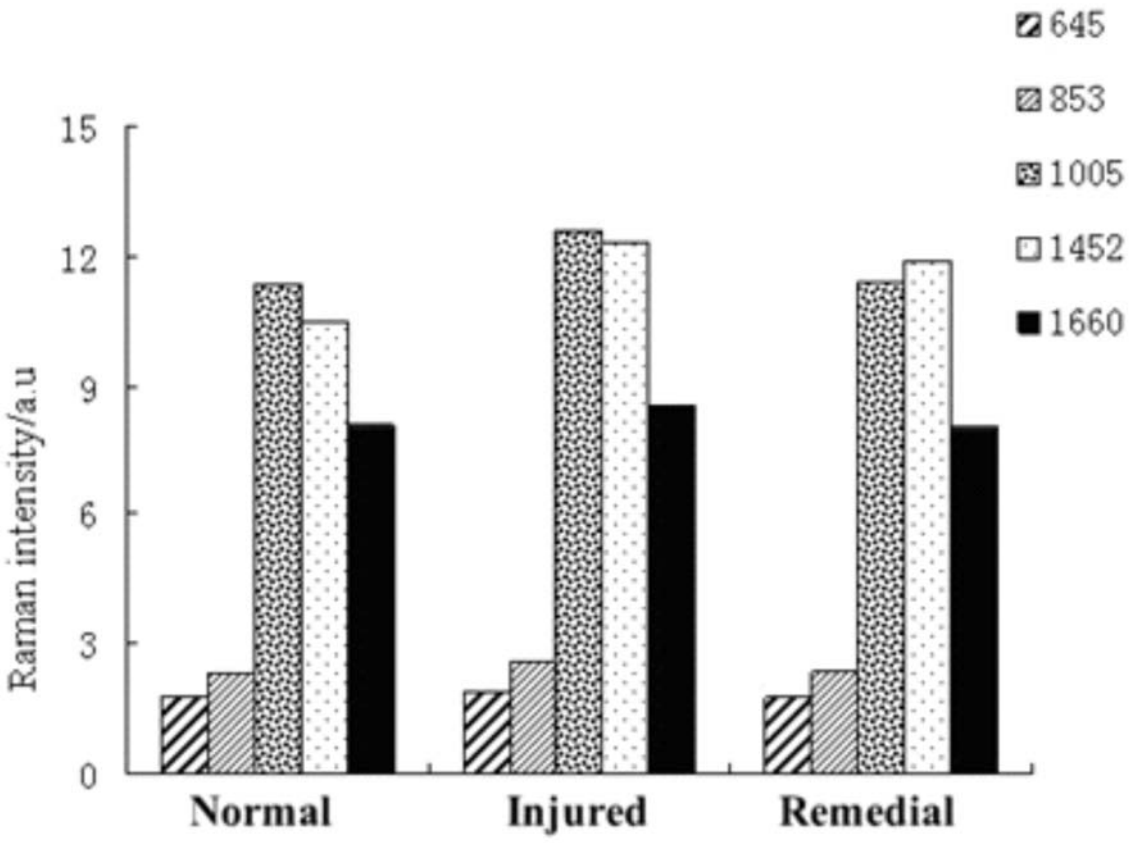


**Figure 7.4: Amplitudes of selected Raman peaks assigned to proteins from spectra of normal, liver injury, and remedial tissues**: (Line position in $cm^{-1}$).

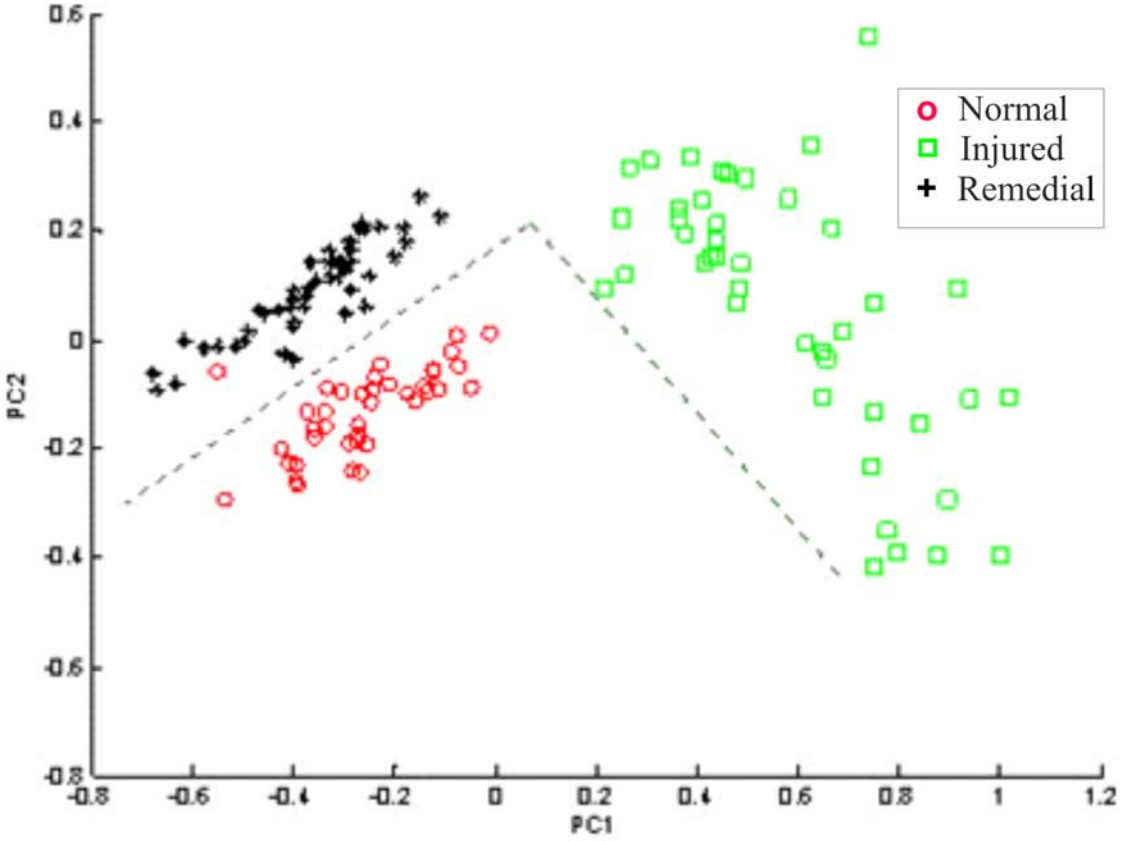


**Figure 7.5: PCA scatter plot for three types of tissue.**

## 7.4 Conclusions

The main objective of the work described in this chapter was to test the capability of micro-Raman spectroscopy (MRS) for evaluation the effect of drug response in the case of liver fibrosis. The results of the present study demonstrate that there are specific differences in Raman intensities for normal versus liver injury and fibrosis tissues, confirming a potential role of MRS in liver disease diagnosis. Until the time of this present work, none of the standard biochemical methods was capable of analyzing the action of I3C against acute alcoholic liver injury *in vivo*. We have demonstrated that Raman spectroscopy in conjunction with a careful peak analysis or even better with statistical analysis provides a rapid, reagent-free, and nondestructive technique for the monitoring of drug treatment on liver disease. This result might useful for *e.g.* decreasing the time needed for clinical studies.

# 8. Synthesis of Gold Nanopeanuts from Gold-Silver Core-Shell Nanoparticles

## Summary

For the investigation on biological systems, surface enhance Raman spectroscopy (SERS) becomes more and more important. One of the main difficulties is the production of reproducible and tunable coin metal substrates. A part of the present PhD research therefore also focused on this topic. In this chapter, a simple method of fabricating shape-tunable Au nanopeanuts from AuAg coreshell nanoparticles is described. The technique is based on both galvanic replacement and reagent reduction.

The nanoparticle fabrication technique and the respective outcomes exhaustively covered in the present chapter have been published as a communication in the following article[208] and in final form at http://pubs.rsc.org/en/Content/ArticleLanding/2009/CC/b905998a:
Wei Xie, Le Su, Patrice Donfack, Aiguo Shen, Xiaodong Zhou, Malte Sackmann, Arnulf Materny and Jiming Hu, (**2009**), Synthesis of gold nanopeanuts by citrate reduction of gold chloride on goldsilver coreshell nanoparticles, *Chem. Commun.*, 5263-5265.

## 8.1 Introduction

Metallic nanostructures have attracted growing interest in the past decade because of their unique optoelectronic and physicochemical properties. They are promising candidates for applications in various fields such as photothermal therapy,[233] bioimaging,[234,235] biosensors,[236,237] surface-enhanced Raman scattering (SERS)[30,238] and catalysis.[239] Their intrinsic properties strongly depend on their composition and shape. Generally, nonspherical nanostructures exhibit more surface plasmon-resonance modes than nanospheres due to dipolar and multipolar electron oscillations along different directions. For example, nanorods have transverse and longitudinal plasmon modes, resulting in two extinction peaks from the visible to the near infrared spectral region.[240] These nanostructures have

been demonstrated to function as two-photon chromophores for biosensors[241] and as photodynamic agents.[242] To date, many strategies have been developed for obtaining Au and Ag nanostructures with non-spherical shapes, including nanorods/wires,[243,244] nanopeanuts,[245,246] nanocubes,[247] nanoplates,[248] and nanocages/boxes.[249,250] In most of these cases, additional surfactants or other capping agents were employed to control the growth of the Au or Ag crystals, such as Au nanorods synthesized in cetyltrimethylammonium bromide (CTAB) solution,[251] and Au nanopeanuts/octahedra grown on nanorods in the presence of glutathione or cysteine.[246] Generally, these capping agents can help to uniform the nanostructures, but may prevent further applications, such as SERS and catalysis because of strong surface coverage. In this work, we are demonstrate that dumbbell-shaped Au nanopeanuts can be synthesized without any additional organic surfactants or capping agents by using only one reducing agent in the whole process.

## 8.2 Novel Synthesis of Nanopeanuts and Characterization

Different methods for the fabrication of hollow nanostructures have recently been described by several groups.[252–255] Especially, various Ag nanostructures were used as sacrificial templates to react with an aqueous $HAuCl_4$ solution. The hollow inner structure was formed after the galvanic replacement due to the different diffusivity of Au and Ag atoms, a phenomenon known as the Kirkendall effect. Core-shell bimetallic nanostructures were also used for this purpose to generate multiple-walled nanoshells and nanorattles.[256] Here, we will demonstrate a new way of fabricating nano-scaled metallic structures, for the first time, based on both galvanic replacement and reagent reduction. Fig. 8.1 illustrates the formation of the Au nanopeanuts. By introducing $HAuCl_4$ and sodium citrate into a Au-Ag core-shell nanoparticle (NPs) solution, the Ag shells were dismantled and a new protuberance developed on each of the Au core spheres.

A typical synthesis was as follows: Au seeds with a diameter of ~ 40 nm were prepared by reduction of $HAuCl_4$ (Aldrich) using sodium citrate (1% w/w, Aldrich) in aqueous solution. In this experiment, 100 mL of 0.01% (w/w) $HAuCl_4$ was reduced by 1 mL sodium citrate solution at 100°C under vigorous magnetic stirring for 20 min. Then, 4 mg $AgNO_3$ (Fluka) was added to the boiling seed solution and, subsequently, 1 ml sodium citrate solution was added dropwise. The solution was left boiling for 1 hour resulting in an orange-colored Au-Ag core-shell product. For the growing process of the peanut-like nanoparticles, a specific volume of $HAuCl_4$/citrate solution was added to the core-shell solution under steady stirring. At different stages of this reaction, sample aliquots were taken from the mixture

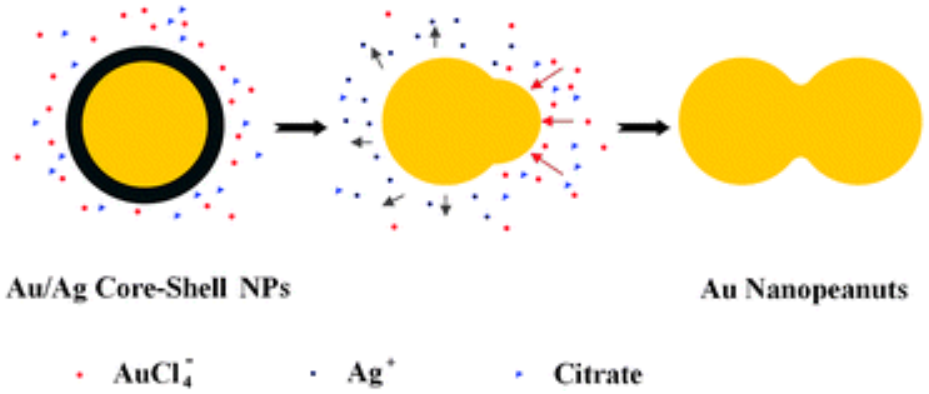


**Figure 8.1: Scheme of the Growth of Au nanopeanuts from Au-Ag core-shell nanoparticles**.

using a glass pipette and anaylized by UV-VIS absorption. Then the AgCl precipitate in each taken sample aliquot was removed for characterization using TEM/HRTEM (JEOL JEM-100CXII microscope for TEM and JEOL JEM-2100 microscope for HRTEM), EDX (FEI Quanta 200) and ICP-OES (Thermo Intrepid XSP Radial). This characterization was performed after adding NaCl powder and washing with water several times. UV-VIS and TEM/HRTEM characterization results are depicted in Fig. 8.2 to Fig. 8.5.
For the control experiment shown in Fig. 8.4, the reaction time was 20 min for varying amounts of $HAuCl_4$/citrate added into the Au-Ag core-shell nanoparticle suspension for the growth of the peanut-like nanoparticles. After the reaction was finished, the heating device was switched off and the product was cooled down to room temperature. Extinction spectra of all samples were recorded on a Varian Cary 100 UV-Vis spectrometer.

Fig. 8.2A shows the extinction spectra of the original Au NPs and AuAg coreshell NPs, and the products obtained at different reaction times. The 522 nm plasmon peak of Au NPs prepared by citrate reduction of gold chloride shifted to 512 nm after Ag coating, and one more plasmon mode due to the coating was found at 370 nm. When adding a 1 mL aliquot of a mixed aqueous solution composed of 1% (w/w) $HAuCl_4$ and 1% (w/w) sodium citrate into a 100 mL AuAg coreshell NP solution, the 512 nm plasmon peak returned back to 522 nm, and the Ag induced 370 nm plasmon mode disappeared while a longitudinal plasmon peak arose out from the original transverse one. As the reaction time was increased to 7 min, the longitudinal plasmon peak gradually red shifted to 750 nm. Surprisingly, after 7 min that peak blue shifted reaching 672 nm after 20 min.
Transmission electron microscopy (TEM) was used to characterize the shape and size evolution of the peanut-like nanoparticles that were allowed to growth while varying the amount of $HAuCl_4$/citrate added into the suspension of the Au-Ag core-shell nanoparticles

in the growing step of the peanut-like nanoparticles. The original Au NPs and Au-Ag core-shell NPs are all spherical with diameters of 43 ± 4.8 nm and 47 ± 5.2 nm, respectively (Fig. 8.2B and C). At the beginning of the reaction, a protuberance grows out from the sphere, thus increasing the length of the nanostructure in that direction (Fig. 8.2D). As the reaction goes on, the products are longitudinally growing, and the protuberance becomes spherical (Fig. 8.2E), which looks like another separate particle rather than a part of the peanut. After 7 min, the Au atoms tend to deposit on the junction of the particles, making their shape more streamlined (Fig. 8.2F) and peanut-like (Fig. 8.2G). The transverse growth

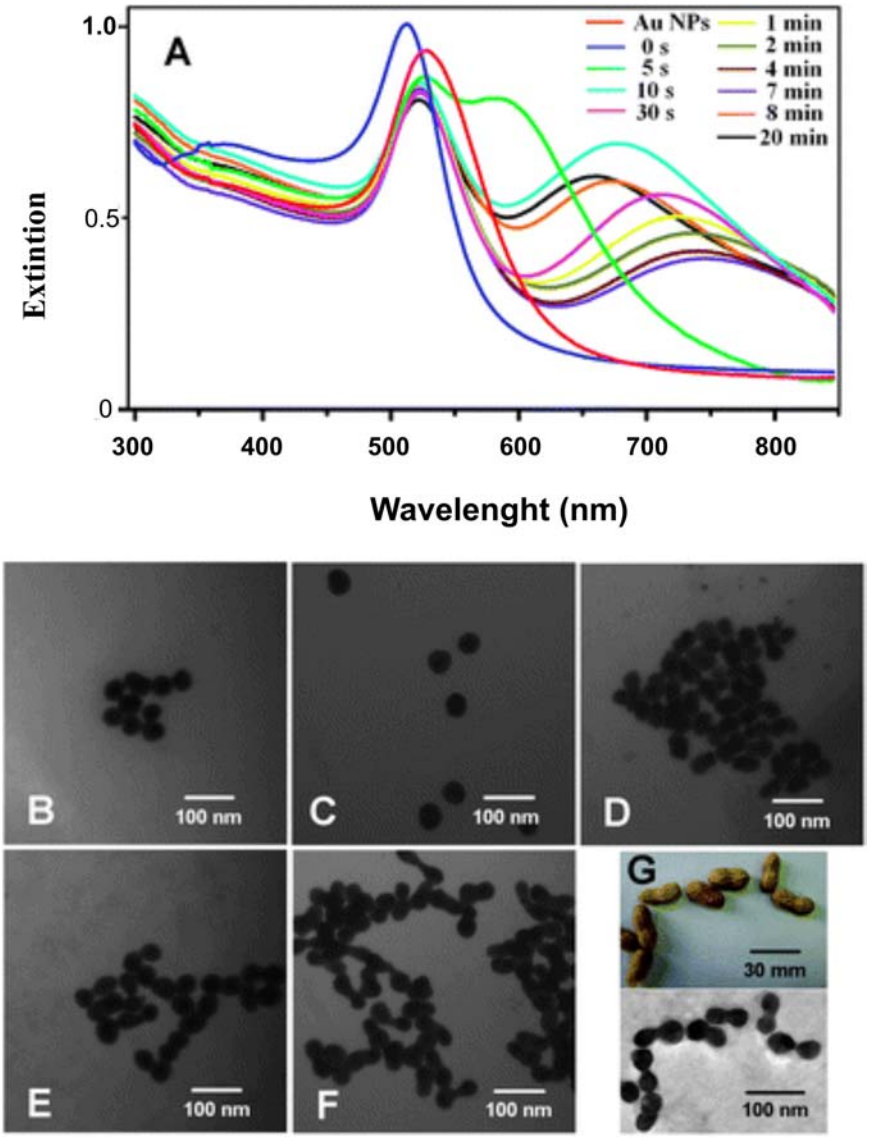


**Figure 8.2: Extinction spectra (A) and TEM images (B-G) of the original Au nanoparticles (NPs) and Au-Ag core-shell NPs, and of the products obtained at different reaction times**: TEM images of Au NPs (B), Au-Ag core-shell NPs (C), and the products at the time 5 s (D), 7 min (E), 20 min (F) and the comparison of nanopeanuts (20 min) and peanuts (G).

of the junction in fact decreases the aspect ratio (length divided by width) of the products, explaining why the longitudinal plasmon peak shifts to the blue. Energy-dispersive X-ray (EDX) and inductively coupled plasma optical emission spectrometry (ICP-OES) results of the products during this nanopeanut growth process are shown in Figs. 8.6, 8.7, 8.8, and 8.9 and Table 8.1, respectively, as additional data at the end of this chapter. No Ag component was found in the nanopeanuts. In our experiment, white solid AgCl precipitates were found to settle at the bottom of the container after the reaction, indicating that Ag atoms were entering the solution because of galvanic replacement. It has been reported that galvanic replacement between AuAg coreshell NPs and $AuCl_4^-$ generates nanorattles,[256] while chemical reduction of $AuCl_4^-$ on bare Au NPs only results in bigger Au NPs. In our experiment, both galvanic replacement and chemical reagent reduction acted on the NPs and finally we obtained nanopeanuts.

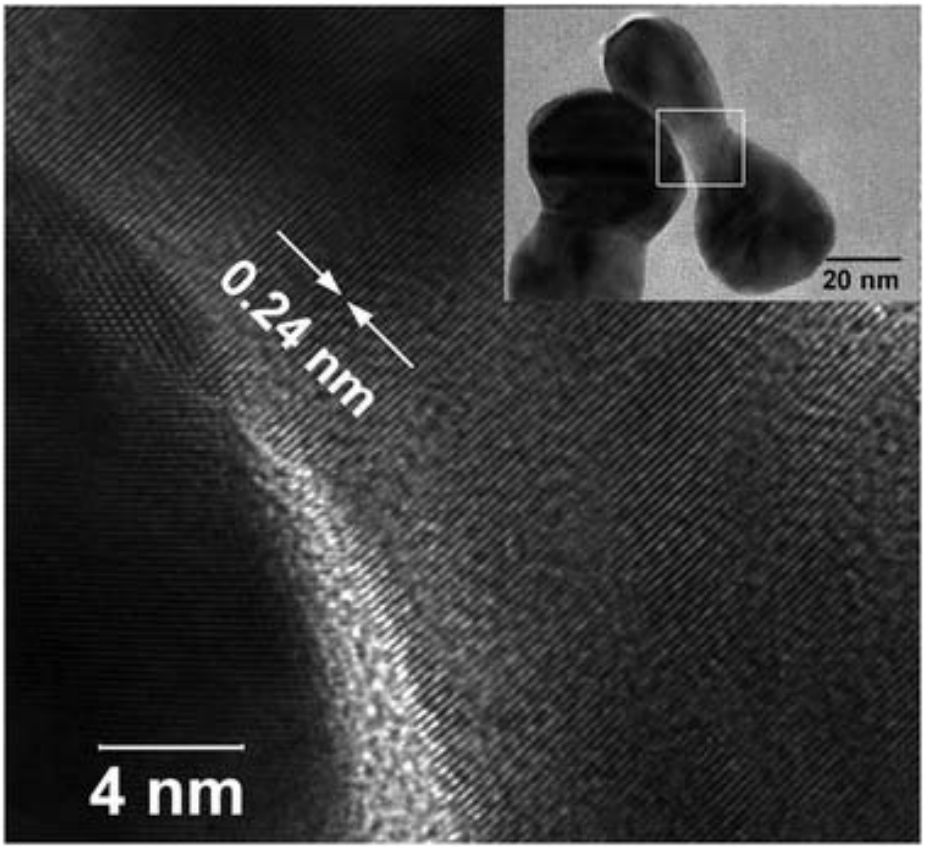


**Figure 8.3: HRTEM image of an Au nanopeanut (from the samples shown in Fig. 8.2F)**: It is oriented in the [111] plane.

High-resolution transmission electron microscopy (HRTEM) was further performed to characterize the crystal structures of the products. The result reveals that the new Au protu-

berances grown on the Au NPs are single-crystalline, and follow the direction of the junction part of their mother spheres. Fig. 8.3 shows a representative image of a nanopeanut. Control experiments were carried out to verify the mechanism of the reaction. By varying the amount of $HAuCl_4$ and citrate added to the AuAg coreshell NP solution, we obtained nanopeanuts with size-controlled protuberances. The extinction spectra shown in Fig. 8.4A exhibit the shift of the longitudinal plasmon peak due to this change. As the volume of the $HAuCl_4$/citrate solution increased, the longitudinal plasmon peak of the obtained products shifts gradually toward red, from 626 nm to 670 nm. We found that the peak does not shift beyond 670 nm even when more $HAuCl_4$/citrate solution is added, indicating that the aspect ratio of the products could not increase any more. Further characterization by TEM was

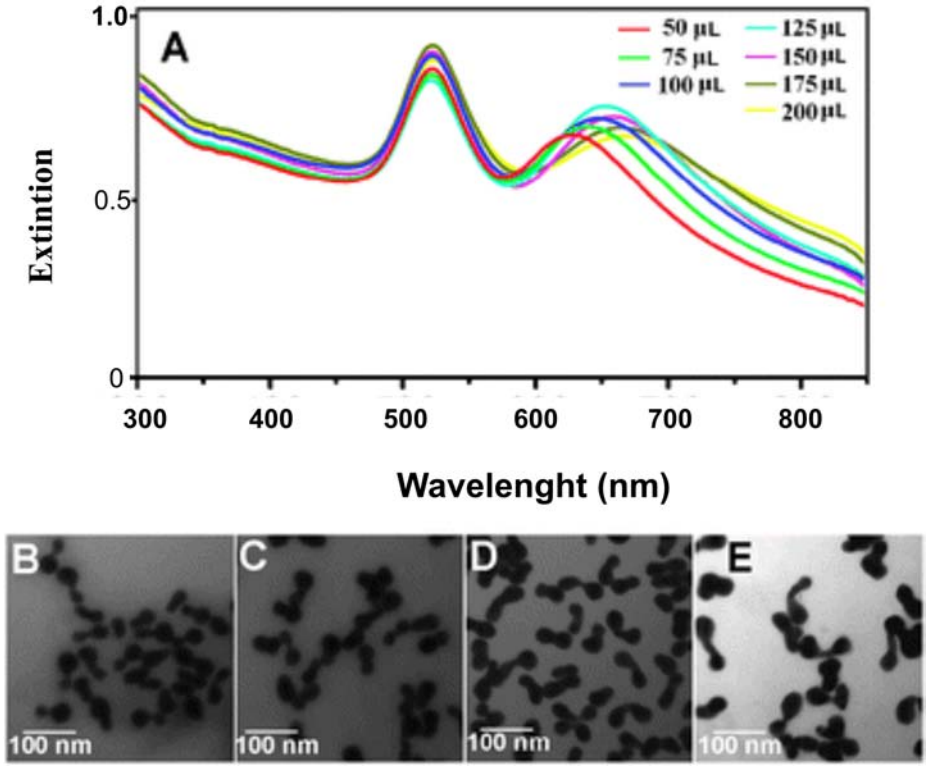


**Figure 8.4: (A) Extinction spectra and (B-E) TEM images of Au nanopeanuts obtained by varying the amount of $HAuCl_4$/citrate added into a 10 mL AuAg coreshell nanoparticle (NPs) solution.** TEM images of the products obtained by adding 50 µL (B), 75 µL (C), 100 µL (D), and 200 µL (E) $HAuCl_4$/citrate solution into the AuAg coreshell NP solution.

performed to investigate changes in the size and shape of the nanopeanuts. Fig. 8.4B shows the image of nanopeanuts with a small "head". This "head" becomes bigger (Fig. 8.4C and D) when more growth material is added. When too much $HAuCl_4$/citrate solution had been added, the products are found to be dominated by bent nanopeanuts, as shown in Fig. 8.4E. In general, a bent nanopeanut has a longer protuberance than a normal nanopeanut. However, the bending actually compensates for this effect on increasing the aspect ratio of the

products. Thus, the longitudinal plasmon peak at 670 nm did not further shift to longer wavelengths. A HRTEM image of a bent nanopeanut is shown in Fig. 8.5. The crystallographic structure of the junction indicates that the growing direction has changed during the reaction process. We attribute this to the high concentration of $AuCl_4^-$/citrate that provides too many Au atoms by the reduction and enables these atoms to deposit on another crystallographic plane.

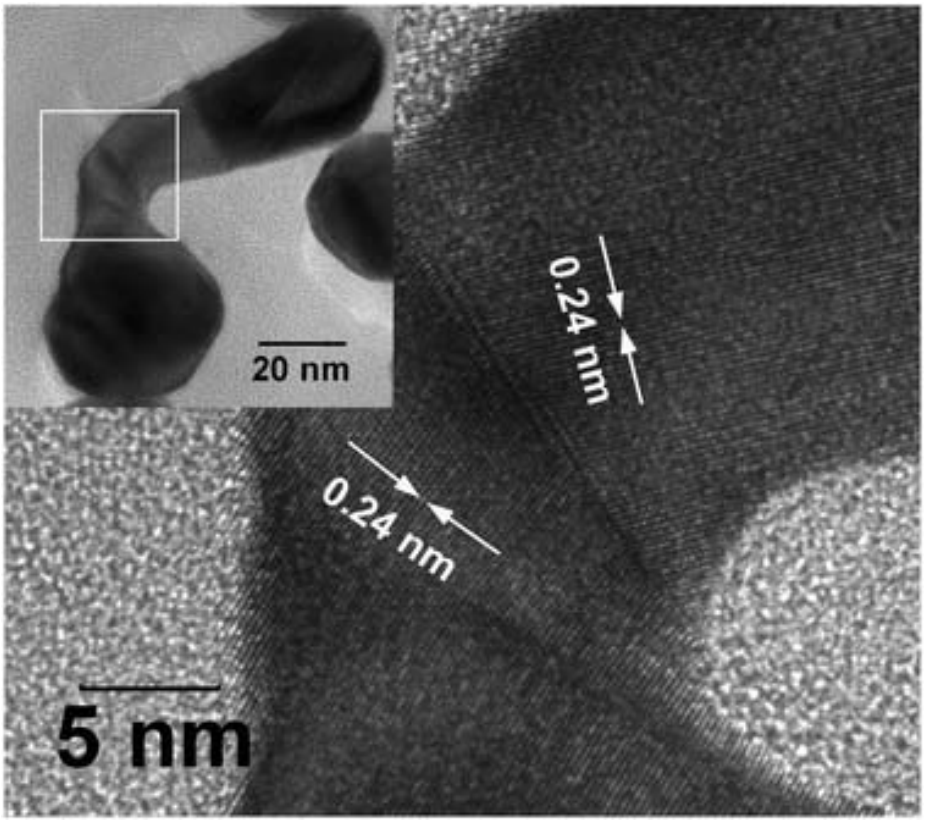


**Figure 8.5: HRTEM image of a bent Au nanopeanut (from the sample in Fig. 8.4E)**. Both original crystal and branch crystal are oriented in the [111] direction.

## Energy Dispersive X-Ray and Inductively Coupled Plasma Optical Emission Spectrometry (ICP-OES) Data of the Products Occurring During the Nanopeanuts Growth Process.

Energy-dispersive X-ray (EDX) and Inductively Coupled Plasma Optical Emission Spectrometer (ICP-OES) were employed to analyze the nature of the products at different stages of the nanopeanuts growth reaction. AgCl precipitate in the samples was removed by adding NaCl powder and washing with water for several times. Before EDX analyses, the samples were dried in vacuum. The spectra shown here indicate that the Ag shells were dissolved completely in the first few seconds (Fig. 8.6-8.7) and no Ag component was de-

tected after 10 seconds (Fig. 8.8-8.9). For ICP-OES detection, the samples are dissolved in *aqua regia*. The result in Table 8.1 also indicates that the Ag component was dissolved in

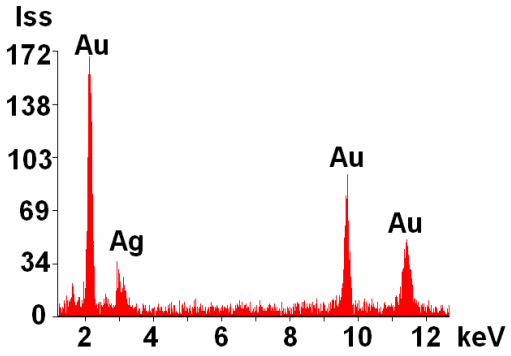


**Figure 8.6: EDX spectrum of the Au-Ag core-shell nanoparticles: sample of Fig. 8.2C**. The Ag:Au atom ratio in this sample is ~ 0.33.

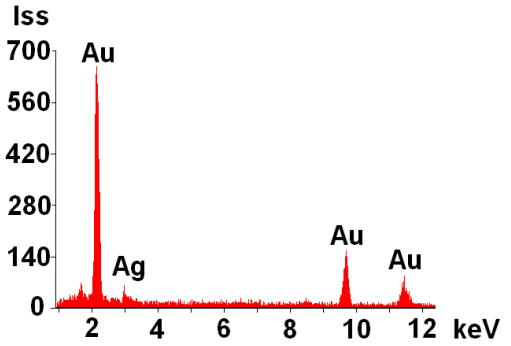


**Figure 8.7: EDX spectrum of the product obtained at 5 s: sample of Fig. 8.2D**. The Ag:Au atom ratio in this sample is ~ 0.15.

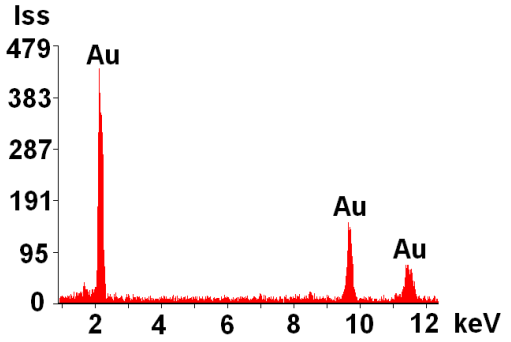


**Figure 8.8: EDX spectrum of the product obtained at 10 s**. No Ag component was found in this sample.

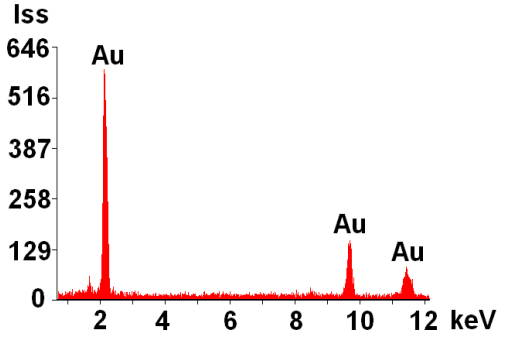


**Figure 8.9: EDX spectrum of the product obtained at 20 min (sample of Fig. 8.2F)**. No Ag component was found in this sample.

| Sample | 0 s | 5 s | 10 s | 20 min |
|---|---|---|---|---|
| Ag:Au | 0.58 | 0.18 | 0 | 0 |
| **Settings for Intrepid XSP Radial ICP-OES** | | | | |
| RF generator power (W) | | | | 1150 |
| Frequency of RF generator (MHz) | | | | 27.12 |
| Coolant gas flow rate (L/min) | | | | 14 |
| Auxiliary gas flow rate (L/min) | | | | 0.5 |
| Carrier gas flow rate (L/min) | | | | 0.6 |
| Max integration times (s) | | | | 15 |
| Analytical wavelength (nm) | | | | |
| Ag | | | | 338.289 |
| Au | | | | 242.795 |

**Table 8.1: Atom ratio Ag:Au of Au-Ag core-shell NPs (0 s) and products obtained at later reaction times measured by ICP-OES.**

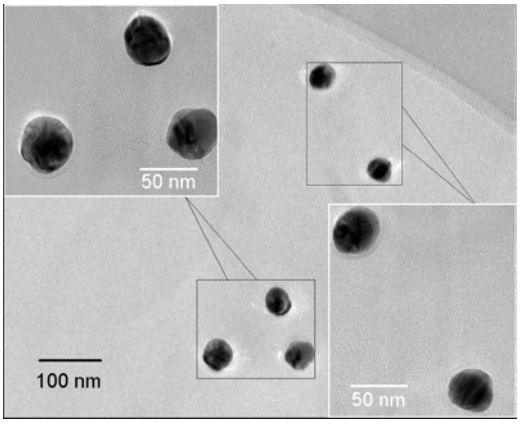


**Figure 8.10: HRTEM image of the Au-Ag core-shell NPs synthesized by reduction of $AgNO_3$ on Au NPs.**

the first 10 seconds. High-resolution transmission electron microscopy (HRTEM) was used to verify the core-shell structure of the starting nanoparticles. The image in Fig. 8.10 shows that the Au NPs are coated by a low-contrast layer, indicating that the starting nanoparticles formed via $AgNO_3$ reduction on Au NPs are Au-Ag core-shell structures.

## 8.3 Conclusions

In summary, we have demonstrated a simple way to grow Au nanopeanuts. Sodium citrate is used as a reducing agent in every step of the synthesis. In the presence of this reducer, Au atoms deposit only on one side of the AuAg coreshell NPs, which makes the product structures being peanut-like. This study provides a means for fabricating nanostructures based on both the galvanic replacement mechanism and the reagent reducing mechanism, and will therefore facilitate the design and preparation of other metallic nanostructures.

# 9. Behavior of Bio-Functional Groups at Metals Substrates – SERS of Glycine


## Summary

A complex concentration-dependence of surface enhanced Raman scattering (SERS) and UV-VIS absorption of Ag-nanoparticles (AgNPs) mixed with Gly has been observed. Surprisingly, while decreasing the Gly concentration, a new band in UV-VIS absorption of AgNPs/Gly mixtures is found to red-shift with increasing intensity, until a turning point at a critical concentration. Further diluting Gly, the new band blue-shifts with decreasing intensity. Similarly, the SERS intensities of Gly bands at 615 and 905 $cm^{-1}$ consistently increase with decreasing Gly concentrations, reaching maxima at the critical concentration. This agrees consistently with the variation in position and intensity of the new developing plasmon absorption band. Interestingly, transmission electron microscopy (TEM) revealed Gly-induced modifications of AgNPs, including a re-assembling and increasing aspect ratio with decreasing Gly concentration. The concentration-dependent behavior of UV-VIS absorption, SERS, and TEM of AgNPs/Gly mixtures is due to the complex nature of Gly-AgNPs interaction depending on the molecular density, as supported by TEM images.


## 9.1 Introduction

In our work, surface enhanced Raman scattering (SERS) is applied to simple biological systems including amino acids that constitute among others the basic building units for most biological architectures. Glycine (Gly) is the smallest member of the amino acids, having two active functional carboxylic (-COOH) and amino (-NH2) groups. In aqueous medium around pH 6.0, Gly exists in the zwitterionic form where both functional groups -COOH and -NH2 are converted into the ionized forms -COO- and -NH3+, respectively. As a matter of fact, Gly in aqueous environment presents two interacting charged poles

and it is therefore an interesting candidate for SERS studies of the simplest and basic biomolecular functions by exploring the particular aspect of the amino acid-metal interaction. In general, spectroscopic studies of amino acids adsorbed on metal surfaces are important because they can provide an insight into the nature of amino acid/metal interactions.[257]

Optical properties of metal nanoparticles have been a subject of great interest due to their wide applications. Metal nanoparticles are rough due to their nanometric scale which leads to the formation of localized surface plasmon resonance (LSPR) on the rough metal surface, which is basically the resonant oscillation of conducting electrons exposed to an appropriate wavelength.[46] The collective oscillation of conducting electrons at the surface of metal nanoparticles has been exploited for investigating various processes, of which SERS is the most important one. In this case, the intensity of the Raman bands is enhanced by several orders of magnitude ($\sim 2$ to $\sim 12$) when the analyte molecules lie in the vicinity of the metal nanoparticles. The enhancement in the intensity of a vibrational mode observed in SERS is associated with two effects, the electromagnetic field enhancement due to LSPR and lightning rod effect and the electronic enhancement due to chemisorption (the so-called chemical effect).[258–260] The electromagnetic effect is the major cause for the enhancement observed in SERS. The chemical enhancement is assumed to occur as a result of the chemical adsorption increasing the molecular polarizability and/or charge transfer interaction between the metal surface and the adsorbate. This interaction modifies the electronic properties of the adsorbed molecule. This may result in an increase of the Raman scattering cross section due to the increased polarizability and/or the creation of a new charge transfer band resulting in a high resonance Raman intensity. In many cases, chemisorption also results in changed Raman line positions. Chemisorption can also be induced by illumination.[261] SERS can help to obtain insights into chemisorption and first-layer metal-molecule interactions. Like Raman, SERS has been proven to be an important tool for obtaining the Raman fingerprint of molecules, while being sensitive at very low concentration. It has been used for monitoring the adsorption of species and for characterizing the structure and orientation of the adsorbed species on the rough metal surface.[261] Some research groups have reported fingerprint-like, ultra-sensitive Raman spectra via SERS using silver nanoparticles particles.[19,23] In view of the applications of SERS to the investigation of biological molecules, the parameters that determine the sensitivity, stability, and reproducibility of SERS are still poorly understood.[262]

Although, experimental studies concerning the aforementioned SERS features have been carried out extensively, not all of them have yielded consistent results. For SERS stud-

ies of biological molecules, silver colloid based substrates have been mostly used.[263,264] In order to explore the interaction between adsorbed biomolecules and colloidal particles, we have undertaken a systematic SERS study of the simple bio-molecule Gly using AgNPs as SERS substrates. At the same time, we also have monitored the UV-absorption and TEM images to see how the Gly molecules, ionized in solution, collectively interact with the charged surface of the AgNPs and vice versa.

In SERS, the size of the nanoparticles and the adsorption geometries play an important role. A very important parameter is the concentration of the analyte molecules, which has to be chosen right in order to optimize the intensity enhancement observed in SERS.[265] Normally, the use of SERS is effective for less concentrated analytes, and the concentration dependence of the enhancement that exhibits weaker enhancement at higher concentration is usually attributed to a saturation of the adsorption onto the metal surface. However, beside the usual type of chemical interactions involved in the so-called chemisorption effect, such as the charge transfer interaction described above, a direct chemical reaction between the analyte molecules and the metal might take place depending on the analyte characteristics. These include the concentration or the protonation level (pH-value), which in turn influence the chemisorption (resp. charge transfer). There have been some previous reports about SERS, addressing namely the pH-dependent SERS behavior.[262,266] Here, also changes in the UV-VIS absorption profile of the colloidal metal nanoparticles were observed. However, these observations were attributed to pH-variation (*i.e.* a change of the ionic state of the analyte), with little consideration of possible direct chemical reactions as mentioned above. It is not clear, which of the aforementioned analyte characteristics or parameters mentioned above are responsible for most of the unusual SERS or UV-VIS observations made. In order to clarify this situation, systematic studies needed to be conducted, in which analyte characteristics are well controlled while testing the effect of any of the parameters independently.

In the present work, we have explored the concentration-dependent interaction of Gly with AgNPs by performing SERS and UV-VIS measurements in a systematic manner, around the isoelectric point of Gly. Physical properties, such as shape, size, and agglomeration state of the AgNPs following Gly addition at different concentrations, were directly visualized via transmission microscopy (TEM). We demonstrate that the interaction of Gly with the AgNPs results in a concentration-dependent variation of the geometry and assembling of the AgNPs, which can be used to explain the observed spectral changes.

## 9.2 Material, Methods, and Experimental Techniques

### 9.2.1 Synthesis of Silver Nanoparticles

Silver nitrate ($AgNO_3$) and sodium borohydride ($NaBH_4$) of analytical grade were purchased from Sigma Aldrich and used without further purification to prepare the Ag sol. Glycine was also obtained from the same company. The colloidal silver solution was prepared in deionized water according to the method described by Creighton *et al.*[42] This method essentially involves the reduction of $1 \times 10^{-3}$ M $AgNO_3$ by an excess amount of 2 $\times 10^{-3}$ M $NaBH_4$. For synthesizing Ag sol, two stock solutions of $2 \times 10^{-3}$ M $NaBH_4$ and $1 \times 10^{-3}$ M $AgNO_3$3 were prepared separately in ice cold water. Both stock solutions were kept in ice after preparation. 4 ml of $1 \times 10^{-3}$ M $AgNO_3$ solution was taken from the ice cold stock solution and kept on a magnetic stirrer for stirring the solution. Then, 12 ml of $2 \times 10^{-3}$ $NaBH_4$ was taken from the ice cold stock solution and gently saturated with $N_2$ using a regular lab nitrogen supply to bubble $N_2$ gas into the solution for about a minute in order to prevent the decomposition of $NaBH_4$. Finally, this ice-cold and $N_2$-saturated $NaBH_4$ solution was added at once to the vigorously stirred 4 ml $AgNO_3$ solution. The volume ratio of $AgNO_3$ and $NaBH_4$ in the final solution was maintained to 1:3. The mixed solution was stirred for 15 min, which was necessary to stabilize the colloidal solution. Afterwards, the newly prepared solution was left at room temperature. After approximately 20 min, the excess $NaBH_4$ had decomposed, resulting in color stabilization; the solution became transparent yellow in color. This procedure leads to nearly mono-dispersed nanoparticles, spherical in shape; the particles' spherical shape and the mono-dispersive nature of Ag nanoparticles in the sol were confirmed by performing UV-VIS absorption and TEM measurements.

### 9.2.2 Preparation of the SERS Probes

A 2.00 M solution of the reference molecule Gly was prepared in ultra-pure water to perform the SERS measurements. Then, differently concentrated solutions of Gly were obtained by systematically diluting the original Gly solution (2.00 M) to half of its initial concentration at each time. Through this process we got ten different aqueous solutions of Gly having concentrations 1.00, $5.00 \times 10^{-1}$, $2.50 \times 10^{-1}$, $1.25 \times 10^{-1}$, $6.25 \times 10^{-2}$, $3.13 \times 10^{-2}$, $1.56 \times 10^{-2}$, $7.81 \times 10^{-3}$, $3.91 \times 10^{-3}$, and $1.95 \times 10^{-3}$ M. First of all, the Ag sol and 2.00 M Gly were mixed at different volume ratios (1:1, 1:2, 1:3, 1:4, 1:5, 2:1, 2:1, 3:1, 4:1, and 5:1) to optimize the maximum enhancement for the SERS measurements. Finally, we observed that the volume ratio 1:1 provides a better enhancement relative to any other ratio.

Then, we prepared the final SERS samples of Gly by mixing 10 of the already prepared Gly solutions at the concentrations from 2.00 to $3.91 \times 10^{-3}$ M with silver sol in a 1:1 ratio, so that the final Gly concentration in the SERS samples was as above (*i.e.*, from 1 .00 to $1.95 \times 10^{-3}$ M) for the ten Gly solutions representing 1 to 10 times dilution of the 2 M Gly stock solution to half the concentration each time. The same mixed solutions of Gly and silver sol (1:1) at each Gly concentration were also used for the UV-visible measurements. The pH of all Gly solutions and the mixtures Gly/AgNps was close to the neutral pH and therefore also close to the isoelectric point of Gly.

### 9.2.3 Raman, UV-VIS Absorption, and TEM Experiments and Instrumentation

The normal Raman and SERS spectra were measured in a back-scattering geometry using the 514.5 nm line of an argon ion laser (Innova 308 Series, Coherent, USA) as the excitation source. A Triax single monochromator (TRIAX 550, Jobin Yvon, France) equipped with three interchangeable holographic gratings (600, 1200, and 2400 grooves/mm) and a liquid nitrogen cooled CCD detector (Symphony 3500, Jobin Yvon, France) were used for the back-scattered signal analysis and detection. An Olympus microscope with different objectives (10×, 50×, and 100×), which was part of a self-built Raman system, was used in order to couple-in the laser and to couple-out the scattered signal. The 50× objective, with an ultra long working distance, was found best suited, and was used to focus the laser into the sample drop. The scattered signal was filtered by a holographic super-notch filter for Rayleigh scattering rejection before focusing it onto the 100 m entrance slit of the spectrometer. The monochromator's 1200 grooves/mm holographic grating was used for signal dispersion, before the detection on the CCD detector with 2048 pixels chip width. With these settings, a spectral resolution of about 3 $cm^{-1}$ was achieved. Spectral calibration was performed using toluene's well known Raman modes. During the measurement, the samples were kept in the form of a drop on the aluminum foil covering a glass slide, which was mounted on the microscope XY table. The laser power on the samples was kept constant at 15 mW. The data acquisition time for each Raman and SERS measurement was 10 s with three averaged signal accumulations. Instrument communications, computer interface, and spectra acquisition and preprocessing were realized using the commercial LabSpec software (Jobin Yvon, France).

UV-VIS spectra of pure Ag sol and its mixtures with differently concentrated Gly solutions, prepared as mentioned above, were measured using a PharmaSpec UV-1700 UV-

Visible spectrometer (Shimadzu Corporation, Kyoto, Japan) controlled by the Shimadzu UVProbe software. The spectrum module of UVProbe was used for wavelength scanning and analysis within [250 - 850 nm]. All absorption spectra were recorded immediately after performing the SERS measurement optimization (optimization of the analyte concentration and colloid/analyte volume ratio for optimal SERS response). The UV-VIS absorption spectra were all repeated directly after the SERS measurements, and in some cases, a couple of times during the following days, to make sure the observed plasmon absorption features reproduced well.

Transmission electron microscopy (TEM) probes were prepared by depositing the neat AgNPs and the AGNPs/Gly mixtures at different concentrations sparsely onto 200 mesh copper grids coated on one side (the deposition side) with a 50 nm thin carbon film. Only very tiny sample drops of AgNPs or AGNPs/Gly were brought onto the grids and were rapidly spread and dehydrated by means of blotting with a filter paper. The little amount of water on the grid quickly evaporated in air. The grid probes were mounted and examined using a Zeiss transmission electron microscope (EM 900, Carl Zeiss, Germany) operated at an accelerating voltage of 80 kV, with an optimum vacuum around $10^{-6}$ mbar. The cathode filament heating was adjusted to suit different image acquisition modes. The TEM probes were imaged in the HR (high resolution) mode with high magnifications, 50000×, 85000×, 140000×, and 250000× successively. Finally, ultra-highly resolved images were taken using the highest magnification operating mode of the system at 250000× of the HR mode to resolve fine details of the particles.

## 9.3 Results and Discussion

### 9.3.1 UV-VIS Absorption of Ag Sol and its Mixtures with Gly at Different Concentrations

Size and shape of the nanoparticles are very important with respect to their application in optical studies such as SERS. SERS is highly sensitive to the position of local surface plasmon resonance (LSPR), which essentially depends on the shape and size of the nanoparticles. The UV-visible spectra of synthesized silver nanoparticles (AgNPs) and of the corresponding mixtures with Gly at ten different concentrations in decreasing order are shown in Fig. 9.1 (a) and (b). While decreasing Gly concentration in the AgNPs/Gly mixtures, the electromagnetic extinction spectra follow an interesting two-phase behavior, which we can refer to as “development” and “recovery” phases. The development phase

is depicted in Fig. 9.1 (a), which presents the UV-VIS absorption features of pure AgNPs along with mixtures AgNPs with Gly at the first five concentrations 1.00, $5.00 \times 10^{-1}$, $2.50 \times 10^{-1}$, $1.25 \times 10^{-1}$, and $6.25 \times 10^{-2}$ M, in decreasing Gly concentration order. The recovery phase is depicted in Fig. 9.1 (b), which shows the absorption behavior of the mixtures of AgNPs with Gly at a concentration of $6.25 \times 10^{-2}$ M and at the next five concentrations, $3.12 \times 10^{-2}$, $1.56 \times 10^{-2}$, $7.81 \times 10^{-3}$, $3.95 \times 10^{-3}$, and $1.95 \times 10^{-3}$ M; for comparison, the absorption spectrum of pure AgNPs has been included in Fig1 (b) as well. The absorption

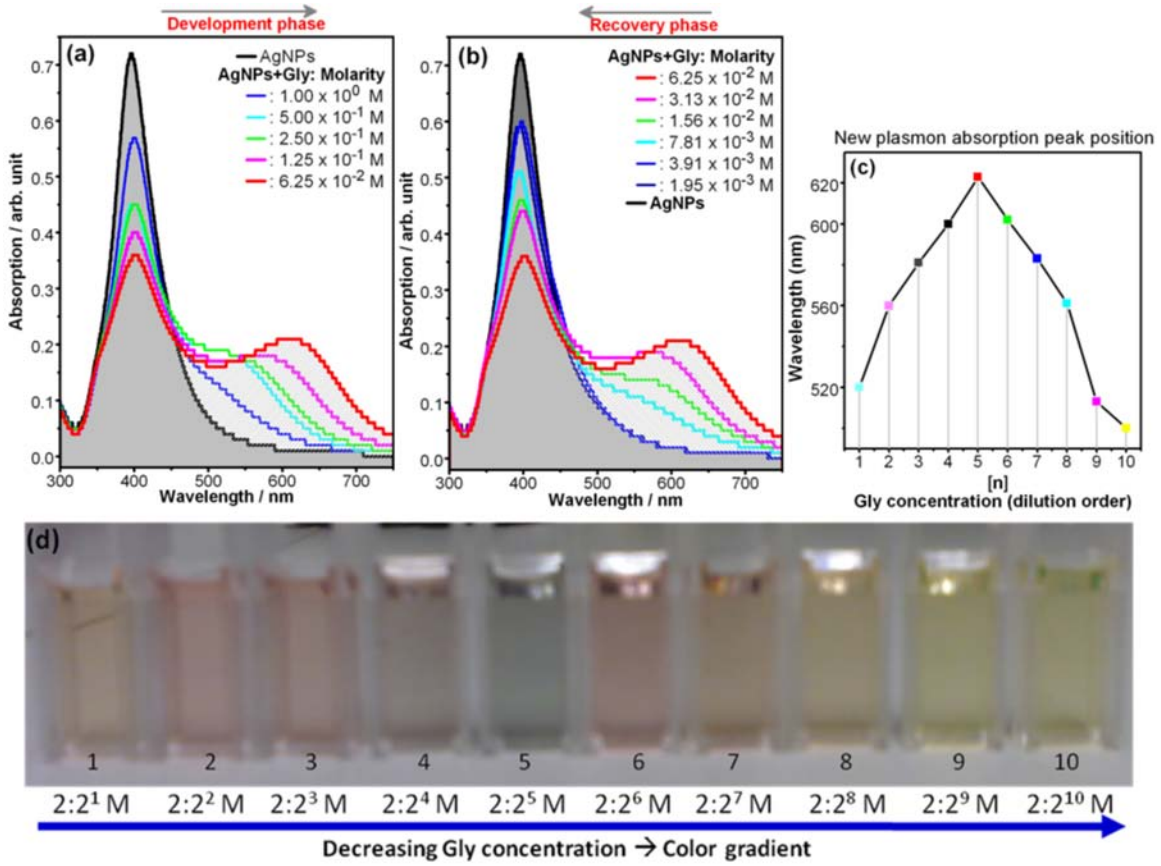


**Figure 9.1: UV-VIS plasmon absorption of AgNPs sol and AgNPs/Gly mixtures at decreasing Gly concentration order**: (a) At the initial five Gly concentrations, and (b) the next five lower Gly concentrations. (c) Variation of the peak position of the new plasmon band of AgNPs/Gly mixtures with the dilution order [$n$] of Gly (*i.e.* the number of times the initial 2 M Gly solution was diluted to half the concentration: $C(n) = 2/2^n$ M, $n$ = 1 to 10). (d) Photo of the corresponding AgNPs/Gly mixed solutions, exhibiting a reversed color change with a turning point at the critical concentration $6.25 \times 10^{-2}$ M ($n$ = 5).

spectra depicted in panels (a) and (b) clearly show an absorption change as a function of the Gly concentration in the Ag sol. Upon addition of Gly, a new absorption band appears, increases in intensity until a maximum is reached, and then starts to vanish again. Additionally the peak position of the new band changes as a function of Gly concentration as shown in panel (c) of Fig. 9.1. These changes in the absorption spectrum of course are also

reflected by changes of the color of the different AgNPs/Gly solutions, yielding a kind of AgNPs/Gly color code, symmetric around a critical color point. In fact, the gradients left and right from this critical point for both the intensity and wavelength changes as function of the Gly concentrations were found to be approximately equal. The demonstration of the interesting AgNPs/Gly color code is illustrated by a photo of the different mixed solutions in Fig.1 (d). In a previous report[262] dealing with pH-dependent SERS study of Phenylalanine, slight color changes were attributed to the variation in pH. In the present study, the pH value remained constant at the isoelectric point. Therefore, the observed color changes can exclusively be attributed to the variation of the Gly concentration. It is obvious that a concentration-dependent change of the interaction between the Gly molecules and the AgNPs must be responsible for the observed phenomenon. The existence of the critical concentration, which is not just a saturation point, but marks a reversion of the behavior points to a complex interaction mechanism of the Gly molecules with AgNPs, which we are going to elucidate in the following.

The synthesis of AgNPs and the UV-VIS measurements of the mixtures of AgNPS with different Gly concentrations were carefully repeated several times to exclude any systematic errors or artifacts during the experiments. The changes in the UV-VIS absorption spectra could be always reproduced. It is quite evident form Fig. 9.1 (a), which we termed "development phase", that upon addition of 1 M Gly to the AgNPs the UV-VIS absorption profile exhibits an asymmetrical line shape developing from the neat AgNPs peak at approx. 390 nm towards the higher wavelength side. Interestingly, when decreasing the Gly concentration this asymmetry is further increased until a new well resolved peak on the red side appears, which as mentioned above, changes its position and intensity as a function of Gly concentration. While the main peak's intensity decreases, the new band intensity increases with decreasing concentration. The absorption spectra of the mixtures of AgNPs with Gly recorded at different Gly concentrations were fitted assuming two lines to determine the position and intensity of the new band exactly. The line position of the new band is shifting to the red with decreasing Gly concentration until at the critical Gly concentration of $6.25 \times 10^{-2}$ M (dilution of the 2.00 M Gly solution to respectively half concentration five times) where a peak position of approx. 623 nm is reached. Upon further dilution of Gly, successively from $6.25 \times 10^{-2}$ to $1.98 \times 10^{-3}$ M, the intensity of the new absorption band starts decreasing and the peak position is shifting back to higher energies as can be seen in Fig. 9.1 (b); we have termed this part "recovery phase". The variation of the peak position of the new band with decreasing Gly concentration (as a function of the dilution order [**n**], *i.e.* the number of times the initial 2.00 M Gly solution is diluted to half

concentration) has been presented in Fig. 9.1 (c). The slopes of the intensity and wavelength changes observed during development and recovery phase in the absorption spectra of AgNPs following addition of the different concentrations of Gly in a decreasing order are found to be almost the same. The appearance of an additional band in the UV-VIS spectra of the AgNPs/Gly mixtures points to some form of aggregation of the original AgNPs. It is well known that the formation of elongated NPs or nanorods yields two absorption bands due to the longitudinal and transverse modes of the plasmons having different resonance frequencies. However, a random aggregation, which is usually reflected by a simple broadening of the initial absorption band of the colloids due to random increase in particle size and random change in particle shape, cannot explain the observed phenomenon. Nevertheless, the modification of the original AgNPs and their assembling resulting in elongated structures would be a reasonable explanation of the observed behavior. Such a modification can include both nucleation and aggregation, but obviously in a well defined symmetry (*e.g.* dimer or trimer formation). Another possible explanation would be the formation of metal-molecule complex structures. Chemisorption and coordination interaction could result in the formation of complexes acting as new chromophoric moiety, which absorbs light at different wavelengths. This was however not the case as will be demonstrated later by TEM examination of the structures of AgNPs mixed with Gly at different concentrations.

### 9.3.2 Concentration Dependent SERS of Gly with AgNPs

It is well known that the color of a silver sol reflects the properties of the AgNPs and their state of agglomeration, which again determine the efficiency of the surface enhancement observed in SERS. Therefore, it is interesting to study the SERS properties of the sols with different Gly concentrations and compare these results to the results obtained using UV-VIS absorption spectroscopy. Gly is a rather weak scattering molecule with poor SERS enhancement, which makes SERS studies on this molecule difficult and less popular compared to other amino acids. Therefore, before any systematic measurement, including UV-VIS absorption, the SERS performance of the synthesized AgNPs was initially evaluated using crystal violet (CV), a well known SERS analyte. CV was chosen in order to establish the efficiency of the prepared colloids on a standard basis. Several analyte-to-colloid volume ratios were measured. Taking the AgNP and CV solutions in a volume ratio of 1:1, an optimally enhanced SERS signal was obtained for CV under excitation at 514.5 nm. The same ratio was found optimal for SERS on Gly. Therefore, the SERS spectra of Gly at the different decreasing Gly concentrations were taken under these conditions. Right after the UV-VIS absorption measurements, the mixed solutions of AgNPs and Gly in the volume ratio 1:1 were further used to investigate the SERS behavior of the AgNPs/Gly and

afterwards again checked by UV-VIS spectroscopy. The Raman and SERS spectra of Gly at different concentrations have been recorded in the spectral range [500-2500 $cm^{-1}$]. The normal Raman spectrum of the neat 2.00 M Gly along with the SERS spectra of AgNPs/Gly at the five different Gly concentrations of 1.00, $2.50 \times 10^{-1}$, $6.25 \times$ , $1.56 \times 10^{-2}$, and $3.90 \times 10^{-3}$ M are shown in Fig. 9.2. The normal Raman spectrum of neat 2.00 M Gly shows ten noticeable Raman bands with different intensities.

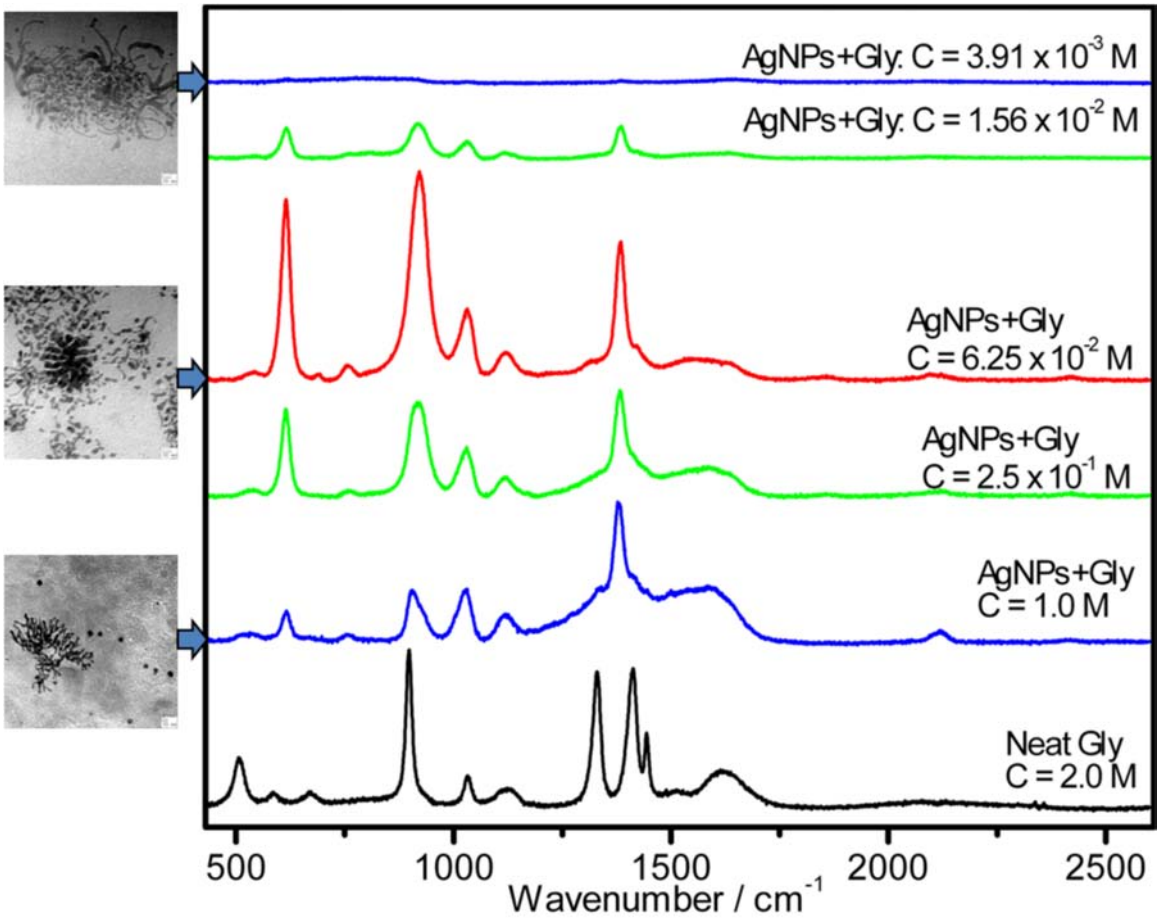


**Figure 9.2: Raman and SERS spectra of Gly and AgNPs/Gly mixtures**: Five different Gly concentrations are shown with the corresponding modified AgNps structures.

A tentative assignment of the Raman bands along with the wavenumber positions of normal Raman and SERS bands have been summarized in Table 9.1. In the Raman spectrum of neat Gly, the bands at 506, 898, 1330, and 1413 $cm^{-1}$ are assigned to the O-H out of plane, C-C out of plane, $CH_2$ wagging vibrations, and the combination mode of $CH_2$ bending and $CH_2$ wagging vibrations, respectively. These bands are more intense compared to the six other Raman bands of Gly.

**Table 9.1:** Raman and SERS bands of Gly and their tentative assignment

| Band position ($cm^{-1}$) | | Tentative assignments |
|---|---|---|
| Raman | SERS | |
| 506 | 523 | O-H out of plane |
| 586 | 615 ($\nu_1$) | (O-H + N-H) out of plane |
| 672 | 758 | C-O out of plane |
| 898 | 905 ($\nu_1$) | C-C out of plane |
| 1033 | 1030 | C-N str. |
| 1121 | 1122 | C-N str. + O-H out of plane |
| 1330 | — | $CH_2$ wag. |
| 1413 | 1378 ($\nu_1$) | $CH_2$ bend + $CH_2$ wag. |
| 1444 | – | $CH_2$ bend |
| 1620 | 1587 | NH3+ asym. str. |
| —- | 2120 | —- |

In the SERS spectra, some vibrational modes behave differently for each Gly concentration. The combination mode of O-H out of plane and N-H out of plane vibrations at 586 $cm^{-1}$ shows only a very weak spontaneous Raman intensity in the spectrum of the neat 2.00 M Gly. However, a new band shifted by 30 $cm^{-1}$ (appearing at 615 $cm^{-1}$) is observed in SERS along with moderate enhancement in intensity for 1.00 M Gly. Overall, the Raman bands of neat Gly at 586 ($\nu_1$), 898 ($\nu_2$), and 1330 $cm^{-1}$ ($\nu_3$) appear to be the mostly affected bands once Gly is mixed with and interact with AgNPs. In fact, in the SERS spectra the three main bands at 615, 905, and 1380 $cm^{-1}$ behave differently upon variation of the Gly concentration. They show an interesting variation in their SERS intensity with decreasing Gly concentration. The SERS intensities and wavenumber positions of these three bands at each Gly concentration have been summarized in Table 9.2. The intensity variation of the SERS bands at 615 and 905 $cm^{-1}$ (shifted $\nu_1$ and $\nu_2$ mode wavenumbers, respectively), has been plotted against the Gly concentration (as a function of the dilution order [$n$], **i.e.** the number of times the initial 2.00 M Gly solution is diluted to half concentration each time) and presented in Fig. 9.3. It can be easily noticed that the change of line intensity with Gly concentration is the same for both SERS bands. The intensity behavior of the third main band at 1380 $cm^{-1}$ is similar to that of the first two bands, but different for the two first concentration values, between which the intensity initially drops. For the sake of clarity, the intensity variation of this band has not been included in the plot of Fig. 3. Besides the three main SERS bands mentioned above, only few other weak bands are observed in the SERS spectra at nearly the same wavenumber positions as the corresponding bands (also

weak) in the normal Raman spectrum of the 2 M Gly. However, no particular trend was observed in the variation of the intensities of those other SERS bands, probably because they are rather weak. The intensity of both SERS bands at 615 and 905 $cm^{-1}$ exhibiting a consistent behavior increases gradually with decreasing Gly concentration, peaking at a maximum at the Gly concentration of $6.25 \times 10^{-2}$ M, the critical concentration point already introduced earlier. Upon further dilution of the Gly below the critical point at $6.25 \times 10^{-2}$ M, the intensity of both peaks starts decreasing and becomes almost zero at a low Gly concentration of $1.98 \times 10^{-3}$ M as one would expect.

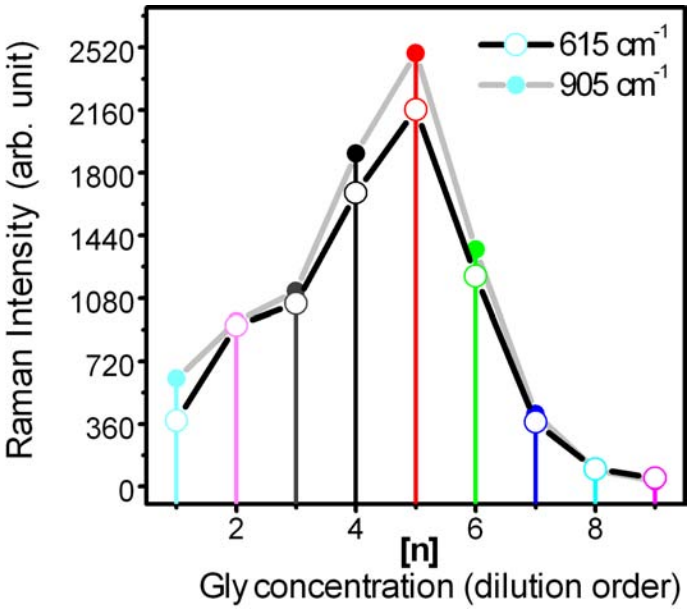


**Figure 9.3: Variation of the SERS intensity of Gly with decreasing Gly concentration**. Two SERS bands shown

A concentration of *e.g.* 2.00 M is rather high and usually SERS measurements access lower concentrations. However, Gly is a weak Raman scatterer and relatively large molecule numbers are required even to see SERS. It is well known that saturation effects play an important role in the concentration dependence of SERS. Above a concentration where complete coverage of the metal surface is achieved, the shielding of the surface prevents a further increase of the intensity and even results in an intensity decrease of the observed signal. At very low concentrations naturally the signal also drops, which in total would result in a concentration dependence of the SERS signal similar to that one observed in the present experiments. The rise and fall of the intensity of the SERS bands at 615 and 905 $cm^{-1}$ with Gly concentration however is perfectly consistent with the evolution behavior of the new plasmon absorption band in the UV-VIS spectra of Ag

sol mixed with different decreasing Gly concentrations as mentioned above, which clearly points against saturation being a possible mechanism for explaining the observed concentration dependence. In addition, the intensity behavior of the strong SERS band at 1380 $cm^{-1}$, which showed an initial decrease in intensity between the first two Gly concentration values (in decreasing order), counts against saturation. The considerable shift of some Raman bands in SERS compared to the Raman spectrum obtained for pure Gly definitely points to a chemisorption, which strongly influences the structural properties of the adsorbed molecules. However, the changes in the UV-VIS spectra and their correlation with the concentration-dependent variation of the intensities of the main SERS bands cannot be explained by chemical enhancement, which still might contribute, but obviously is not dominating the observed concentration-dependent intensity changes. The correlation of the enhancement of the main bands with the appearance of the newly developing plasmon band in the UV-VIS absorption spectrum suggests that the moderate enhancement observed is due to the electromagnetic effect. At higher concentration, Gly molecules only feel a weak plasmon around 520 nm as an asymmetric tail on the higher wavelength side of the original neat AgNPs plasmon absorption. While the Gly concentration is decreasing, the SERS intensity increases reversibly until the critical Gly concentration point, which is accompanied not only by the maximum growth in intensity, but also by the maximum red shift of the new plasmon absorption band. Because of the latter, the relative enhancement remains moderate. In fact, the new plasmon absorption band, while developing, shifts to the red far from the fixed laser excitation at 514.5 nm. Finally, the net enhanced spectra (data not shown) for the different Gly concentrations were obtained by normalizing the intensity with respect to the different concentration values (the spectrum at each concentration was scaled by multiplying it by the dilution order, *i.e.*, the number of times the original 2 M Gly solution was diluted to half its concentration). It follows that the net enhancement follows the concentration dependence as the intensity of the raw spectra at different concentrations. However, the net maximum enhancement occurs after the critical concentration value of $6.25 \times 10^{-2}$ M, where the AgNPs/Gly mixture shows the new plasmon absorption band with the maximum red shift and absorbance. Consequently, if the observed enhancement is mostly of EM origin as already mentioned above, then the modification of the original AgNPs, already mentioned in the section about UV-VIS absorption, is such that the modified AgNPs structures in the AgNPs/Gly mixture at Gly concentration immediately below the critical concentration value have a greater enhancement capability. Therefore, a closer investigation of the structural changes caused by the concentration changes is of importance.

**Table 9.2:** Peak positions and intensities of three SERS bands of Gly mixed with AgNPs at different Gly concentrations

| Molar concentration | SERS band peak positions and intensities | | | | | |
|---|---|---|---|---|---|---|
| | $\nu_1$ | | $\nu_2$ | | $\nu_3$ | |
| | Position ($cm^{-1}$) | Intensity (count) | Position ($cm^{-1}$) | Intensity (count) | Position ($cm^{-1}$) | Intensity (count) |
| 1 | 615 | 376 | 905 | 620 | 1380 | 1669 |
| $5 \times 10^{-1}$ | 615 | 925 | 918 | 947 | 1383 | 1124 |
| $2.5 \times 10^{-1}$ | 615 | 1050 | 918 | 1120 | 1383 | 1272 |
| $1.25 \times 10^{-1}$ | 615 | 1684 | 918 | 1910 | 1383 | 1625 |
| $6.25 \times 10^{-2}$ | 615 | 2162 | 918 | 2488 | 1383 | 1642 |
| $3.13 \times 10^{-2}$ | 615 | 1205 | 918 | 1359 | 1383 | 1020 |
| $1.56 \times 10^{-2}$ | 615 | 370 | 918 | 418 | 1384 | 391 |
| $7.81 \times 10^{-3}$ | 615 | 101 | 918 | 96 | 1384 | 65 |
| $3.91 \times 10^{-3}$ | 615 | 50 | 918 | 30 | 1382 | 30 |
| $1.95 \times 10^{-3}$ | - | - | - | - | - | - |

### 9.3.3 Glycine-Induced Modification of AgNPs as Evidenced by TEM Measurement

Since our findings strongly point to a structural change of the Ag nanostructures due to the interaction with different concentrations of Gly, these structures were investigated in more detail. For this, transmission electron microscopy (TEM) measurements of the Ag sol and its mixture with Gly at three different concentrations, 1.00, $6.25 \times 10^{-2}$, and $3.95 \times 10^{-3}$ M have been performed. The three different concentrations represent the "development" phase, the critical (or optimum) point, and the recovery phase defined above with respect to the UV-VIS absorption behavior of AgNPs/Gly mixtures in decreasing Gly concentrations order. The TEM images of pure AgNPs and their mixtures with Gly at the three different concentrations mentioned above are shown in panels (a), (b), (c), and (d) of Fig. 9.4, respectively. Additionally, the TEM images of the AgNPs/Gly mixtures are also displayed next to the SERS spectra shown in Fig. 9.2. The pure AgNPs are spherical in shape, well mono-dispersed in nature with particle sizes in the range between 15 and 30 nm. A 1.00 M Gly solution added to the Ag sol modifies the shape of the AgNPs considerably. The new structures now look like nanorods. At the same time, the AgNPs are more closely assembled or even connected with one another as shown in Fig. 9.4 (b). Interestingly, upon further and consecutive dilutions of Gly, the shape, density and length of the modified nanoparticles have increased consistently as depicted in panels (c) and (d). This interesting observation appears as a complex Gly-induced modification of AgNPs with a well defined symmetry, in which a clear realignment together with lengthening (dimerization, trimerization, etc.) of the original AgNPs spreading outward from new centers is observed. As

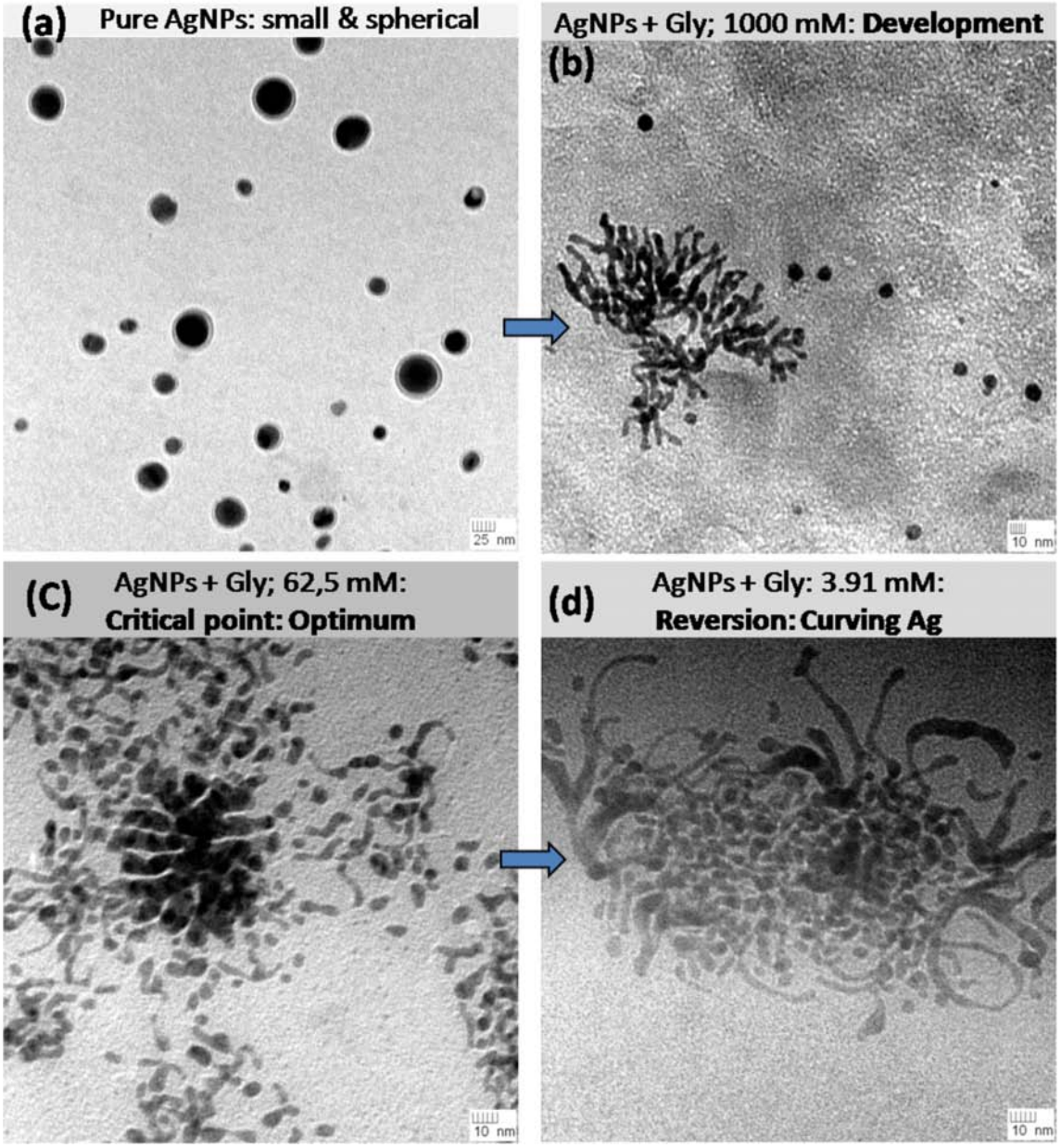


**Figure 9.4: TEM images of AgNPs and AgNPs/Gly mixtures**, at Gly concentration of ( a) 0 M (pure AgNPs), (b) 1.00 M, (c) 6.25 X $10^{-2}$ M, and (d) 3.95 X $10^{-3}$ M.

clearly evidenced by panels (b) and (c) of Fig. 9.4, with decreasing Gly concentration, each branch-like pattern develops progressively until the Gly concentration value of $6.25 \times 10^{-2}$ M (panel (c) of Fig. 9.4), where the rearrangement/realignment of the AgNPs is optimum with the maximum aspect ratio of the NPs. This consistently agrees with and explains the UV-VIS absorption behavior termed the development phase. Therefore, the concentration value at $6.25 \times 10^{-2}$ M is a rather critical point. Upon further decrease of Gly concentration, the interesting phenomenon does continue to evolve as already mentioned. However,

the AgPNs have already attained a maximum aspect ratio and their continued lengthening forces them to curve as shown in Fig. 9.4 (d), which in turn causes the overall aspect ratio of the AgNPs to reduce. At very low Gly concentration the phenomenon is extremely pronounced, where the NPs have curved in several turns and therefore appear as optically closed or bulky surfaces. This situation also perfectly agrees with and explains the behavior of the UV-VIS absorption spectra termed the "recovery phase". The modification of the shape, size and density of the AgNPs after addition of Gly molecules at decreasing concentrations is responsible for the appearance and disappearance of the new plasmon absorption band and also explains the electromagnetic enhancement in the SERS spectra. In fact, as mentioned above, the modified AgNPs structures start to curve right below the critical Gly concentration value, and although the plasmon absorption of such curved structures diminishes, their EM enhancement capability is greater than that of the optimal rod-like structure at the critical point. As a matter of fact, the observed concentration-dependent variation of SERS of glycine is due to the specific nature of its interaction with the AgNPs as a function of the density of Gly molecules on the rough metal surface, which is well supported by the changes in the UV-visible features and TEM micrographs of AgNPs mixed with Gly at different concentrations.

## 9.4 Conclusions

In the present report, the concentration dependent interaction behavior of Gly with AgNPs has been systematically studied by performing UV-VIS absorption, SERS, and TEM measurements. The appearance of a new absorption band is observed in the UV-VIS spectra of AgNPs/Gly mixtures up to a certain Gly critical concentration of $6.25 \times 10^{-2}$ M corresponding to the existence of a new plasmon absorption of silver shifted far into the red (625 nm). At this point, the phenomenon is reversed. Upon further dilution of Gly below the critical concentration, the new peak starts disappearing and vanishes completely at Gly concentration of approx. $1.95 \times 10^{-3}$ M. The appearance and disappearance of the new absorption band could be correlated to the modification in the shape, size, and aspect ratio of the AgNPs due to the interaction with the Gly molecules in a well defined and reproducible way based on the UV-VIS and TEM results. Surprisingly, the extent of Gly-mediated modification (resizing, reshaping and lengthening) of the original AgNPs appears more and more pronounced with decreasing Gly concentration! The modification can be depicted in two main steps; (i) a development phase, in which an optimum symmetric realignment and unidirectional aggregation of the original AgNPs is achieved with the maximum aspect ratio at the critical concentration point; and (ii) a recovery phase arising upon further

dilution, where the Ag modification does continue to extend, but with the continued lengthening of the AgNPs resulting in a curling of the silver tails and by this, a reduction of the aspect ratio. These observations are in perfect agreement with the reversible behavior observed in the UV-VIS absorption of AgNPs/Gly mixtures at decreasing Gly concentration. The SERS intensities of Gly mixed with AgNPs for the SERS bands at 615 and 905 $cm^{-1}$ show a consistent increase on decreasing Gly concentration, reaching maximum values at the critical concentration $6.25 \times 10^{-2}$ M. A further decrease in the Gly concentration below the critical concentration causes the intensity of both SERS bands to drop drastically. Since in all experiments the pH remained constant at the isoelectric point, this observed concentration-dependent variation of SERS of Gly can be attributed to the specific nature of its strong interaction with AgNPs as a function of analyte density on the metal surface. The result is a Gly-mediated metal surface modification which is indicated by the changes in the UV-visible features and further confirmed by TEM images of AgNPs/Gly mixtures at decreasing Gly concentrations.

The results discussed in this chapter have been submitted for publication in the following article:

Animesh K. Ojha, Patrice Donfack and Arnulf Materny; Complex Concentration Dependence of SERS and UV-VIS Absorption of Glycine/Ag-Substrates Due to Glycine-Mediated Ag-Nanostructures Modifications; *Journal of Raman Spectroscopy* **2010**, Submitted.

# 10. General Conclusion and Outlook

This thesis addresses several aspects of the potential of Raman spectroscopy for biomedical applications. These include the monitoring of key biological events, such as cancer transformation and development, biological rhythms and hormonal deregulation, phenotypic variation and chaperon properties, therapy response, and biomolecular interaction at metal substrates. First of all, a brief introduction of Raman spectroscopy and related techniques has been presented, together with an overview of the related biomedical applications. One general interest in this thesis is to emphasize the capability of Raman spectroscopy to discriminate not only some specific types of cancer but also other histopathological conditions, with concrete examples. It has been pointed out that, this thesis has striven to demonstrate the potential of Raman spectroscopy for studying detailed mechanisms in tumorigenicity, toward noninvasive targeting of disease biomarkers,which might help to gain a better understanding of the molecular basis of disease incidence and development. The approach is to track detailed spectral information associated to even slight molecular changes, by implementing Raman investigations with detailed spectral analysis in combination with multivariate analysis.

First, HaCaT keratinocytes and their cancerous counterparts A5RT3 cells have been used as model cell lines for Raman studies of skin carcinoma in order to demonstrate that differences in their Raman spectra can be assigned to characteristic features on the biomolecular level. The corresponding results demonstrate that Raman spectroscopy is capable of differentiating non-tumorigenic human HaCaT from the tumorigenic A5RT3. It reveals a higher lipid content and mainly proteins in $\alpha$-helical conformation (like e.g. histone, keratin and collagen) in HaCaT cells, and more disordered and partially deregulated and degraded proteins in A5RT3 cells. Interestingly, the Raman results show different patterns for HaCaT differentiation. In addition, the discrimination of short-passed and long-passed HaCaT, together with the passage numbers, have been found to correlate linearly with the degree of tumorigenicity, an important result supporting the possibility of a positive correlation between tumorigenic transformation and primarily genetic instabilities in HaCaT cells.

Furthermore, Raman spectroscopy has been successfully applied for the monitoring of lymphoma infiltration and lymphoma histological subtypes in subjects at risk. This potential has been demonstrated evaluated using spleen tissue of the AKR/J lymphoma mouse model. The associated characteristic Raman spectral changes have been detected, and have been found to be related to key biomolecules, including amino and nucleic acids, and protein secondary structures. The benefit of using different excitation wavelengths has been highlighted. In fact this has helped to selectively reveal additional and clearer characteristic changes, including changes associated with the complex secondary structure of protein. The observation of these changes is crucial for a rapid and ultimate discrimination between healthy spleen and the histological subtypes of lymphoma infiltration in the spleen tissue of AKR/J mice. Especially, using a red laser excitation at 647 nm, resulted in both fast spectra acquisition and spectral information of high quality in this case.

Moreover, using a light sensitive Djungarian hamster model, a Raman spectroscopic approach for the study of biological rhythms in situ has been evaluated. Especially, Raman spectra of the testis tissues from Djungarian hamsters have shown that the hamsters non-responsive ((large testes)) to short-day photoperiods exhibit the same characteristic photoperiod response as the long-day control group. Interestingly, it has been revealed that short-day responsive (reduced testes) hamsters exhibit, among other spectral differences, marked and reproducible changes mainly in specific lipid bands including phospholipds, in tryptophan residues and in tyrosine residues. These molecular species are important for androgen regulation. Therefore, the associated 'Characteristic and relevant' spectral changes represent the Raman signatures of the photoperiodically induced molecular changes in the gonads of male hamsters. These molecular changes depend on the rhythmic switch in the internal biological clock resulting in seasonal regulation of the reproductive functions in the short-day responsive male Djungarian hamsters. These results demonstrate the capability of Raman spectroscopy as a rather interesting complementary or alternative approach for the study of biological rhythms.

A very important part of this work dealt with exploiting the possibility to split a unique colon carcinoma cell line CX2 into the sublines CX- and CX+. This thesis has shed light on the Raman spectroscopy potential for noninvasive and nondestructive phenotypic sorting of such similar cells sublines. This has helped to probe detailed steps of tumorigenicity and the mechanisms associated with Hsp70 chaperon properties and immune response. Ultimately, specific insights into intracellular mechanisms leading to the chaperon effect of Hsp70 and the associated phenotypic variation observed in the colon carcinoma sublines

is of paramount significance. Here, changes in the DNA/RNA pyrimidine ring modes, due to bases destacking indicative of DNA/RAN/protein binding interactions, have been found to be the most relevant and specific Raman fingerprints for the Hsp70 associated phenotypic variation between the CX- and CX+ sublines. This particularly interesting result suggests that different precursor transcription mechanisms may be the onset of the different transport pathways leading to the CX-/CX+ differential Hsp70 expression patterns at the cellular membrane. The potential of Raman spectroscopy for an overall noninvasive and nondestructive monitoring of the phenotypic variation between CX- and CX+ associated with their differential Hsp70 expression patterns, has also been demonstrated via a careful and systematic data analysis combined with robust multivariate analysis. The results of this particular contribution represent the first Raman spectroscopy characterization of the phenotypic state within an autologous CX2 tumor system of very similar sublines, paving the way for Raman label-free cell-sorting of these sublines in a near future.

Moreover, *in vivo* monitoring of drug response in the case of liver injury/fibrosis using microRaman spectroscopy has been demonstrated in this work. The livers from mouse models, including normal, alcohol injured, fibrotic, and I3C-treated liver tissues have been investigated. Raman spectral changes, indicative of liver injury/fibrosis associated biochemical changes (loss of reduced glutathione and the increase of collagen) and of the effect of I3C treatment on injured liver tissues, were observed.

Surface enhanced Raman spectroscopy (SERS) is of growing importance for biomedical applications. Therefore, part of this work dealt with the development of new types of SERS substrates as well as the investigation of metal nanoparticles with biomolecules. In this connection, a simple fabrication procedure of peanuts-like nanoparticles has been proposed. These nanoparticles form dimers and trimers, that can offer hot spots for giant enhancement of the Raman signal. Since they can be produced in a reproducible manner, they can be modified to be used as SERS sensors for biomarkers or for an eventual discovery of biomarkers. In this respect, it was also important to characterize the behavior of the key biological functions at the metal interface on a single molecule level. Therefore, as the last part of this thesis, SERS has been applied to the simplest amino acid glycine. This interesting study revealed that proteinaceous biomolecules can have a complex concentration-dependent interaction at metal interfaces. This implies that special designs should be implemented for the fabrication of nanoparticles or metal substrates that can be beneficial for surface enhanced Raman investigations of biological systems.

## *Notes*

In view of the relevance for realistic noninvasive and nondestructive sensing and visualization of important biological events, this thesis is far from being a complete story. The author acknowledges that both linear and nonlinear Raman techniques are being implemented or further developed as potential versatile tools. This thesis research focuses mostly on resolving the slightest spectral information provided by linear Raman, in order to probe even small molecular changes characteristic of key biological events. For the moment, spontaneous Raman has at least the benefit of providing this detailed and small spectral information in a noninvasive and nondestructive way, as opposed to nonlinear Raman techniques. However, despite this fact, this work also has weaknesses and insufficiencies: It is highly inefficient (with linear Raman as in this work) or even impossible (with non linear Raman) to spatially resolve the detailed and small biochemical information within, *e.g.*, the cell, cell membrane, or a cell organelle. Current nonlinear Raman techniques, although very fast and highly sensitive (but not suited for traces; like *e.g.* CARS) cannot image very weak Raman features. Probably, in a near future, technological advancement would turn nonlinear Raman techniques, especially stimulated Raman and CARS, into those tools expected to image the wealth of tiny but biologically significant hyperspectral information available in the Raman spectrum. However, most likely, spontaneous Raman and non linear Raman spectroscopy would not earn the merit to achieve hyperspectral and multiplex characterization together with temporally and spatially resolved visualization all alone. This leaves enough room for improvement, not only in the individual techniques, but also in the combination of different techniques toward a multimodal characterization approach that also includes other spectroscopic methods.

# References


[1] C.V. Raman and K.S. Krishnan. **A NEW TYPE OF SECONDARY RADIATION**. *Nature*, **121**:501–502, 1928. 1, 44

[2] Fran Adar, Michel Delhaye, and Edouard DaSilva. **Evolution of instrumentation for detection of the Raman Effect as driven by available technologies and by developing applications**, 2003. 2, 3

[3] Fran Adar, Michel Delhaye, and Edouard DaSilva. **Evolution of instrumentation for detection of the Raman Effect as driven by available technologies and by developing applications**. *Journal of Chemical Education*, **84**(1):50, 2007. 2, 3

[4] R. C. C. Leite and S. P. S. Porto. **Enhancement of Raman cross section in CdS due to resonant absorption**. *Physical Review Letters*, **17**(1):10–12, Jul 1966. 2

[5] R. C. C. Leite, J. F. Scott, and T. C. Damen. **Multiple-phonon resonant Raman scattering in CdS**. *Physical Review Letters*, **22**(15):780–782, Apr 1969.

[6] Miles V. Klein and S. P. S. Porto. **Multiple-Phonon-Resonance Raman Effect in CdS**. *Physical Review Letters*, **22**(15):782–784, Apr 1969.

[7] J. F. Scott, R. C. C. Leite, and T. C. Damen. **Resonant Raman Effect in semiconductors**. *Physical Review*, **188**(3):1285–1290, Dec 1969.

[8] J. F. Scott, T. C. Damen, W.T. Silfvast, R.C.C. Leite, and L. E. Cheesman. **Resonant Raman scattering in ZnS and ZnSe with the cadmium laser**. *Optics Communications*, **1**(8):397–399, 1970.

[9] D. Schaupp, H. Czerwinski, F. Smend, R. Wenskus, M. Schumacher, A. H. Millhouse, and H. Schenk-Strauss. **Resonant Raman scattering of synchrotron X-rays by neodymium: Observation of fine structure in K-L-RRS and of K-N-RRS**. *Zeitschrift für Physik A Hadrons and Nuclei*, **319**:1–7, 1984. 2

[10] A. James McQuillan. **The discovery of surface-enhanced Raman scattering**. *Notes and Records of the Royal Society*, **63**(1):105–109, March 20, 2009 2009. 3

[11] M. Fleischmann, P.J. Hendra, and A.J. McQuillan. **Raman spectra of pyridine adsorbed at a silver electrode**. *Chemical Physics Letters*, **26**(2):163 –166, 1974.

[12] Patrick Hendra. **Editorial: A Special Edition featuring SERS**. *Internet Journal of Vibrational Spectroscopy*, **4**(2):1, 2000.

[13] David L. Jeanmaire and Richard P. Van Duyne. **Surface raman spectroelectrochemistry: Part I. Heterocyclic, aromatic, and aliphatic amines adsorbed on the anodized silver electrode**. *Journal of Electroanalytical Chemistry*, **84**(1):1–20, 1977.

[14] M. Grant Albrecht and J. Alan Creighton. **Anomalously intense Raman spectra of pyridine at a silver electrode**. *Journal of the American Chemical Society*, **99**(15):5215–5217, 1977. 3

[15] R. P. Van Duyne. **Laser excitation of Raman scattering from adsorbed molecules on electrode surfaces**. In C. Bradley Moore, editor, *Biochemical Applications of Lasers*, **4**, page 10185, New York, 1979. Academic Press.

[16] Christy L. Haynes, Chanda Ranjit Yonzon, Xiaoyu Zhang, and Richard P. Van Duyne. **Surface-enhanced Raman sensors: early history and the development of sensors for quantitative biowarfare agent and glucose detection**. *Journal of Raman Spectroscopy*, **36**(6-7):471–484, 2005. 3

[17] K. Kneipp, Y. Wang, H. Kneipp, L. T. Perelman, I. Itzkan, R. Dasari, and M. S. Feld. **Single molecule detection using surface-enhanced Raman scattering (SERS)**. *Physical Review Letters*, **78**(9):1667–1670, Mar 3 1997. 3, 28, 45

[18] K. Kneipp, H. Kneipp, V. B. Kartha, R. Manoharan, G. Deinum, I. Itzkan, R. R. Dasari, and M. S. Feld. **Detection and identification of a single DNA base molecule using surface-enhanced Raman scattering (SERS)**. *Physical Review E*, **57**(6):R6281–R6284, Jun 1998.

[19] K. Kneipp, H. Kneipp, R. Manoharan, E. B. Hanlon, I. Itzkan, R. R. Dasari, and M. S. Feld. **Extremely large enhancement factors in surface-enhanced Raman scattering for molecules on colloidal gold clusters**. *Applied Spectroscopy*, **52**(12):1493–1497, Dec 1998. 28, 161

[20] K. Kneipp, H. Kneipp, R. Manoharan, I. Itzkan, R. R. Dasari, and M. S. Feld. **Near-infrared surface-enhanced Raman scattering can detect single molecules and observe 'hot' vibrational transitions**. *Journal of Raman Spectroscopy*, **29**(8):743–747, Aug 1998.

[21] K. Kneipp, H. Kneipp, R. Manoharan, I. Itzkan, R. R. Dasari, and M. S. Feld. **Surface-enhanced Raman scattering (SERS) - a new tool for single molecule detection and identification**. *Bioimaging*, **6**(2):104–110, Jun 1998. 4, 25, 33

[22] K. Kneipp, H. Kneipp, I. Itzkan, R. R. Dasari, and M. S. Feld. **Surface-enhanced non-linear Raman scattering at the single-molecule level**. *Chemical Physics*, **247**(1):155–162, Aug 1 1999.

[23] Shuming Nie and Steven R. Emory. **Probing single molecules and single nanoparticles by surface-enhanced raman scattering**. *Science*, **275**(5303):1102–1106, Feb 21 1997. 28, 45, 161

[24] K. Kneipp and H. Kneipp. **Surface enhanced Raman scattering - A tool for ultrasensitive trace analysis**. *Canadian Journal of Analytical Sciences and Spectroscopy*, **48**(2):125–131, 2003.

[25] K. Kneipp, H. Kneipp, and J. Kneipp. **Surface-enhanced Raman scattering in local optical fields of silver and gold nanoaggregatess - From single-molecule Raman spectroscopy to ultrasensitive probing in live cells**. *Accounts of Chemical Research*, **39**(7):443–450, Jul 18 2006. 3, 29

[26] Richard D. Schaller, Joseph Ziegelbauer, Lynn F. Lee, Louis H. Haber, and Richard J. Saykally. **Chemically selective imaging of subcellular structure in human hepatocytes with coherent anti-stokes Raman scattering (CARS) near-field scanning optical microscopy (NSOM)**. *Journal of Physical Chemistry B*, **106**(34):8489–8492, Aug 29 2002. 4, 25, 33, 45

[27] S. W. E. van de Poll, D. J. M. Delsing, J. W. Jukema, H. M. G. Princen, L. M. Havekes, G. J. Puppels, and A. van der Laarse. **Raman spectroscopic investigation of atorvastatin, amlodipine, and both on atherosclerotic plaque development in APOE*3 Leiden transgenic mice**. *Atherosclerosis*, **164**(1):65–71, Sep 2002.

[28] Kerstin Ramser, Erik J. Bjerneld, Camilla Fant, and Mikael Käll. **Importance of substrate and photo-induced effects in Raman spectroscopy of single functional erythrocytes**. *Journal of Biomedical Optics*, **8**(2):173–178, Apr 2003.

[29] T. Vo-Dinh, F. Yan, and M. B. Wabuyele. **Surface-enhanced Raman scattering for medical diagnostics and biological imaging**. *Journal of Raman Spectroscopy*, **36**(6-7):640–647, Jun-Jul 2005. 33

[30] W. Xie, L. Wang, Y. Y. Zhang, L. Su, A. G. Shen, J. Q. Tan, and J. M. Hu. **Nuclear targeted nanoprobe for single living cell detection by surface-enhanced Raman scattering**. *Bioconjugate Chemistry*, **20**(4):768–773, Apr 2009. 4, 25, 33, 151

[31] G. Placzek. *Rayleigh-Streuung und Raman-Effekt*, **6** of *in Handbuch der Radiologie*. E. Marx, Akademische Verlag, Leipzig, 2 edition, 1934. (NTIS UCRL-Trans-526(L)). 8, 17

# REFERENCES


[32] D. A. Long. *Raman spectroscopy*. McGraw-Hill, UK, 1977.

[33] Derek. A. Long. *The Raman effect - A unified treatment of the theory Raman scattering by Molecules*. John Wiley & Sons, 2002. 45

[34] Bernhard Schrader, editor. *Infrared and Raman Spectroscopy, Methods and Applications*. VCH Verlagsgesellschaft, Weinheim, 1995. 8, 17

[35] W. H. Yang and G. C. Schatz. **Abinitio and semiempirical molecular-orbital studies of surface enhanced and bulk hyper-Raman scattering from pyridine**. *Journal of Chemical Physics*, **97**(5):3831–3845, Sep 1 1992. 28, 45

[36] P. F. Liao and A. Wokaun. **Lightning rod effect in surface enhanced Raman scattering**. *Journal of Chemical Physics*, **76**:751–752, 1982.

[37] C. Oubre and P. Nordlander. **Optical properties of metallodielectric nanostructures calculated using the finite difference time domain method**. *Journal of Physical Chemistry B*, **108**(46):17740–17747, Nov 18 2004.

[38] Patrik Johansson. **Illustrative direct ab initio calculations of surface Raman spectra**. *Physical Chemistry Chemical Physics*, **7**(3):475–482, 2005. 45

[39] L. L. Zhao, L. Jensen, and G. C. Schatz. **Pyridine-Ag-20 cluster: A model system for studying surface-enhanced Raman scattering**. *Journal of the American Chemical Society*, **128**(9):2911–2919, Mar 8 2006. 28

[40] K. Kneipp, H. Kneipp, R. R. Dasari, and M. S. Feld. **Single molecule Raman spectroscopy using silver and gold nanoparticles**. *Indian Journal of Physics and Proceedings of the Indian Association for the Cultivation of Science-Part B*, **77B**(1):39–47, Feb 2003. 28

[41] K. Li, M. I. Stockman, and D. J. Bergman. **Self-similar chain of metal nanospheres as an efficient nanolens**. *Physical Review Letters*, **91**(22):227402, Nov 28 2003. 28

[42] J. A. Creighton, C. G. Blatchford, and M. G. Albrecht. **Plasma resonance enhancement of Raman-scattering by pyridine adsorbed on silver or gold sol particles of size comparable to the excitation wavelength**. *Journal of the Chemical Society-Faraday Transactions 2*, **75**:790–798, 1979. 29, 163

[43] Sudipa Panigrahi, Snigdhamayee Praharaj, Soumen Basu, Sujit Kumar Ghosh, Subhra Jana, Surojit Pande, Tuan Vo-Dinh, Hongjin Jiang, and Tarasankar Pal. **Self-assembly of silver nanoparticles: Synthesis, stabilization, optical properties, and application in surface-enhanced Raman scattering**. *Journal of Physical Chemistry B*, **110**(27):13436–13444, Jul 13 2006. 30

[44] David S. Dos Santos Jr., Paul J. G. Goulet, Nicholas P. W. Pieczonka, Osvaldo N. Oliveira Jr., and Ricardo F. Aroca. **Gold nanoparticle embedded, self-sustained chitosan films as substrates for surface-enhanced Raman scattering**. *Langmuir*, **20**(23):10273–7, Nov 9 2004.

[45] P. Nordlander, C. Oubre, E. Prodan, K. Li, and M. I. Stockman. **Plasmon hybridizaton in nanoparticle dimers**. *Nano Letters*, **4**(5):899–903, May 2004.

[46] J. B. Lassiter, J. Aizpurua, L. I. Hernandez, D. W. Brandl, I. Romero, S. Lal, J. H. Hafner, P. Nordlander, and N. J. Halas. **Close encounters between two nanoshells**. *Nano Letters*, **8**(4):1212–1218, Apr 2008. 30, 161

[47] P. J. Caspers, G. W. Lucassen, E. A. Carter, H. A. Bruining, and G. J. Puppels. **In vivo confocal Raman microspectroscopy of the skin: Noninvasive determination of molecular concentration profiles**. *Journal of Investigative Dermatology*, **116**(3):434–442, Mar. 2001. 32, 40, 45, 46

[48] M. Rajadhyaksha, G. Menaker, S. Gonzalez, J. Zavislan, and P. Dwyer. **Confocal cross-polarized imaging of skin cancers to potentially guide mohs micrographic surgery**. *Optics and Photonics News*, **12**(12):30, December 2001. 32, 40

[49] Andreas Zumbusch, Gary R. Holtom, and X. Sunney Xie. **Three-Dimensional Vibrational Imaging by Coherent Anti-Stokes Raman Scattering**. *Physical Review Letters*, **82**(20):41424145, 17 May 1999. 32

[50] Ji xin Cheng, Andreas Volkmer, Lewis D. Book, , and X. Sunney Xie. **An Epi-Detected Coherent Anti-Stokes Raman Scattering (E-CARS) Microscope with High Spectral Resolution and High Sensitivity**. *Journal of Physical Chemistry B*, **105**(7):1277–1280, 2001.

[51] J. X Cheng, Y. K. Jia, G. Zheng, and X. S. Xie. **Laser-scanning coherent anti-Stokes Raman scattering microscopy and applications to cell biology.** *Biophysical Journal*, **83**:502509, 2002. 32

[52] Conor L. Evans and X. Sunney Xie. **Coherent Anti-Stokes Raman Scattering Microscopy: Chemical Imaging for Biology and Medicine**. *Annual Review of Analytical Chemistry*, **1**(1):883–909, 2008. 33

[53] Andrew Downes and Alistair Elfick. **Raman Spectroscopy and Related Techniques in Biomedicine**. *Sensors*, **10**:1871–1889, 2010. 33, 40

[54] Musundi B. Wabuyele, Fei Yan, Guy D. Griffin, and Tuan Vo-Dinh. **Hyperspectral surface-enhanced Raman imaging of labeled silver nanoparticles in single cells**. *Review of Scientific Instruments*, **76**(6):063710–063716, Jun 2005. 33, 34

[55] Han-Wei Wang, Ning Bao, Thuc L. Le, Cheng Lu, and Ji-Xin Cheng. **Microfluidic CARS cytometry**. *Optics Express*, **16**(8):5782–5789, April 2008. 33, 108, 129

[56] C. Freudiger, W. Min, B. Saar, S. Lu, G. Holtom, C. He, J. Tsai, J. Kang, and X. Xie. **Label-free biomedical imaging with high sensitivity by stimulated Raman scattering microscopy**. *Science*, **322**:18571861, 2008. 34

[57] Glauco R. Souza, Dawn R. Christianson, Fernanda I. Staquicini, Michael G. Ozawa, Evan Y. Snyder, Richard L. Sidman, J. Houston Miller, Wadih Arap, and Renata Pasqualini. **Networks of gold nanoparticles and bacteriophage as biological sensors and cell-targeting agents**. *Proceedings of the National Academy of Sciences of the United States of America*, **103**(5):1215–1220, Jan 31 2006. 34

[58] U. Utzinger and R. R. Richards-Kortum. **Fiber optic probes for biomedical optical spectroscopy**. *Journal of Biomedical Optics*, **8**(1):121–147, Jan 2003. 34, 40

[59] Stanley L. Robbins, Ramzi S. Cotran, and Vinay Kumar. *Pathologic Basis of Disease*. W.B. Saunders Company, 3rd edition edition, January 1984. 40

[60] T. Falguieres, M. Maak, Weyhern C. von, M. Sarr, X. Sastre, M.F. Poupon, S. Robine, L. Johannes, and K.P. Janssen. **Human colorectal tumors and metastases express Gb3 and can be targeted by an intestinal pathogen-based delivery tool**. *Molecular Cancer Therapy*, **7**(8):2498–2508, August 2008. 40, 105

[61] Anita Mahadevan-Jansen and Rebecca Richards-Kortum. **Raman spectroscopy for the detection of cancers and precancers**. *Journal of Biomedical Optics*, **1**(1):31–70, January 1996. 40, 45, 59, 60, 61, 97, 108, 116, 117, 118, 122, 128, 130, 131, 132, 145, 146

[62] W. M. White, M. Rajadhyaksha, S. Gonzalez, R. L. Fabian, and R. R. Anderson. **Noninvasive imaging of human oral mucosa in vivo by confocal reflectance microscopy**. *Laryngoscope*, **109**(10):1709–1717, Oct 1999.

[63] N. Stone, P. Stavroulaki, C. Kendall, M. Birchall, and H. Barr. **Raman spectroscopy for early detection of laryngeal malignancy: Preliminary results**. *Laryngoscope*, **110**(10):1756–1763, Oct 2000. 45, 60, 61

[64] L. P. Choo-Smith, H. G. Edwards, H. P. Endtz, J. M. Kros, F. Heule, H. Barr, Jr. Robinson, J. S., H. A. Bruining, and G. J. Puppels. **Medical applications of Raman spectroscopy: from proof of principle to clinical implementation**. *Biopolymers*, **67**(1):1–9, 2002. DA - 20020213. 40, 45, 47, 60, 108, 117

[65] Pothur R. Srinivas, Mukesh Verma, Yinming Zhao, and Sudhir Srivastava. **Proteomics for cancer biomarker discovery**. *Clinical Chemistry*, **48**(8):1160–1169, Aug 2002.

[66] Lilian de Oliveira Nunes, Arton Abraho Martin, Landulfo Silveira Jr., and Marcelo Zampieri. **FT-Raman spectroscopy study for skin cancer diagnosis**. *Spectroscopy*, **17**(2):597–602, 2003. 40

[67] G. Perna, M. Lastella, M. Lasalvia, E. Mezzenga, and V. Capozzi. **Raman spectroscopy and atomic force microscopy study of cellular damage in human keratinocytes treated with HgCl2**. *Journal of Molecular Structure*, **834**:182–187, May 27 2007. 40

[68] S. Keller, B. Schrader, A. Hoffmann, W. Schrader, K. Metz, A. Rehlaender, J. Pahnke, M. Ruwe, and W. Budach. **Application of near-infrared Fourier-transform Raman spectroscopy in medical research**. *Journal of Raman Spectroscopy*, **25**(7-8):663–671, Jul-Aug 1994. 40

[69] U. Utzinger, D. L. Heintzelman, A. Mahadevan-Jansen, A. Malpica, M. Follen, and R. Richards-Kortum. **Near-infrared Raman spectroscopy for in vivo detection of cervical precancers**. *Applied Spectroscopy*, **55**(8):955–959, Aug 2001. 40

[70] U. Utzinger, M. Bueeler, S. Oh, D. L. Heintzelman, E. S. Svistun, M. Abd-El-Barr, A. Gillenwater, and R. Richards-Kortum. **Optimal visual perception and detection of oral cavity neoplasia**. *IEEE Transactions on Biomedical Engineering*, **50**(3):396–399, Mar 2003.

[71] A. Mahadevan-Jansen, M. F. Mitchell, N. Ramanujam, A. Malpica, S. Thomsen, U. Utzinger, and R. Richards-Kortum. **Near-infrared Raman spectroscopy for in vitro detection of cervical precancers**. *Photochemistry and Photobiology*, **68**(1):123–32, Jul 1998. 45, 60, 61, 117, 122

[72] A. Mahadevan-Jansen, M. F. Mitchell, N. Ramanujam, U. Utzinger, and R. Richards-Kortum. **Development of a fiber optic probe to measure NIR Raman spectra of cervical tissue in vivo**. *Photochemistry and Photobiology*, **68**(3):427–431, Sep 1998.

[73] N. Shah, A. Cerussi, C. Eker, J. Espinoza, J. Butler, J. Fishkin, R. Hornung, and B. Tromberg. **Noninvasive functional optical spectroscopy of human breast tissue**. *Proceedings of the National Academy of Sciences of the United States of America*, **98**(8):4420–4425, Apr 10 2001.

[74] Katrin Kneipp, Abigail S. Haka, Harald Kneipp, Kamran Badizadegan, Noriko Yoshizawa, Charles Boone, Karen E. Shafer-Peltier, Jason T. Motz, Ramachandra R. Dasari, and Michael S. Feld. **Surface-enhanced Raman spectroscopy in single living cells using gold nanoparticles**. *Applied Spectroscopy*, **56**(2):150–154, Feb 2002. 40, 45

[75] J. Smith, C. Kendall, A. Sammon, J. Christie-Brown, and N. Stone. **Raman spectral mapping in the assessment of axillary lymph nodes in breast cancer**. *Technology in Cancer Research and Treatment*, **2**(4):327–331, Aug 2003. 40

[76] J. Smith, N. Stone, C. Kendall, J. Christie-Brown, N. Shepherd, A. Sammon, and H. Barr. **Raman spectroscopy: a novel optical technique for the diagnosis and management of carcinoma of the oesophagus and breast, and lymph node metastases**. *British Journal of Surgery*, **90**(5):637–637, May 2003. 40

[77] L. M. McIntosh, M. Jackson, H. H. Mantsch, J. R. Mansfield, A. N. Crowson, and J. W. P. Toole. **Near-infrared spectroscopy for dermatological applications**. *Vibrational Spectroscopy*, **28**(1):53–58, Feb 28 2002. 40

[78] Annieke Nijssen, Tom C Bakker Schut, Freerk Heule, Peter J Caspers, Donal P Hayes, Martino H A Neumann, and Gerwin J Puppels. **Discriminating basal cell carcinoma from its surrounding tissue by Raman spectroscopy**. *Journal of Investigative Dermatology*, **119**(1):64–69, Jul 2002. 40, 45, 46, 47, 55, 60

[79] Shoji Kaminaka, Hiroya Yamazaki, Toshiaki Ito, Eiichi Kohda, and Hiro O. Hamaguchi. **Near-infrared Raman spectroscopy of human lung tissues: possibility of molecular-level cancer diagnosis**. *Journal of Raman Spectroscopy*, **32**(2):139–141, Feb 2001.

[80] P. Crow, N. Stone, C. Kendall, J. Uff, A. Ritchie, and M. Wright. **Optical diagnostics in bladder cancer: The use of Raman spectroscopy to differentiate between bladder pathologies in vitro**. *Journal of Urology*, **169**(4):225–225, Apr 2003. 40

[81] P. Crow, N. Stone, C. A. Kendall, J. S. Uff, J. A. M. Farmer, H. Barr, and M. P. J. Wright. **The use of Raman spectroscopy to identify and grade prostatic adenocarcinoma in vitro**. *British Journal of Cancer*, **89**(1):106–108, Jul 7 2003.

[82] P. Crow, N. Stone, C. A. Kendall, R. A. Persad, and M. P. J. Wright. **Optical diagnostics in urology: current applications and future prospects**. *Bju International*, **92**(4):400–407, Sep 2003.

[83] P. Crow, B. Barrass, M. H. Prieto, C. Kendall, M. Wright, and N. Stone. **The use of Raman spectroscopy to differentiate between different cultured prostate cancer cell lines in vitro**. *Journal of Urology*, **171**(4):114–114, Apr 2004. 40

[84] Christoph Krafft, Snezana Miljanic, Stephan B. Sobottka, Gabriele Schackert, and Reiner Salzer. **Near-infrared Raman spectroscopy to study the composition of human brain tissue and tumors**. In Georges A. Wagnieres, editor, *Diagnostic Optical Spectroscopy in Biomedicine II*, **5141** of *Proc. SPIE*, pages 230–236, Munich, Germany, 2003. SPIE. 40, 45, 60, 61, 122

[85] N. Uzunbajakava, A. Lenferink, Y. Kraan, E. Volokhina, G. Vrensen, J. Greve, and C. Otto. **Nonresonant confocal Raman imaging of DNA and protein distribution in apoptotic cells**. *Biophysical Journal*, **84**(6):3968–3981, Jun 2003. 40

[86] N. Uzunbajakava, A. Lenferink, Y. Kraan, B. Willekens, G. Vrensen, J. Greve, and C. Otto. **Nonresonant Raman imaging of protein distribution in single human cells**. *Biopolymers*, **72**(1):1–9, 2003. 40

[87] R. Manoharan, J. J. Baraga, M. S. Feld, and R. P. Rava. **Quantitative histochemical analysis of human artery using Raman spectroscopy**. *J. Photochem. Photobiol. B*, **16**(2):211–233, 1992. DA - 19930202. 40

[88] Ramasamy Manoharan, Yang Wang, and Michael S. Feld. **Histochemical analysis of biological tissues using Raman spectroscopy**. *Spectrochimica Acta Part A-Molecular and Biomolecular Spectroscopy*, **52**(2):215–249, February 1996. 40, 45, 60, 61, 95, 108, 116, 117, 118, 122, 128

[89] Andrew Downes, Rabah Mouras, and Alistair Elfick. **Optical spectroscopy for non-invasive monitoring of stem cell differentiation**. *Journal of Biomedicine and Biotechnology*, **2010**:10 pages, 2010. 40

[90] Patrice. Donfack, Maren. Rehders, Klaudia. Brix, Petra. Boukamp, and Arnulf. Materny. **Micro Raman spectroscopy for monitoring alterations between human skin keratinocytes HaCaT and their tumorigenic derivatives A5RT3-toward a Raman characterization of a skin carcinoma model**. *Journal of Raman Spectroscopy*, **41**(1):16–26, 2010. 44, 108, 113, 122, 132, 135, 136

[91] Paul A. Khavari. **Modelling cancer in human skin tissue**. *Nature Reviews Cancer*, **6**(4):270–280, Apr 2006. 44, 47

[92] Margareta M. Mueller, Wolfgang Peter, Marion Mappes, Andrea Huelsen, Heinrich Steinbauer, Petra Boukamp, Michael Vaccariello, Jonathan Garlick, and Norbert E. Fusenig. **Tumor progression of skin carcinoma cells in vivo promoted by clonal selection, mutagenesis, and autocrine growth regulation by granulocyte colony-stimulating factor and granulocyte-macrophage colony-stimulating factor**. *American journal of pathology*, **159**(4):1567–1579, Oct 2001. 44, 45, 47, 48, 54

[93] Benjamin G. Janesko and Gustavo E. Scuseria. **Surface enhanced Raman optical activity of molecules on orientationally averaged substrates: Theory of electromagnetic effects**. *Journal of Chemical Physics*, **125**(12):124704–124715, Sep 28 2006. 45

[94] Alberto Vivoni, Ronald L. Birke, Richard Foucault, and John R. Lombardi. **Ab initio frequency calculations of pyridine adsorbed on an adatom model of a SERS active site of a silver surface**. *Journal of Physical Chemistry B*, **107**:5547–5557, 2003.

[95] Juan F. Arenas, Juan Soto, Daniel Pelaez, David J. Fernandez, and Juan C. Otero. **Understanding complex surface-enhanced Raman scattering, using quantum chemical calculations**. *International Journal of Quantum Chemistry*, **104**:681–694, 2005.

[96] K. Kneipp, H. Kneipp, G. Deinum, I. Itzkan, R. R. Dasari, and M. S. Feld. **Single-molecule detection of a cyanine dye in silver colloidal solution using near-infrared surface-enhanced Raman scattering**. *Applied Spectroscopy*, **52**(2):175–178, Feb 1998. 45

# REFERENCES


[97] Christoph Krafft, Thomas Knetschke, Axel Siegner, Richard H. W. Funk, and Reiner Salzer. **Mapping of single cells by near infrared Raman microspectroscopy**. *Vibrational Spectroscopy*, **32**(1):75–83, Aug 5 2003. 45

[98] Aritake Mizuno, Takashi Hayashi, Kouichi Tashibu, Shuichi Maraishi, Kazuaki Kawauchi, and Yukihiro Ozaki. **Near-Infrared Ft-Raman Spectra of the Rat-Brain Tissues**. *Neuroscience Letters*, **141**(1):47–52, Jul 6 1992.

[99] J. Choi, J. Choo, H. Chung, D. G. Gweon, J. Park, H. J. Kim, S. Park, and C. H. Oh. **Direct observation of spectral differences between normal and basal cell carcinoma (BCC) tissues using confocal Raman microscopy**. *Biopolymers*, **77**(5):264–272, Apr 5 2005. 45, 46, 60

[100] M. Gniadecka, H. C. Wulf, N. N. Mortensen, O. F. Nielsen, and D. H. Christensen. **Diagnosis of basal cell carcinoma by Raman spectroscopy**. *Journal of Raman Spectroscopy*, **28**(2-3):125–129, Feb-Mar 1997. 46, 47, 55, 60, 61, 94, 95, 96, 108, 117, 122

[101] M. Gniadecka, H. C. Wulf, O. F. Nielsen, D. H. Christensen, and J. Hercogova. **Distinctive molecular abnormalities in benign and malignant skin lesions: Studies by Raman spectroscopy**. *Photochemistry and Photobiology*, **66**(4):418–423, Oct 1997. 46, 47, 55, 117

[102] Y. K. Min, T. Yamamoto, E. Kohda, T. Ito, and H. Hamaguchi. **1064 nm near-infrared multichannel Raman spectroscopy of fresh human lung tissues**. *Journal of Raman Spectroscopy*, **36**(1):73–76, Jan 2005.

[103] Zhiwei Huang, Annette McWilliams, Harvey Lui, David I. McLean, Stephen Lam, and Haishan Zeng. **Near-infrared Raman spectroscopy for optical diagnosis of lung cancer**. *International Journal of Cancer*, **107**(6):1047–1052, Dec 20 2003. 61, 145

[104] Sharon R. Hawi, William B. Campbell, André Kajdacsy-Balla, Robert Murph, Fran Adar, and Kasem Nithipatikom. **Characterization of normal and malignant human hepatocytes by Raman microspectroscopy**. *Cancer Letters*, **110**(1-2):35–40, Dec 20 1996. 45, 60

[105] I. Notingher, S. Verrier, H. Romanska, A. E. Bishop, J. M. Polak, and L. L. Hench. **In situ characterisation of living cells by Raman spectroscopy**. *Spectroscopy-An International Journal*, **16**(2):43–51, 2002.

[106] Xiaoling Gao, Ian S. Butler, and Richard Kremer. **A near-infrared Fourier transform Raman spectroscopy of epidermal keratinocytes: changes in the protein-DNA structure following malignant transformation**. *Spectrochimica Acta Part A-Molecular and Biomolecular Spectroscopy*, **61**(1-2):27–35, Jan 1 2005. 47

[107] C. K. Johansson, D. H. Christensen, and O. F. Nielsen. **Near-infrared Fourier transform Raman spectral studies of human skin**. *Danski Kemi*, **80**(8):12–13, 1999. 46, 60, 61

[108] Abigail S. Haka, Karen E. Shafer-Peltier, Maryann Fitzmaurice, Joseph Crowe, Ramachandra R. Dasari, and Michael S. Feld. **Diagnosing breast cancer by using Raman spectroscopy**. *P. Natl. Acad. Sci. USA*, **102**(35):12371–12376, 2005. 45, 60, 141, 148

[109] B. G. Frushour and J. L. Koenig. **Raman spectroscopic study of poly(beta-benzyl-L-aspartate) and sequential polypeptides**. *Biopolymers*, **14**(10):2115–2135, 1975. 60, 61

[110] Dieter Naumann. **FT-infrared and FT-Raman spectroscopy in biomedical research**. *Applied Spectroscopy Reviews*, **36**(2&3):239–298, 2001. 60, 61, 116, 122

[111] Monika Gniadecka, Peter Alshede Philipsen, Sigurdur Sigurdsson, Sonja Wessel, Ole Faurskov Nielsen, Daniel Højgaard. Christensen, Jana Hercogova, Kristian Rossen, Henrik Klem Thomsen, Robert Gniadecki, Lars Kai Hansen, and Hans Christian Wulf. **Melanoma diagnosis by Raman spectroscopy and neural networks: Structure alterations in proteins and lipids in intact cancer tissue**. *Journal of Investigative Dermatology*, **122**(2):443–449, Feb 2004. 45, 60, 61

[112] Tissa R Hata, Theresa A Scholz, Igor V Ermakov, Robert W McClane, Frederick Khachik, Werner Gellermann, and Lynn K Pershing. **Non-invasive raman spectroscopic detection of carotenoids in human skin**. *Journal of Investigative Dermatology*, **115**(3):441–8, Sep 2000. 46, 60, 61

[113] N. Stone, C. Kendall, J. Smith, P. Crow, and H. Barr. **Raman spectroscopy for identification of epithelial cancers**. *Faraday Discussions*, **126**:141–157, 2004. 45, 60, 61, 97

[114] Jian Dong, Zhu-Li Wan, Ying-Chi Chu, Satoe N. Nakagawa, Panayotis G. Katsoyannis, Michael A. Weiss, and Paul R Carey. **Isotope-edited Raman spectroscopy of proteins: A general strategy to probe individual peptide bonds with application to insulin**. *Journal of the American Chemical Society*, **123**(32):7919–7920, Aug 15 2001. 61

[115] Run Zheng, Xiaojing Zheng, Jian Dong, and Paul R. Carey. **Proteins can convert to beta-sheet in single crystals**. *Protein Science*, **13**(5):1288–1294, May 2004. 61

[116] S. Fendel and B. Schrader. **Investigation of skin and skin lesions by NIR-FT-Raman spectroscopy**. *Fresenius Journal of Analytical Chemistry*, **360**(5):609–613, Mar 1998. 45, 46, 60

[117] Monika Gniadecka, Hans C. Wulf, Ole F. Nielsen, Daniel H. Christensen, and Jana Hercogova. **Potential of NIR-FT Raman spectroscopy for the diagnosis of malignant melanoma**. In Pedro Carmona, Raquel Navarro, and Antonio Hernanz, editors, *Spectroscopy of biological molecules: modern trends*, Seventh European Conference on Spectroscopy of Biological Molecules, pages 449–450. Springer, Madrid, 1997. Selected papers presented at the 1997 European Conference on Spectroscopy of Biological Molecules, the seventh in a biennial series of conferences. 60, 61

[118] Nicholas Stone, Catherine Kendall, Neil Shepherd, Paul Crow, and Hugh Barr. **Near-infrared Raman spectroscopy for the classification of epithelial pre-cancers and cancers**. *Journal of Raman Spectroscopy*, **33**(7):564–573, 2002. 45, 60, 61, 97, 108, 117, 118, 122, 128

[119] G. J. Puppels, H. S. Garritsen, G. M. Segers-Nolten, F. F. de Mul, and J. Greve. **Raman microspectroscopic approach to the study of human granulocytes**. *Biophysical Journal*, **60**(5):1046–1056, 1991. 45, 61, 108, 118, 122, 131

[120] P Boukamp, RT Petrussevska, D Breitkreutz, J Hornung, A Markham, and NE Fusenig. **Normal keratinization in a spontaneously immortalized aneuploid human keratinocyte cell line**. *Journal of Cell Biology*, **106**:761–771, 1988. 45, 48, 54, 59

[121] K. Christian Schuster, Ingo Reese, Eva Urlaub, J. Richard Gapes, and Bernhard Lendl. **Multidimensional information on the chemical composition of single bacterial cells by confocal Raman microspectroscopy**. *Analytical Chemistry*, **72**:5529–5534, 2000. 46

[122] M Lastella, M Lasalvia, G Perna, P F Biagi, and V. Capozzi. **Atomic force microscopy study on human keratinocytes treated with $HgCl_2$**. *Journal of Physics: Conference Series*, **61**(1):920–925, 2007. 47, 55

[123] Petra Boukamp, Susanne Popp, Susanne Altmeyer, Andrea Hülsen, Clare Fasching, Thomas Cremer, and Norbert E. Fusenig. **Sustained nontumorigenic phenotype correlates with a largely stable chromosome content during long-term culture of the human keratinocyte line HaCaT**. *Genes, Chromosomes and Cancer*, **19**:201–214, 1997. 54

[124] Petra Boukamp, Eric J. Stanbridge, Debra Yin Foo, Peter A. Cerutti, and Norbert E. Fusenig. **c-Ha-ras oncogene expression in immortalized human keratinocytes (HaCaT) alters growth potential in vivo but lacks correlation with malignancy**. *Cancer Research*, **50**(9):2840–2847, May 1990. 54

[125] Petra Boukamp, S. Popp, K. Bleuel, E. Tomakidi, A. Bürkle, and N. E. Fusenig. **Tumorigenic conversion of immortal human skin keratinocytes (HaCaT) by elevated temperature**. *Oncogene*, **18(41)**:5638–5645, 1999. 54

[126] K. Wischermann, S. Popp, S. Moshir, K. Scharfetter-Kochanek, M. Wlaschek, F. de Gruijl, W. Hartschuh, R. Greinert, B. Volkmer, A. Faust, A. Rapp, P. Schmezer, and P. Boukamp. **UVA radiation causes DNA strand breaks, chromosomal aberrations and tumorigenic transformation in HaCaT skin keratinocytes**. *Oncogene*, **27**(31):4269–4280, Jul 17 2008. 54

[127] Rachel E. Kast, Gulay K. Serhatkulu, Alex Cao, Abhilash K. Pandya, Houbei Dai, Jagdish S. Thakur, Vaman M. Naik, Ratna Naik, Michael D. Klein, Gregory W. Auner, and Raja Rabah. **Raman spectroscopy can differentiate malignant tumors from normal breast tissue and detect early neoplastic changes in a mouse model**. *Biopolymers*, **89**(3):235–241, 2008. 61, 122

[128] S. K. Chattopadhyay, W. P. Rowe, N. M. Teich, and D. R. Lowy. **Definitive evidence that the murine C-type virus inducing locus Akv-1 is viral genetic material**. *Proceedings of the National Academy of Sciences of the United States of America*, **72**:906–910, 1975. 65

[129] J. W. Hartley, N. K. Wolford, L. J. Old, and W. P. Rowe. **A new class of murine leukemia virus associated with development of spontaneous lymphomas**. *Proceedings of the National Academy of Sciences of the United States of America*, **74**:789–792, 1977.

[130] D. Steffen, S. Bird, W. P. Rowe, and R. A. Weinberg. **Identification of DNA fragments carrying ecotropic proviruses of AKR mice**. *Proceedings of the National Academy of Sciences of the United States of America*, **76**:4554–4558, 1979. 65

[131] Dieter Näf, Debra M. Krupke, John P. Sundberg, Janan T. Eppig, and Carol J. Bult. **The mouse tumor biology database: A public resource for cancer genetics and pathology of the mouse**. *Cancer Research*, **62**:1235–1240, March 2002. 65

[132] D. Malkin, F. P. Li, L. C. Strong, J. F. J. Fraumeni, C. E. Nelson, D. H. Kim, J. Kassel, M. A. Gryka, F. Z. Bischoff, and M. A. Tainsky. **Germ line p53 mutations in a familial syndrome of breast cancer, sarcomas, and other neoplasms**. *Science*, **250:**:1233–1238, 1990. 67

[133] A. M. Sommer and A. Lerchl. **The risk of lymphoma in AKR/J mice does not rise with life long exposure to 50 Hz magnetic fields**. *Radiation Research*, **162**:194–200, 2004. 67, 68, 69, 70, 77, 78

[134] Angela Sommer, Joachim Streckert, Andreas Bitz, Volkert Hansen, and Alexander Lerchl. **No effects of GSM-modulated 900 MHz electromagnetic fields on survival rate and spontaneous development of lymphoma in female AKR/J mice**. *BMC Cancer*, **4**(1):77, 2004. 69, 78, 80

[135] Angela M. Sommer, Andreas K. Bitz, Joachim Streckert, Volkert W. Hansen, and Alexander Lerchl. **Lymphoma development in mice chronically exposed to UMTS-modulated radiofrequency rlectromagnetic fields**. *Radiation Research*, **168**(1):72–80, 2007. 67, 68, 69, 77, 78, 80

[136] W. Drobyski, L. Baxter-Lowe, and R. Truitt. **Detection of residual leukemia by polymerase chain reaction and sequence-specific oligonucleotide probe hybridization after allogeneic bone marrow transplantation for AKR leukemia: A murine model for minimal residual disease**. *Blood*, **81**:551–559, 1993. 67

[137] Eoghan Ó Faoláin, Mary B. Hunter, Joe M. Byrne, Peter Kelehan, Helen A. Lambkin, Hugh J. Byrne, and Fiona M. Lyng. **Raman spectroscopic evaluation of efficacy of current paraffin wax section dewaxing agents**. *Journal of Histochemistry and Cytochemistry*, **53**(1):121–9, Jan 2005. 71

[138] Eoghan Ó Faoláin, Mary B. Hunter, Joe M. Byrne, Peter Kelehan, Mary McNamara, Hugh J. Byrne, and Fiona M. Lyng. **A study examining the effects of tissue processing on human tissue sections using vibrational spectroscopy**. *Vibrational Spectroscopy*, **38**(1-2):121–127, 2005. 71

[139] Russel J. Reiter, Dun-Xian Tan, Lucien C. Manchester, Sergio D. Paredes, Juan C. Mayo, and Rosa M. Sainz. **Melatonin and Reproduction Revisited**. *Biology of Reproduction*, **81**(3):445–456, 2009. 88, 89

[140] Xudong Qiu, Tida Kumbalasiri, Stephanie M. Carlson, Kwoon Y. Wong, Vanitha Krishna, Ignacio Provencio, and David M. Berson. **Induction of photosensitivity by heterologous expression of melanopsin**. *Nature*, **433**(7027):745–749, 2005. 10.1038/nature03345. 88

[141] R. Y. Moore, J. C. Speh, and J. P. Card. **The retinohypothalamic tract originates from a distinct subset of retinal ganglion cells**. *Journal of comparative neurology*, **352**(3):351–366, 1995. Research Support, Non-U.S. Gov't, Research Support, U.S. Gov't, P.H.S. 88

[142] S. Hattar, H.-W. Liao, M. Takao, D. M. Berson, and K.-W. Yau. **Melanopsin-Containing Retinal Ganglion Cells: Architecture, Projections, and Intrinsic Photosensitivity**. *Science*, **295**(5557):1065–1070, 2002. 88

[143] Robert Y. Moore MD. **Circadian rhythms: Basic neurobiology and clinical applications**. *Annual Review of Medicine*, **48**(1):253–266, 1997. 88

[144] Érika R. Ribeiro-Barbosa, Ana Lúcia Skorupa, and Newton S. Cipolla-Neto, Joséand Canteras. **Projections of the basal retrochiasmatic area: a neural site involved in the photic control of pineal metabolism**. *Brain Research*, **839**(1):35–40, 1999. 88

[145] Jiri Vanecek. **Cellular mechanisms of melatonin action**. *Physiological Reviews*, **78**(3):687–721, 1998. 88

[146] Beatriz Díaz López, E. Díaz Rodríguez, Colmenero Urquijo, and C. Fernández Álvarez. **Melatonin influences on the neuroendocrine-reproductive axis**. *Annals of the New York Academy of Sciences*, **1057**(1):337–364, 2005. 88

[147] Dennis S. Carter and Bruce D. Goldman. **Antigonadal effects of timed melatonin infusion in pinealectomized male Djungarian hamsters (Phodopus Sungorus Sungorus): Duration is the critical parameter**. *Endocrinology*, **113**(4):1261–1267, 1983. 89

[148] Alexander Lerchl and Stefan Schlatt. **Serotonin content and melatonin production in the pineal gland of the male Djungarian hamster (Phodopus sungorus)**. *Journal of Pineal Research*, **12**(3):128–134, 1992. 89

[149] A. Lerchl and S. Schlatt. **Influence of photoperiod on pineal melatonin synthesis, fur color, body weight, and reproductive function in the female djungarian hamster, phodopus sungorus**. *Neuroendocrinology*, **57**(2):359–364, 1993. 90, 93

[150] P. Niklowitz, A. Lerchl, and E. Nieschlag. **Photoperiodic responses in Djungarian hamsters (Phodopus Sungorus): Importance of light history for pineal and serum melatonin profiles.** *Biology of Reproduction*, **51**(4):714–724, 1994.

[151] Alexander Lerchl and Eberhard Nieschlag. **Diurnal Variations of Serum and Testicular Testosterone and Dihydrostestosterone (DHT) in Djungarian Hamsters (Phodopus sungorus): Testes Are the Main Source for Circulating DHT**. *General and Comparative Endocrinology*, **98**(2):129 – 136, 1995. 89, 93

[152] Curtis J. Gravis. **Testicular involution following optic enucleation: The Leydig cell**. *Cell and Tissue Research*, **185**:303–313, 1977. 10.1007/BF00220291. 89

[153] Johannes V. Swinnen and Guido Verhoeven. **Androgens and the control of lipid metabolism in human prostate cancer cells**. *Journal of Steroid Biochemistry and Molecular Biology*, **65**(1-6):191 – 198, 1998. 89

[154] Aino Alila-Johansson. *Daily and seasonal rhythms of melatonin, cortisol, leptin, free fatty acids and glycerol in goats*. PhD thesis, Department of Basic Veterinary Sciences, Faculty of Veterinary Medicine, University of Helsinki, Helsinki, Finland, 2008.

[155] Fatim-Zorah El-Hajjaji, Abdelkader Oumeddour, Aurélien J. C. Pommier, Aurélia Ouvrier, Emilie Viennois, Julie Dufour, Franoise Caira, Jo¨l R. Drevet, David H. Volle, Silvère Baron, Fabrice Saez, and Jean-Marc A. Lobaccaro. **Liver X receptors, lipids and their reproductive secrets in the male**. *Biochimica et Biophysica Acta-Molecular Basis of Disease*, **In Press, Corrected Proof**:–, 2011. 89

[156] Jing Shen, Alexander Lerchl, Patrice Donfack, Jiming Hu, and Arnulf Materny. **The influence of short-day photoperiods on bone composition of hamsters: A Raman spectroscopic investigation**. *Zeitschrift für Physikalische Chemie*, **225**(6-7):765–774, 2011. 89

[157] S.D. Markowitz and M.M. Bertagnolli. **Molecular origins of cancer: Molecular basis of colorectal cancer**. *New England Journal of Medicine*, **361**(25):2449–2460, December 2009. 104

[158] K Simons and R. Ehehalt. **Cholesterol, lipid rafts, and disease**. *Journal of Clinical Investigation*, **110**(5):597–603, 2002. 105

# REFERENCES


[159] M. R. Freeman and K. R. Solomon. **Cholesterol and prostate cancer**. *Journal of Cellular Biochemistry*, **91**(1):54–69, 2004. 105

[160] S. K. Patra. **Dissecting lipid raft facilitated cell signaling pathways in cancer**. *Biochimica et Biophysica Acta*, **1785**(2):182–206, 2008. 105

[161] VD. Di, K. R. Solomon, and M. R. Freeman. **Cholesterol and cholesterol-rich mem-branes in prostate cancer: an update**. *Tumori*, **94**(5):633–639, 2008. 105

[162] Gabriele Multhoff, Claus Botzler, Marion Wiesnet, Eva Müller, Thomas Meier, Wolfgang Wilmanns, and Rolf D. Issels. **A stress-inducible 72-kDa heat-shock protein (HSP72) is expressed on the surface of human tumor cells, but not on normal cells**. *International Journal of Cancer*, **61**(2):272–279, 1995. 105

[163] Stefan Stangl, Mathias Gehrmann, Ralf Dressel, Frauke Alves, Christian Dullin, George Themelis, Vasilis Ntziachristos, Eva Staeblein, Axel Walch, Isabel Winkelmann, and Gabriele Multhoff. **In vivo imaging of CT26 mouse tumours by using cmHsp70.1 monoclonal antibody**. *Journal of Cellular and Molecular Medicine*, **15**(4):874–887, 2011. 105, 106, 130, 131

[164] Mathias Gehrmann, Gerhard Liebisch, Gerd Schmitz, Robin Anderson, Claudia Steinem, Antonio De Maio, Graham Pockley, and Gabriele Multhoff. **Tumor-specific Hsp70 plasma membrane localization is enabled by the glycosphingolipid Gb3**. *PLoS ONE*, **3**(4):e1925, 2008. 105, 107, 109, 114, 115, 129, 130, 131

[165] G. Multhoff, C. Botzler, L. Jennen, J. Schmidt, J. Ellwart, and R. Issels. **Heat shock protein 72 on tumor cells: a recognition structure for natural killer cells**. *Journal of Immunology*, **158**(9):4341–4350, May 1997. 105, 106, 110, 115, 117

[166] Catharina Gross, Walter Koelch, Antonio DeMaio, Nelson Arispe, and Gabriele Multhoff. **Cell Surface-bound Heat Shock Protein 70 (Hsp70) Mediates Perforin-independent Apoptosis by Specific Binding and Uptake of Granzyme B**. *Journal of Biological Chemistry*, **278**(42):41173–41181, October 2003. 105, 106, 117, 130, 131

[167] J Radons and G Multhoff. **Immunostimulatory functions of membrane-bound and exported heat shock protein 70**. *Exercise Immunology Review*, **11**:17–33, 2005. 106, 107, 109, 114, 115, 129, 130

[168] G. Multhoff. **Heat shock protein 72 (HSP72), a hyperthermia-inducible immunogenic determinant on leukemic K562 and Ewing's sarcoma cells**. *International Journal of Hyperthermia*, **13**(1):39–48, 1997. DA - 19970430. 105, 106

[169] Harm H. Kampinga and Elizabeth A. Craig. **The HSP70 chaperone machinery: J proteins as drivers of functional specificity**. *Nature Reviews Molecular Cell Biology*, **11**(8):579–592, 2010. 10.1038/nrm2941. 105

[170] Richard I. Morimoto. **Cells in stress: transcriptional activation of heat shock genes**. *Science*, **259**(5100):1409–1410, March 5, 1993 1993. 106, 130, 131

[171] G. Riddihough and H. R Pelham. **Activation of the Drosophila Hsp27 promoter by heat shock and by ecdysone involves independent and remote regulatory sequences**. *EMBO Journal*, **5**(7):1653–1658, July 1986.

[172] D D Mosser, N G Theodorakis, and R I Morimoto. **Coordinate changes in heat shock element-binding activity and HSP70 gene transcription rates in human cells**. *Molecular and Cellular Biology*, **8**(11):4736–4744, November 1, 1988 1988.

[173] N F Cunniff, J Wagner, and W D Morgan. **Modular recognition of 5-base-pair DNA sequence motifs by human heat shock transcription factor**. *Molecular and Cellular Biology*, **11**(7):3504–3514, July 1, 1991 1991.

[174] H O Park and E A Craig. **Transcriptional regulation of a yeast HSP70 gene by heat shock factor and an upstream repression site-binding factor**. *Genes & Development*, **5**(7):1299–1308, July 1, 1991 1991.

[175] K Abravaya, M P Myers, S P Murphy, and R I Morimoto. **The human heat shock protein hsp70 interacts with HSF, the transcription factor that regulates heat shock gene expression**. *Genes & Development*, **6**(7):1153–1164, July 1, 1992 1992.

[176] Anne M. Fourie, Ted R. Hupp, David P. Lane, Bi-Ching Sang, Miguel S. Barbosa, Joseph F. Sambrook, and Mary-Jane H. Gething. **HSP70 Binding Sites in the Tumor Suppressor Protein p53**. *Journal of Biological Chemistry*, **272**(31):19471–19479, August 1, 1997 1997.

[177] Mami Hata and Kenzo Ohtsuka. **Characterization of HSE sequences in human Hsp40 gene: structural and promoter analysis**. *Biochimica et Biophysica Acta-Gene Structure and Expression*, **1397**(1):43–55, 1998.

[178] Gregory L. Blatch, Jeffrey L. Brodsky, and Andreas Bracher. **Nucleotide exchange factors for Hsp70 molecular chaperones**. In *Networking of Chaperones by Co-Chaperones*, Molecular Biology Intelligence Unit, pages 1–12. Springer New York, 2007.

[179] Jianwen Jiang, E. Guy Maes, Alexander B. Taylor, Liping Wang, Andrew P. Hinck, Eileen M. Lafer, and Rui Sousa. **Structural basis of J cochaperone binding and regulation of Hsp70**. *Molecular Cell*, **28**(3):422–433, 2007.

[180] Päivi Östling, Johanna K. Björk, Pia Roos-Mattjus, Valérie Mezger, and Lea Sistonen. **Heat shock factor 2 (HSF2) contributes to inducible expression of hsp genes through interplay with HSF1**. *Journal of Biological Chemistry*, **282**(10):7077–7086, March 9, 2007 2007.

[181] L. Shaner and K. A. Morano. **All in the family: atypical Hsp70 chaperones are conserved modulators of Hsp70 activity**. *Cell Stress & Chaperones*, **12**(1):1–8, Spring 2007. 131

[182] Dörthe M. Katschinski. **On heat and cells and proteins**. *Physiology*, **19**(1):11–15, February 1, 2004 2004. 106, 130, 131

[183] Claus Botzler, Jörg Schmidt, Arne Luz, Luise Jennen, Rolf Issels, and Gabriele Multhoff. **Differential Hsp70 plasma-membrane expression on primary human tumors and metastases in mice with severe combined immunodeficiency**. *International Journal of Cancer*, **77**(6):942–948, 1998. 106

[184] Markus Hantschel, Karin Pfister, Andreas Jordan, Regina Scholz, Reinhard Andreesen, Gerd Schmitz, Helga Schmetzer, Wolfgang Hiddemann, and Gabriele Multhoff. **Hsp70 plasma membrane expression on primary tumor biopsy material and bone marrow of leukemic patients**. *Cell Stress & Chaperones*, **5**(5):438–442, 2000/11/01 2000.

[185] K. Steiner, M. Graf, K. Hecht, S. Reif, L. Rossbacher, K. Pfister, H. J. Kolb, H. M. Schmetzer, and G. Multhoff. **High HSP70-membrane expression on leukemic cells from patients with acute myeloid leukemia is associated with a worse prognosis**. *Leukemia*, **20**(11):2076–2079, 2006.

[186] Fuad Lechin, Bertha van der Dijs, and Alex E. Lechin. **Natural killer cells activity and neuroimmunological treatment of cancer**. *Clinical Cancer Research*, **10**(23):8120–8121, December 1, 2004 2004.

[187] Feifan Zhou, Da Xing, and Wei R. Chen. **Dynamics and mechanism of HSP70 translocation induced by photodynamic therapy treatment**. *Cancer Letters*, **264**(1):135–144, 2008. 106

[188] Tamás Henics, Eszter Nagy, Hyun Ju Oh, Péer Csermely, Alexander von Gabain, and John R. Subjeck. **Mammalian Hsp70 and Hsp110 proteins bind to RNA motifs involved in mRNA stability**. *Journal of Biological Chemistry*, **274**(24):17318–17324, June 11, 1999 1999. 106

[189] Sirpa Lepp'a, Risto Kajanne, Laura Arminen, and Lea Sistonen. **Differential Induction of Hsp70-encoding Genes in Human Hematopoietic Cells**. *Journal of Biological Chemistry*, **276**(34):31713–31719, August 24, 2001 2001.

[190] Hollie S. Skaggs, Hongyan Xing, Donald C. Wilkerson, Lynea A. Murphy, Yiling Hong, Christopher N. Mayhew, and Kevin D. Sarge. **HSF1-TPR interaction facilitates export of stress-induced HSP70 mRNA**. *Journal of Biological Chemistry*, **282**(47):33902–33907, November 23, 2007 2007. 106

[191] Gabriele Multhoff, Karin Pfister, Mathias Gehrmann, Markus Hantschel, Catharina Gross, Michael Hafner, and Wolfgang Hiddemann. **A 14-mer Hsp70 peptide stimulates natural killer (NK) cell activity**. *Cell Stress & Chaperones*, **6**(4):337–344, 2001. 107, 109, 114, 115, 129, 130

[192] M. Gehrmann, J. Marienhagen, H. Eichholtz-Wirth, E. Fritz, J. Ellwart, M. Jaattela, T. Zilch, and G. Multhoff. **Dual function of membrane-bound heat shock protein 70 (Hsp70), Bag-4, and Hsp40: protection against radiation-induced effects and target structure for natural killer cells**. *Cell Death and Differentiation*, **12**(1):38–51, 2005. 107, 109, 114, 115, 129, 130

[193] M. Diem, M. Romeo, S. Boydston-White, M. Miljkovic, and C. Matthaus. **A decade of vibrational micro-spectroscopy of human cells and tissue (1994-2004)**. *Analyst*, **129**(10):880–885, 2004. 108

[194] Kurt W. Short, Susan Carpenter, James P. Freyer, and Judith R. Mourant. **Raman spectroscopy detects biochemical changes due to proliferation in mammalian cell cultures**. *Biophysical Journal*, **88**(6):4274–4288, 2005.

[195] R. Malini, K. Venkatakrishna, J. Kurien, Keerthilatha M. Pai, Lakshmi Rao, V. B. Kartha, and C. Murali Krishna. **Discrimination of normal, inflammatory, premalignant, and malignant oral tissue: A Raman spectroscopy study**. *Biopolymers*, **81**(3):179–193, 2006. 108

[196] Tobias J. Moritz, Douglas S. Taylor, Christopher R. Polage, Denise M. Krol, Stephen M. Lane, and James W. Chan. **Effect of cefazolin treatment on the nonresonant raman signatures of the metabolic state of individual escherichia coli cells**. *Analytical Chemistry*, **82**(7):2703–2710, 2010. 108

[197] Ning Bao, Jun Wang, and Chang Lu. **Recent advances in electric analysis of cells in microfluidic systems**. *Analytical and Bioanalytical Chemistry*, **391**(3):933–942, June 2008. 108

[198] Hsiang-Yu Wang, Ning Bao, and Chang Lu. **A microfluidic cell array with individually addressable culture chambers**. *Biosensors & Bioelectronics*, **24**(4):613–617, December 2008. 108

[199] Dakota A. Watson, Leif O. Brown, Daniel F. Gaskill, Mark Naivar, Steven W. Graves, Stephen K. Doorn, and John P. Nolan. **A flow cytometer for the measurement of Raman spectra**. *Cytometry part A*, **73**(2):119–128, February 2008. 108, 129

[200] Alexandru S. Biris, Ekaterina I. Galanzha, Zhongrui Li, Meena Mahmood, Yang Xu, and Vladimir P. Zharov. **In vivo Raman flow cytometry for real-time detection of carbon nanotube kinetics in lymph, blood, and tissues**. *Journal of Biomedical Optics*, **14**(2):021006, 2009. 108

[201] J. Dong, A. C. Drohat, J. T. Stivers, K. W. Pankiewicz, and P. R. Carey. **Raman spectroscopy of uracil DNA glycosylase-DNA complexes: Insights into DNA damage recognition and catalysis**. *Biochemistry*, **39**(43):13241–13250, Oct 31 2000. 122, 130

[202] Enoch W. Small and Warner L. Peticolas. **Conformational dependence of the Raman scattering intensities from polynucleotides**. *Biopolymers*, **10**(1):69–88, 1971. 130, 131

[203] P. Yakovchuk, E. Protozanova, and M. D. Frank-Kamenetskii. **Base-stacking and base-pairing contributions into thermal stability of the DNA double helix**. *Nucleic Acids Research*, **34**(2):564–574, 2006. 122, 132

[204] G. J. Thomas, Jr, G. C. Medeiros, and K. A. Hartman. % bf The dependence of raman scattering on the conformation of ribosomal RNA. *Biochemical and Biophysical Research Communications*, **44**(3):587 – 592, 1971. 130

[205] V. Reipa, G. Niaura, and D. H. Atha. **Conformational analysis of the telomerase RNA pseudoknot hairpin by Raman spectroscopy**. *RNA-A Publication of the RNA Society*, **13**(1):108–115, Jan 2007. 130

[206] L. Movileanu, J. M. Benevides, and G. J. Thomas. **Temperature dependence of the Raman spectrum of DNA. II. Raman signatures of premelting and melting transitions of poly(dA)-poly(dT) and comparison with poly(dA-dT)-poly(dA-dT)**. *Biopolymers*, **63**(3):181–194, Mar 2002. 130, 131

[207] Martin Hedegaard, Christoph Krafft, Henrik J. Ditzel, Lene E. Johansen, Soren Hassing, , and Jürgen Popp. **Discriminating isogenic cancer cells and identifying altered unsaturated fatty acid content as associated with metastasis status, using k-means clustering and partial least squares-discriminant analysis of Raman maps**. *Analytical Chemistry*, **82**:2797–2802, 2010. 133

[208] Aiguo Shen, Benjian Zhang, Jie Ping, Wei Xie, Patrice Donfack, Seong-Joon Baek, Xiaodong Zhou, Hui Wang, Arnulf Materny, and Jiming Hu. **In vivo study on the protection of indole-3-carbinol (I3C) against the mouse acute alcoholic liver injury by micro-Raman spectroscopy**. *Journal of Raman Spectroscopy*, **40**(5):550–555, 2009. 139, 151

[209] D. S. Xu. **Study survey of the pathogenesis of alcoholic liver disease**. *Chinese Journal of Gastroenterology*, **9**:46, 2004. 140

[210] P. A. Bonis, S. L. Friedman, and M. M. Kaplan. **Is liver fibrosis reversible?** *New England Journal of Medicine*, **344**(6):452–4, Feb 8 2001. 140

[211] R. Bataller and D. A. Brenner. **Hepatic stellate cells as a target for the treatment of liver fibrosis**. *Seminars in Liver Disease*, **21**(3):437–4351, Aug 2001. 140

[212] N. H. Afdhal and D. Nunes. **Evaluation of liver fibrosis: a concise review**. *The American journal of gastroenterology*, **99**(6):1160–1174, Jun 2004. 140

[213] Y. S. Kim and J. A. Milner. **Targets for indole-3-carbinol in cancer prevention**. *Journal of Nutritional Biochemistry*, **16**(2):65–73, Feb 2005. 140

[214] C. Zhang and H. Wang. **Protection of indole-3-carbinol against ethanol-induced hepatotoxicity in precision liver-cut slices of rats**. *Chinese Pharmacology Bulletin*, **20**:660–663, 2004. 140

[215] X. Q. Wu, H. Wang, and Z. X. Liao. **Effects of indole232carbinol on hepatic stellate cells activated by acetaldehyde in precision-cut liver slices.** *Chinese Pharmacology Bulletin*, **23**:441–445, 2007. 140

[216] J. Ping and H. Wang. 8th International Society for the Study of Xenobiotics (ISSX) Meeting, Japan, October 2007. 140

[217] S. L. Friedman. **Molecular regulation of hepatic fibrosis, an integrated cellular response to tissue injury**. *Journal of Biological Chemistry*, **275**(4):2247–2250, Jan 28 2000. 140, 147

[218] J. R. Perno, C. A. Grygon, and T. G. Spiro. **Ultraviolet Raman excitation profiles for the nucleotides and for the nucleic-acid duplexes poly(Ra)-poly(Ru) and poly(Dg-Dc)**. *Journal of Physical Chemistry*, **93**(15):5672–5678, Jul 27 1989. 141

[219] A. T. Tu. **Peptide backbone conformation and microenvironment of protein side chains**. In R. J. H. Clark and R. E. Hester, editors, *Spectroscopy of Biological Systems*, **13**, page 47. JohnWiley & Sonsx, New York, 1986. 141

[220] G. Deinum, D. Rodriguez, T. J. Romer, M. Fitzmaurice, J. R. Kramer, and M. S. Feld. **Histological classification of Raman spectra of human coronary artery atherosclerosis using principal component analysis**. *Applied Spectroscopy*, **53**(8):938–942, Aug 1999. 141

[221] A. G. Shen, Y. Ye, J. W. Zhang, X. H. Wang, J. M. Hu, W. Xie, and J. Shen. **Screening of gastric carcinoma cells in the human malignant gastric mucosa by confocal Raman microspectroscopy**. *Vibrational Spectroscopy*, **37**(2):225–231, Mar 17 2005. 141

[222] A. G. Shen, Y. Ye, X. H. Wang, C. C. Chen, H. B. Zhang, and J. M. Hu. **Raman scattering properties of human pterygium tissue**. *Journal of Biomedical Optics*, **10**(2):024036, Apr. 13 2005. 141

[223] P. Rösch, M. Harz, M. Schmitt, and J. Popp. **Raman spectroscopic identification of single yeast cells**. *Journal of Raman Spectroscopy*, **36**(5):377–379, May 2005. 141

[224] P. J. Caspers, A. C. Williams, E. A. Carter, H. G. M. Edwards, B. W. Barry, H. A. Bruining, and G. J. Puppels. **Monitoring the penetration enhancer dimethyl sulfoxide in human stratum corneum in vivo by confocal Raman spectroscopy**. *Pharmaceutical Research*, **19**(10):1577–1580, Oct 2002. 141

[225] A. G. Shen, Z. X. Liao, H. Wang, L. H. Goan, Y. Wu, X. H. Wang, Z. Y. Yu, and J. M. Hu. **Study on the in vitro and in vivo activation of rat hepatic stellate cells by Raman spectroscopy**. *Journal of Biomedical Optics*, **12**(3):034003, May-Jun 2007. 141

# REFERENCES


[226] J. Ping, H. Wang, M. Huang, and Z. S. Liu. **Genetic analysis of glutathione S-transferase A1 polymorphism in the Chinese population and the influence of genotype on enzymatic properties**. *Toxicological Sciences*, **89**(2):438–443, Feb 2006. 142

[227] S. J. Baek, A. Park, J. Kim, A. G. Shen, and J. M. Hu. **A simple background elimination method for Raman spectra**. *Chemometrics and Intelligent Laboratory Systems*, **98**(1):24–30, Aug 15 2009. 143

[228] Y. G. Hu, T. Jiang, A. G. Shen, W. Li, X. P. Wang, and J. M. Hu. **A background elimination method based on wavelet transform for Raman spectra**. *Chemometrics and Intelligent Laboratory Systems*, **85**(1):94–101, Jan 15 2007. 144

[229] J. T. Edsall, J. W. Otvos, and A. Rich. **Raman Spectra of Amino Acids and Related Compounds .7. Glycylglycine, Cysteine, Cystine and Other Amino Acids**. *Journal of the American Chemical Society*, **72**(1):474–477, 1950. 145, 147

[230] Joke De Gelder, Kris De Gussem, Peter Vandenabeele, and Luc Moens. **Reference database of Raman spectra of biological molecules**. *Journal of Raman Spectroscopy*, **38**(9):1133–1147, 2007. 145

[231] J. Zhao, H. Chen, and Y. Li. **Protective effect of bicyclol on acute alcohol-induced liver injury in mice**. *European Journal of Pharmacology*, **586**(1-3):322–331, May 31 2008. 147

[232] C. J. Frank, R. L. Mccreery, and D. C. B. Redd. **Raman-Spectroscopy of Normal and Diseased Human Breast Tissues**. *Analytical Chemistry*, **67**(5):777–783, Mar 1 1995. 147

[233] X. H. Huang, I. H. El-Sayed, W. Qian, and M. A. El-Sayed. **Cancer cell imaging and photothermal therapy in the near-infrared region by using gold nanorods**. *Journal of the American Chemical Society*, **128**(6):2115–2120, Feb 15 2006. 151

[234] Y. T. Lim, M. Y. Cho, B. S. Choi, J. M. Lee, and B. H. Chung. **Paramagnetic gold nanostructures for dual modal bioimaging and phototherapy of cancer cells**. *Chemical Communications*, (40):4930–4932, 2008. 151

[235] P. Sharma, S. Brown, G. Walter, S. Santra, and B. Moudgil. **Nanoparticles for bioimaging**. *Advances in Colloid and Interface Science*, **123-126**:471–485, Nov 16 2006. 151

[236] Y. C. Cao, R. Jin, and C. A. Mirkin. **Nanoparticles with Raman spectroscopic fingerprints for DNA and RNA detection**. *Science*, **297**(5586):1536–40, Aug 30 2002. 151

[237] S. J. Park, T. A. Taton, and C. A. Mirkin. **Array-based electrical detection of DNA with nanoparticle probes**. *Science*, **295**(5559):1503–1506, Feb 22 2002. 151

[238] X. M. Qian and S. M. Nie. **Single-molecule and single-nanoparticle SERS: from fundamental mechanisms to biomedical applications**. *Chemical Society Reviews*, **37**(5):912–920, May 2008. 151

[239] S. Alayoglu and B. Eichhorn. **Rh-Pt bimetallic catalysts: synthesis, characterization, and catalysis of core-shell, alloy, and monometallic nanoparticles**. *Journal of the American Chemical Society*, **130**(51):17479–86, Dec 24 2008. 151

[240] M. Pelton, M. Liu, H. Y. Kim, G. Smith, P. Guyot-Sionnest, and N. F. Scherer. **Optical trapping and alignment of single gold nanorods by using plasmon resonances**. *Optics Letters*, **31**(13):2075–2077, Jul 1 2006. 151

[241] C. Z. Li, K. B. Male, S. Hrapovic, and J. H. Luong. **Fluorescence properties of gold nanorods and their application for DNA biosensing**. *Chemical Communications*, (31):3924–3926, Aug 21 2005. 152

[242] H. Wang, T. B. Huff, D. A. Zweifel, W. He, P. S. Low, A. Wei, and J. X. Cheng. **In vitro and in vivo two-photon luminescence imaging of single gold nanorods**. *Proceedings of the National Academy of Sciences of the United States of America*, **102**(44):15752–15756, Nov 1 2005. 152

[243] Hyung Ju Ryu, Luz Sanchez, Heidrun A. Keul, Aanchal Raj, and Michael R. Bockstaller. **Imidazolium-based ionic liquids as efficient shape-regulating solvents for the synthesis of gold nanorods**. *Angewandte Chemie International Edition*, **47**(40):7639–7643, 2008. 152

[244] F. Kim, K. Sohn, J. Wu, and J. Huang. **Chemical synthesis of gold nanowires in acidic solutions**. *Journal of the American Chemical Society*, **130**(44):14442–14443, Nov 5 2008. 152

[245] J. H. Song, F. Kim, D. Kim, and P. Yang. **Crystal overgrowth on gold nanorods: tuning the shape, facet, aspect ratio, and composition of the nanorods**. *Chemistry*, **11**(3):910–916, Jan 21 2005. 152

[246] X. Kou, S. Zhang, Z. Yang, C. K. Tsung, G. D. Stucky, L. Sun, J. Wang, and C. Yan. **Glutathione- and cysteine-induced transverse overgrowth on gold nanorods**. *Journal of the American Chemical Society*, **129**(20):6402–4, May 23 2007. 152

[247] Y. Sun and Y. Xia. **Shape-controlled synthesis of gold and silver nanoparticles**. *Science*, **298**(5601):2176–2179, Dec 13 2002. 152

[248] J. Song, Y. Chu, Y. Liu, L. Li, and W. Sun. **Room-temperature controllable fabrication of silver nanoplates reduced by aniline**. *Chemical Communications*, (10):1223–1225, Mar 14 2008. 152

[249] J. Chen, J. M. McLellan, A. Siekkinen, Y. Xiong, Z. Y. Li, and Y. Xia. **Facile synthesis of gold-silver nanocages with controllable pores on the surface**. *Journal of the American Chemical Society*, **128**(46):14776–7, Nov 22 2006. 152

[250] X. Lu, L. Au, J. McLellan, Z. Y. Li, M. Marquez, and Y. Xia. **Fabrication of cubic nanocages and nanoframes by dealloying Au/Ag alloy nanoboxes with an aqueous etchant based on Fe(NO3)3 or NH4OH**. *Nano Letters*, **7**(6):1764–1769, Jun 2007. 152

[251] T. K. Sau and C. J. Murphy. **Self-assembly patterns formed upon solvent evaporation of aqueous cetyltrimethylammonium bromide-coated gold nanoparticles of various shapes**. *Langmuir*, **21**(7):2923–2929, Mar 29 2005. 152

[252] Y. Yin, C. Erdonmez, S. Aloni, and A. P. Alivisatos. **Faceting of nanocrystals during chemical transformation: from solid silver spheres to hollow gold octahedra**. *Journal of the American Chemical Society*, **128**(39):12671–12673, Oct 4 2006. 152

[253] X. Lu, H. Y. Tuan, J. Chen, Z. Y. Li, B. A. Korgel, and Y. Xia. **Mechanistic studies on the galvanic replacement reaction between multiply twinned particles of Ag and HAuCl4 in an organic medium**. *Journal of the American Chemical Society*, **129**(6):1733–1742, Feb 14 2007.

[254] Y. Sun and Y. Xia. **Mechanistic study on the replacement reaction between silver nanostructures and chloroauric acid in aqueous medium**. *Journal of the American Chemical Society*, **126**(12):3892–3901, Mar 31 2004.

[255] B. G. Prevo, S. A. Esakoff, A. Mikhailovsky, and J. A. Zasadzinski. **Scalable routes to gold nanoshells with tunable sizes and response to near-infrared pulsed-laser irradiation**. *Small*, **4**(8):1183–1195, Aug 2008. 152

[256] S. E. Skrabalak, J. Chen, Y. Sun, X. Lu, L. Au, C. M. Cobley, and Y. Xia. **Gold nanocages: synthesis, properties, and applications**. *Accounts of Chemical Research*, **41**(12):1587–1595, Dec 2008. 152, 155

[257] T. Shoeib, A. Cunje, A. C. Hopkinson, and K. W. M. Siu. **Gas-phase fragmentation of the Ag+-phenylalanine complex: Cation-pi interactions and radical cation formation**. *Journal of the American Society for Mass Spectrometry*, **13**(4):408–416, Apr 2002. 161

[258] A. Otto. **Surface-Enhanced Raman-Scattering - Classical and Chemical Origins**. In M. Cardona and G. Gntherodt, editors, *Light Scattering in Solids IV*, **54** of *Topics of Applied Physics*, pages 289–418. Springer-Verlag, Berlin, 1984. 161

[259] George C. Schatz and Richard P. Van Duyne. **Electromagnetic mechanism of surface-enhanced spectroscopy**. In J. M. Chalmers and P. R. Griffiths, editors, *Handbook of Vibrational Spectroscopy*, pages 1–16. John Wiley & Sons, Ltd, 2006.

[260] R. L. Birke and J. R. Lombardi. **Surface-enhanced Raman scattering**. In R. J. Gale, editor, *Spectroelectrochemistry: Theory and Practice*, chapter 6, pages 263–348. Plenum Press, New York, 1988. 161

[261] K. Kneipp, H. Kneipp, I. Itzkan, R. R. Dasari, and M. S. Feld. **Ultrasensitive chemical analysis by Raman spectroscopy**. *Chemical Reviews*, **99**(10):2957, Oct 1999. 161

[262] A. Singha, S. Dasgupta, and A. Roy. **Comparison of metal-amino acid interaction in Phe-Ag and Tyr-Ag complexes by spectroscopic measurements**. *Biophysical Chemistry*, **120**(3):215–224, Apr 1 2006. 161, 162, 167

[263] E. J. Zeman and G. C. Schatz. **An Accurate Electromagnetic Theory Study of Surface Enhancement Factors for Ag, Au, Cu, Li, Na, Al, Ga, in, Zn, and Cd**. *Journal of Physical Chemistry*, **91**(3):634–643, Jan 29 1987. 162

[264] A. Otto, I. Mrozek, H. Grabhorn, and W. Akemann. **Surface-enhanced Raman scattering**. *Journal of Physics-Condensed Matter*, **4**(5):1143–1212, Feb 3 1992. 162

[265] M. Sackmann and A. Materny. **Surface enhanced Raman scattering (SERS) - a quantitative analytical tool?** *Journal of Raman Spectroscopy*, **37**(1-3):305–310, Jan-Mar 2006. 162

[266] Haiying Zhao, Bo Yuan, and Xiaoming Dou. **The effects of electrostatic interaction between biological molecules and nano-metal colloid on near-infrared surface-enhanced Raman scattering**. *Journal of Optics A-Pure and Applied Optics*, **6**(9):900, 2004. 162

# List of Publications

## • Selected Journal Articles & Book Chapter

1. Elena A. Sagitova, **Patrice Donfack**, Kirill A. Prokhorov, Goulnara Yu. Nikolaeva, Viktor A. Gerasin, Nadezhda D. Merekalova, Arnulf Materny, Evgeny M. Antipov and Pavel P. Pashinin; Raman Spectroscopic Characterization of the Interlayer Structure of $Na^+$-Montmorillonite Clay Modified by Ditetradecyl Dimethyl Ammonium Bromide; *Journal of Physical Chemistry B*, **2009** May 28, Vol. 113 (21), 7482-7490.

2. **Patrice Donfack**, Maren Rehders, Klaudia Brix, Petra Boukamp and Arnulf Materny; Micro Raman spectroscopy for Monitoring Alterations Between Human Skin Keratinocytes HaCaT and Their Tumorigenic Derivatives A5RT3 - Toward a Raman Characterization of a Skin Carcinoma Model; *Journal of Raman Spectroscopy*, **2010**, Vol. 41 (1), 16-26.

3. **Patrice Donfack**, Gabriele Multhoff and Arnulf Materny; Label-Free Nondestructive Discrimination of Colon Carcinoma Sublines and Biomolecular Insights into Their Differential Hsp70 Expression - DNA/RNA Nucleobase Specific Changes; *ChemBioChem*, **2010**, in Press.

4. Aiguo Shen, Jie Ping, Wei Xie, **Patrice Donfack**, Seong-Joon Baek, Xiaodong Zhou, Hui Wang, Arnulf Materny and Jiming Hu; *In vivo* Study on the Protection of Indole-3-Carbinol (I3C) Against the Mouse Acute Alcoholic Liver Injury by Micro-Raman Spectroscopy; *Journal of Raman Spectroscopy*, **2009**, Vol. 40 (5), 550-555.

5. Wei Xie, Le Su, **Patrice Donfack**, Aiguo Shen, Xiaodong Zhou, Malte Sackmann, Arnulf Materny and Jiming Hu; Synthesis of Gold Nanopeanuts by Citrate Reduction of Gold Chloride on Gold-Silver Core-Shell Nanoparticles; *Chemical Communications*, **2009** (35), 5263-5265.

6. Jing Shen, Alexander Lerchl, **Patrice Donfack**, Arnulf Materny and Jiming Hu; The Influence of Short-Day Photoperiods on Bone Composition of Hamsters: A Raman Spectroscopic Investigation; *Zeitschrift für Physikalische Chemie* **2011**, Vol. 225 (6-7), 765-774

7. Rasha M. El-Abassy, **Patrice Donfack** and Arnulf Materny; Rapid Determination of Free Fatty Acid in Extra Virgin Olive Oil by Raman Spectroscopy and Multivariate Analysis; *Journal of the American Oil Chemists' Society*, **2009**, Vol. 86 (6), 507-511.

8. Rasha M. El-Abassy, **Patrice Donfack** and Arnulf Materny; Visible Raman Spectroscopy for the Discrimination of Olive Oils from Different Vegetable Oils and the Detection of Adulteration; *Journal of Raman Spectroscopy*, **2009**, Vol. 40 (9), 1284-1289.

9. Rasha M. El-Abassy, **Patrice Donfack** and Arnulf Materny; Assessment of Conventional and Microwave Heating Induced Degradation of Carotenoids in Olive Oil by VIS Raman Spectroscopy and Classical Methods; *Food Research International*, **2010**, Vol. 43 (3), 694-700.

10. Rasha M. El-Abassy, Pinkie J. Eravuchira, **Patrice Donfack**, Bernd von der Kammer and Arnulf Materny; Fast Determination of Milk Fat Content Using Raman Spectroscopy; *Vibrational Spectroscopy*, (**2011**) May, Vol.56 (1), 3-8.

11. Rasha M. El-Abassy, **Patrice Donfack** and Arnulf Materny; Discrimination Between Arabica and Robusta Green Coffee Using Visible Micro Raman Spectroscopy and Chemometric Analysis; *Food Chemistry*, [**2010** Vol. 126 (3), 1 June 2011, 1443-1448] Received 16 September 2009, revised 16 September 2010; accepted 22 November. Available online 26 November 2010.

12. Rasha M. El-Abassy, Pinkie J. Eravuchira, **Patrice Donfack**, Bernd von der Kammer and Arnulf Materny; Direct Determination of Unsaturation Level of Milk Fat Using Raman Spectroscopy; *Applied Spectroscopy*, (Submitted: 2010) **2011**, Accepted.

13. **'Book Chapter'**
Rasha M. El-Abassy, **Patrice Donfack** and Arnulf Materny (2011). Assessment of Microwave versus Conventional Heating Induced Degradation of Olive Oil by VIS Raman Spectroscopy and Classical Methods; Advances in Induction and Microwave Heating of Mineral and Organic Materials, Stanislaw Grundas (Ed.), ISBN: 978-953-307-522-8, InTech, Available from: http://www.intechopen.com/articles/show/title/assessment-of-microwave-versus-conventional-heating-induced-degradation-of-olive-oil-by-vis-raman-sp

**{ Articles under consideration: Note eventual changes due to revision in the publications in final form }**

14. Elena A. Sagitova, **Patrice Donfack**, Kirill A. Prokhorov, Goulnara Yu. Nikolaeva, Viktor A. Gerasin, Nadezhda D. Merekalova, Arnulf Materny, Evgeny M. Antipov, and Pavel P. Pashinin (2011); Symmetric C-C Stretching Mode Splitting *vs.* Alkyl Conformation Order in Sodium Montmorillonite Modified by Cetyltrimethylammonium Bromide; *Soft Matter*, **2011**, submitted.

15. Animesh K. Ojha, **Patrice Donfack** and Arnulf Materny; Complex Concentration Dependence of SERS and UV-VIS Absorption of Glycine/Ag-Substrates Due to Glycine-Mediated Ag-Nanostructures Modifications; *Journal of Raman Spectroscopy* **2010**, Submitted.

16. **Patrice Donfack**, Karen Grote, Alexander Lerchl and Arnulf Materny; Probing Lymphoma Infiltration in the Spleens of AKR/J Lymphoma Mice Chronically Exposed in Risk Assessment Studies to Electromagnetic Fields, Toward Raman Spectroscopic Discrimination and Modeling of Cancer Incidence; *Physical Biology*, **2011**, Submitted.

17. **Patrice Donfack**, Karen Grote, Alexander Lerchl, and Arnulf Materny; Raman Spectroscopic Approach for *in-situ* Biological Rhythm Studies in Light-Sensitive Mammals - Probing Physiological Response of Short/Long Day Photoperiods in Hamster Tissues; *Physical Biology*, **2011**, submitted.

18. Pinkie Jacob Eravuchira, Rasha M. El-Abassy, Bernd von der Kammer, **Patrice Donfack** and Arnulf Materny; Rapid Classification of Citrus Oils and their Carotenoid Content Quantification Using Raman Spectroscopy; **2011**, submitted.

## • Selected Works Published in Conference Books of Abstracts

## [2011]

1. **Patrice Donfack**, Elena A. Sagitova, Kirill A. Prokhorov, Kirill V. Vodopianov, Goulnara Yu. Nikolaeva, Viktor A. Gerasin, Nadezhda D. Merekalova, Arnulf Materny, Evgeny M. Antipov and Pavel P. Pashinin.
Unique Splitting Behavior of the C-C Symmetric Stretching Mode as a Raman Signature of Conformational Order of Intercalated Alkyl Chains in Modified Clay Composites; "**Nanoparticles and Composite Materials I**"
*Book of Abstracts*, **DPG-Tagung 2011**; TU Dresden, Dresden, Germany.

2. **Patrice Donfack**, Gabriele Multhoff and Arnulf Materny.
Towards Non-Invasive Cell Sorting and Specific Insights into Differential Hsp70 Expression in Colon Carcinoma Sublines; "**Biopolymers & Biomaterials**"
*Book of Abstracts*, **DPG-Tagung 2011**; TU Dresden, Dresden, Germany.

3. **Patrice Donfack**, Animesh K. Ojha and Arnulf Materny.
Complex Concentration Dependence of Glycine-Induced Structural Modification of Silver Nanoparticles Investigated by UV-VIS, SERS, and TEM; "**Linear and nonlinear Raman Spectroscopy**"
*Book of Abstracts*, **DPG-Tagung 2011**; TU Dresden, Dresden, Germany.

4. **Patrice Donfack**, Kirill A. Prokhorov, Elena A. Sagitova, Goulnara Yu. Nikolaeva, M. Guseva, Viktor A. Gerasin, Arnulf Materny, Evgeny M. Antipov, Pavel P. Pashinin.
Raman Evaluation of the Structure of Organic Materials by Analyzing the Region of Stretching Vibrations of $CH_2$ and $CH_3$ Groups - Benefits and Limitations
European Polymer Congress EPF 2011, and XII Congress of the Specialized Group of Polymers GEP **EPF 2011 and XII GEP**; Granada Congress Centre "Palacio de Exposiciones y Congresos", Granada, Spain.

# [2010]

5. **Patrice Donfack**, Kirill V. Vodopianov, Kirill A. Prokhorov, Elena A. Sagitova, Goulnara Yu. Nikolaeva, Viktor A. Gerasin, B. Shklyaruk, Arnulf Materny, Evgeny M. Antipov and Pavel P. Pashinin.
Raman Characterization of n-Alkanes, Alkylammonium Salts, and Simple Polyolefins: Common Features and New Approaches for Structural Analysis;
*ESOPS 18 - Book of Abstracts*, P14, 18th European Symposium on Polymer spectroscopy **ESOPS 18, 2010**; Zadar, Croatia.

6. Elena A. Sagitova, **Patrice Donfack**, Kirill A. Prokhorov, Kirill V. Vodopianov, Goulnara Yu. Nikolaeva, Pavel P. Pashinin, Viktor A. Gerasin, Nadezhda D. Merekalova, Arnulf Materny and Evgeny M. Antipov.
Raman Spectroscopy Of Novel Polymer Composites "**Modern Trends in Laser Physics**"
*LPHYS'10 Book of Abstracts*, 19th International Laser Physics Workshop **LPHYS 2010**; Foz do Iguaçu, Brazil.

7. **Patrice Donfack**, Gabriele Multhoff and Arnulf Materny.
Probing Molecular Profiles of Tumorigenicity in Colon Carcinoma Differential Tumor Cells Associated with a Tumor-Specific Lipid Marker by Raman Spectroscopy; "**Molecular Physics: Biomecules**"
*Book of Abstracts*, **DPG-Tagung 2010**; Leibniz University Hannover, Hannover, Germany.

8. **Patrice Donfack**, Animesh K. Ojha and Arnulf Materny.
Critical Concentration Dependent SERS of Glycine Consistent with Silver Nanoparticles Modification Induced by Glycine-Silver Interaction; "**SERS (substrate development, single molecule, theory) II**"
*ICORS-2010 Book of Abstracts*, XXII International Conference on Raman Spectroscopy **ICORS 2010**; Boston, Massachusetts, USA.

9. **Patrice Donfack**, Gabriele Multhoff and Arnulf Materny.
Raman Spectroscopic Probing of Molecular Profiles of Tumorigenicity in Colon Carcinoma Differential Cell Lines Associated with a Tumor-Specific Lipid Marker; "**Biomedical Applications**"
*ICORS-2010 Book of Abstracts*, XXII International Conference on Raman Spectroscopy **ICORS 2010**; Boston, Massachusetts, USA.

# [2009]

10. Elena A. Sagitova, **Patrice Donfack**, Kirill A. Prokhorov, Goulnara Yu. Nikolaeva, Viktor A. Gerasin, Nadezhda D. Merekalova, Arnulf Materny, Evgeny M. Antipov and Pavel P. Pashinin.
Raman Study and Modeling of $CH_2$-Chains in Confined Nanosize Space of Modified Clays "**Modern Trends in Laser Physics**"
*LPHYS'09 Book of Abstracts*, 18th International Laser Physics Workshop **LPHYS 2009**; Barcelona, Spain.

11. Yu.V. Shemouratov, **Patrice Donfack**, Kirill V. Vodopianov, Kirill A. Prokhorov, Elena A. Sagitova, Goulnara Yu. Nikolaeva, Viktor A. Gerasin, Nadezhda D. Merekalova, Arnulf Materny, Evgeny M. Antipov and Pavel P. Pashinin.
Raman Spectroscopy of Hydrocarbons "**Modern Trends in Laser Physics**"
*LPHYS'09 Book of Abstracts*, 18th International Laser Physics Workshop **LPHYS 2009**; Barcelona, Spain.

12. **Patrice Donfack**, Alexander Lerchl and Arnulf Materny.
Raman Study of AKR/J Mice Spleen at Different Excitation and Bleaching Profiles, and of Hormonal and Tumorigenic Changes in Hamsters; "**Molecular Physics: Biomecules**"
*Book of Abstracts*, **DPG-Tagung 2009**; Hamburg University, Hamburg, Germany.

# [2008]

13. Elena A. Sagitova, Kirill A. Prokhorov, **Patrice Donfack**, Arnulf Materny, Goulnara Yu. Nikolaeva, Viktor A. Gerasin, Nadezhda D. Merekalova and Pavel P. Pashinin.
Interlayer Structure of Fillers For Polymer-Clay Nanocomposites Revealed By Raman Scattering "**Modern Trends in Laser Physics**"
*LPHYS'08 Book of Abstracts*, 17th International Laser Physics Workshop **LPHYS 2008**; Norwegian University of Science and Technology (NTNU), Trondheim, Norway.

14. **Patrice Donfack**, Jing Shen, Alexander Lerchl and Arnulf Materny.
Raman Spectroscopy for the Characterization of Animal Tissue - Toward Molecular Monitoring of Tumorigenicity and Hormonal Changes; "**Molecular Physics: Biomecules**"
*Book of Abstracts*, **DPG-Tagung 2008**; Darmstadt, Germany.

15. **Patrice Donfack**, Maren Rehders, Klaudia Brix and Arnulf Materny.
Raman Spectroscopy Discrimination of HaCaT and A5RT3 Human Skin Model Cell Lines; "**Molecular Physics: Biomecules**"
*Book of Abstracts*, **DPG-Tagung 2008**; Darmstadt, Germany.

# [2007]

16. **Patrice Donfack**, Malte Sackmann and Arnulf Materny.
Screening Biological Systems by Raman Scattering Techniques - Towards Specific Characterization of Tumors on a Molecular Level; "**Molecular Physics: Biomecules**"
*Book of Abstracts*, **DPG-Tagung 2007**; Heinrich-Heine-University Düsseldorf, Düsseldorf, Germany.

# CURRICULUM VITAE


## Patrice Donfack

*Current address & contact information*

- *Nationality*: **Cameroon**
- *Birth date:* **20-03-1978**
- *In:* **Ndungated, Cameroon**
- *Gender:* **Male**
- *Marital Status:* **Single**
- **Campus Ring 1, 28759, Bremen, Germany**
- *Contact:* **p.donfack@jacobs-university.de**
- *Tel.:* **04212005107**


## Education — Degree/Achievements

**4/2006 – 5/2011** — **Jacobs University,** School of Engineering and Science**, Germany**
Doctoral research (PhD): • Physics • Chemical/bio/medical/nanophysics
**Doctor of Philosophy in Physics**

**10/2000-2/2003** — **University of Yaoundé I, Cameroon:** Graduate studies: Physics
Material Science physics. Diploma (PhD qualifying exam) program and public defense of the thesis. Topic: **Triplet Excitons in Crystals**
**Master's Degree in Physics**
**DEA (PhD Qualifying ) Degree**
(Specialization: Material Science)

**10/1999-9/2000** — **University of Dschang, Cameroon:** Undergraduate studies: Physics and chemistry: 1st year. Physics: 2nd, 3rd (specialization: Electronics) year.
**Bachelor of Science in Physics:**

## Teaching experience and Extracurricular Activities

**10/2002 - 9/2005** — **University of Yaoundé I, Cameroon** : **A cumulative two-year (four semesters) teaching experience**
Physics lab courses (PH 105, PH 122): 1st-year university majors (physics/chemistry/mathematics/life Science)

**9/2007 to date** — **Jacobs University, Bremen, Germany** • **Resident Associate** in the Alfried Krupp College • Member of the student and staff football teams, athletic club (till 2010), and olympics organization committee (till 2009)

## Scientific Achievements, Awards and Distinctions

**Publications** — **See list of publications: Journal publications and conference contributions**

**Awards**
- **Research grant** (2003); Ministry of higher Education, Cameroon: "Research Work Finalization Support"
- **DAAD Scholarship** (2005-2009): Grant for Doctoral Research, including 6-month German course

**Distinctions**
- **PhD Degree awarded with Distinction** (2011)
- **DAAD nominee and awarded invitation to the Landau 2008 Nobel meeting dedicated to physics**

## Practical Experience

**10/2002 - 9/2005** — **University of Yaoundé I, Cameroon :** Assembling electronic and optical setups for physics lab courses

**12/2006 to date** — **Jacobs University, Bremen, Germany**
- Expertise: Laser systems, optical alignment, UV-VIS spectrometers, Raman systems adjustment, etc.
  - Optimization: Triple spectrometer single mode and motorized options for Raman imaging
  - Testing a single beam Multiplex CARS for resonant detection resp. cancer diagnosis
- Experience with transmission electron (TEM), atomic force (AFM), fluorescence microscopes, etc.

## Wide Scope Research and Project Experience and International Collaboration

**9/2001-2/2003** — **University of Yaoundé I, Cameroon:** Diploma research. Topic: **Triplet Excitons in Crystals**

**4/2006 to date** — **Jacobs University, Bremen, Germany**: Main PhD research. Thesis**:** **Raman Spectroscopic Probing of Key Biological Events – Tumorigenesis, Hsp70 Chaperon Mechanisms, and Therapy Response**

**5/2007 to date** — **Collaboration in applications of Raman spectroscopy combined with simulation or statistics:**

- Food quality control (edible oils, coffee, milk, etc)**:** At the host institution **(Jacobs University, Germany)**
- Filler's (clay) nano-sized interlayer gallery structure modeling and determination, and realistic models for nanocomposite engineering: **(Jacobs University,** with my collaborator from **Moscow University, Russia)**
- Tissue/cells diagnosis, drug response, and nanoscience (fabrication of tunable metal nanoparticles): Research visits in 2007 & 2008 (**Wuhan University,** School of Chemistry & Molecular Biology, **China)**

# CURRICULUM VITAE

## Skills and Hobby

**Languages:**
- **French** (official, first; mother tongue) • **English** (official, first; fluent) • **German** (third, C2-grade)
- **Spanish (**forth; basics) • **Chinese** (beginner level) • Computer languages: **Pascal**, **Fortran 90**, etc.

**Platform/Software**
- **Windows**/ Proficient in Word, Latex, Origin, Photoshop, CorelDraw, statistical analysis (Unscrambler), etc.
- Other softwares (Open Office, MatLab, Gaussian, etc.)

**Accessories**
- **Reading**, Debating & **Learning more Languages** • Sports (**football**, **running**, cycling) • **Dance**

## National Workshops and Conferences, and International Conferences

**Workshops/**
- **Summer school** 24/06-01/07 2006, Jacobs University, Germany:
  "Complex Material: Cooperative project of the Natural, Engineering and Biosciences".
- **DAAD Sommerakademie**, 12/08 – 25/08/2007, Rot an der Rot, Germany:
  Cortical Reorganization Following Macular Degeneration (oral presentation)

**Conferences (International):**
- **Attended: ICORS-2010; XXII International Conference on Raman Spectroscopy;**
  **Boston, Massachusetts, USA: Two accepted contributions**

1) Raman Spectroscopic Probing of Molecular Profiles of Tumorigenicity in Colon Carcinoma Differential Cell Lines Associated with a Tumor-Specific Lipid Marker
2) Critical Concentration Dependent SERS of Glycine Consistent with Silver Nanoparticles Modification Induced by Glycine-Silver Interaction

❖ **Other Contributed International conferences**

• European Polymer Congress EPF 2011, and XII Congress of the Specialized Group of Polymers GEP (**Granada, Spain)** • 18th European Symposium on Polymer spectroscopy (ESOPS 2010, **Zadar, Croatia**) • International Laser Physics Workshops (■ LPHYS 2010, Foz do **Iguacu, Brazil**; ■ LPHYS 2009, **Barcelona, Spain** (twice); ■ LPHYS 2008, **Trondheim, Norway**)

**(National):**

❖ **All DPG (German physical Society) conferences from 2007 to 2011, Germany attended**:

- **DPG 2011 (Dresden):** One poster and two oral presentations:

1) Towards Non-Invasive Cell Sorting and Specific Insights into Differential Hsp70 Expression in Colon Carcinoma Sublines.
2) Unique Splitting Behavior of the C-C Symmetric Stretching Mode as a Raman Signature of Conformational Order of Intercalated Alkyl Chains in Modified Clay Composites.
3) Complex Concentration Dependence of Glycine-Induced Structural Modification of Silver Nanoparticles Investigated by UV-VIS, SERS, and TEM

• **DPG 2010** (Hannover): a poster • **DPG 2009:** a poster presentation • **DPG 2008** (Darmstadt): a poster and an oral presentations • **DPG 2007** (Düsseldorlf): a poster presentation

See details about other attended national and contributed international conferences in the list of publications